High-resolution temporal records of magmatism, sedimentation, and faulting at evolving plate boundaries

By

Michael Patterson Eddy

B.A. Geoscience
Princeton University, 2011

Submitted to the Department of Earth, Atmospheric, and Planetary Sciences
in partial fulfillment of the requirements for the degree of

Doctor of Philosophy

in Geology

at the

MASSACHUSETTS INSTITUTE OF TECHNOLOGY

February 2017

Author: Signature redacted
Department of Earth, Atmospheric, and Planetary Sciences
September 22, 2016

Certified by: Signature redacted
Oliver Jagoutz
Associate Professor of Geology
Thesis Supervisor

Accepted by: Signature redacted
Robert Van der Hilst
Schlumberger Professor of Earth and Planetary Sciences
Department Head

Spatial and Temporal Record of Magmatism, Sedimentation, and Faulting During Paleogene Ridge-Trench Interaction in the Pacific Northwest

by

Michael Patterson Eddy

Submitted to the Department of Earth, Atmospheric, and Planetary Sciences
on September 22, 2016
in partial fulfillment of the requirements for the degree of
Doctor of Philosophy in Geology

Abstract

This dissertation uses high-precision U-Pb zircon geochronology to document the spatial and temporal distribution of magmatism, deformation, and sedimentation during Paleogene ridge-trench interaction in western Washington. Chapter 1 creates a regional stratigraphy for nonmarine sedimentary and volcanic rocks throughout central and western Washington and demonstrates that the depositional history of these rocks is consistent with accretion of over thickened oceanic crust (Siletzia terrane) and passage of a triple-junction. Chapter 2 establishes the volcanic stratigraphy of northern Siletzia and show that it is consistent with its origin as an accreted oceanic plateau, possibly developed above a long-lived Yellowstone hot spot. Chapter 3 quantifies magma emplacement rates in a large, granitoid intrusive complex (Golden Horn batholith) that was emplaced during Paleogene ridge-trench interaction. Parts of this batholith were constructed at the highest rate ever documented in a large granitoid intrusive complex (~0.0125 km^3/a). This high emplacement rate may be related to its unique tectonic setting. The second tectonic setting is the rift-to-drift transition in the Newfoundland-Iberia rift. This rift is considered the type example of a magma-poor rifted margin and both margins consist of broad areas of exhumed subcontinental lithospheric mantle. Chapter 5 documents time-transgressive magmatism from east to west across both margins and suggests that mantle was exhumed during a single period of detachment faulting.

Thesis Supervisor: Oliver Jagoutz

Acknowledgements

Many people have helped make my time at MIT both enriching and rewarding. I especially want to thank Oli Jagoutz and the rest of my committee (Tim Grove, Wiki Royden, and Blair Schoene) for helping me make it to the finish line and Bob Miller for mentoring me in the field and imparting a love for the geology of the North Cascades.

The geology of Washington is complex and key outcrops are often inaccessible due to rain forest vegetation or rough terrain. It takes a special breed to do work in that terrain and I want to thank the many collaborators and colleagues that I've gained over the past few years, including Paul Umhoefer, and Erin Donaghy from Northern Arizona University, Ken Clark and Jeff Tepper from the University of Puget Sound, Stacia Gordon and Kirsten Sauer from the University of Nevada Reno, and Michael Polenz and Joe Dragovich from the Washington Department of Natural Resources. I have learned from all of you and appreciate your collegiality. I can't imagine a better place to have cut my geological teeth.

I also want to thank all of the Geology, Geochemistry, and Geobiology students, and particularly the students in the Bowring and Jagoutz labs with whom I overlapped (Noah McLean, Terry Blackburn, Erin Shea, and Seth Burgess). Special thanks go to Ann Bauer, who has put up with my shenanigans for over 5 years and to Ben Klein, who has done his best to keep me honest over the years. I also want to thank Mauricio Ibanez-Mejia, Jahan Ramezani, Shokofeh Khadevi, Kaori Tsukoi, Pat Walsh, and Annora Borden for keeping the Bowring laboratory a vibrant place to work over the past few years. I'd also be remiss for not thanking my wife, Bianca, who has tolerated the long hours I've spent in the Green Building and on fieldtrips around the world.

Finally, I want to thank Sam Bowring for his unwavering support through the years. He has continually challenged me to critically evaluate my own ideas and has helped me sharpen my research. I cannot fully express my gratitude for his mentorship nor my sadness in his absence from the lab.

Table of Contents

4. Rapid assembly and crystallization of a fossil, large-volume, silicic magma chamber

5. Timing the Rift-to-Drift Transition in the Newfoundland-Iberia Rift

List of Figures

Chapter 2

Chapter 3

Chapter 4

Chapter 5

List of Tables

Chapter 2

Chapter 3

Chapter 4

Chapter 5

Chapter 1

Introduction

Plate reconstructions of the Pacific basin require that at least one oceanic spreading center intersected the North American margin during the Paleogene (e.g., Atwater, 1970; Engebretson et al., 1985). Nevertheless, the location of this intersection is difficult to constrain because the oceanic crust needed to delineate the spreading ridge has been subducted. Geologic evidence for Paleogene ridge-trench interaction has been documented along the southern Alaska margin (e.g., Bradley et al., 2003) as well as the North American margin at the latitude of Washington and southern British Columbia (e.g., Groome et al., 2003) and has led to several proposed plate geometries (Engebretson et al., 1985; Cowan, 2003; Haeussler et al., 2003; Madsen et al., 2006). Nevertheless, paleomagnetic data suggests that the terranes that compose southern Alaska have experienced significant northward movement since the Paleogene (Plumley et al., 1983; Bol et al., 1992), complicating simple plate reconstructions based on evidence for ridge-trench interaction in this area. Western Washington and southern British Columbia have experienced much more modest northward displacement since the Paleogene (<200 km) and may provide a robust constraint on the location of Paleogene ridge-trench interaction. However, the existence of a triple-junction in this location is almost exclusively based on geochemically anomalous forearc magmatism (Cowan, 2003; Groome et al., 2003). In **Chapters 2, 3, and 4** I expand on other studies of ridge-trench interaction in western Washington and show that the spatial and temporal record of magmatism, sedimentation, and deformation in this area is consistent with this tectonic setting.

In **Chapter 2**, I use U-Pb zircon geochronology to correlate structurally isolated sections of nonmarine sedimentary rock and bimodal volcanics throughout central and western Washington. These rocks are largely exposed between large strike-slip faults and significant controversy exists as to whether they represent pull-apart basins developed during major strike-slip faulting (e.g., Johnson, 1985) or erosional remnants of a regional depositional system (Cheney, 1994, 2003; Cheney and Hayman, 2009). Our data establishes that the oldest

nonmarine sedimentary rocks formed a large coherent forearc sedimentary basin from ≤59.9 to 51.3 Ma that was inverted between 51.3 and 49.9 Ma. Inversion was immediately followed by initiation, or significant acceleration, of dextral strike-slip faulting throughout the region and led to the development of the Chumstick strike-slip sedimentary basin. This history is consistent with the accretion of over thickened oceanic crust (Siletzia terrane) and the southward jump of the Kula-Farallon-North America, or Resurrection-Farallon-North America triple-junction.

Chapter 3 establishes the timing of volcanism in northern Siletzia. This terrane is considered to represent over thickened oceanic crust generated near the Kula-Farallon, or Resurrection-Farallon, spreading center (Duncan, 1982; McCrory and Wilson, 2013; Wells et al., 2014). However, in Washington it is believed to be floored by a thick (1-2 km) sequence of turbidites that are clearly derived from the continent (Tabor and Cady, 1978; Einarsen, 1987). This observation has led to an alternative hypothesis in which Siletzia represents a volcanic rifted margin (e.g., Babcock et al., 1992). Through the use of high-precision geochronology, I show that the turbidites are <44.72 Ma and much younger than the rest of northern Siletzia (53-48 Ma). This discrepancy suggests that these sediments were thrust under the terrane long after its initial construction. Our revised volcanic stratigraphy is similar to that established for the rest of the terrane (Wells et al., 2014) and we agree with those authors that it represents an accreted oceanic plateau possibly developed above a long-lived Yellowstone hotspot. The timing of accretion in Washington is tightly constrained by 51.3-49.9 Ma shortening in central and western Washington (**Chapter 1**) and overlaps with Siletzia's construction. I speculate that the buoyancy of this young plateau led to its accretion and preservation.

The accreted Siletzia terrane is geophysically continuous with tomographic images of a 'hanging slab' of oceanic lithosphere beneath eastern Washington, Idaho, and eastern Oregon suggesting that slab breakoff occurred following the terrane's accretion (Schmandt and Humphreys, 2011). In eastern Washington slab breakoff and roll back may be recorded by Eocene intrusions that are time-transgressive from east to west across the state (Caulfield and Tepper, 2015). The Golden Horn batholith lies near the western termination of this trend and is composed of peralkaline and calc-alkaline granitoids (Stull, 1969). In **Chapter 4** I present the first complete geologic map of the batholith and show that it is composed of five subhorizontal intrusive sheets. Excellent vertical exposure allows reliable volume estimates for four of these five sheets and I use high-precision U-Pb zircon geochronology to calculate magma

emplacement rates for four of these sheets. The largest intrusive sheet, a >424 km^3 sheet of rapakivi granite and granodiorite, was constructed at a rate of ~0.0125 km^3/a. This is the highest rate documented in a granitoid intrusive complex, and is the only one to meet the thermally modeled requirements for generating the type of magma reservoir that source 'supereruptions' (e.g., Annen, 2009; Gelman et al., 2013). The high rates of melt production needed to feed such a rapidly assembled reservoir may be related to the batholith's tectonic setting above an area of slab breakoff.

The high-resolution temporal record of Paleogene magmatism, faulting, and sedimentation presented in this dissertation strengthens the case for the presence of an oceanic spreading ridge at this latitude during the Paleogene. In **Chapter 2** I show that the Paleogene sedimentary record of central and western Washington is consistent with accretion and capture of part of the Farallon plate and the southward jump of a triple-junction. **Chapter 3** discusses the reason for accretion/capture of oceanic crust, which may relate to the production of over thickened oceanic crust (Siletzia) above a long-lived Yellowstone hotspot (e.g., Wells et al., 2014). Finally, following the accretion/capture of part of the Farallon plate, slab breakoff occurred and may have contributed to the rapid construction of the large granitoid plutonic complex discussed in **Chapter 4**.

Chapter 5 uses U-Pb zircon geochronology to document the spatial and temporal distribution of magmatism and faulting in a different tectonic setting: the transition to seafloor spreading in the Newfoundland-Iberia rift. This rift extended slowly and is marked by broad areas on both conjugate margins that include exhumed subcontinental lithospheric mantle. This mantle is thought to be exhumed along large detachment faults (e.g., Manatschal and Müntener, 2009), but the transition from asymmetric exhumation along detachments to symmetric seafloor spreading remains debated between models that propose asymmetric exhumation continues until breakup (e.g., Lemoine et al., 1987) and those that propose a transitional period of nonvolcanic spreading similar to that seen at ultra-slow spreading centers (e.g., Sibuet et al., 2007). I show that magmatism in the exhumed mantle of both margins was time-transgressive from east to west and that it is consistent with continued asymmetric exhumation prior to lithospheric breakup. I also provide a new age constraint of lithospheric rupture at 114 Ma, ~ 5-10 Ma younger than the most widely considered date for initial seafloor spreading.

All of the following chapters are written as individual manuscripts that are published (**Chapters 2 and 4**), in review (**Chapter 5**), or in preparation (**Chapter 3**). References for these manuscripts are listed below. Please note that the word 'we' throughout this dissertation refers to the coauthors for each manuscript and myself.

References for Chapters

Eddy, M.P., Bowring, S.A., Umhoefer, P.J., Miller, R.B., McLean, N.M., and Donaghy, E.E., 2016, High resolution temporal and stratigraphic record of Siletzia's accretion and triple junction migration from nonmarine sedimentary basins in central and western Washington: Geological Society of America Bulletin, v. 128, p. 425-441, doi: 10.1130/B31335.1.

Eddy, M.P., Clark, K.C., and Polenz, M., *in preparation*, Volcanic stratigraphy of the Siletzia LIP in Washington and Vancouver Island: Geosphere.

Eddy, M.P., Bowring, S.A., Miller, R.B., and Tepper, J.H., 2016, Rapid assembly and crystallization of a fossil large-volume silicic magma chamber: Geology, v. 44, p. 331-334, doi: 10.1130/G37631.1.

Eddy, M.P., Jagoutz, O., and Ibanez-Mejia, M., *in review*, Timing the rift-to-drift transition in the Newfoundland-Iberia rift: Geology.

References

Annen, C., 2009, From plutons to magma chambers: thermal constraints on the accumulation of eruptible silicic magma in the upper crust: Earth and Planetary Science Letters, v. 284, p. 409-416, doi: 10.1016/j.epsl.2009.05.006.

Atwater, T., 1970, Implications of plate tectonics for the Cenozoic tectonic evolution of North America: Geological Society of America Bulletin, v. 81, p. 3513-3536, doi: 10.1130/0016-7606(1970)81[3513:IOPTFT]2.0.CO;2.

Babcock, R.S., Burmester, R.R., Engebretson, D.C., Warnock, A.C., Clark, K.P., 1992, A rifted margin origin for the Crescent basalts and related rocks in the northern Coast Range Volcanic Province, Washington and British Columbia: Journal of Geophysical Research, v. 97, p. 6799-6821, doi: 10.1029/91JB02926.

Bol, A.J., Coe, R.S., Gromme, S., and Hillhouse, J.W., 1992, Paleomagnetism of the Resurrection Peninsula, Alaska: implicatiosn for the tectonics of southern Alaska and the Kula-Farallon ridge: Journal of Geophysical Research, v. 97, p. 17213-17232, doi: 10.1029/92JB01292.

Bradley, D.C., Kusky, T., Haeussler, P.J., Goldfarb, R., Miller, M.L., Dumoulin, J., Nelson, S.W., and Karl, S., 2003, Geologic signature of early Tertiary ridge subduction in Alaska, in Sisson, V.B., Roeske, S.M., and Pavlis, T.L., eds., Geology of a transpressional orogen developed during ridge-trench interaction along the north Pacific margin: Geological Society of America Special Paper 371, p. 19-49, doi: 10.1130/0-8137-2371-X.19.

Caulfield, L., and Tepper, J.H., 2015, Geochemistry and geochronology of Eocene plutons in northeastern Washington: a test of Farallon slab rollback as a cause for the Challis event: Abstract V23B-3120 presented at 2015 Fall Meeting, AGU, San Francisco, California, 14-18 December.

Cheney, E.S., 1994, Cenozoic Unconformity-bounded sequences of central and eastern Washington: Washington Division of Geology and Earth Resources Bulletin 80, p. 115-139.

Cheney, E.S., 2003, Regional Tertiary sequence stratigraphy and regional structure on the eastern flank of the central Cascade range, Washington, in Swanson, T.W., ed., Western Cordillera and Adjacent Areas: Geological Society of America Field Guide 4, p. 177-199, doi: 10.1130/0-8137-0004-3.177.

Cheney, E.S., and Hayman, N.W., 2009, the Chiwaukum structural low: Cenozoic shortening of the central Cascade Range, Washington State, USA: Geological Society of America Bulletin, v. 121, p. 1135-1153, doi: 10.1130/B26446.1.

Cowan, D.S., 2003, Revisiting the Baranof-Leech River hypothesis for early Tertiary coastwise transport of the Chugach-Prince William terrane: Earth and Planetary Science Letters, v. 213, p. 463-475, doi: 10.1016/S0012-821X(03)00300-5.

Duncan, R.A., 1982, A captured island chain in the coast range of Oregon and Washington: Journal of Geophysical Research, v. 87, p. 827-837, doi: 10.1029/JB087iB13p10827.

Einarsen, J.M., 1987, The petrography and tectonic significance of the Blue Mountain unit, Olympic Peninsula, Washington [M.S. Thesis]: Bellingham, Western Washington University, 175 p.

Engebretson, D.C., Cox, A., and Gordon, R.G., 1985, Relative motions between oceanic and continental plates in the Pacific basin: Geological Society of America Special Papers, v. 206, p. 1-60, doi: 10.1130/SPE206-p1.

Gelman, S.E., Gutierrez, F.J., and Bachmann, O., 2013, On the longevity of large upper crustal silicic magma reservoirs: Geology, v. 41, p. 759-762, doi: 10.1130/G34241.1.

Groome, W.G., Thorkelson, D.J., Friedman, R.M., Mortensen, J.K., Massey, N.W.D., Marshall, D.D., and Layer, P.W., 2003, Magmatic and tectonic history of the Leech River Complex, Vancouver Island, British Columbia: evidence for ridge-trench intersection and accretion of the Crescent terrane, in Sisson, V.B., Roeske, S.M., and Pavlis, T.L., eds., Geology of a transpressional orogen developed during ridge-trench interaction along the north Pacific margin: Geological Society of America Special Paper 371, p. 327-353, doi: 10.1130/0-8137-2371-X.327.

Haeussler, P.J., Bradley, D.C., Wells, R.E., and Miller, M.L., 2003, Life and death of the Resurrection plate: evidence for its existence and subduction in the northeastern Pacific in Paleocene-Eocene time: Geological Society of America Bulletin, v. 115, p. 867-880, doi: 10.1130/0016-7606(2003)115<0867:LADOTR>2.0.CO;2.

Johnson, S.Y., 1985, Eocene strike-slip faulting and nonmarine basin formation in Washington, in Biddle, K.T., and Christie-Blick, N., eds., Strike-Slip Deformation, Basin Formation, and Sedimentation: Society of Economic Paleontologists and Mineralogists Special Publication 37, p. 283-302.

Lemoine, M., Tricart, P., and Boillot, G., 1987, Ultramafic and gabbroic ocean floor of the Ligurian Tethys (Alps, Corsica, Apennines): in search of a genetic model: Geology, v. 15, p. 622-625, doi: 10.1130/0091-7613(1987)15<622:UAGOFO>2.0.CO;2.

Madsen, J.K., Thorkelson, D.J., Friedman, R.M., and Marshall, D.D., 2006, Cenozoic to recent plate configurations in the Pacific basin: ridge subduction and slab window magmatism in western North America: Geosphere, v. 2, p. 11-34, doi: 10.1130/GES00020.1.

McCrory, P.A., and Wilson, D.S., 2013, A kinematic model for the formation of the Siletz-Crescent forearc terrane by capture of coherent fragments of the Farallon and Resurrection plates: Tectonics, v. 32, p. 718-736, doi: 10.1002/tect.20045.

Manatschal, G., and Müntener, O., 2009, A type sequence across an ancient magma-poor ocean-continent transition: the example of the western Alpine Tethys ophiolites: Tectonophysics, v. 473, p. 4-19, doi: 10.1016/j.tecto.2008.07.021.

Plumley, P.W., Coe, R.S., and Byrne, T., 1983, Paleomagnetism of the Paleocene Ghost Rocks Formation, Prince William Terrane, Alaska: Tectonics, v. 2, p. 295-314, doi: 10.1029/TC002i003p00295.

Sibuet, J.C., Srivastava, S., and Manatschal, G., 2007, Exhumed mantle-forming transitional crust in the Newfoundland-Iberia rift and associated magnetic anomalies: Journal of Geophysical Research, v. 112, B06105, doi:10.1029/2005JB003856.

Stull, R.J., 1969, The geochemistry of the southeastern portion of the Golden Horn batholith, Northern Cascades, Washington [Ph.D. thesis]: Seattle, University of Washington, 127 p.

Tabor, R.W., and Cady, W.M., 1978, Geologic map of the Olympic Peninsula, Washington: U.S. Geological Survey, scale 1:125,000, 2 sheets.

Wells, R.E., Bukry, D., Friedman, R., Pyle, D., Duncan, R., Haeussler, P., and Wooden, J., 2014, Geologic history of Siletzia, a large igneous province in the Oregon and Washington Coast Range: correlation to the geomagnetic polarity time scale and implications for a long-lived Yellowstone hotspot: Geosphere, v. 10, p. 692-719, doi: 10.1130/GES01018.1.

Chapter 2

High-resolution temporal and stratigraphic record of Siletzia's accretion and triple junction migration from non-marine sedimentary basins in central and western Washington

Abstract

The presence of early Eocene near-trench magmatism in western Washington and southern British Columbia has led to speculation that this area experienced ridge-trench interaction during that time. However, the effects of this process as they are preserved in other parts of the geologic record are poorly known. We present high-precision U-Pb zircon geochronology from Paleogene non-marine sedimentary and volcanic sequences in central and western Washington that preserve a record of tectonic events between ca. 60 - 45 Ma. The data reveals that the Swauk, Chuckanut, and Manastash Fms. formed a non-marine sedimentary basin along the North American margin between $\leq$ 59.9 – 51.3 Ma. This basin experienced significant disruption that culminated in basin-wide deformation, uplift, and partial erosion during accretion of the Siletzia terrane between 51.3 and 49.9 Ma. Immediately following accretion, dextral strike-slip faulting began, or accelerated, on the Darrington-Devil's Mtn., Entiat, Leavenworth, Eagle Creek, and Straight Creek-Fraser fault zones between 50 and 46 Ma. During this time, the Chumstick Fm. was deposited in a strike-slip basin coeval with near-trench magmatism. Faulting continued on the Entiat, Eagle Creek, and Leavenworth faults until a regional sedimentary basin was re-established $\leq$ 45.9 Ma, and may have continued on the Straight Creek-Fraser fault until 35 - 30 Ma. This record of basin disruption, volcanism, and strike-slip faulting is consistent with ridge-trench interaction and supports the presence of an oceanic spreading ridge at this latitude along the North American margin during the early Eocene.

Introduction

Ridge-trench interaction is a fundamental tectonic process that can dramatically alter the geology of convergent margins. Such interactions have occurred several times over the past 60

Myr in western North America as oceanic plates were consumed in east-dipping subduction zones. Most recently (ca. 30 Ma - present), the intersection of the Pacific-Farallon ridge with the continent has led to the fragmentation of the Farallon plate into multiple microplates (Stock and Lee, 1994), the development of the San Andreas fault (Atwater, 1970), and the generation of geochemically anomalous magmas above slab windows and areas of slab breakoff (e.g., Johnson and O'Neil, 1984; Benoit et al., 2002). Plate reconstructions for the northern Pacific basin also require subduction of the Kula-Farallon ridge or Kula-Resurrection and Resurrection-Farallon ridges along North America's western margin during the early Cenozoic (Fig. 1A: Atwater, 1970; Grow and Atwater, 1970; Wells et al., 1984; Engebretson et al., 1985; Haeussler et al., 2003; Madsen et al., 2006). However, the precise timing and location(s) of this ridge-trench interaction remain uncertain, as the oceanic crust needed to constrain the position of these ridges is completely subducted. Instead, the location of past triple junctions, and consequently the geometry of past plate configurations, must be constrained through the careful identification of the effects of ridge-trench interaction, as they are preserved in the North American geologic record.

Previous studies have identified two areas in the Pacific Northwest that may record Paleogene ridge-trench interaction; the terranes that compose the southern Alaska margin (Fig. 1A) and the Paleogene forearc of southern British Columbia/western Washington. These observations have led to several potential plate reconstructions that place oceanic spreading centers intersecting North America along the southern Alaska margin, at the latitude of Washington, or simultaneously in both areas between ca. 60 - 50 Ma (Fig. 1A; Wells et al., 1984; Engebretson et al., 1985; Cowan, 2003; Haeussler et al., 2003; Madsen et al., 2006). Yet, while the effects of ridge-trench interaction are well documented in southern Alaska (Bradley et al., 2003, and references therein), evidence for ridge-trench interaction at the latitude of Washington relies almost exclusively on the existence, and age, of geochemically anomalous near-trench and backarc magmatism (Breitsprecher et al., 2003; Groome et al., 2003; Haeussler et al., 2003; Madsen et al., 2006; Ickert et al., 2009). This tectonic setting has also been invoked, at least in part, to explain the origin and accretion of the oceanic Siletzia terrane to this part of North America during the early Eocene (McCrory et al., 2013; Wells et al., 2014). Nevertheless, few studies have considered other manifestation of Paleogene ridge-trench interaction at this latitude.

In central and western Washington, a series of well-studied Paleogene non-marine sedimentary and volcanic sequences preserve a record of sedimentation, deformation, and volcanism that may be related to ridge-trench interaction and the consequent triple junction migration. However, the tectonic significance of these rocks remains controversial due to disagreements over whether they record sediment accumulation within regional or local basins. Precise geochronology could resolve this issue by temporally correlating these sequences and constraining the age, duration, and spatial extent of tectonic events, and we present 22 high-precision U-Pb zircon dates with this goal in mind. The data reveals an abrupt tectonic change at ca. 50 Ma marked by deformation, bimodal volcanism, and initiation, or significant acceleration, of dextral strike-slip faulting. This change coincides with near-trench magmatism along the Washington and British Columbian coasts (e.g., Madsen et al., 2006), as well as the accretion of the Siletzia terrane to North America (Wells et al., 2014), and we suggest that all of these events are related to triple junction migration.

Paleogene Non-marine Sedimentary and Volcanic Sequences

Non-marine sedimentary and volcanic rocks of Paleogene age are exposed as isolated sequences along and between the Straight Creek-Fraser, Darrington-Devil's Mtn., Entiat, and Leavenworth fault zones in central and western Washington (Fig. 1B). They rest unconformably on pre-Tertiary metamorphic basement and are in turn unconformably overlain by Oligocene and younger (33 Ma – present) sedimentary and volcanic rocks. The Paleogene sequences are composed of sandstone, mudstone, and conglomerate deposited in fluvial and lacustrine environments near the Paleogene coastline and are divided into seven formations as well as several informal units. To the west lie marine sedimentary rocks of approximately the same age in the Puget Group and within the Siletzia terrane (Fig. 1B: Vine, 1969; Buckovic, 1979; Einarsen, 1987; Johnson and O'Connor, 1994), but the precise temporal and depositional relationship between these areas is unknown.

Post-depositional faulting has partly obscured the role that regional strike-slip faults played in the formation of the Paleogene sedimentary sequences discussed in this paper. This uncertainty has resulted in disagreement as to whether they represent distinct basins formed by strike-slip faulting (Johnson, 1985), erosional remnants of a regional depositional system (Cheney, 1994, 2003; Cheney and Hayman, 2009), or a regional system that was later partitioned

into distinct strike-slip basins (Evans, 1994). These different models can be tested using a well-constrained correlation scheme. However, while detailed stratigraphic, paleocurrent, and petrologic data is available for each sequence, existing geochronology is too imprecise to make accurate temporal correlations. Despite this difficulty, previous correlation efforts have used a variety of stratigraphic arguments, in addition to existing geochronology, to create regional histories for sedimentation (e.g., Tabor et al., 1984; Cheney, 1994) and fault motion (Gresens et al., 1981; Tabor et al., 1984; Taylor et al., 1988; Evans, 1994; Evans and Ristow, 1994; Cheney, 2003; Cheney and Hayman, 2009). We use our data to test and expand upon these earlier studies.

U-Pb Geochronology Methods

We dated 22 samples of volcanic and sedimentary rock from the Paleogene non-marine sedimentary and volcanic sequences in central and western Washington using U-Pb zircon chemical abrasion-isotope dilution thermal ionization mass spectrometry (CA-IDTIMS) geochronology. U-Pb zircon dates represent the age of zircon crystallization and are interpreted as the age of eruption/deposition for volcanic rocks, emplacement for plutonic rocks, or as a maximum depositional age for the youngest detrital zircon grain in sedimentary samples. For detrital analyses, zircons were pre-screened using laser ablation-inductively coupled plasma mass spectrometry (LA-ICPMS) at the Arizona Laserchron Facility to identify the youngest grains for CA-IDTIMS analyses. Methods for CA-IDTIMS are modified from those outlined in Mattinson (2005) and are discussed in more detail in Appendix A. All isotopic ratios were measured on the VG Sector 54 or Isotopx X62 thermal ionization mass spectrometers at MIT, and this data is presented in Table A1 and shown as concordia plots in Figure A1. Our preferred date for each sample is shown in Table 1.

All reported dates represent a weighted mean of ^{238}U-^{206}Pb zircon dates, or a single grain ^{238}U-^{206}Pb date for samples where taking a weighted mean is inappropriate. A correction for preferential exclusion of ^{230}Th during zircon crystallization was made using a calculated Th/U for each zircon and an assumed magmatic Th/U ratio of 2.8 ± 1 (2σ), which encompasses the range of values seen in most felsic igneous liquids (Machlus et al., 2015). The first time that a date is presented, uncertainty is reported in the format ± X/Y/Z, where X is the analytical uncertainty, Y is the analytical uncertainty plus the uncertainty in the isotopic composition of the tracer solution, and Z also includes the uncertainty in the ^{238}U decay constant. However, since all

of the dates reported in this paper were produced using the same isotopic tracer and ^{238}U decay constant, only the analytical uncertainty (2σ) is used in subsequent discussion. For samples where a weighted mean is used, the mean square weighted deviation (MSWD) is reported, along with the number of grains (n) used in the calculation.

Complex zircon populations are common in volcanic rocks and age dispersion beyond that expected from analytical uncertainty can arise from a variety of sources, including the incorporation of xenocrystic zircon during eruption or deposition and/or protracted zircon crystallization prior to eruption. Some of our volcanic samples contain grains that are > 1 Myr older than the main population of zircon dates, and we exclude them from our age calculations. Dispersion of zircon dates at the < 1 Myr level is more difficult to evaluate and we use the MSWD of weighted means to help determine whether this dispersion can be explained by analytical uncertainty (MSWD $\approx$ 1) or whether it represents resolvable age differences (MSWD >> 1). The range of acceptable MSWD values for different size zircon populations (n) can be calculated using the expected variability of the MSWD (Wendt and Carl, 1991), and we treat samples with MSWD values within the expected 2σ variability as a single population. Samples with age dispersion that cannot be explained by analytical uncertainty are discussed individually in the following sections.

Previous geochronology from these sedimentary sequences is compiled and presented in Tabor et al. (1982, 1984, 1987, 1993, 2000, 2002). These dates were produced using K-Ar or fission track zircon methods and have associated 2σ uncertainties at the 10-1% level. Although these dates were invaluable to previous correlation efforts (e.g., Tabor et al., 1984) and largely agree with the U-Pb zircon CA-IDTIMS dates presented in this paper, their large uncertainties inhibit their use to constrain basin evolution at fine timescales, and they are not discussed further.

Results

Chuckanut Formation

The Chuckanut Fm. is the farthest north of the sedimentary sequences discussed in this paper (Fig. 1B) and comprises 4000 - 5000 m of fluvial sandstone, conglomerate, and very rare pyroclastic rock (Fig. 2). Johnson (1984) and Breedlovestrout (2011) described the formation's

stratigraphy in detail and provided thickness estimates and sedimentologic data for each of its members. It is interpreted to represent deposits along SW-flowing streams, and Johnson (1984) suggested that it had a distal sediment source in eastern Washington or Idaho. However, the Governor's Point and Maple Falls Mbrs. (Fig. 2) may have been derived from local topographic highs (Johnson, 1984). After deposition, the Chuckanut Fm. was deformed into a NW-trending fold belt and eroded, resulting in an angular unconformity between the formation and the overlying Oligocene Huntingdon Fm. (Miller and Misch, 1963; Johnson, 1984).

A date for a tuff (NC-203) collected from the lower Bellingham Bay Mbr. (Fig. 2) provides a temporal constraint on the beginning of sediment accumulation in the Chuckanut Fm. Individual zircons from this sample have dates that span 870 kyr, and exceed the dispersion expected from analytical uncertainty (MSWD=6.5 for all 16 grains). The date for the youngest zircon overlaps with the next 5 youngest grains within 2σ uncertainty and a weighted mean of these grains gives our preferred eruption/depositional age of 56.835 ± 0.050/0.062/0.087 Ma (n=6, MSWD=1.3), demonstrating that sediment accumulation began in the Chuckanut Fm. prior to this date (Fig. 2). Other high-precision dates from this formation were reported in Breedlovestrout et al. (2013) and include a tuff that is interbedded within the upper Slide Mbr. (Fig. 2) and a rhyolitic dike that intrudes the lower Padden Mbr. Zircons from the tuff gave a weighted mean date of 53.676 ± 0.023/0.035/0.067 Ma and provide a constraint on the age of the middle Chuckanut Fm., whereas zircons from the dike gave a weighted mean date of 49.858 ± 0.025/0.035/0.063 Ma. To our knowledge, this is the only dike reported within the Chuckanut Fm. and its significance in relation to regional magmatism remains uncertain. Nevertheless, its intrusive relationship with the Padden Mbr. requires the member to have been deposited prior to 49.858 ± 0.025 Ma.

Southeastern Chuckanut Formation

To the SE of the main outcrop belt of the Chuckanut Fm. lie thick packages of sedimentary and volcanic rock that are cut by splays of the Darrington-Devil's Mtn. fault zone (Fig. 1B). Evans and Ristow (1994) called these rocks the SE Chuckanut Fm. and described two detailed stratigraphic sections. The first is exposed in the area around Mt. Higgins (Fig. 1B) and was informally split into the Coal Mtn. and Higgins Mtn. units based on a reversal in paleocurrent direction from SW to NE. The Coal Mtn. unit records SW-directed paleoflow and

consists of 2250 m of sandstone with minor shale, coal, and conglomerate (Fig. 3). It is conformably overlain by the Higgins Mtn. unit, which consists of 1700 m of sandstone, shale, and minor conglomerate that record NE-directed paleoflow (Fig. 3). Conglomerate clasts within the Higgins Mtn. unit are dominantly quartz, phyllite, tuff, and chert (Evans and Ristow, 1994). These lithologies are common in the western and eastern mélange belts (Fig. 1B), and their presence within the Higgins Mtn. unit, along with the unit's NE-directed paleoflow, suggest that the mélange belts were uplifted and eroding during its deposition. Evans and Ristow (1994) described an unconformable contact between the Higgins Mtn. unit and the overlying rhyolite and andesite flows of the Barlow Pass Volcanics (Fig. 3). However, angular discordance in this area is slight and Tabor (1994) and Tabor et al. (1993, 2002) did not consider the unconformity to be significant.

Zircons separated from a rhyolitic tuff (NC-MPE-421) at the base of the Barlow Pass Volcanics in the Higgins Mtn. area (Fig. 3) have dates that span 460 kyr and exceed the age dispersion expected from analytical uncertainty. The youngest five grains overlap within 2σ uncertainty and give a weighted mean date of 49.933 ± 0.059/0.078/0.095 Ma (n=5, MSWD=1.9). This date constrains the initiation of Barlow Pass volcanism and demonstrates that both the Higgins Mtn. and Coal Mtn. units are > 49.933 ± 0.059 Ma. A bentonite (NC-MPE-420B) interbedded with a sequence of black shale was also collected from this area. Zircons from this sample do not form a single population of dates within analytical uncertainty, and therefore we treat the date of the youngest grain, 48.999 ± 0.029/0.036/0.063 Ma, as a maximum depositional age. Cruver (1981), Evans and Ristow (1994), and Dragovich et al. (2003) all considered this sequence to belong to Higgins Mtn. unit. However, our maximum depositional age shows that they are younger than the basal Barlow Pass Volcanics (Fig. 3). This date is consistent with mapping by Tabor et al. (2002) that showed that these rocks overlie the Barlow Pass Volcanics, and we therefore consider this small sedimentary section to be distinct from the Higgins Mtn. unit.

In the area around Barlow Pass, Evans and Ristow (1994) measured 1900 m of steeply dipping sedimentary rock that they informally named the Sperry Pk. unit (Fig. 3). This unit unconformably overlies metamorphic bedrock and consists of sandstone and shale that record NE-directed paleoflow, as well as conglomerate with a high percentage of chert clasts. Like the Higgins Mtn. unit, the NE paleoflow and high percentage of chert clasts in the Sperry Pk. unit

suggest a sediment source in the western and eastern mélange belts and these features provide circumstantial evidence for the correlation of these two units (Evans and Ristow, 1994). Overlying the Sperry Pk. unit is > 1200 m of basalt and minor rhyolite that form part of the Barlow Pass Volcanics (Fig. 3). The volcanics dip gently to the east and Vance (1957) and Evans and Ristow (1994) considered them to unconformably overlie the Sperry Pk. unit based on their contrasting degree of deformation. However, the Barlow Pass Volcanics and Sperry Pk. unit are only seen in fault contact and Tabor et al. (2002) suggested that this difference might represent proximity to active structures or a difference in mechanical properties rather than an angular unconformity.

None of our samples from the Barlow Pass area yielded zircon. Nevertheless, we follow Evans and Ristow (1994) and consider the Sperry Pk. and Higgins Mtn. units to be correlative based on their overall sedimentological similarities. It is important to note that Tabor et al. (1994, 2002) considered the Coal Mtn., Higgins Mtn., and Sperry Pk. units to be a sedimentary facies of the Barlow Pass Volcanics. These authors emphasized the presence of abundant tuffs in the sedimentary rock near Mt. Higgins (e.g., Cruver, 1981) and did not consider the unconformity between the SE Chuckanut Fm. and the overlying volcanics to be significant. Our geochronologic data shows that the tuff bearing rocks described by Cruver (1981) are younger than the SE Chuckanut Fm. as described by Evans and Ristow (1994) and like these authors we consider the SE Chuckanut Fm. and the Barlow Pass Volcanics to be distinct.

Naches Formation

The Naches Fm. is a sequence of basalt and rhyolite flows interbedded with non-marine sedimentary rock exposed near the presumed southern termination of the Straight Creek-Fraser fault (Fig. 1B). An accurate thickness is difficult to obtain due to a lack of marker beds and complex folding and faulting, but Tabor et al. (1984) estimated a total thickness between 1500 and 3000 m (Fig. 4). The non-marine sedimentary rocks that compose the lower Naches Fm. are named the Guye Mbr. and are interbedded with rhyolite flows of the Mt. Catherine rhyolite (Tabor et al., 1984). A sample collected from the Mount Catherine rhyolite near the top of the Guy Mbr. gives a U-Pb zircon date of 49.711 ± 0.024/0.036/0.064 Ma (n=7, MSWD=2.1) and provides a minimum age for the underlying sedimentary rocks as well as a maximum age for the ca. 1500 m of basalt, andesite, and rhyolite that form the upper Naches Fm. (Fig. 4).

Interestingly, the sandstones and conglomerates in the Guye Mbr. are rich in chert (Foster, 1960) and may represent the same period of west-derived sedimentation as the Higgins Mtn. and Sperry Pk. units.

Manastash River Block

The Manastash River block of Tabor et al. (1984) consists of a ca. 1750 - 2250 m section of sedimentary and volcanic rock exposed between two splays of the southern Straight Creek-Fraser fault (Fig. 1B). The oldest formation exposed in this sequence is the Manastash Fm. and comprises 500 to 750 m of arkosic sandstone and minor shale, conglomerate, and coal unconformably deposited on pre-Tertiary bedrock (Fig. 5: Tabor et al., 1984, 2000). The Manastash Fm. is in turn overlain by a 1000 m of andesitic to rhyolitic flows named the Taneum Fm. (Fig. 5). A sample of a rhyolitic tuff (NC-MPE-419B) collected from the Taneum Fm. yielded a youngest population of five zircons that give a date of 51.309 ± 0.024/0.035/0.065 Ma (n=5, MSWD=2.1), which places a minimum age constraint on the underlying Manastash Fm. Overlying the Taneum Fm. with an ambiguous contact is the 250 to 500 m thick Basalt of Frost Mtn. (Fig. 5). Tabor et al. (1984) suggested that there was an unconformity between these two volcanic sequences. However, it is difficult to evaluate this relationship because there is little to no angular discordance between them.

Teanaway River Block

The Teanaway River block (Tabor et al., 1984) comprises three sedimentary and volcanic formations of Paleogene age that lie between the Straight Creek-Fraser and Leavenworth fault zones (Fig. 1B). The Swauk Fm. is the oldest formation in this sequence and is composed of fluvial and lacustrine sedimentary rocks that unconformably overlie pre-Tertiary bedrock (Fig. 5). The total thickness of the formation is difficult to determine due to a lack of marker beds, pervasive intrusion of basaltic dikes, and post-depositional shortening. However, Tabor et al. (2000) estimated that it could be as thick as 8000 m based on combined sections from the eastern and western part of its outcrop area. The western part of the Swauk Fm. remains poorly studied, whereas Taylor et al. (1988) described the upper 4000 m of the eastern part of the Swauk Fm. in detail. The lower portion of their section is dominated by arkosic sandstones and rare tuff interpreted to have been deposited in a low-energy fluvial environment with paleoflow to the

SSW, and the upper ca. 2000 m is composed of conglomerate, shale, and sandstone that largely record paleoflow to the NE (Fig. 5). Taylor et al. (1988) correlated the tuffs in their study area to the Silver Pass Mbr., which comprises 1800 m of andesitic and rhyolitic flows interbedded with the western part of the Swauk Fm. However, this correlation has never been tested using high-precision geochronology.

We produced three U-Pb zircon dates from the Swauk Fm. A detrital zircon from a sandstone (NC-MPE-016) collected < 10 m above the base of the formation gives a maximum depositional age of 59.919 ± 0.098/0.10/0.12 Ma (Fig. 5). Two samples of the Silver Pass Volcanic Mbr. were also dated (Fig. 5). The first is a rhyolite (NC-190) collected from the type area for the Silver Pass Mbr. in the western Swauk Fm. It contains zircons that have ages that span 971 kyr and greatly exceed the age dispersion expected from analytical uncertainty (MSWD=50 for all 11 grains). The youngest grain overlaps within 2σ uncertainty with the next five youngest grains and they collectively give a weighted mean date of 51.364 ± 0.029/0.038/0.067 Ma (n=6, MSWD=2.1). A tuff (NC-MPE-358B) collected ca. 3000 m below the top of the formation in the eastern part of the Swauk Fm. contains abundant detrital zircon ranging in age from 90 to 52 Ma. Nevertheless, the three youngest zircons form a distinct population with a weighted mean date of 51.515 ± 0.028/0.037/0.067 Ma (n=3, MSWD=3.0), which we interpret as an eruption/deposition age. The similarity between the ages of NC-MPE-358B and NC-190 confirms a temporal correlation between the tuffs in the eastern Swauk Fm. and the Silver Pass Volcanic Mbr. in the western Sauk Fm., and therefore supports Tabor et al.'s (2000) thickness estimate of ca. 8000 m for the formation as a whole.

The Swauk Fm. was shortened into a W-NW-trending fold belt (Doran, 2009), eroded, and unconformably overlain by 800 to 1200 m of basaltic flows and tuffs, and minor rhyolites and fluvial sedimentary rocks named the Teanaway Fm. (Fig. 5: Clayton, 1973). The five youngest zircons from a rhyolite (NC-MPE-456) sampled ca. 200 m above the base of the Teanaway Fm. give a weighted mean date of 49.341 ± 0.033/0.046/0.070 Ma (n=5, MSWD=2.2) and tightly constrain the period of shortening recorded by the Swauk Fm. to between 51.364 ± 0.029 and 49.341 ± 0.033 Ma (Fig. 5). This date also provides our best estimate for the age of a NE-striking swarm of basaltic dikes that intrude the Swauk Fm. and likely fed the overlying basalt flows in the Teanaway Fm. (Clayton, 1973; Doran, 2009). In an attempt to date the upper Teanaway Fm., two samples of rhyolite were collected from isolated outcrops with uncertain

field relationships near the formation's contact with the overlying Roslyn Fm. Clayton (1973) considered these rhyolites to be part of the Teanaway Fm., but subsequent geochronology reported by Tabor et al. (1982) suggested that they might be considerably younger. Our dates of 25.611 ± 0.014/0.019/0.033 Ma (n=6, MSWD=1.6) from a shallow rhyolite intrusion (NC-MPE-417A) and 24.216 ± 0.011/0.016/0.030 Ma (n=3, MSWD=1.7) from a poorly exposed rhyolitic tuff (NC-MPE-418) confirm the earlier geochronology and demonstrate that these rhyolites are much younger than the Paleogene sequences discussed in this paper.

Conformably overlying the Teanaway Fm. is ca. 2500 m of non-marine arkosic sandstone named the Roslyn Fm., which contains abundant coal seams and was deposited along W-flowing streams (Fig. 5: Walker, 1980; Tabor et al., 1984; Barnett, 1985). Cheney and Hayman (2009) correlated this formation to the Chumstick Fm. based on their similar lithologies and paleocurrent direction, but this correlation remains controversial and untested with high-precision geochronology. Two maximum depositional ages of 48.80 ± 0.11/0.12/0.13 Ma from the lower (NC-MPE-015) and 47.580 ± 0.028/0.035/0.062 Ma from the upper (NC-MPE-014) Roslyn Fm. will be used to further evaluate this correlation.

Chumstick Formation

The Chumstick Fm. is exposed between the Leavenworth and Entiat fault zones (Fig. 1B), and the formation's thickness, stratigraphy, and relationship to these fault systems remain controversial. Johnson (1985, 1996) interpreted the formation as a strike-slip basin, while Evans (1994, 1996) concluded that only part of it was deposited during strike-slip faulting. More recently, Cheney and Hayman (2009) correlated it to the Roslyn Fm. across the Leavenworth fault zone and rejected syn-depositional strike-slip faulting. Therefore, different interpretations of this formation can result in dramatically different histories for regional strike-slip faulting. Given its importance, we produced nine U-Pb zircon dates that help resolve these issues.

Gresens et al. (1981) and Evans (1994) presented the most detailed studies of the Chumstick Fm., recognized that the Eagle Creek fault (Fig. 1B) divides it into two sedimentary sections, and established its most widely used stratigraphic nomenclature. The thickness of each section was given by Evans (1994) and is 12800 m to the west and 4100 m to the east of the Eagle Creek fault. Both of these sections are extremely thick and previous geochronology suggested rapid accumulation (Evans, 1994). However, Cheney and Hayman (2009) suggested

that these thicknesses were overstated and gave a more conservative thickness of ca. 5200 m for the Chumstick Fm. based on their mapping.

The oldest member of the Chumstick Fm. is named the Clark Canyon Mbr. and consists of sandstone, mudstones, and conglomerate deposited by W-flowing streams (Fig. 6: Evans, 1994). It is currently exposed between the Eagle Creek and Leavenworth fault zones, but its original extent is debated (Evans, 1994; Johnson, 1996; Cheney and Haymen, 2009). McClincy (1986) and Evans (1994) used 18 interbedded tuffs as marker beds and estimated a total thickness of 10600 m for this member, but Cheney and Haymen (2009) disputed whether these tuffs were traceable over long distances and suggested that the member is substantially thinner. In order to check the validity of the McClincy (1986) and Evans (1994) stratigraphy, we produced six dates from tuffs interbedded with the lower, middle, and upper parts of the Clark Canyon Mbr. and one maximum depositional age from a sample of sandstone collected from the upper Clark Canyon Mbr.

Zircons from the stratigraphically lowest sample (Fairview Canyon tuff; ED072413-147) give a date of 49.147 ± 0.041/0.051/0.073 Ma (n=6, MSWD=0.9) and constrain the age of initial sediment accumulation within the Chumstick Fm. (Fig. 6). Five additional tuffs were dated from stratigraphic positions above the Fairview Canyon tuff and the resulting dates are presented in Table 1 and shown on Fig. 6. All of these samples with the exception of the Clark Canyon #7 tuff contained a single population of zircon dates and are interpreted to represent the age of eruption/deposition. The Clark Canyon #7 tuff (NC-MPE-365B) contained a mixed population of zircon dates, and we take the conservative approach of using the youngest grain as a maximum depositional age. A sample of sandstone collected from ca. 300 m above the Clark Canyon #2 tuff (Fig. 6) contained a zircon with a date of 47.847 ± 0.085/0.088/0.10 Ma, and provides a maximum depositional age for the uppermost part of Clark Canyon Mbr. Notably, all of the dates agree with the stratigraphy proposed by McClincy (1986) and Evans (1994), support their thickness estimates, and confirm rapid sediment accumulation rates of ca. 6 - 7 m/kyr within the lower and middle Clark Canyon Mbr., and ca. 2 - 3.3 m/kyr in the upper Clark Canyon Mbr. (Fig. 6).

The Tumwater Mtn. Mbr. of the Chumstick Fm. is interbedded with the Clark Canyon Mbr. along the Leavenworth fault zone and is composed of conglomerate, sandstone, and mudstones whose facies distribution, paleocurrent indicators, and distinctive clast lithologies

suggest a proximal sediment source across the fault zone (Evans, 1994). Evidence for syn-depositional faulting on the Leavenworth fault zone comes from soft-sediment deformation that is compatible with paleo-earthquake activity (Evans, 1994) and extremely coarse conglomerates (clasts > 1 m in diameter) near the southern end of the member that are monolithologic and separated by > 30 km along the Leavenworth fault zone from their distinctive source areas (Gresens et al., 1981; Evans, 1994). The precise age of this member is poorly constrained, but it is interbedded with rocks of the Clark Canyon Mbr. and therefore must have been deposited between ca. 49 and 47 Ma.

The Nahahum Canyon Mbr. is the stratigraphically lowest member of the Chumstick Fm. exposed to the east of the Eagle Creek fault. Evans (1994) considered it to be younger than the Clark Canyon Mbr. since it lacks interbedded tuffs, it represents disruption of the W-directed drainage system that fed the Clark Canyon Mbr., and it contains distinctive lacustrine sequences. The member has a minimum thickness of 1900 m (Fig. 6) and Evans (1994) interpreted it as a strike-slip basin between the Eagle Creek and Entiat fault systems. There is abundant sedimentologic data to support this interpretation, including coarse-grained facies adjacent to the member's bounding faults, basin axial paleoflow, and soft-sediment deformation compatible with syn-depositional earthquake activity (Evans, 1994). A detrital zircon from sandstone (ED071613-127) in the middle of the Nahahum Canyon Mbr. gives a maximum depositional age of 46.902 ± 0.076/0.082/0.096 Ma, and a minimum age for major displacement on the Eagle Creek fault is provided by a U-Pb zircon date of 44.447 ± 0.027/0.035/0.059 Ma from a shallow rhyodacite intrusion that seals this structure (Gilmour, 2012).

The 2200 m thick Deadhorse Canyon Mbr. is described by Evans (1994) and unconformably overlies both the eastern and western sections of the Chumstick Fm. (Fig. 6). This member records W-directed paleoflow and contains no evidence for a syn-depositional relationship with adjacent fault zones. Indeed, small outcrops of this member are present on both sides of the Eagle Creek and Entiat fault zones and preclude major strike-slip motion on these structures after its deposition. Zircons from a clast of flow-banded rhyolite collected from the Deadhorse Canyon Mbr. (NC-MPE-020) give a date of 45.910 ± 0.021/0.029/0.057 Ma (n=4, MSWD=0.7) and provide a maximum depositional age for this member.

Our nine new U-Pb dates from the Chumstick Fm. directly bear on the correlation of these rocks with the formations in the adjacent Teanaway River Block. The 49.147 ± 0.041 Ma

date for the Fairview Canyon tuff near the base of the Clark Canyon Mbr. demonstrates that sediment accumulation in the Chumstick Fm. initiated during eruption of the lower Teanaway Fm. and that it is younger than the adjacent Swauk Fm. Our maximum depositional ages of 48.80 ± 0.11 Ma and 47.580 ± 0.028 Ma for the lower and middle Roslyn Fm. make it possible that this formation is, in part, correlative with the Chumstick Fm. (Cheney, 2003; Cheney and Hayman, 2009). However, we think that the Roslyn Fm. is distinctly younger than most of the Chumstick Fm. because 1) the Roslyn Fm. does not contain abundant tuffs, 2) there is substantial evidence for uplift along the Leavenworth fault preserved in the Tumwater Mtn. Mbr. of the Chumstick Fm., precluding a continuous depositional system across this structure until after ca. 47 Ma, and 3) the Roslyn Fm. contains no evidence for syn-depositional strike-slip faulting. Instead, we consider the Clark Canyon, Tumwater Mtn., and Nahahum Canyon Mbrs. of the Chumstick Fm. to represent a distinct sedimentary package that was deposited during strike-slip faulting starting slightly before 49.147 ± 0.041 Ma and ending prior to 44.447 ± 0.027 Ma (Table 2), and the Deadhorse Canyon Mbr. and Roslyn Fm. to represent a continuous depositional system that is younger than 45.910 ± 0.021 Ma (Table 2).

Stratigraphic Correlations and Basin Evolution

Swauk Basin

Restoration of 100-150 km of dextral motion on the Straight Creek-Fraser fault (e.g., Umhoefer and Miller, 1996) places the Chuckanut and Swauk Fms. adjacent to one another (Fig. 7), and has long led to speculation that they accumulated within a single depositional system (e.g., Frizzell, 1979). The U-Pb zircon geochronology presented in this paper confirms that both of these formations, along with the Manastash Fm., were deposited during the same period of time between ≤ 59.9 and > 49.9 Ma (Fig. 8). Paleocurrent indicators suggest that sediment accumulation occurred along W- or SW-flowing streams between ≤ 59.9 and 51.3 Ma, followed by a reversal in paleoflow direction to the NE between 51.3 and > 49.9 Ma (Fig. 7). Sediment accumulation ended before 49.9 Ma (Fig. 8), and was marked by NNE-SSW directed shortening and basin inversion. Given that these formations record similar patterns of paleoflow, were deposited over the same period of time, and restore adjacent to one another across the Straight Creek-Fraser fault, we believe that they represent erosional remnants of a single depositional

system that we call the Swauk basin. Our preferred correlation scheme for rocks within the Swauk basin is shown in Table 2. Most of these correlations are not new, and have been previously discussed at both the local and regional levels (e.g., Frizzell, 1979; Tabor et al., 1984; Cheney, 1994, 2003; Evans, 1994; Evans and Ristow, 1994; Cheney and Hayman, 2009). However, they have never been presented collectively, nor has geochronologic data been able to confirm their temporal relationships.

We define the lower Swauk basin as those rocks that record W- or SW-directed paleoflow between $\leq$ 59.9 to 51.3 Ma in the Chuckanut, Manastash, and Swauk Fms. Sediment accumulation rates for this part of the basin are difficult to determine because of poor exposure and sparse isotopic dates, but rates of ca. 0.63 m/kyr for the Chuckanut Fm. (Fig. 2) and ca. 0.60 m/kyr for the lower Swauk Fm. (Fig. 5) are in good agreement and suggest moderately high sediment accumulation during this period. The tectonic setting of the lower Swauk basin remains uncertain. Geophysical data suggests that the boundary between Siletzia and North America represents a Paleogene subduction zone (e.g., Clowes et al., 1987; Hyndman et al., 1990; Gao et al., 2011; Schmandt and Humphreys, 2011), and since the Swauk basin is immediately adjacent to this boundary (Fig. 7) it may represent a forearc basin (Fig. 9A). However, this interpretation is complicated by the absence of arc magmatism in central and western Washington from ca. 60 to 51 Ma (e.g., Miller et al., 2009). This apparent contradiction could be explained by low-angle or flat slab subduction (e.g., Humphreys, 2009), which may also explain the prolonged presence of thick (> 30 km), partially molten crust in Washington and British Columbia during much of the Paleocene and early Eocene (Gordon et al., 2008, 2010; Krukenburg et al., 2008). Nevertheless, forearc basins are typically inverted during flat slab subduction (e.g., Finzel et al., 2011) and the steady subsidence of the lower Swauk basin would be anomalous for this setting.

Accretion of Siletzia and Bimodal Volcanism

The upper Swauk basin records a major change in tectonic setting marked by a reversal of paleoflow direction from SSW to NE (Fig. 7), a dramatic increase in sediment accumulation rate to > 1.61 m/kyr (Fig. 5) and, in places, abundant conglomerate clasts likely sourced from rocks in the western and eastern mélange belts (Fig. 1B) between 51.3 and 49.9 Ma (Fig. 8). We infer this change to mark the development of near-trench topography during accretion of Siletzia, and propose that the upper Swauk basin acted as a foreland basin during this collision (Fig. 9B).

Regionally extensive, west-verging fold and thrust belts of Eocene age are associated with the accretion of Siletzia on Vancouver Island (Johnston and Acton, 2003) and in Oregon (Wells et al., 2014), but one has not been described from western Washington. Nevertheless, the lack of a well-described Eocene fold-and-thrust belt in this area need not preclude its existence, because bedrock of Eocene-age or older is largely covered by rocks related to the modern Cascade Arc or Quaternary deposits to the SW of the Swauk basin (Fig. 1B). Interestingly, the exhumed mid-crustal rocks of the Skagit Gneiss Complex (Fig. 1B) also record NE-SW directed shortening between ca. 51 and > 46 Ma (Wintzer, 2012), suggesting that the accretion of Siletzia may have led to shortening in both the upper and middle crust.

Most bathymetric features on the ocean floor subduct easily, leaving little or no geologic record. Two exceptions are thick (> 30 km) or young (< 10 Myr) oceanic lithosphere, which is buoyant enough to resist subduction and cause uplift and deformation in the upper plate of a subduction zone (e.g., Cloos, 1993). Siletzia may have represented lithosphere with both of these features. The exposed portion of northern Siletzia is much thicker (10 – 20 km) than typical oceanic crust (Wells et al., 2014), and existing geochronology suggests that northern Siletzia was formed after 52 Ma (Fig. 8). Interestingly, detrital zircons from the base of the Crescent Fm., which forms the thickest part (ca. 16 km) of northern Siletzia, overlap in age with ca. 51.5 – 50.5 Ma $^{40}Ar/^{39}Ar$ dates from the top of the formation (Fig. 8) and imply that this sequence was erupted immediately prior to, or concurrent with, accretion. Nevertheless, Wells et al. (2014) reports a date of 46 Ma for one detrital zircon from the base of the Crescent Fm., and if this analysis is accurate, it would require a complex magmatic history for this part of Siletzia that includes voluminous pre-, syn-, and post-accretion magmatism.

Following accretion of Siletzia, thick sequences of basalt with minor rhyolite were emplaced throughout much of the former Swauk basin and are preserved as the Teanaway Fm., Basalt of Frost Mtn., Naches Fm., and Barlow Pass Volcanics. The initiation of this volcanic episode is dated in three locations and occurred between 49.933 ± 0.059 Ma and 49.341 ± 0.033 Ma, but its termination is poorly constrained (Fig. 8).

Strike-Slip Faulting

As described above, abundant evidence exists for syn-depositional strike-slip faulting on the Entiat and Eagle Creek faults during deposition of the ≤ 46.902 ± 0.076 Ma to > 44.447 ±

0.027 Ma Nahahum Canyon Mbr. of the Chumstick Fm. and on the Leavenworth fault zone during deposition of the ca. 49 to 47 Ma Tumwater Mtn. Mbr. of the Chumstick Fm. It is unclear whether the Entiat fault was active prior to ca. 47 Ma. However, the ca. 49 to 47 Ma Clark Canyon Mbr. of the Chumstick Fm. records westerly paleoflow, high sediment accumulation rates (2 – 7 m/kyr), and rapid lateral movement of depocenters (Evans, 1994; Johnson, 1996). These features are consistent with deposition in a strike-slip basin, and we suggest that both the Entiat and Leavenworth fault zones were active during deposition of the Clark Canyon Mbr.

Two other high-angle fault systems in western Washington record dextral displacements during the early to middle Eocene. The Straight Creek-Fraser fault displaces the Swauk basin and pre-Cenozoic rocks 100 - 150 km, requiring this displacement to have occurred after ca. 50 Ma and before the structure was sealed by 35 - 30 Ma granite intrusions (Tabor et al., 2003). To the north of our field area, the Straight Creek-Fraser fault cuts the Yalakom fault and offsets it ca. 100 km from its likely southern continuation as the Ross Lake fault. Deformed granites along the Yalakom fault are as young as 48 - 46 Ma, indicating that ca. 100 km of dextral displacement occurred on the Straight Creek-Fraser fault after 46 Ma in this area (Coleman and Parrish, 1990). Motion on the Darrington-Devil's Mtn. fault zone (Fig. 1B) is also constrained to after ca. 50 Ma, because this structure cuts the SE Chuckanut Fm. and displaces blocks of the Manastash Fm. along dextral faults (Tabor, 1994).

Return to Regional Depositional System

The Deadhorse Canyon Mbr. of the Chumstick Fm., shows no evidence for syn-depositional faulting, has paleocurrent indicators that suggest W to SW paleoflow, and is deposited on both sides of the Entiat and Eagle Creek fault zones (Evans, 1994). Therefore, major motion on these structures ceased prior to its deposition. We follow Evans (1994) and correlate these rocks with the Roslyn Fm., which also records W-directed paleoflow, lacks tuffs, and lacks evidence for syn-depositional faulting (Walker, 1980; Tabor et al., 1984; Barnett, 1985). Collectively, we refer to the Deadhorse Canyon Mbr. of the Chumstick Fm. and the Roslyn Fm. as the Roslyn basin (Table 2) and consider it to represent the return of a regional depositional system along this part of the North American margin $\leq 45.910 \pm 0.021$ Ma, with a possible western continuation in the Puget Group (Fig. 1B; Vine, 1969, Buckovic, 1979). However, the connection between these two areas remains uncertain, because the Straight Creek-

Fraser fault may have been active during this time (e.g., Coleman and Parrish, 1990; Umhoefer and Miller, 1996).

Relationship to Triple-Junction Migration

Plate reconstructions require the subduction of the Kula-Farallon or both the Kula-Resurrection and Resurrection-Farallon ridges along the North American margin during the Paleogene (e.g., Atwater, 1970; Wells et al., 1984; Engebretson et al., 1985; Haeussler et al., 2003; Madsen et al., 2006). Eocene near-trench magmatism (Cowan, 2003; Groome, 2003; Haeussler et al., 2003; Madsen et al., 2006) and geochemically anomalous backarc magmatism (Breitsprecher et al., 2003; Ickert et al., 2009) in southern British Columbia and Washington have been linked to this tectonic setting. The sedimentary, volcanic, and structural history of the Swauk, Chumstick, and Roslyn basins is also consistent with triple junction migration and we discuss their evolution within this framework.

Near-trench magmatism is typically associated with areas of ridge-trench interaction (e.g., Marshak and Karig, 1977) and can result from a variety of processes. In areas where triple junction geometry results in the formation of a slab window, near-trench magmatism can arise from decompression melting as asthenospheric mantle rises through slab gaps and crustal melting as metasedimentary rocks in the forearc are heated (DeLong et al., 1979; Groome and Thorkelson, 2009). Geochemically anomalous magmas are expected in this setting and include crustal melts (e.g., Hill et al., 1981; Barker et al., 1992) and adakites (Thorkelson and Breitsprecher, 2005). Alternatively, the formation and capture of oceanic microplates can also occur during ridge-trench interaction (e.g., Stock and Lee, 1994) and is sometimes associated with slab breakoff, which can lead to similar magmatism (Ferrari, 2004; Pallares et al., 2007).

Early Eocene near-trench magmatism on southern Vancouver Island and in western Washington includes peraluminous granites that represent melts derived from forearc metasedimentary rocks and dacitic rocks with adakitic geochemistry that may represent melts derived from subducted basalt or underplated mafic crust. Dated near-trench magmatism includes the ca. 51 Ma, peraluminous Walker Creek intrusions (Fig. 1B: Groome et al., 2003), the ca. 49 Ma, peraluminous Mt. Pilchuck intrusive suite (Fig. 1B: Wiebe, 1963; Yeats and Engels, 1971), ca. 48-47 Ma dacitic dikes with adakitic compositions that intrude northern Siletzia in the Bremerton Hills (Fig. 1B: Tepper et al., 2004), and the ca. 51 – 49 Ma Flores

volcanics and Clayoquot intrusions on Vancouver Island (Irving and Brandon, 1990; Madsen et al., 2006). Undated adakite localities include block and ash flow deposits near Port Townsend (Fig. 1B; Tepper et al., 2004) and dacite in the ca. 47 - 36 Ma Mt. Persis volcanics (Fig. 1B; Macdonald et al., 2012). All of this near-trench magmatism occurred over a short interval between ca. 51 and 47 Ma (Fig. 8) and has similar compositional diversity to near-trench magmatic suites in areas where ridge-trench interaction is well-documented, including the southern Alaska margin (Hill et al., 1981; Barker et al., 1996; Harris et al., 1996) and Taitao peninsula in Chile (Forsythe et al., 1986; Kaeding et al., 1990; Guivel et al., 1999). These similarities have led Cowan (2003), Groome et al. (2003), Haeussler et al. (2003), and Madsen et al. (2006) to suggest that the near-trench magmatism in western Washington and on Vancouver Island occurred at a ridge-trench-trench triple junction and we follow these authors by placing either the Kula-Farallon-North America or Resurrection-Farallon-North America triple junction on Vancouver Island between 51 - 49 Ma (Fig. 9B). Dates for near-trench magmatism in Washington are slightly younger than those on Vancouver Island (Fig. 8), albeit still within uncertainty, and may indicate that the triple junction was migrating southward at this time.

Initial disruption of the Swauk basin coincides with the earliest forearc magmatism on Vancouver Island at ca. 51 Ma (Figs. 8 and 9) and was likely caused by accretion of both young (< 2 Myr) and thick (10 - 20 km) oceanic crust belonging to Siletzia. The tectonic setting required to generate such thickened crust remains enigmatic. However, the projected position of the Yellowstone hotspot during the Paleogene is in western Oregon (Johnston and Thorkelson, 2000) and northern Siletzia may represent oceanic crust developed at a spreading ridge influenced by the presence of a mantle plume (e.g., McCrory et al., 2013; Wells et al., 2014). The attempted subduction of northern Siletzia culminated in the development of a WNW-trending fold-and-thrust belt in the Swauk basin between 51.3 and 49.9 Ma (Fig. 9B) and was followed by bimodal volcanism.

Uplift and the development of unconformities have been documented in other forearc basins during ridge-trench interaction (e.g., Gulick et al., 2002; Trop et al., 2003), indicating that it might be a common effect of this process. The driving force behind uplift may be shortening related to the subduction of young, buoyant crust (e.g., Cloos, 1993), development of dynamic topography above slab windows (e.g., Groome and Thorkelson, 2009; Guillaume et al., 2010), or some combination of the two processes. In the Swauk basin, shortening is linked to the accretion

of Siletzia, which likely represented young, thick, and buoyant oceanic crust. The attempted subduction of such anomalous crust may explain why shortening occurred from Vancouver Island to southern Oregon (Johnston and Acton, 2003; Wells et al., 2014) compared to the less pronounced shortening described from the Matanuska Valley-Talkeetna Mountains basin during Paleogene ridge-trench (Trop et al., 2003) or the more localized uplift and shortening associated with the modern Mendocino triple junction (McCrory, 2000; Gulick et al., 2002).

Dextral strike-slip faulting began, or accelerated, on the Entiat, Leavenworth, Darrington Devil's Mtn., Eagle Creek, and Straight Creek-Fraser fault zones in western Washington immediately following the accretion of Siletzia at 51.3 to 49.9 Ma and lasted 5 to 15 Myr. Precise estimates for the offset on most of these faults are not available. However, we interpret the 100 - 150 km of post ca. 50 Ma displacement on the Straight Creek-Fraser fault as well as the initiation, or acceleration, of dextral motion on the other fault systems described in this paper to be indicative of a change to significant dextral motion along this part of the North American plate boundary. These faults form the southern portion of a series of major strike-slip faults that run through the northern Cordillera, each of which record large dextral displacements (> 100 km) during the Late Cretaceous and early Cenozoic (Lanphere, 1978; Gabrielse, 1985; Wyld et al., 2006; Pavlis and Roeske, 2007). The driving force for this faulting was oblique motion between the Kula, and possibly the Resurrection, plate(s) and North America, and we infer that the initiation, or acceleration, of strike-slip motion in central and western Washington marks the southward migration, or jump, of the Kula-Farallon-North America or Resurrection-Farallon-North America triple junction following accretion of Siletzia (Fig. 9C).

Near-trench magmatism to the south of our field area that may mark the location of the triple junction after the events discussed in this paper includes a regional series of gabbroic sills that are found from western Washington to southern Oregon constrained to between 46 and 42 Ma in age and the 42 to 34 Ma bimodal Tillamook, Yachats, Cascade Head, and Grays River volcanics (Chan et al., 2012; Wells et al., 2014). However, the tectonic setting for this magmatism is controversial and it may represent near-trench magmatism related to ridge-trench interaction (Wells et al., 1984; Madsen et al., 2006), magmatism related to the Yellowstone hotspot (Wells et al., 2014), or a combination of the two settings (Chan et al., 2012).

Conclusions

The relationship between structurally isolated Paleogene non-marine sedimentary sequences in central and western Washington has been a longstanding problem. The high-precision U-Pb zircon geochronology presented in this paper allows their temporal correlation and reveals a semi-continuous and self-consistent stratigraphy from ca. 60 to 45 Ma. Restoration of 100-150 km of dextral motion on the Straight Creek-Fraser fault places the Chuckanut, Manastash, and Swauk Fms. adjacent to one another and on the basis of sedimentological and temporal similarities we consider these formations to have formed a single sedimentary basin from $\leq$ 59.9 to > 49.9 Ma, that we call the Swauk basin. This basin was deposited along westward flowing streams from $\leq$ 59.9 to 51.3 Ma, but experienced significant disruption between 51.3 and > 49.9 Ma, starting with a reversal in paleoflow direction and culminating in basin inversion and the development of a WNW-trending fold belt that we attribute to the attempted subduction of young, thick, and buoyant oceanic crust belonging to Siletzia. Following the accretion of Siletzia, the Swauk basin was dismembered by dextral strike-slip faults and the Chumstick strike-slip basin formed between the Entiat and Leavenworth faults. Sedimentary rocks belonging to the Roslyn basin are $\leq$ 45.9 Ma and span the Entiat, Eagle Creek, and Leavenworth fault zones, precluding significant strike-slip faulting on these structures during its deposition. However, strike-slip faulting may have continued on the Straight Creek-Fraser fault until 35 - 30 Ma. The record of Paleogene sediment accumulation, volcanism, and strike-slip faulting described in this paper can be linked to events along the plate margin and we consider the initiation, or acceleration, of dextral strike-slip faulting in central and western Washington to mark the southward migration of the Kula-Farallon or Resurrection-Farallon ridge along the North American margin. This interpretation is consistent with the timing of near-trench and geochemically anomalous backarc magmatism at this latitude and provides further support for the presence of one of these ridges along this part of the Pacific Northwest during the early Eocene.

Appendix A

Zircons were separated from each sample using standard crushing and density separation techniques. Rocks were first sledged to < 1 cm^3 pieces, and then subjected to repeated short duration runs (< 5 s) in a Spex Shatterbox in an effort to liberate individual mineral grains. This material was then sieved through a 500 μm mesh and the resulting < 500 μm fraction was

washed by hand for an initial, crude density separation. The remaining sample was run through a Frantz magnetic separator at 0.6A/20°. A final density separation was done using MEI on the nonmagnetic fraction, and a pure zircon separate was obtained by hand picking under a binocular microscope.

Individual zircons selected for CA-IDTIMS analysis were annealed at 900°C for 60 hours and then partially digested in 29M HF in a Parr vessel held at 215°C for 12 hours. The partially digested grains were rinsed in ultrapure H_2O, fluxed on a hot plate (~ 80°C) in 6.2N HCl, re-rinsed in ultrapure H_2O, and loaded into individual Teflon microcapsules. The capsules were spiked with the EARTHTIME ^{205}Pb-^{233}U-^{235}U isotopic tracer (Condon et al., 2015) and the partially digested grains were completely dissolved in 29M HF in a Parr vessel held at 215°C for 48 hours. The resulting solutions were dried down, dissolved in 6.2N HCl and held at 180°C for ca. 12 hours. Samples were then converted to 3N HCl, and U and Pb were separated on anion exchange columns following the procedure of Krogh (1973). The samples were then dried down to a chloride salt, re-dissolved in silica gel, and loaded onto outgassed, zone-refined Re filaments for thermal ionization mass spectrometry.

All isotopic measurements were made on either the VG Sector 54 or Isotopx X62 thermal ionization mass spectrometers at the Massachusetts Institute of Technology. Pb isotopes were measured by peak hopping on a Daly detector and corrected for fractionation based on repeat analyses of the NBS 981 Pb isotopic standard. U was measured statically on Faraday cups and corrected for fractionation using the ^{233}U-^{235}U double spike. We assume that zircon grains incorporate no initial Pb during crystallization and that all measured ^{204}Pb comes from laboratory blank (Pb_c). The mass of Pb_c measured in all the analyses in this paper is indistinguishable from the range of Pb_c seen in total procedural blanks and provides strong support for the assumption. We corrected all Pb isotopic ratios for laboratory blank using $^{206}Pb/^{204}Pb$ = 17.910828 ± 0.371937, $^{207}Pb/^{204}Pb$ = 15.204620 ± 0.261366, and $^{208}Pb/^{204}Pb$ = 36.841963 ± 0.726065 (1σ, absolute) based on 53 total procedural blanks measured between August 2013 and January 2015. All analyses are corrected for exclusion of ^{230}Th during zircon crystallization. ^{230}Th is a long-lived ($t^{1/2}$ = 75.380 kyr) daughter product of ^{238}U and its preferential exclusion from zircon can result in a $^{238}U/^{206}Pb$ date that is too young by as much as ca. 100 kyr. We correct for this initial ^{230}Th deficiency using a calculated Th/U for the zircon and an assumed Th/U ratio of 2.8 ± 1 (2σ) for the magma (Machlus et al., 2015). Data reduction was done using the U-Pb_Redux

software package (Bowring et al., 2011) and used the decay constants for ^{238}U and ^{235}U presented in Jaffey et al. (1971). All isotopic data is reported in Table A1, and shown on concordia plots in Figure A1. Only the youngest population of zircon dates for each sample is shown in Figure A1. For dates of zircon grains that we interpret as detrital, please refer to Table A1.

Dates for four of the samples presented in this paper were previously reported in McLean (2011) and differ by up to ca. 20 kyr. This difference arises from additional zircon analyses and the application of a new laboratory blank isotopic composition.

References

Atwater, T., 1970, Implications of plate tectonics for the Cenozoic tectonic evolution of North America: Geological Society of America Bulletin, v. 81, p. 3513-3536, doi: 10.1130/0016-7606(1970)81[3513:IOPTFT]2.0.CO;2.

Babcock, R.S., Hirsch, D.M., and Clark, K.P., 2006, Geochemistry and petrology of a thick sequence of Crescent basalt in the Dosewallips River Valley, Olympic Peninsula, Washington State: Geological Society of America Abstracts with Programs, v. 38, n. 5, p. 95.

Barker, F., Farmer, G.L., Ayuso, R.A., Plafker, G., and Lull, J.S., 1992, The 50 Ma granodiorite of the eastern Gulf of Alaska: melting in an accretionary prism in the forearc: Journal of Geophysical Research: Solid Earth, v. 97, p. 6757-6778, doi: 10.1029/92JB00257.

Barnett, D.B., 1985, A paleoenvironmental reconstruction of the upper Roslyn Formation, central Washington, with implications for coal exploration [M.S. Thesis]: Cheney, Eastern Washington University, 334 p.

Benoit, M., Aguillon-Robles, A., Calmus, T., Maury, R.C., Bellon, H., Cotton, J., Bourgois, J., and Michaud, F., 2002, Geochemical diversity of late Miocene volcanism in southern Baja California, Mexico: implication of mantle and crustal sources during the opening of an asthenospheric window: The Journal of Geology, v. 110, p. 627-648, doi: 10.1086/342735.

Bradley, D.C., Kusky, T., Haeussler, P.J., Goldfarb, R., Miller, M.L., Dumoulin, J., Nelson, S.W., and Karl, S., 2003, Geologic signature of early Tertiary ridge subduction in Alaska, *in* Sisson, V.B., Roeske, S.M., and Pavlis, T.L., eds., Geology of a transpressional orogen

developed during ridge-trench interaction along the north Pacific margin: Geological Society of America Special Paper 371, p. 19-49, doi: 10.1130/0-8137-2371-X.19.

Breedlovestrout, R.L., 2011, Paleofloristic studies in the Paleogene Chuckanut Basin, western Washington, USA [Ph.D. Thesis]: Moscow, University of Idaho, 954 p.

Breedlovestrout, R.L., Evraets, B.J., Parrish, J.T., 2013, New Paleogene paleoclimate analysis of western Washington using physiognomic characteristics from fossil leaves: Palaeogeography, Palaeoclimatology, Palaeoecology, v. 392, p. 22-40, doi: 10.1016/j.palaeo.2013.08.013.

Breitsprecher, K., Thorkelson, D.J., Groome, W.G., and Dostal, J., 2003, Geochemical confirmation of the Kula-Farallon slab window beneath the Pacific Northwest in Eocene time: Geology, v. 31, p. 351-354, doi: 10.1130/0091-7613(2003)031<0351:GCOTKF> 2.0.CO;2.

Bowring, J.F., McLean, N.M., and Bowring, S.A., 2011, Engineering cyber infrastructure for U-Pb geochronology: Tripoli and U-Pb_Redux: Geochemistry, Geophysics, and Geosystems, v. 12, doi: 10.1029/2010GC003479.

Buckovic, W.A., 1979, The Eocene deltaic system of west-central Washington, *in* Armentrout, J.M., Cole, M.R., and TerBest, H., eds., Cenozoic paleogeography of the western United States: Society of Economic Paleontologists and Mineralogists, Pacific Coast Section, Pacific Coast Paleogeography Symposium 3, p. 147-164.

Chan, C.F., Tepper, J.H., and Nelson, B.K., 2012, Petrology of the Grays River volcanics, southwester Washington: plume-influenced slab window magmatism in the Cascadia forearc: Geological Society of America Bulletin, v. 124, p. 1324-1338, doi: 10.1130/B30576.1.

Cheney, E.S., 1994, Cenozoic unconformity-bounded sequences of central and eastern Washington: Washington Division of Geology and Earth Resources Bulletin 80, p. 115-139.

Cheney, E.S., 2003, Regional Tertiary sequence stratigraphy and regional structure on the eastern flank of the central Cascade Range, Washington, *in* Swanson, T.W., ed., Western Cordillera and Adjacent Areas: Geological Society of America Field Guide 4, p. 177-199, doi: 10.1130/0-8137-0004-3.177.

Cheney, E.S., and Hayman, N.W., 2009, The Chiwaukum structural low: Cenozoic shortening of the central Cascade Range, Washington state, USA: Geological Society of America Bulletin, v. 121, p. 1135-1153, doi: 10.1130/B26446.

Clayton, D.N., 1973, Volcanic history of the Teanaway Basalt, east-central Cascade Mountains, Washington [M.S. Thesis]: Seattle, University of Washington, 55 p.

Cloos, M., 1993, Lithospheric buoyancy and collisional orogenesis: subduction of orogenic plateaus, continental margins, island arcs, spreading ridges, and seamounts: Geological Society of America Bulletin, v. 105, p. 715-737, doi: 10.1130/0016-7606(1993)105<0715:LBACOS>2.3.CO;2.

Clowes, R.M., Brandon, M.T., Green, A.G., Yorath, C.J., Sutherland Brown, A., Kanasewich, E.R., and Spencer, C., 1987, LITHOPROBE-southern Vancouver Island: Cenozoic subduction complex imaged by deep seismic reflections: Canadian Journal of Earth Sciences, v. 24, p. 31-51, doi: 10.1139/e87-004.

Coleman, M.E., and Parrish, R.R., 1991, Eocene dextral strike-slip and extensional faulting in the Bridge River Terrane, southwest British Columbia: Tectonics, v. 10, p. 1222-1238, doi: 10.1029/91TC01078.

Condon, D.J., Schoene, B., McLean, N.M., Bowring, S.A., and Parrish, R.R., 2015, Metrology and traceability of U-Pb isotope dilution geochronology (EARTHTIME tracer calibration Part I): Geochemica et Cosmochimica Acta, doi: 10.1016/j.gca.2015.05.026 (in press).

Cowan, D.S., 2003, Revisiting the Baranof-Leech River hypothesis for early Tertiary coastwise transport of the Chugach-Prince William terrane: Earth and Planetary Science Letters, v. 213, p. 463-475, doi: 10.1016/S0012-821X(03)00300-5.

Cruver, S.K., 1981, The geology and mineralogy of bentonites and associated rocks of the Chuckanut Formation, Mt. Higgins area, North Cascades Washington [M.S. Thesis]: Bellingham, Western Washington University, 105 p.

DeLong, S.E., Schwarz, W.M., and Anderson, R.N., 1979, Thermal effects of ridge subduction: Earth and Planetary Science Letters, v. 44, p. 239-246, doi: 10.1016/0012-821X(79)90172-9.

Doran, B.A., 2009, Structure of the Swauk formation and Teanaway dike swarm, Washington Cascades [M.S. Thesis]: San Jose, San Jose State University, 97 p.

Dragovich, J.D., Logan, R.L., Schasse, H.W., Walsh, T.J., Lingley Jr., W.S., Norman, D.K., Gerstel, W.J., Lapen, T.J., Schuster, E., and Meyers, K.D., 2002, Geologic map of Washington-northwest quadrant: Washington Department of Natural Resources Geologic Map GM-50, scale 1:250,000, 3 sheets, 72 p. text.

Dragovich, J.D., Stanton, B.W., Lingley Jr., W.S., Griesel, G.A., and Polenz, M., 2003, Geologic map of the Mount Higgins 7.5-minute quadrangle, Skagit and Snohomish counties, Washington: Washington Department of Natural Resources, scale 1:24,000, 1 sheet.

Einarsen, J.M., 1987, The petrography and tectonic significance of the Blue Mountain Unit, Olympic Peninsula, Washington [M.S. thesis]: Bellingham, Western Washington University, 175 p.

Engebretson, D.C., Cox, A., and Gordon, R.G., 1985, Relative motions between oceanic and continental plates in the Pacific basin: Geological Society of America Special Papers, v. 206, p. 1-60, doi: 10.1130/SPE206-p1.

Evans, J.E., 1994, Depositional history of the Eocene Chumstick Formation: implications of tectonic partitioning for the history for he Leavenworth and Entiat-Eagle Creek fault systems, Washington: Tectonics, v. 13, p. 1425-1444, doi: 10.1029/94TC01321.

Evans, J.E., 1996, Depositional history of the Eocene Chumstick Formation: implications of tectonic partitioning for the history for he Leavenworth and Entiat-Eagle Creek fault systems, Washington: Reply: Tectonics, v. 15, p. 510-514, doi: 10.1029/95TC03695.

Evans, J.E., and Ristow Jr., R.J., 1994, Depositional history of the southeastern outcrop belt of the Chuckanut Formation: implications for the Darrington – Devil's Mountain and Straight Creek fault zones, Washington (USA): Canadian Journal of Earth Sciences, v. 31, p. 1727-1743, doi: 10.1139/e94-154.

Ferrari, L., 2004, Slab detachment control on mafic volcanic pulse and mantle heterogeneity in central Mexico: Geology, v. 32, p. 77-80, doi: 10.1130/G19887.1.

Finzel, E.S., Trop, J.M., Ridgeway, K.D., and Enkelmann, E., 2011, Upper plate proxies for flat-slab subduction processes in southern Alaska: Earth and Planetary Science Letters, v. 303, p. 348-360, doi: 10.1016/j.epsl.2011.01.014.

Forsythe, R.D., Nelson, E.P., Carr, M.J., Kaeding, M.E., Herve, M., Mpodozis, C., Soffia, J.M., and Harambour, S., 1986, Pliocene near-trench magmatism in southern Chile: a possible

manifestation of ridge collision: Geology, v. 14, p. 23-27, doi: 10.1130/0091-7613(1986)14<23:PNMISC>2.0.CO;2.

Foster, R.J., 1960, Tertiary geology of a portion of the central Cascade Mountains, Washington: Geological Society of America Bulletin, v. 71, p. 99-126, doi: 10.1130/0016-7606(1960)71[99:TGOAPO]2.0.CO;2.

Frizzell Jr., V.A., 1979, Petrology and stratigraphy of Paleogene nonmarine sandstones, Cascade Range, Washington: U.S. Geological Survey Open-File Report 79-1149, 151 p.

Gabrielse, H., 1985, Major dextral transcurrent displacements along the Northern Rocky Mountain Trench and related lineaments in north-central British Columbia: Geological Society of America Bulletin, v.96, p. 1-14, doi: 10.1130/0016-7606(1985)96<1:MDTDAT>2.0.CO;2.

Gao, H., Humphreys, E.D., Yao, H., and van der Hilst, R.D., 2011, Crust and lithosphere structure of northwestern U.S. with ambient noise tomography: terrane accretion and Cascade arc development: Earth and Planetary Science Letters, v. 304, p. 202-211, doi: 10.1016/j.epsl.2011.01.033.

Gilmour, L.A., 2012, U/Pb ages of Eocene and younger rocks on the eastern flank of the central Cascade Range, Washington, USA [M.S. Thesis]: Seattle, University of Washington, 48 p.

Gordon, S.M., Whitney, D.L., Teyssier, C., Grove, M., and Dunlap, W.J., 2008, Timescales of migmatization, melt crystallization, and cooling in a Cordilleran gneiss dome: Valhalla complex, southeastern British Columbia: Tectonics, v. 27, TC4010, doi: 10.1029/2007TC002103.

Gordon, S.M., Bowring, S.A., Whitney, D.L., Miller, R.B., and McLean, N.M., 2010, Timescales of metamorphism, deformation, and crustal melting in a continental arc, North Cascades USA: Geological Society of America Bulletin, v. 122, p. 1308-1330, doi: 10.1130/B30060.1.

Gresens, R.L., Naeser, C.W., and Whetten, J.W., 1981, Stratigraphy and age of the Chumstick and Wenatchee Formations: Tertiary fluvial and lacustrine rocks, Chiwaukum graben, Washington: Geological Society of America Bulletin, v. 92, p. 841-876, doi: 10.1130/GSAB-P2-92-841.

Groome W.G., and Thorkelson, D.J., 2009, The three-dimensional thermo-mechanical signature of ridge subduction and slab window migration: Tectonophysics, v. 464, p. 70-83, doi: 10.1016/j.tecto.2008.07.003.

Groome, W.G., Thorkelson, D.J., Friedman, R.M., Mortensen, J.K., Massey, N.W.D., Marshall, D.D., and Layer, P.W., 2003, Magmatic and tectonic history of the Leech River Complex, Vancouver Island, British Columbia: evidence for ridge-trench intersection and accretion of the Crescent terrane, *in* Sisson, V.B., Roeske, S.M., and Pavlis, T.L., eds., Geology of a transpressional orogen developed during ridge-trench interaction along the north Pacific margin: Geological Society of America Special Paper 371, p. 327-353, doi: 10.1130/0-8137-2371-X.327.

Grow, J.A., and Atwater, T., 1970, Mid-Tertiary tectonic transition in the Aleutian arc: Geological Society of America Bulletin, v. 81, p. 3715-3722, doi: 10.1130/0016-7606(1970)81[3715:MTTITA]2.0.CO;2.

Guillaume, B., Moroni, M., Funiciello, F., Martinod, J., and Faccenna, C., 2010, Mantle flow and dynamic topography associated with slab window opening: insights from laboratory models: Tectonophysics, v. 496, p. 83-98, doi: 10.1016/j.tecto.2010.10.014.

Guivel, C., Lagabrielle, Y., Bourgois, J., Maury, R.C., Fourcade, S., Martin, H., Arnaud, N., 1999, New geochemical constraints for the origin of ridge-subduction-related plutonic and volcanic suites from the Chile Triple Junction (Taitao Peninsula and Site 862, LEG ODP141 on the Taitao Ridge): Tectonophysics, v. 311, p. 83-111, doi: 10.1016/S0040-1951(99)00160-2.

Gulick, S.P.S, Meltzer, A.S., and Clarke Jr., S.H., 2002, Effect of the northward-migrating Mendocino triple junction on the Eel River forearc basin, California: stratigraphic development: Geological Society of America Bulletin, v. 114, p. 178-191, doi: 10.1130/0016-7606(2002)114<0178:EOTNMM>2.0.CO;2.

Haeussler, P.J., Clark, K.P., 2000, Geologic map of the Wildcat Lake 7.5' quadrangle, Kitsap and Mason counties, Washington: U.S. Geological Survey, Open-File Report OF-2000-356, scale 1:24,000.

Haeussler, P.J., Bradley, D.C., Wells, R.E., and Miller, M.L., 2003, Life and death of the Resurrection plate: evidence for its existence and subduction in the northeastern Pacific

in Paleocene-Eocene time: Geological Society of America Bulletin, v. 115, p. 867-880, doi: 10.1130/0016-7606(2003)115<0867:LADOTR>2.0.CO;2.

Harris, N.R., Sisson, V.B., Wright, J.E., and Pavlis, T.L., 1996, Evidence for Eocene mafic underplating during fore-arc intrusive activity, eastern Chugach Mountains, Alaska: Geology, v. 24, p. 263-266, doi: 10.1130/0091-7613(1996)024<0263:EFEMUD>2.3.CO;2.

Hill, M., Morris, J., and Whelan, J., 1981, Hybrid granodiorites intruding the accretionary prism, Kodiak, Shumagin, and Sanak islands, southwest Alaska: Journal of Geophysical Research: Solid Earth, v. 86, p. 10569-10590, doi: 10.1029/JB086iB11p10569.

Humphreys, E., 2009, Relation of flat subduction to magmatism and deformation in the western United States, in Kay, S.M., Ramos, V.A., and Dickinson, W.R., eds., Backbone of the Americas: shallow subduction, plateau uplift, and ridge and terrane collision: Geological Society of America Memoir 204, p. 85–98, doi: 10.1130/2009.1204(04).

Hyndman, R.D., Yorath, C.J., Clowes, R.M., and Davis, E.E., 1990, The northern Cascadia subduction zone at Vancouver Island: seismic structure and tectonic history: Canadian Journal of Earth Sciences, v. 27, p. 313-329, doi: 10.1139/e90-030.

Ickert, R.B., Thorkelson, D.J., Marshall, D.D., and Ullrich, T.D., 2009, Eocene adakitic volcanism in southern British Columbia: remelting of arc basalt above a slab window: Tectonophysics, v. 464, p. 164-185, doi: 10.1016/j.tecto.2007.10.007.

Irving, E., and Brandon, M.T., 1990, Paleomagnetism of the Flores volcanics, Vancouver Island, in place by Eocene time: Canadian Journal of Earth Sciences, v. 27, p. 811-817, doi: 10.1139/e90-083.

Jaffey, A.H., Flynn, K.F., Glendenin, L.E., Bentley, W.C., Essling, A.M., 1971, Precision measurement of half-lives and specific activities of 235U and 38U: Physical Review C, v. 4, p. 1889-1906, doi: 10.1103/PhysRevC.4.1889.

Johnson, C.M., and O'Neil, J.R., 1984, Triple junction magmatism: a geochemical study of Neogene volcanic rocks in western California: Earth and Planetary Science Letters, v. 71, p. 241-262, doi: 10.1016/0012-821X(84)90090-6.

Johnson, S.Y., 1984, Stratigraphy, age, and paleogeography of the Eocene Chuckanut Formation, northwest Washington: Canadian Journal of Earth Sciences, v. 21, p. 92-106, doi: 10.1139/e84-010.

Johnson, S.Y., 1985, Eocene strike-slip faulting and nonmarine basin formation in Washington, *in* Biddle, K.T., Christie-Blick, N., eds., Strike-slip deformation, basin formation and sedimentation, Society of Economic Paleontologists and Mineralogists, Special Publication, p. 283– 302.

Johnson, S.Y., 1996, Depositional history of the Eocene Chumstick Formation: implications of tectonic partitioning for the history of the Entiat-Eagle Creek fault systems, Washington: Comment: Tectonics, v. 15, p. 506-509, doi: 10.1029/95TC03694.

Johnson, S.Y., and O'Connor, J.T., 1994, Stratigraphy, sedimentology, and provenance of the Raging River Formation (early? and middle Eocene), King County, Washington: U.S. Geological Survey Bulletin 2085-A, p. A1-A33.

Johnston, S.T., and Acton, S., 2003, The Eocene Southern Vancouver Island Orocline – seamount accretion and the cause of fold-and-thrust belt and extensional basin formation: Tectonophysics, v. 365, p. 165-183, doi: 10.1016/S0040-1951(03)00021-0.

Johnston, S.T., and Thorkelson, D.J., 2000, Continental flood basalts: episodic magmatism above long-lived hotspots: Earth and Planetary Science Letters, v. 175, p. 247-256, doi: 10.1016/S0012-821X(99)00293-9.

Kaeding, M., Forsythe, R.D., and Nelson, E.P., 1990, Geochemistry of the Taitao ophiolite and near-trench intrusions from the Chile Margin Triple Junction: Journal of South American Earth Science, v. 3, p. 161-177, doi: 10.1016/0895-9811(90)90001-H.

Krogh, T.E., 1973, Low-contamination method for hydrothermal decomposition of zircon and extraction of U and Pb for isotopic age determinations: Geochemica Cosmochimica Acta, v. 37, p. 485-494.

Krukenburg, S.C., Whitney, D.L., Teyssier, C., Fanning, C.M., and Dumlap, W.J., 2008, Paleocene-Eocene migmatite crystallization, extension, and exhumation in the hinterland of the northern Cordillera: Okanogan dome, Washington USA: Geological Society of America Bulletin, v. 120, p. 912-929, doi: 10.1130/B26153.1.

Lanphere, M.A., 1978, Displacement history of the Denali fault system, Alaska and Canada: Canadian Journal of Earth Sciences, v. 15, p. 817-822, doi: 10.1139/e78-086.

MacDonald, J.H., Dragovich, J.D., Littke, H.A., Anderson, M., and Dufrane, A.S., 2013, The volcanic rocks of Mount Persis: an Eocene continental arc that contains adakitic magmas: Geological Society of America Abstracts with Programs, v. 45, n. 7, p. 392.

Machlus, M.L., Ramezani, J., Bowring, S.A., Hemming, S.R., Tsukui, K., and Clyde, W.C., 2015, A strategy for cross-calibrating U-Pb chronology and astrochronology of sedimentary sequences: an example from the Green River Formation, Wyoming, USA: Earth and Planetary Sciences, v. 413, p. 70-78, doi:10.1016/j.epsl.2014.12.009.

Madsen, J.K., Thorkelson, D.J., Friedman, R.M., and Marshall, D.D., 2006, Cenozoic to recent plate configurations in the Pacific basin: ridge subduction and slab window magmatism in western North America: Geosphere, v. 2, p. 11-34, doi: 10.1130/GES00020.1.

Marshak, R.S., and Karig, D.E., 1977, Triple junctions as a cause for anomalously near-trench igneous activity between the trench and volcanic arc: Geology, v. 5, p. 233-236, doi: 10.1130/0091-7613(1977)5<233:TJAACF>2.0.CO;2.

Massey, N.W., 1986, Metchosin Igneous Complex, southern Vancouver Island: ophiolite stratigraphy developed in an emergent island setting: Geology, v. 14, p. 602-605, doi: 10.1130/0091-7613(1986)14<602:MICSVI>2.0.CO;2.

Massey, N.W., MacIntyre, D.G., Desjardins, P.J., and Cooney, R.T., 2005, Geology of British Columbia: BC Ministry of Energy, Mines, and Petroleum Resources Geoscience Map 2005-3, scale 1:1,000,000, 3 sheets.

Mattinson, J.M., 2005, Zircon U-Pb chemical abrasion ("CA-TIMS") method: Combined annealing and multi-step partial dissolution analysis for improved precision and accuracy of zircon ages: Chemical Geology, v. 220, p. 47-66, doi: 10.1016/j.chemgeo.2005.03.011.

McClincy, M.J., 1986, Tephrostratigraphy of the middle Eocene Chumstick Formation, Cascade Range, Douglas county, Washington [M.S. Thesis]: Portland, Portland State University, 254 p.

McCrory, P.M., 2000, Upper plate contraction north of the migration Mendocino triple junction northern California: implications for the partitioning of strain: Tectonics, v. 19, p. 1144-1160, doi: 10.1029/1999TC001177.

McCrory, P.A., and Wilson, D.S., 2013, A kinematic model for the formation of the Siletz-Crescent forearc terrane by capture of coherent fragments of the Farallon and Resurrection plates: Tectonics, v. 32, p. 718-736, doi: 10.1002/tect.20045.

McLean, N.M., 2011, Statistical considerations in high precision U-Pb geochronology with an application to the tectonic evolution of the North Cascades, Washington [PhD Thesis]: Cambridge, Massachusetts Institute of Technology, 186 p.

Miller, G.M., and Misch, P., 1963, Early Eocene angular unconformity at western front of northern Cascades, Whatcom County, Washington: American Association of Petroleum Geologists, v. 47, p. 163-174.

Miller, R.B., Gordon, S.M., Bowring, S.A., Doran, B.A., McLean, N.M., Michels, Z.D., Shea, E.K., Whitney, D.L., Wintzer, N.E., and Mendoza, M.K., 2009, Linking deep and shallow crustal processes in an exhumed continental arc, North Cascades, Washington, *in* O'Connor, J.E., Dorsey, R.J., and Madin, I.P., eds., Volcanoes to vineyards: geologic field trips through the dynamic landscape of the Pacific Northwest: Geological Society of America Field Guide 15, p. 373-406, doi: 10.1130/GES00669.1.

Pallares, C. Maury, R.C., Bellon, H., Royer, J., Calmus, T., Aguillon-Robles, A., Cotton, J., Benoit, M., Michaud, F., and Bourgois, J., 2007, Slab-tearing following ridge-trench collisions: evidence from Miocene volcanism in Baja California, Mexico: Journal of Volcanology and Geothermal Research, v. 161, p. 95-117, doi: 10.1016/j.jvolgeores.2006.11.002.

Pavlis, T.L., Roeske, S.M., 2007, The Border Ranges fault system, southern Alaska, *in* Ridgeway, K.D., Trop, J.M., Glen, J.M., and O'Neill, M.J. eds., Tectonic growth of a collisional continental margin: crustal evolution of southern Alaska: Geological Society of America Special Paper 431, p. 95-127, doi: 10.1130/2007.2431(05).

Schmandt, B., and Humphreys, E., 2011, Seismically imaged relict slab from the 55 Ma Siletzia accretion to the northwest United States: Geology, v. 39, p. 175-178, doi: 10.1130/G31558.1.

Schuster, J.E., Gulick, C.W., Reidel, S.P., Fecht, K.R., and Zurenko S., 1997, Geologic map of Washington-northeast quadrant: Washington Division of Geology and Earth Resources Geologic Map GM-45, scale 1:250,000, 2 sheets, 20 p. text.

Stock, J.M., and Lee J., 1994, Do microplates in subduction zones leave a geological record?: Tectonics, v. 13, p. 1472-1487, doi: 10.1029/94TC01808.

Stoffel, K.L., Joseph, N.L., Waggoner, S.Z., Gulick, C.W., Korosec, M.A., and Bunning, B.B., 1991, Geologic map of Washington-northeast quadrant: Washington Division of Geology and Earth Resources Geologic Map GM-39, scale 1:250,000, 3 sheets, 36 p. text.

Tabor, R.W., 1994, Late Mesozoic and possible early Tertiary accretion in western Washington state: the Helena-Haystack mélange and the Darrington-Devils Mountain fault zone:

Geological Society of America Bulletin, v. 106, p. 217-232, doi: 10.1130/0016-7606(1994)106<0217:LMAPET>2.3.CO;2.

Tabor, R.W., Waitt, R.B., Frizzell Jr., V.A., Swanson, D.A., Byerly, G.R., and Bentley, R.D., 1982, Geologic map of the Wenatchee 1:100,000 quadrangle, central Washington: U.S. Geological Survey, scale 1:100,000, 1 sheet, 26 p. text.

Tabor, R.W., Frizzell Jr., V.A., Vance, J.A., and Naeser, C.W., 1984, Ages and stratigraphy of lower and middle Tertiary sedimentary and volcanic rocks of the central Cascades: application to the tectonic history of the Straight Creek Fault: Geological Society of America Bulletin, v. 95, p. 26-44, doi: 10.1130/0016-7606(1984)95<26:AASOLA>2.0.CO;2.

Tabor, R.W., Frizzell Jr., V.A., Whetten, J.T., Waitt, R.B., Swanson, D.A., Byerly, G.R., Booth, D.B., Hetherington, M.J., and Zartman, R.E., 1987, Geologic map of the Chelan 30' × 60' quadrangle, Washington: U.S. Geological Survey, scale 1:100,000, 1 sheet, 33 p. text.

Tabor, R.W., Frizzell Jr., V.A., Booth, D.B., Waitt, R.B., Whetten, J.T., and Zartman, R.E., 1993, Geologic map of the Skykomish River 30' × 60' quadrangle, Washington: U.S. Geological Survey, scale 1:100,000, 1 sheet, 42 p. text.

Tabor, R.W., Frizzell Jr., V.A., Booth, D.B., and Waitt, R.B., 2000, Geologic map of the Snoqualmie Pass 30' × 60' minute quadrangle, Washington: U.S. Geological Survey, scale 1:100,000, 1 sheet, 57 p. text.

Tabor, R.W., Booth, D.B., Vance, J.A., and Ford, A.B., 2002, Geologic map of the Sauk River 30' × 60' quadrangle, Washington: U.S. Geological Survey, scale 1:100,000, 2 sheets, 67 p. text.

Tabor, R.W., Haugerud, R.A., Hildreth, W., and Brown, E.H., 2003, Geologic map of the Mount Baker 30' × 60' quadrangle, Washington: U.S. Geological Survey, scale 1:100,000, 2 sheets, 73 p. text.

Taylor, S.B., Johnson, S.Y., Fraser, G.T., and Roberts, J.W., 1988, Sedimentation and tectonics of the lower and middle Eocene Swauk Formation in eastern Swauk Basin, central Cascades, central Washington: Canadian Journal of Earth Sciences, v. 25, p. 1020-1036, doi: 10.1139/e88-100.

Tepper, J.H., Clark, K., Asmerom, Y., and Mcintosh, W., 2004, Eocene adakites in the Cascadia forearc: implications for the position of the Kula-Farallon ridge: Geological Society of America Abstracts with Programs, v. 36, n. 4, p. 69.

Thorkelson, D.J., and Breitsprecher, K., 2005, Partial melting of slab window margins: genesis of adakitic magmas: Lithos, v. 79, p. 25-41, doi: 10.1016/j.lithos.2004.04.049.

Trop, J.M., Ridgeway, K.D., and Spell, T.L., 2003, Sedimentary record of transpressional tectonics and ridge-subduction in the Tertiary Matanuska Valley-Talkeetna Mountains forearc basin, southern Alaska, in Sisson, V.B., Roeske, S.M., and Pavlis, T.L., eds., Geology of a transpressional orogen developed during ridge-trench interaction along the north Pacific margin: Geological Society of America Special Paper 371, p. 89-188, doi: 10.1130/0-8137-2371-X.89.

Umhoefer, P.J., and Miller, R.B., 1996, Mid-Cretaceous thrusting in the southern Coast Belt, British Columbia and Washington, after strike-slip fault reconstruction: Tectonics, v. 15, p. 545-565, doi: 10.1029/95TC03498.

Vance, J.A., 1957, The geology of the Sauk River area in the Northern Cascades of Washington [Ph.D. Thesis]: Seattle, University of Washington, 312 p.

Vine, J.D., 1969, Geology and coal resources of the Cumberland, Hobart, and Maple Valley quadrangles, King county, Washington: U.S. Geological Survey Professional Paper 624, 67 p.

Walker, C.W., 1980, Geology and energy resources of the Roslyn-Cle Elum area, Kittitas County, Washington: Washington Division of Geology and Earth Resources Open-File Report 80-1, scale 1:24,000, 1 sheet, 59 p. text.

Walsh, T.J., Korosec, M.A., Phillips, W.M., Logan, R.L., and Schasse, H.W., 1987, Geologic map of Washington-southwest quadrant: Washington Division of Geology and Earth Resources Geologic Map GM-34, scale 1:250,000, 2 sheets, 28 p. text.

Wells, R.E., Engebretson, C.D., Snavely Jr., P.D., and Coe, R.S., 1984, Cenozoic plate motions and the volcano-tectonic evolution of western Oregon and Washington: Tectonics, v. 3, p. 275-294, doi: 10.1029/TC003i002p00275.

Wells, R.E., Weaver, C.S., Blakely, R.J., 1998, Fore-arc migration in Cascadia and its neotectonic significance: Geology, v. 26, p. 759-762, doi: 10.1130/0091-7613(1998) 026<0759:FAMICA>2.3.CO;2.

Wells, R., Bukry, D., Friedman, R., Pyle, D., Duncan, R., Haeussler, P., and Wooden, J., 2014, Geologic history of Siletzia, a large igneous province in the Oregon and Washington Coast Range: correlation to the geomagnetic polarity time scale and implications for a long-lived Yellowstone hotspot: Geosphere, v. 10, p. 692-719, doi: 10.1130/GES01018.1.

Wendt, I., and Carl, C., 1991, The statistical distribution of the mean squared weighted deviation: Chemical Geology, v. 86, p. 275-285, doi: 10.1016/0168-9622(91)90010-T.

Wiebe, R.A., 1963, The geology of Mt. Pilchuck [M.S. Thesis]: Seattle, University of Washington, 52 p.

Wintzer, N.E., 2012, Deformational episodes recorded in the Skagit Gneiss Complex, North Cascades, Washington, USA: Journal of Structural Geology, v. 42, p. 127-139, doi: 10.1016/j.jsg.2012.06.004.

Wyld, S.J., Umhoefer, P.J., and Wright, J.E., 2006, Reconstructing northern Cordilleran terranes along known Cretaceous and Cenozoic strike-slip faults: implications for the Baja British Columbia hypothesis and other models, *in* Haggart, J.W., Enkin, R.J., and Monger, J.W.H., eds., Paleogeography of the North American cordillera: evidence for and agains large-scale displacements: Geological Association of Canada Special Paper 46, p. 277-298, doi:

Yeats, R.S., and Engels, J.C., 1971, Potassium-argon ages of plutons in the Skykomish-Stillaguamish areas, North Cascades, Washington: U.S. Geological Survey Professional Paper 750-D, p. D34-D38.

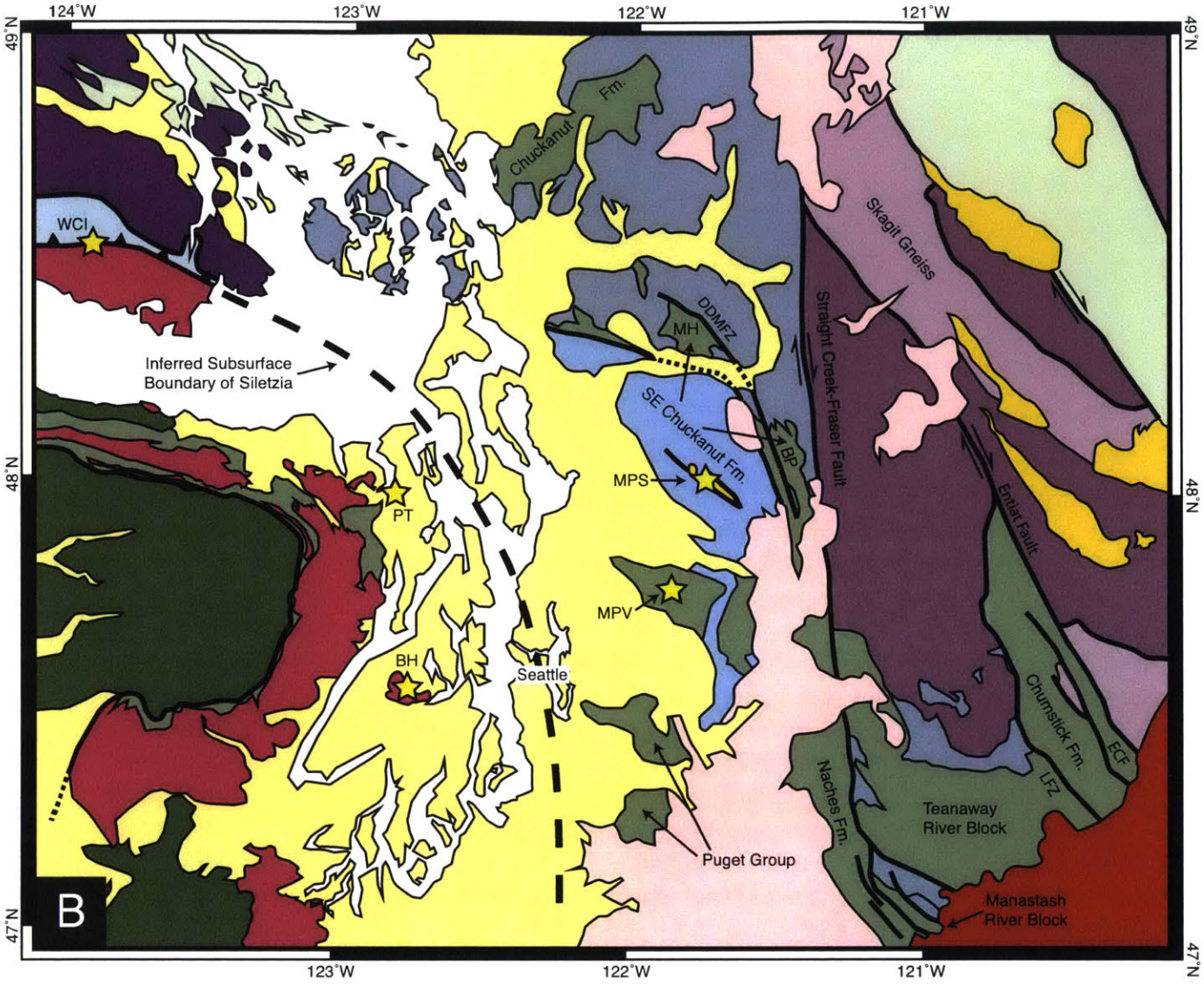

0 km 50 100

Oligocene to Present

- Quaternary alluvium
- Columbia River Basalts (ca. 16 Ma)
- Sedimentary rock and Quaternary sediment (33 Ma - Present)
- Cascade Arc magmatism (40 Ma - Present)

Paleocene and Eocene

- Major granitic intrusive complexes (50 - 46 Ma)
- Northern Siletzia (ca. 52 - 49 Ma)
- Sedimentary rock
- Ortho- and paragneiss with Eocene cooling ages

Mesozoic

- Leech River Schist
- Western and eastern melange belts
- Sedimentary units of the Methow Basin
- Northwest Cascades Thrust System
- Wrangellia
- Ortho- and paragneiss with dominantly Mesozoic cooling ages

- Paleogene Adakites and Peraluminous Granites
- Faults
- Contacts

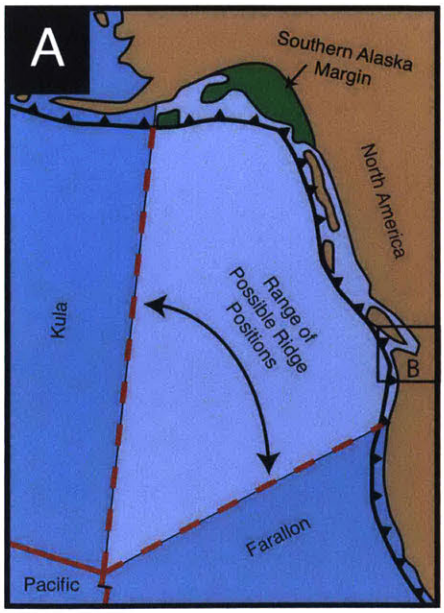

Figure 1 (*on previous page*)**: (A)** Map of the Pacific Northwest that shows possible locations for the Kula- Farallon spreading ridge during the early Paleogene, modified from Haeussler et al. (2003). If the terranes that compose southern Alaska are far-traveled from a more southerly location in the early Paleogene (e.g., Cowan, 2003), the range of possible positions would narrow along the WA and BC coasts. Alternatively, if the Chugach Terrane is not far-traveled, the Resurrection oceanic plate may have existed and would have resulted in two or more ridges intersecting North America (Haeussler et al., 2003; Madsen et al., 2006). **(B)** Generalized geologic map of central and northwest Washington, including southern Vancouver Island, modified from Walsh et al. (1987), Stoffel et al. (1991), Schuster et al. (1997), Dragovich et al. (2002), and Massey et al. (2005). Paleogene-aged sedimentary formations and regional strike-slip faults discussed in this paper are labeled and abbreviations are: MH: Mount Higgins area, BP: Barlow Pass area, ECF: Eagle Creek fault, LFZ: Leavenworth fault zone, and DDMFZ: Darrington-Devil's Mtn. fault zone. Stars denote the locations of Paleogene-aged adakites, abbreviated: BH: Bremerton Hills, MPV: Mt. Persis Volcanics, PT: Port Townsend and peraluminous granites, abbreviated: WCI: Walker Creek intrusions, MPS: Mt. Pilchuck suite (Tepper et al., 2004; Madsen et al., 2006; MacDonald et al., 2013). The heavy dashed line marks the inferred boundary between Siletzia and North America (Wells et al., 1998).

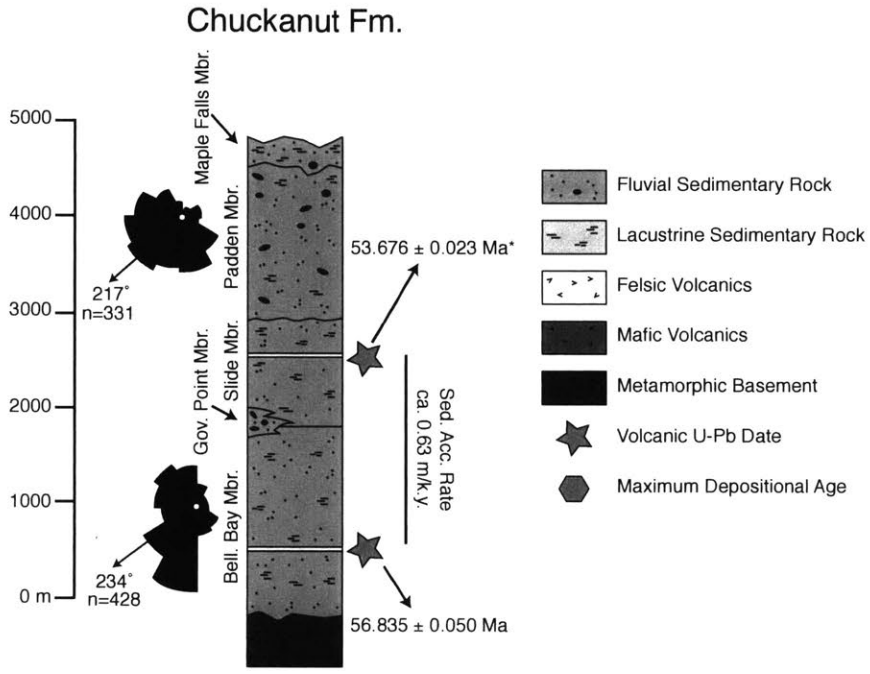

Figure 2: Generalized stratigraphic column of the Chuckanut Fm. Member thicknesses and paleocurrent data are from Breedlovestrout (2011) and Johnson (1985). All dates are U-Pb zircon CA-IDTIMS dates reported in this paper with the exception of the date denoted with an *, which was previously reported in Breedlovestrout et al. (2013). Sediment accumulation (Sed. Acc.) rates are assumed to be linear.

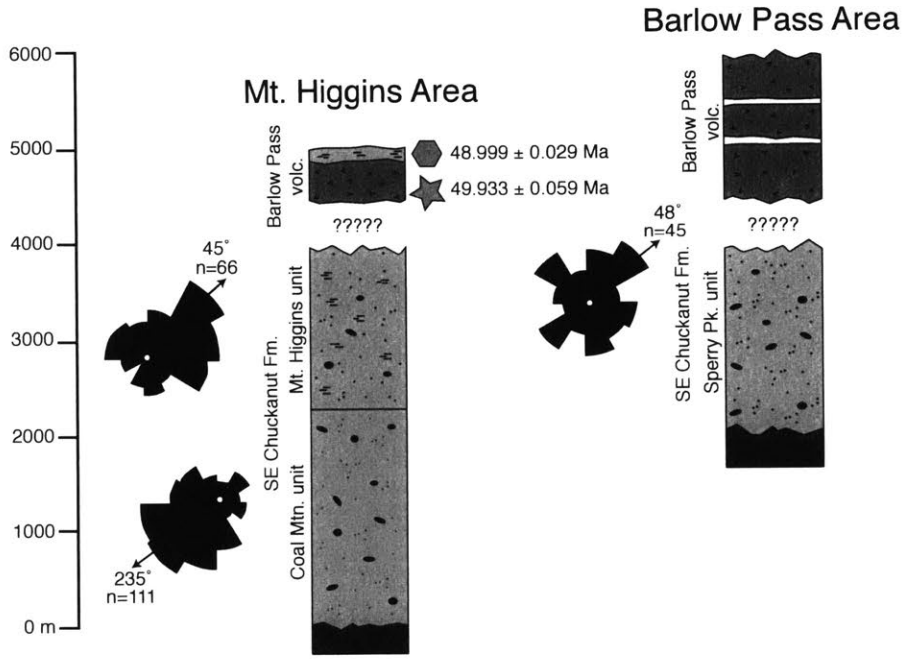

Figure 3: Generalized stratigraphic column of the SE Chuckanut Fm. Unit thicknesses and paleocurrent data are from Evans and Ristow (1994). All dates are U-Pb zircon CA-IDTIMS dates reported in this paper and the columns are hung so that correlative sedimentary units are adjacent to one another. Symbols are the same as Fig. 2.

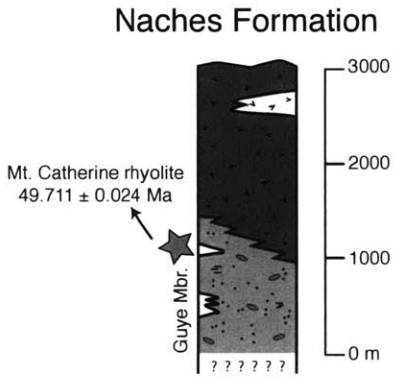

Figure 4: Generalized stratigraphic column of the Naches Fm. Thicknesses are based on Tabor et al. (1984, 2000). The date is an U-Pb zircon CA-IDTIMS date reported in this paper. Symbols are the same as Fig. 2.

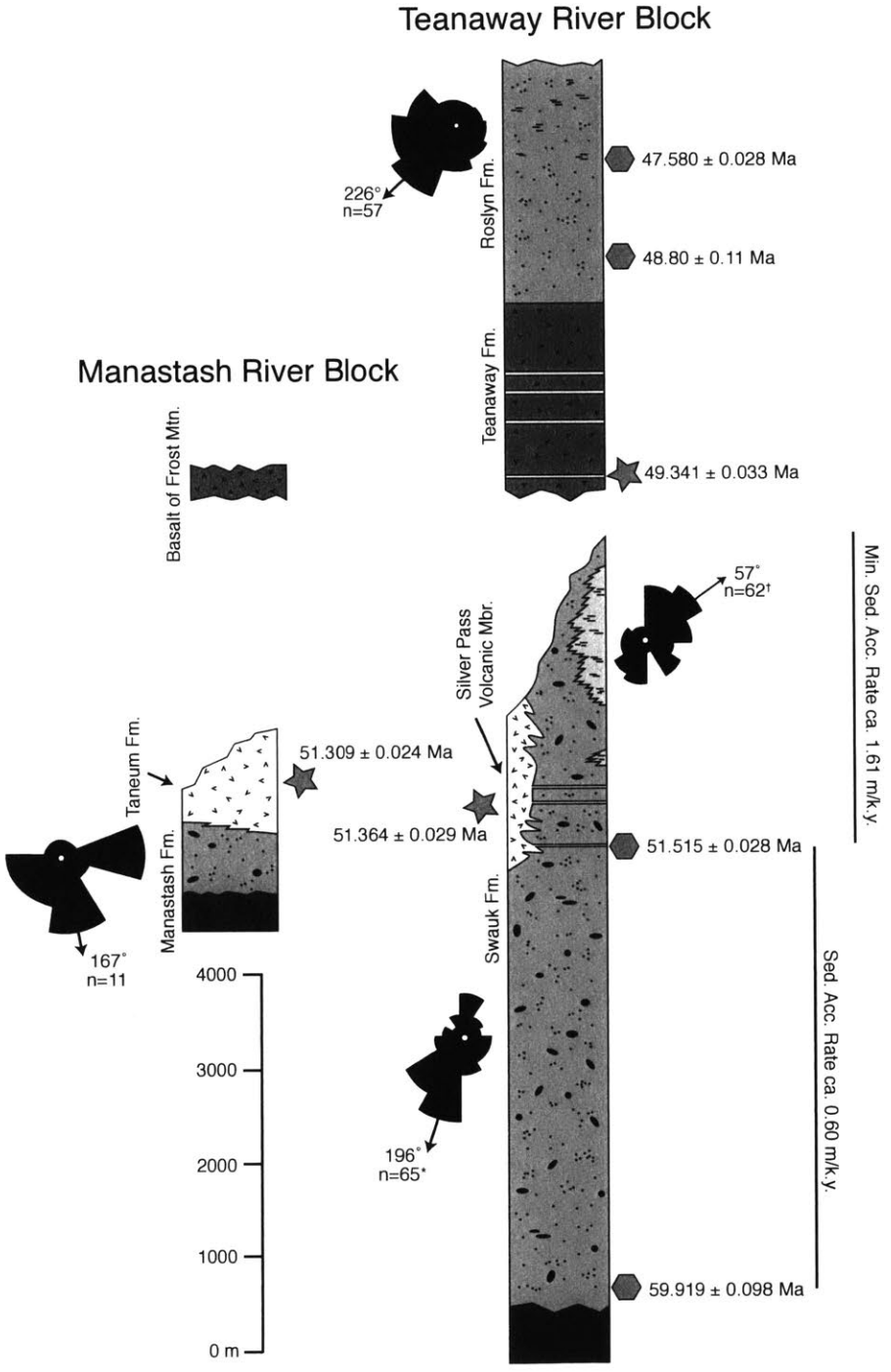
Teanaway River Block
226°
n=57
Roslyn Fm.
47.580 ± 0.028 Ma
48.80 ± 0.11 Ma
Teanaway Fm.
49.341 ± 0.033 Ma
Manastash River Block
Basalt of Frost Mtn.
57°
n=62†
Silver Pass
Volcanic Mbr.
Min. Sed. Acc. Rate ca. 1.61 m/k.y.
Taneum Fm.
51.309 ± 0.024 Ma
51.364 ± 0.029 Ma
51.515 ± 0.028 Ma
Manastash Fm.
Swauk Fm.
167°
n=11
4000
3000
2000
1000
0 m
196°
n=65*
Sed. Acc. Rate ca. 0.60 m/k.y.
59.919 ± 0.098 Ma

Figure 5: Generalized stratigraphic column of sedimentary and volcanic rocks preserved in the Manastash River and Teanaway River blocks. Thicknesses are from Clayton (1973), Tabor et al. (1982, 1984, 2000), and Taylor et al. (1988), and paleocurrent data is from Barnett (1985), Johnson (1985), and Taylor et al. (1988). The rose diagrams for the lower and upper Swauk Fm. represent measurements from the sandstone of Swauk Pass (*) and shale facies of Tronson Ridge (†) respectively. All dates represent U-Pb zircon CA-IDTIMS dates presented in this paper and the columns are hung so that correlative sedimentary and volcanic formations are adjacent to one another. Symbols are the same as Fig. 2 and sediment accumulation (Sed. Acc.) rates are assumed to be linear.

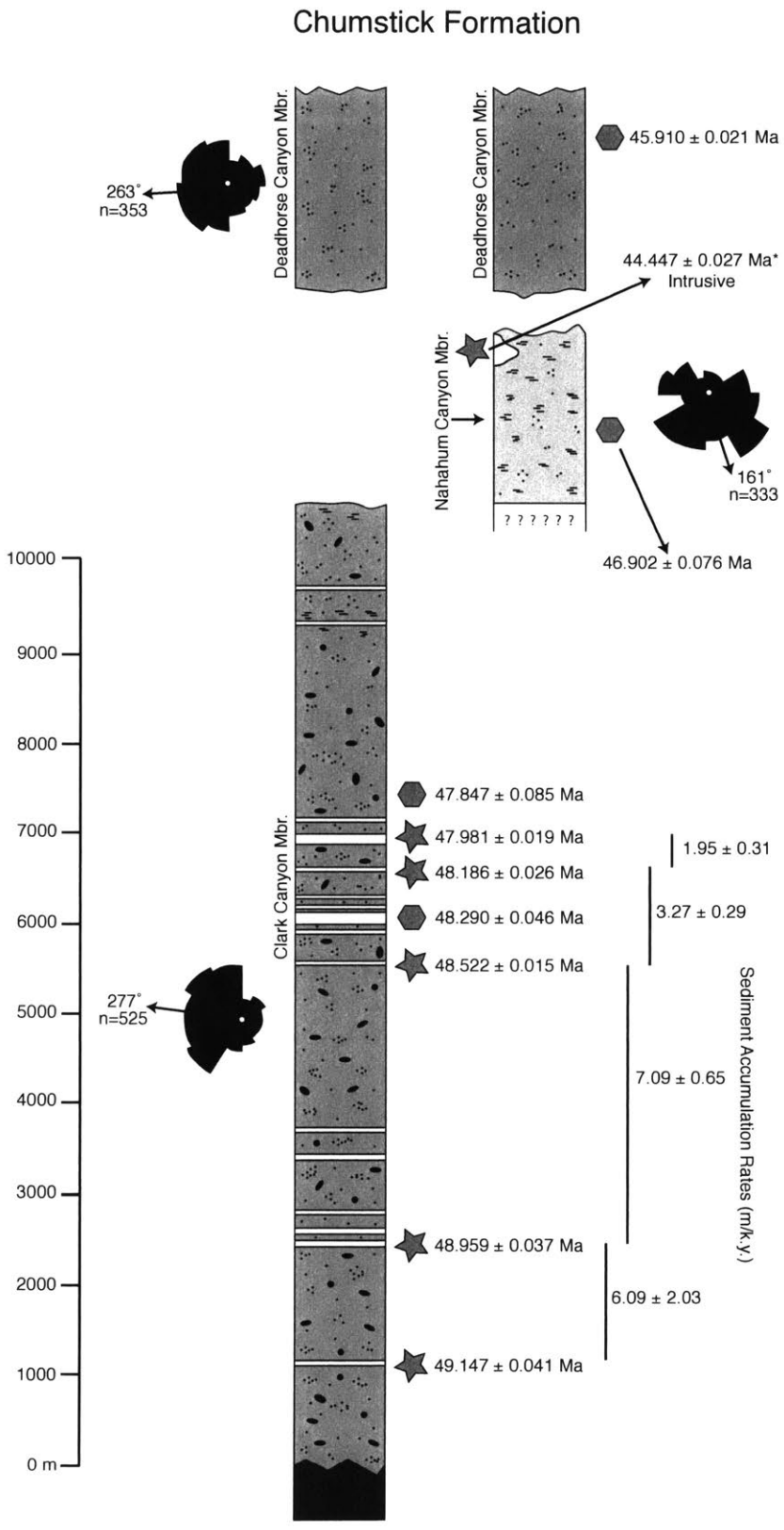
Chumstick Formation
Deadhorse Canyon Mbr.
263°
n=353
Deadhorse Canyon Mbr.
45.910 ± 0.021 Ma
44.447 ± 0.027 Ma*
Intrusive
Nahahum Canyon Mbr.
? ? ? ? ? ?
161°
n=333
46.902 ± 0.076 Ma
10000
9000
8000
7000
6000
5000
4000
3000
2000
1000
0 m
Clark Canyon Mbr.
47.847 ± 0.085 Ma
47.981 ± 0.019 Ma
48.186 ± 0.026 Ma
48.290 ± 0.046 Ma
48.522 ± 0.015 Ma
277°
n=525
48.959 ± 0.037 Ma
49.147 ± 0.041 Ma
1.95 ± 0.31
3.27 ± 0.29
7.09 ± 0.65
6.09 ± 2.03
Sediment Accumulation Rates (m/k.y.)

Figure 6: Generalized stratigraphic column from the Chumstick Fm. The Tumwater Mtn. Mbr. is not shown, but is interbedded with the Clark Canyon Mbr. along the Leavenworth fault zone. Thicknesses and paleocurrent data are from Evans (1994), and all dates represent U-Pb zircon CA-IDTIMS dates presented in this paper, with the exception of the date denoted with an *, which was previously reported by Gilmour (2012). Columns are hung so that correlative members are adjacent to one another. Symbols are the same as Fig. 2 and sediment accumulation rates are assumed to be linear.

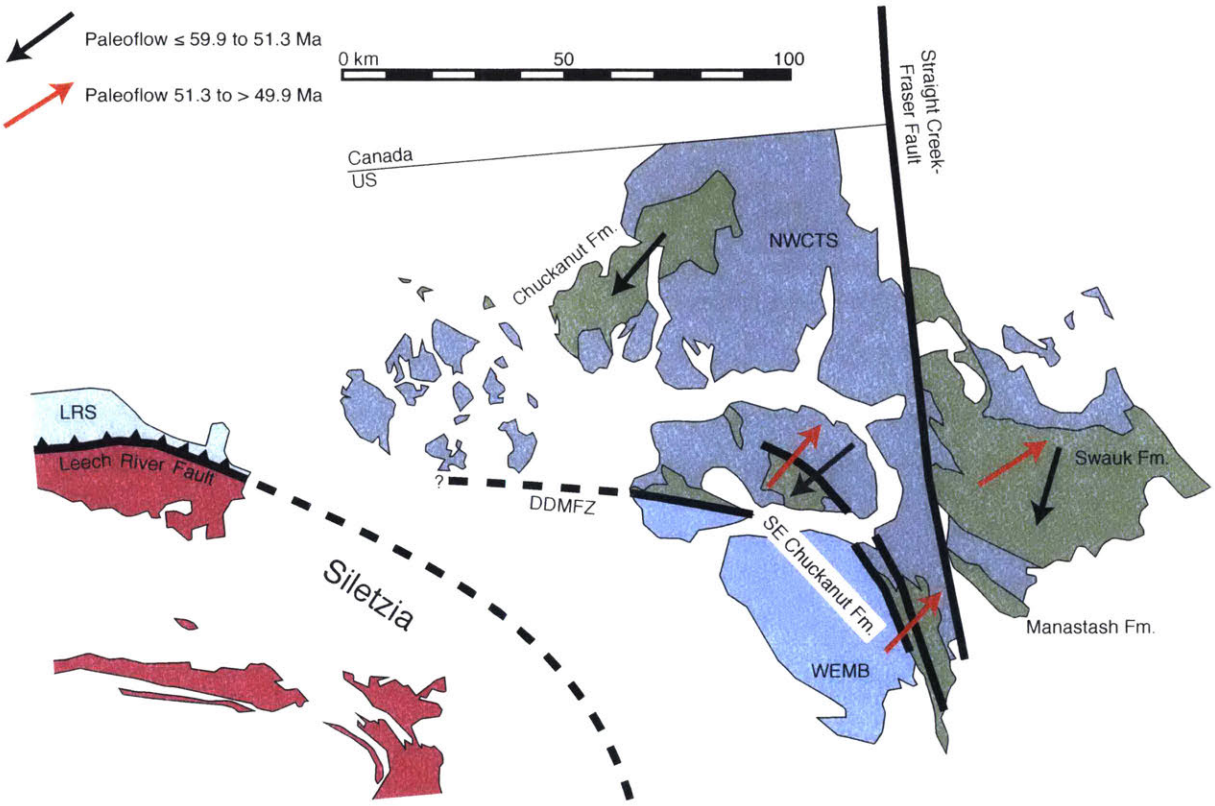

Figure 7: Map showing the relative position of the formations that compose the Swauk basin with restoration of 125 km of dextral offset on the Straight Creek-Fraser fault. The positions of the Northwest Cascades Thrust System (NWCTS), western and eastern mélange belts (WEMB), Leech River Schist (LRS), and Siletzia are also shown. The Darrington-Devil's Mtn. fault zone is abbreviated DDMFZ.

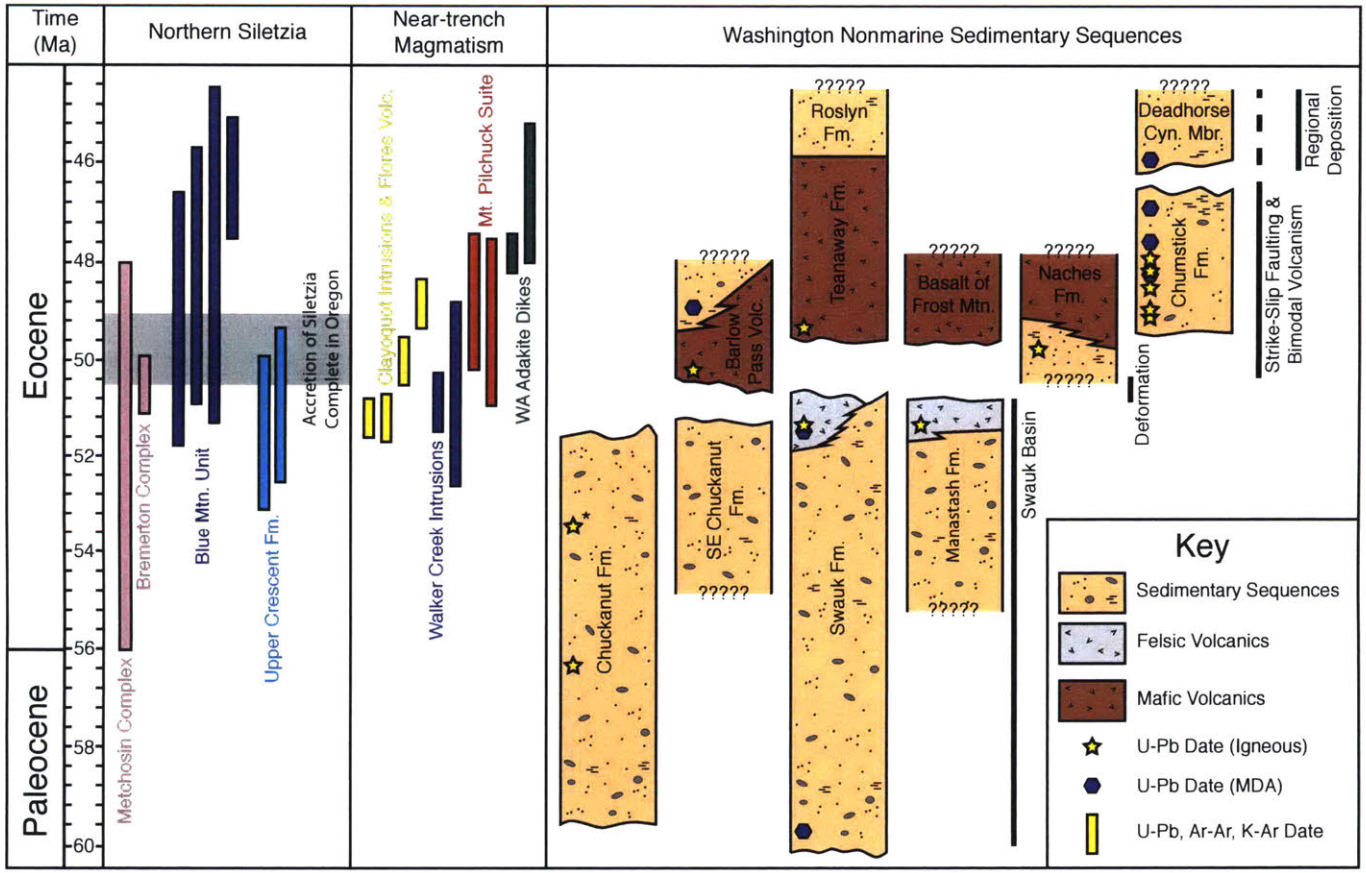

Figure 8: Temporal evolution of the sedimentary sequences discussed in this paper compared to available geochronology from northern Siletzia and near-trench magmatism in western Washington and southern Vancouver Island. All geochronology is shown with 2σ uncertainties, with the exception of the CA-IDTIMS data from the non-marine sedimentary basins, which have uncertainties smaller than the symbols. Geochronology is from 1) Metchosin Complex (Massey, 1986), 2) Bremerton Complex (Haeussler et al., 2000), 3) Blue Mtn. Unit at base of the ca. 16 km thick Crescent Fm. (Wells et al., 2014), 4) upper Crescent Fm. (Babcock et al., 2006), 5) Clayoquot Intrusions and Flores Volcanics (Irving and Brandon, 1990; Madsen et al., 2006), 6) Walker Creek Intrusions (Groome et al., 2003), 7) Mt. Pilchuck Stock (Yeats and Engels, 1971), and 8) adakite dikes from western Washington (Tepper et al., 2004). All other dates are reported in this paper, with the exception of the date denoted with a *, which was previously reported by Breedlovestrout et al. (2013). Maximum depositional age is abbreviated MDA.

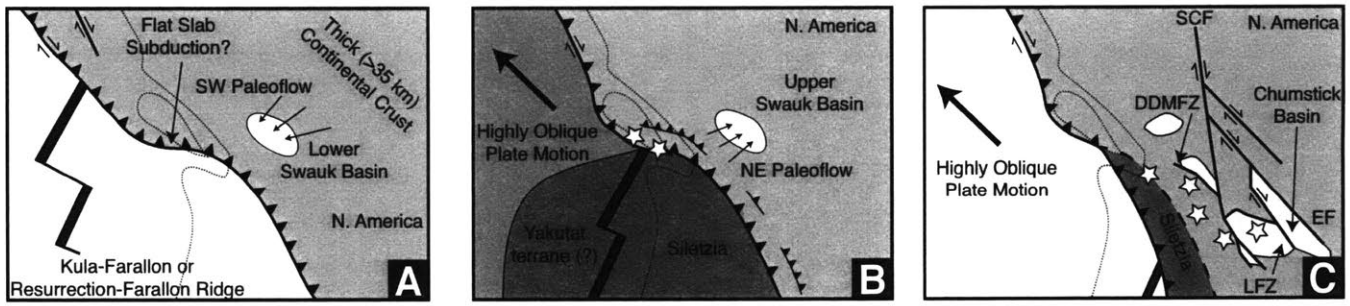

Figure 9: Cartoon maps showing our proposed tectonic evolution of Washington and surrounding area (dashed line denotes modern coastline) ca. 60 to 45 Ma as described in the text. Abbreviations are DDMFZ: Darrington-Devil's Mtn. fault zone, EF: Entiat fault, LFZ: Leavenworth fault zone, and SCF: Straight Creek-Fraser fault. Stars denote the location of Paleogene adakites, peraluminous granites, bimodal volcanism, and other near-trench magmatism. The basaltic Yakutat terrane is shown emplaced adjacent to Siletzia (e.g., Wells et al., 2014), prior to its northward transport and modern collision with southern Alaska.

Figure A1: CA-IDTIMS U-Pb zircon geochronology results presented as traditional concordia diagrams.

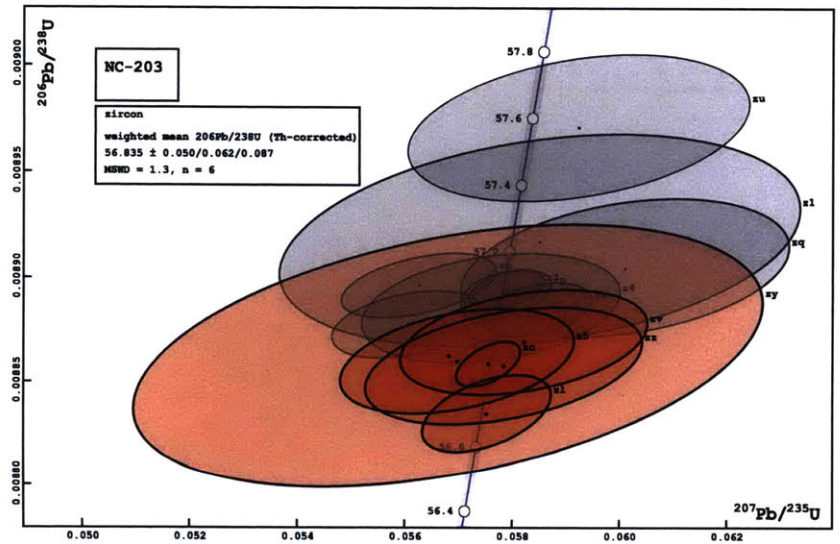

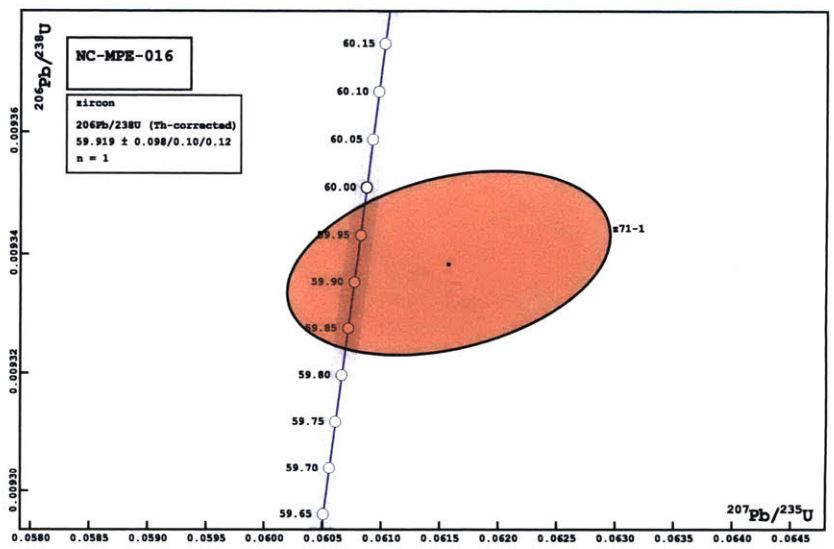

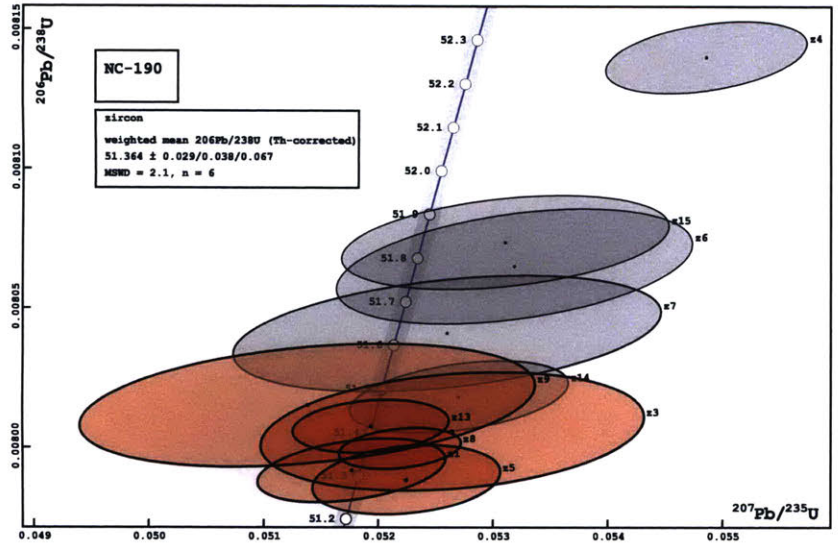

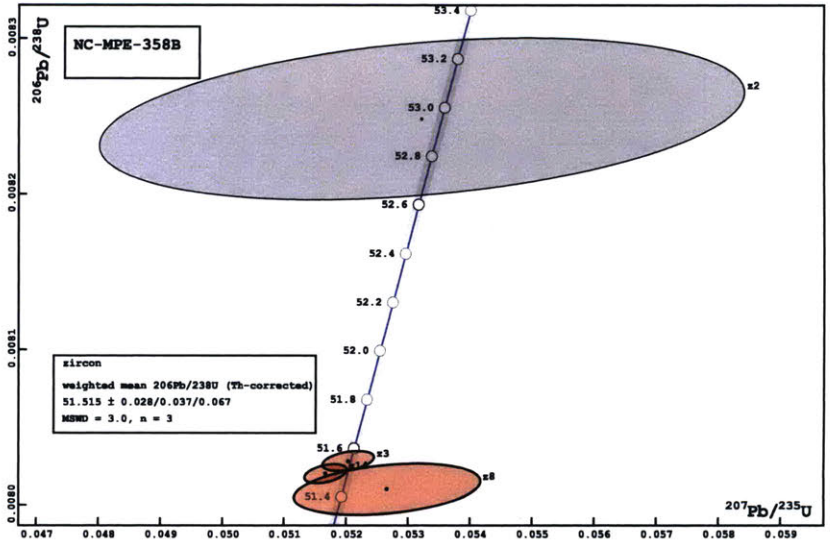

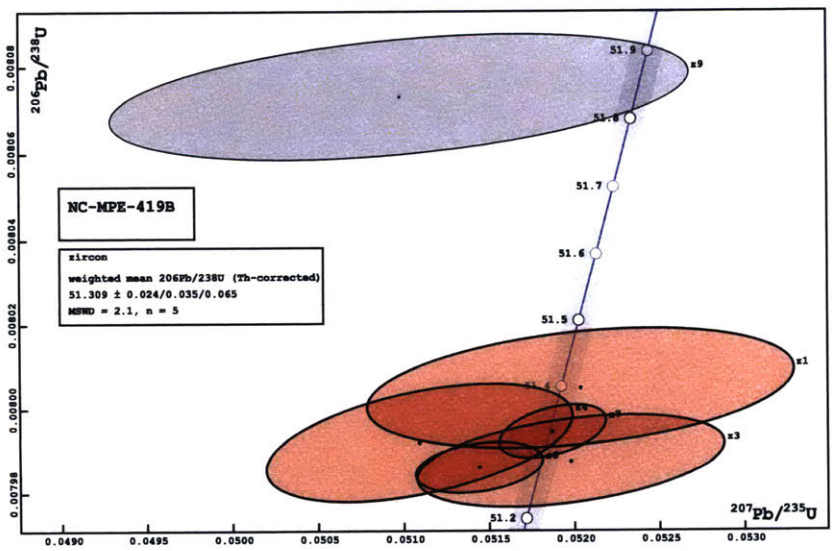
NC-MPE-419B
zircon
weighted mean 206Pb/238U (Th-corrected)
51.309 ± 0.024/0.035/0.065
MSWD = 2.1, n = 5
206Pb/238U
207Pb/235U

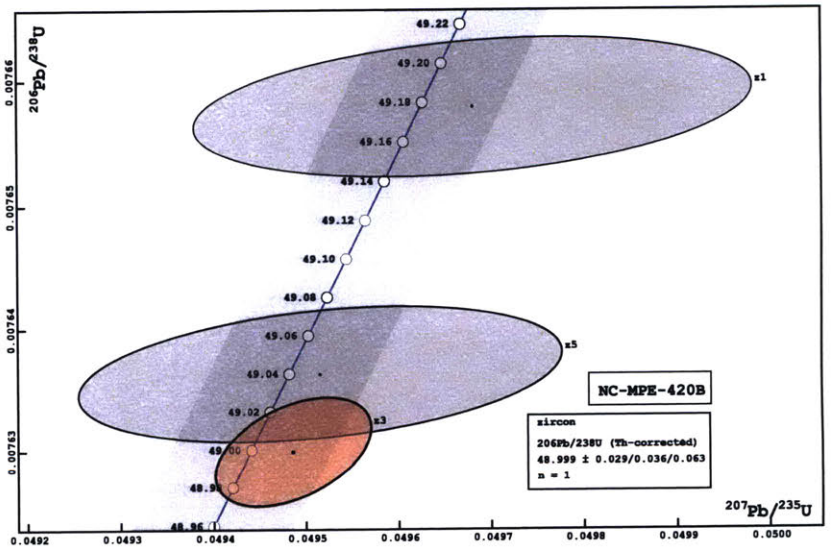
NC-MPE-420B
zircon
206Pb/238U (Th-corrected)
48.999 ± 0.029/0.036/0.063
n = 1
206Pb/238U
207Pb/235U

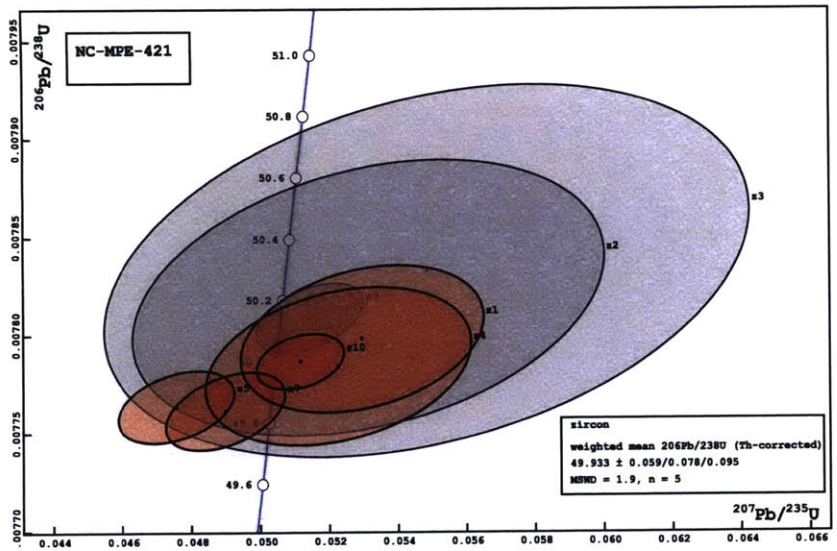
NC-MPE-421
zircon
weighted mean 206Pb/238U (Th-corrected)
49.933 ± 0.059/0.078/0.095
MSWD = 1.9, n = 5
206Pb/238U
207Pb/235U

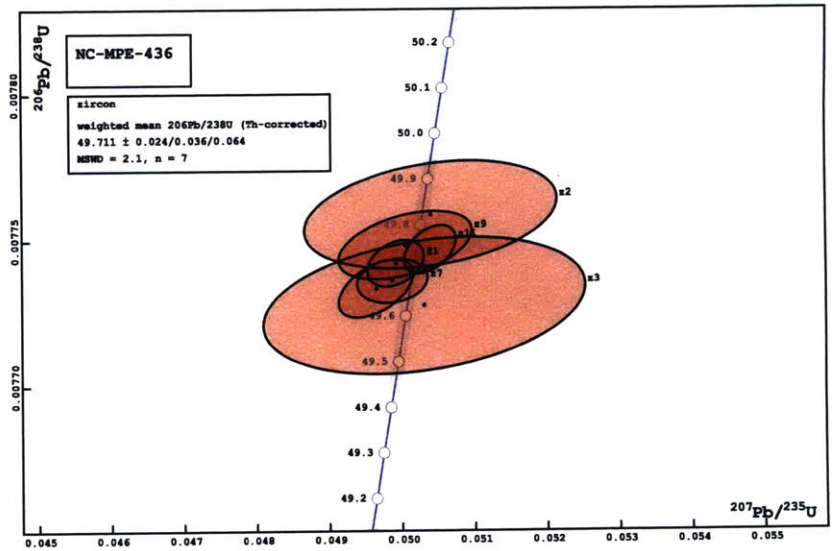
NC-MPE-436
zircon
weighted mean 206Pb/238U (Th-corrected)
49.711 ± 0.024/0.036/0.064
MSWD = 2.1, n = 7
206Pb/238U
207Pb/235U

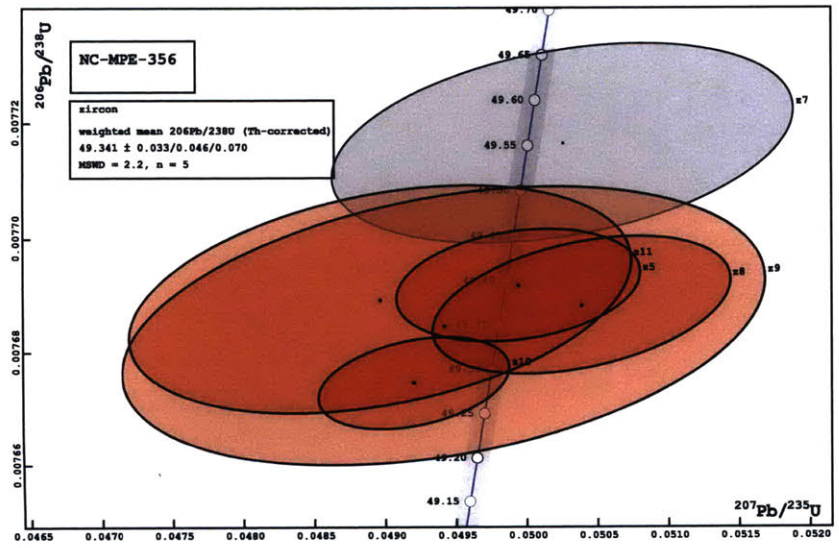
NC-MPE-356
zircon
weighted mean 206Pb/238U (Th-corrected)
49.341 ± 0.033/0.046/0.070
MSWD = 2.2, n = 5
206Pb/238U
207Pb/235U

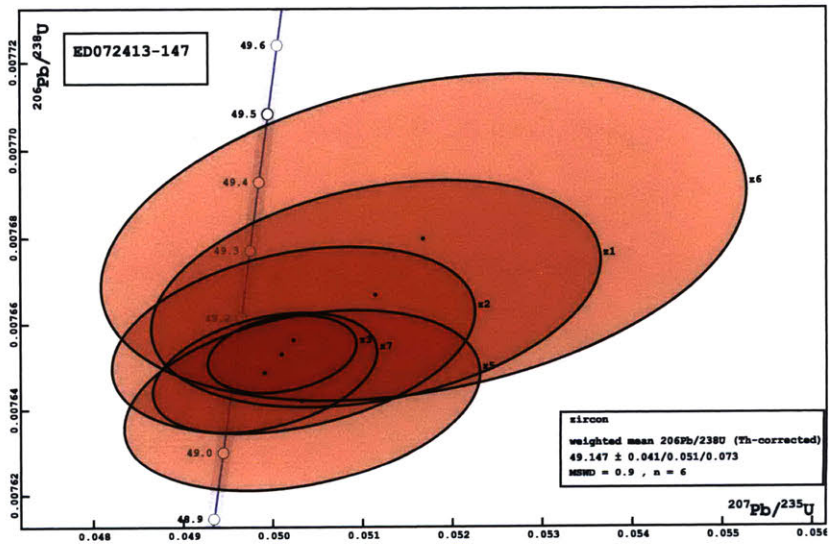
ED072413-147
zircon
weighted mean 206Pb/238U (Th-corrected)
49.147 ± 0.041/0.051/0.073
MSWD = 0.9 , n = 6
206Pb/238U
207Pb/235U

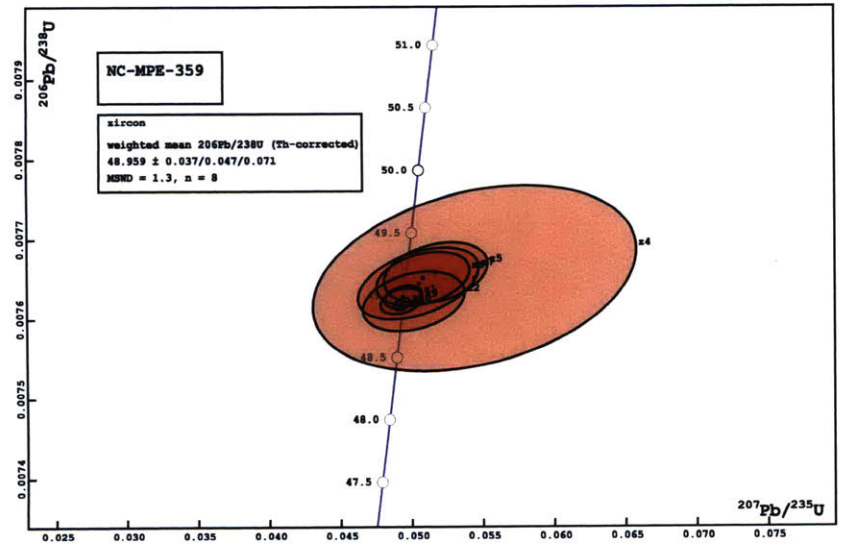
NC-MPE-359
zircon
weighted mean 206Pb/238U (Th-corrected)
48.959 ± 0.037/0.047/0.071
MSWD = 1.3, n = 8
206Pb/238U
207Pb/235U

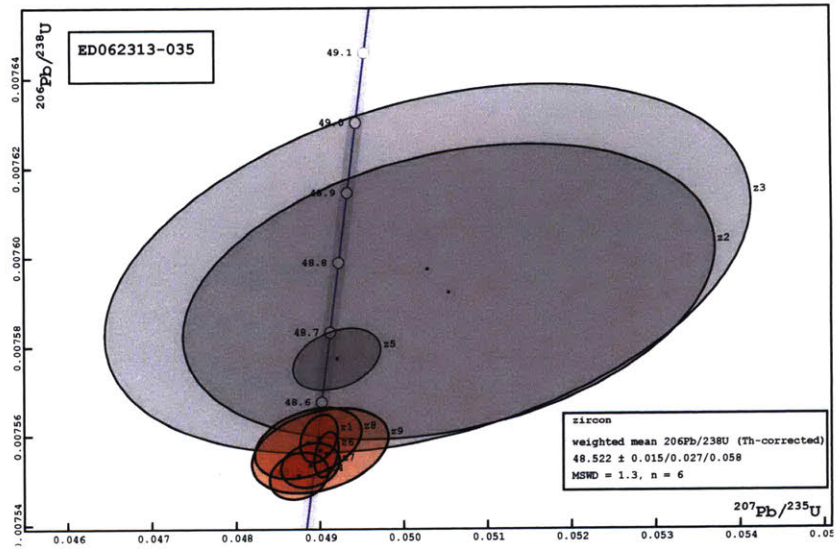
ED062313-035
zircon
weighted mean 206Pb/238U (Th-corrected)
48.522 ± 0.015/0.027/0.058
MSWD = 1.3, n = 6
206Pb/238U
207Pb/235U

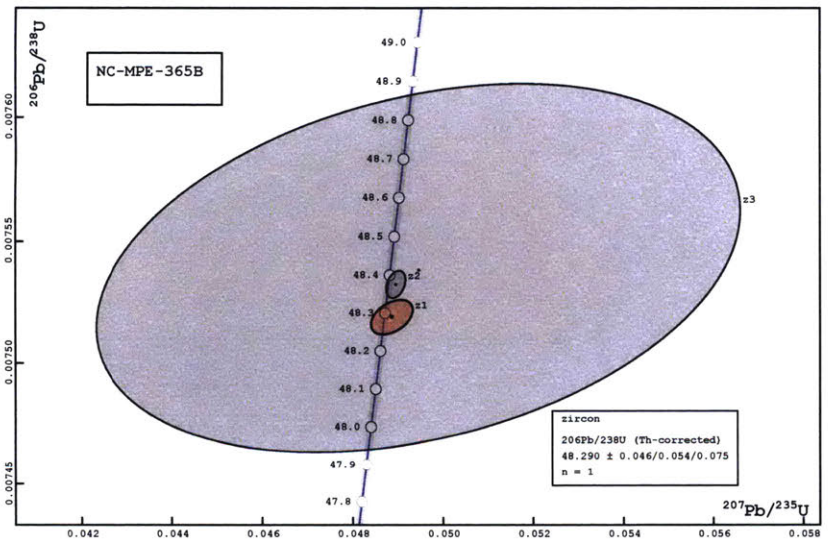
NC-MPE-365B
zircon
206Pb/238U (Th-corrected)
48.290 ± 0.046/0.054/0.075
n = 1
z1
z2
z3
206Pb/238U
207Pb/235U

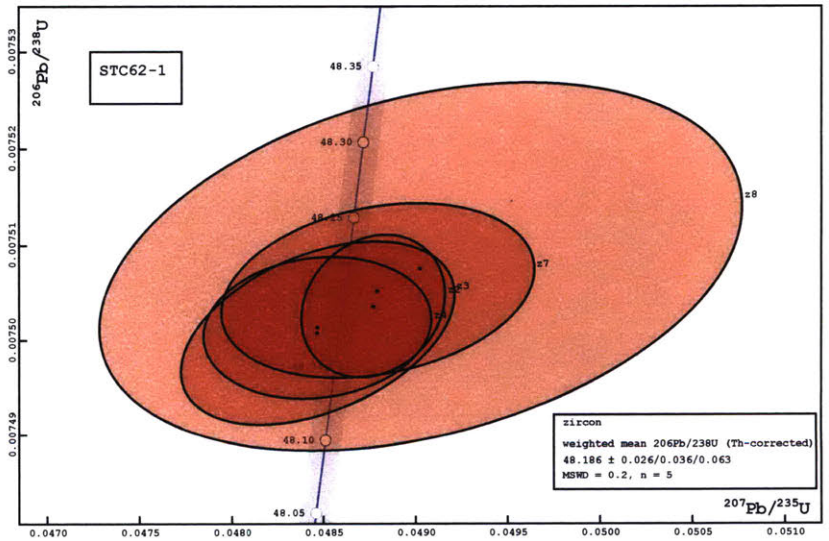
STC62-1
zircon
weighted mean 206Pb/238U (Th-corrected)
48.186 ± 0.026/0.036/0.063
MSWD = 0.2, n = 5
z3
z7
z8
206Pb/238U
207Pb/235U

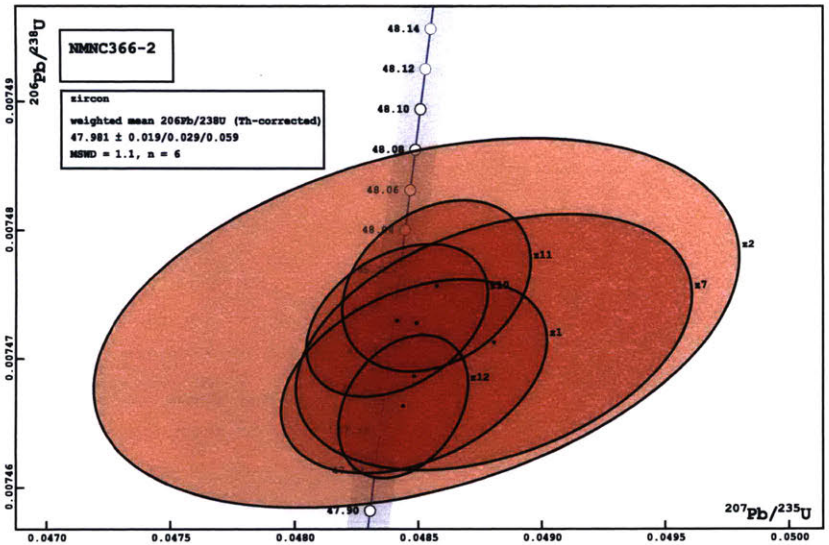
NMNC366-2
zircon
weighted mean 206Pb/238U (Th-corrected)
47.981 ± 0.019/0.029/0.059
MSWD = 1.1, n = 6
z1
z2
z7
z11
z12
206Pb/238U
207Pb/235U

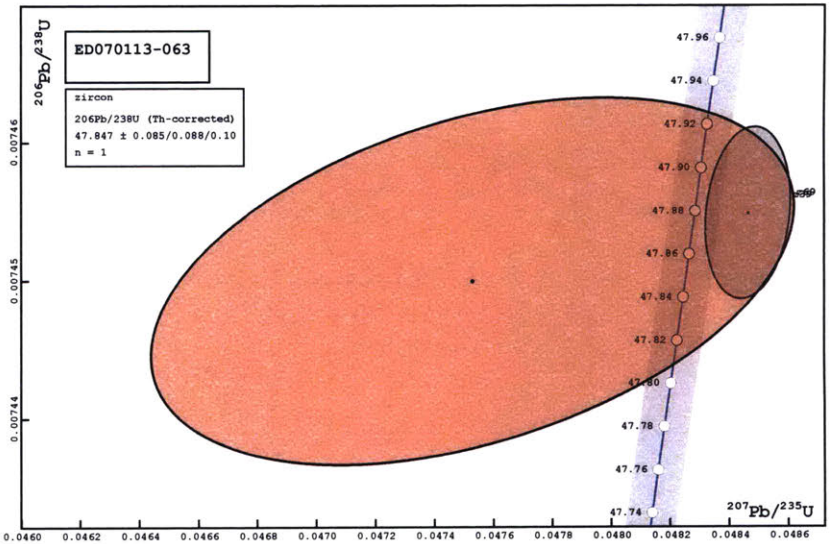
ED070113-063
zircon
206Pb/238U (Th-corrected)
47.847 ± 0.085/0.088/0.10
n = 1
206Pb/238U
207Pb/235U

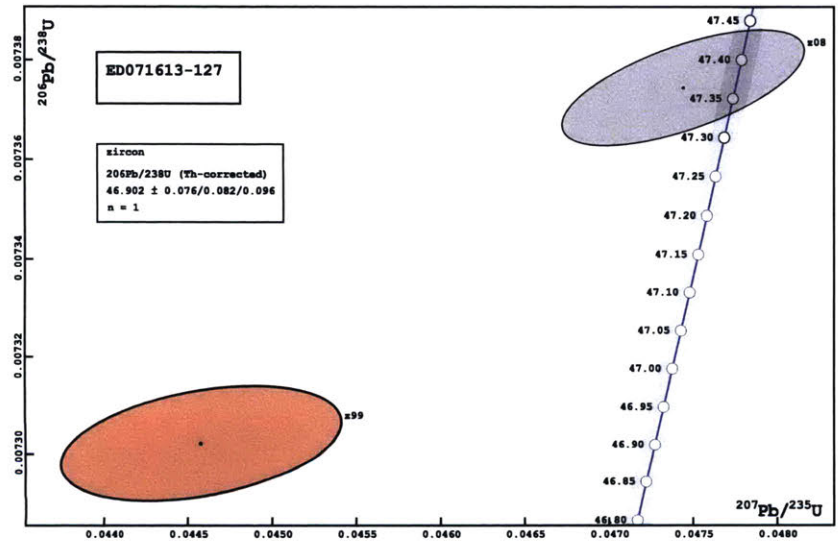
ED071613-127
zircon
206Pb/238U (Th-corrected)
46.902 ± 0.076/0.082/0.096
n = 1
z08
z99
47.45
47.40
47.35
47.30
47.25
47.20
47.15
47.10
47.05
47.00
46.95
46.90
46.85
46.80
0.00738
0.00736
0.00734
0.00732
0.00730
0.0440
0.0445
0.0450
0.0455
0.0460
0.0465
0.0470
0.0475
0.0480
206Pb/238U
207Pb/235U

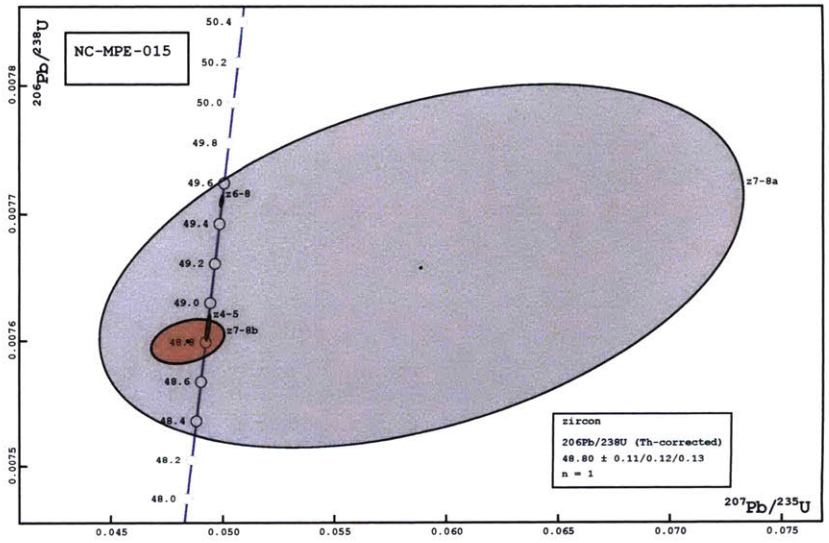
NC-MPE-015
zircon
206Pb/238U (Th-corrected)
48.80 ± 0.11/0.12/0.13
n = 1
z7-8a
z6-8
z4-5
z7-8b
50.4
50.2
50.0
49.8
49.6
49.4
49.2
49.0
48.8
48.6
48.4
48.2
48.0
0.0078
0.0077
0.0076
0.0075
0.045
0.050
0.055
0.060
0.065
0.070
0.075
206Pb/238U
207Pb/235U

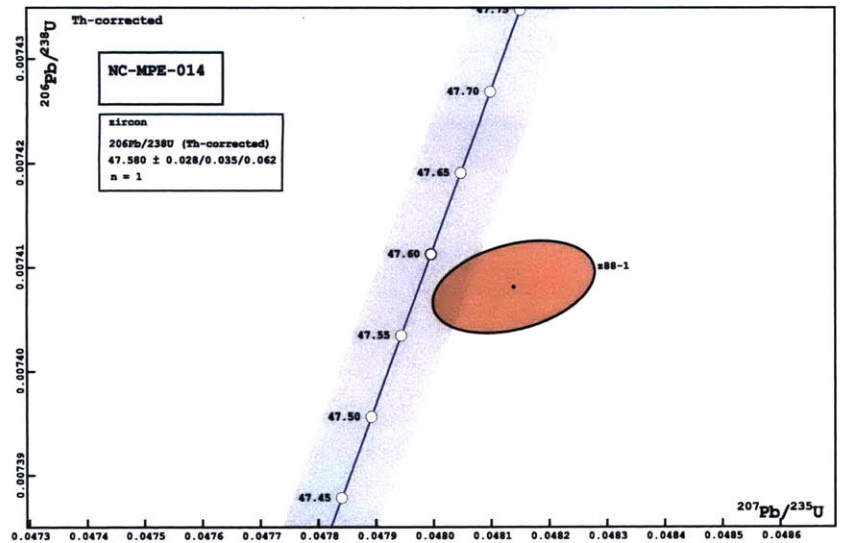
Th-corrected
NC-MPE-014
zircon
206Pb/238U (Th-corrected)
47.580 ± 0.028/0.035/0.062
n = 1
z88-1
47.70
47.65
47.60
47.55
47.50
47.45
0.00743
0.00742
0.00741
0.00740
0.00739
0.0473
0.0474
0.0475
0.0476
0.0477
0.0478
0.0479
0.0480
0.0481
0.0482
0.0483
0.0484
0.0485
0.0486
206Pb/238U
207Pb/235U

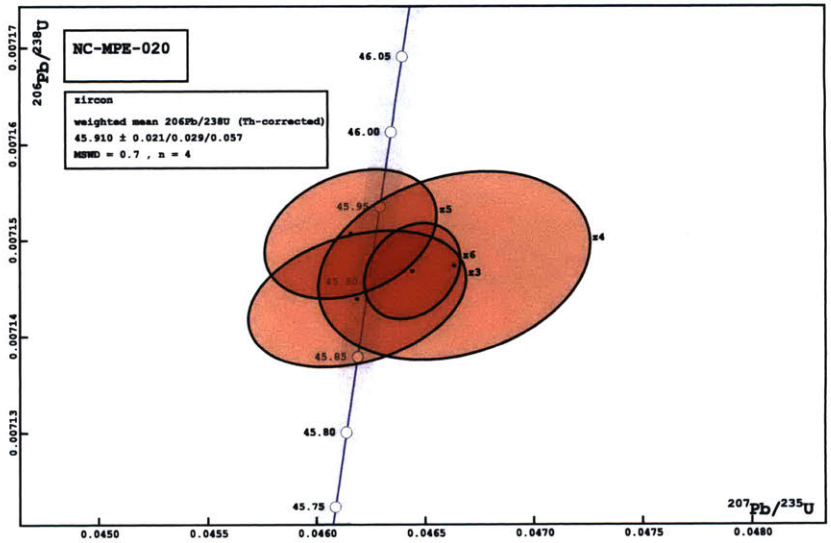
NC-MPE-020
zircon
weighted mean 206Pb/238U (Th-corrected)
45.910 ± 0.021/0.029/0.057
MSWD = 0.7 , n = 4
z5
z4
z6
z3
46.05
46.00
45.95
45.90
45.85
45.80
45.75
0.00717
0.00716
0.00715
0.00714
0.00713
0.0450
0.0455
0.0460
0.0465
0.0470
0.0475
0.0480
206Pb/238U
207Pb/235U

NC-MPE-417A
zircon
weighted mean 206Pb/238U (Th-corrected)
25.611 ± 0.014/0.019/0.033
MSWD = 1.6, n = 6
206Pb/238U
207Pb/235U
0.00401
0.00400
0.00399
0.00398
0.0245
0.0250
0.0255
0.0260
0.0265
0.0270
0.0275
0.0280
25.80
25.78
25.76
25.74
25.72
25.70
25.68
25.66
25.64
25.62
25.60
25.58
25.56
z1
z2
z3
z4
z5
z6

NC-MPE-418
zircon
weighted mean 206Pb/238U (Th-corrected)
24.216 ± 0.011/0.016/0.030
MSWD = 1.7, n = 3
206Pb/238U
207Pb/235U
0.003775
0.003770
0.003765
0.003760
0.003755
0.0236
0.0237
0.0238
0.0239
0.0240
0.0241
0.0242
0.0243
0.0244
0.0245
0.0246
24.30
24.28
24.26
24.24
24.22
24.20
24.18
24.16
24.14
z1
z2
z3

Table 1: CA-ID-TIMS U-Pb Zircon Dates

Sample	Lat. (°N)	Long. (°W)	Lithology	Fm., Mbr., or Unit	U-Pb Zircon ID-CATIMS Date	Interpretation
Lower Swauk basin						
NC-203	48.64150	122.48415	Silicic tuff	Chuckanut Fm.	56.835 ± 0.050/0.062/0.087 Ma (n=6, MSWD=1.3)	Eruption age
NC-MPE-016	47.44661	121.05611	Sandstone	Basal Swauk Fm.	59.919 ± 0.098/0.10 /0.12 Ma	MDA*
Upper Swauk basin						
NC-190	47.32132	121.18959	Rhyolite	Silver Pass Volcanic Mbr.	51.364 ± 0.029/0.038/0.067 Ma (n=6, MSWD=2.1)	Eruption age
NC-MPE-358B	47.33449	120.63271	Lapilli tuff	Silver Pass Volcanic Mbr.	51.515 ± 0.028/0.037/0.067 Ma (n=3, MSWD=3.0)	Eruption age
NC-MPE-419B	47.06567	120.91241	Rhyolitic tuff	Taneum Fm.	51.309 ± 0.024/0.035/0.065 Ma (n=5, MSWD=2.1)	Eruption age
Bimodal volcanics						
NC-MPE-420B	48.36277	121.78906	Bentonite	Barlow Pass volcanics	48.999 ± 0.029/0.036/0.063 Ma	MDA
NC-MPE-421	48.36696	121.78710	Silicic tuff	Barlow Pass volcanics	49.933 ± 0.059/0.078/0.095 Ma (n=5, MSWD=1.9)	Eruption age
NC-MPE-436	47.37613	121.39405	Rhyolite	Naches Fm.	49.711 ± 0.024/0.036/0.064 Ma (n=7, MSWD=2.1)	Eruption age
NC-MPE-356	47.30607	120.76079	Rhyolite	Teanaway Fm.	49.341 ± 0.033/0.046/0.070 Ma (n=5, MSWD=2.2)	Eruption age
Chumstick basin						
ED072413-147	47.47495	120.43283	Silicic tuff	Fairview Canyon tuff†	49.147 ± 0.041/0.051/0.073 Ma (n=6, MSWD=0.9)	Eruption age
NC-MPE-359	47.52874	120.48180	Silicic tuff	Yaxon Canyon #3 tuff†	48.959 ± 0.037/0.047/0.071 Ma (n=8, MSWD=1.3)	Eruption age
ED062313-035	47.63974	120.55926	Silicic tuff	Eagle Creek tuff†	48.522 ± 0.015/0.027/0.058 Ma (n=6, MSWD=1.3)	Eruption age
NC-MPE-365B	47.67877	120.60127	Silicic tuff	Clark Canyon #7 tuff†	48.290 ± 0.046/0.054/0.075 Ma	MDA
STC62-1	47.33763	120.42613	Silicic tuff	Clark Canyon #4 tuff†	48.186 ± 0.026/0.036/0.063 Ma (n=5, MSWD=0.2)	Eruption age
NMNC366-2	47.71413	120.63692	Silicic tuff	Clark Canyon #2 tuff†	47.981 ± 0.019/0.029/0.059 Ma (n=6, MSWD=1.1)	Eruption age
ED070113-063	47.62061	120.66200	Sandstone	Clark Canyon Mbr., Chumstick Fm.	47.847 ± 0.085/0.088/0.10 Ma	MDA
ED071613-127	47.65514	120.52099	Sandstone	Nahahum Canyon Mbr., Chumstick Fm.	46.902 ± 0.076/0.082/0.096 Ma	MDA
Roslyn basin						
NC-MPE-015	47.27604	121.07018	Sandstone	Lower Roslyn Fm.	48.80 ± 0.11 /0.12 /0.13 Ma	MDA
NC-MPE-014	47.22681	120.98922	Sandstone	Middle Roslyn Fm.	47.580 ± 0.028/0.035/0.062 Ma	MDA
NC-MPE-020	47.38746	120.28250	Congl. clast	Deadhorse Canyon Mbr., Chumstick Fm.	45.910 ± 0.021/0.029/0.057 Ma (n=4, MSWD=0.7)	MDA
Cascade Arc magmatism						
NC-MPE-417A	47.29772	120.82146	Felsic intrusion	Unknown§	25.611 ± 0.014/0.019/0.033 Ma (n=6, MSWD=1.6)	Emplacement age
NC-MPE-418	47.33387	120.86729	Rhyolitic tuff	Unknown§	24.216 ± 0.011/0.016/0.030 Ma (n=3, MSWD=1.7)	Eruption age

*MDA=Maximum Depositional Age

†Informal names for tuffs in Clark Canyon Mbr. of the Chumstick Fm. established by McClincy (1987)

§These rhyolites were previously considered part of the Teanaway Fm. (Clayton, 1973)

Table 2: Regional Correlations

Unit Name	Age	Included Sedimentary Sequences	Description
Renewed regional depositional system			
Roslyn basin	≤ 45.9 Ma	Deadhorse Canyon Mbr. of the Chumstick Fm., Roslyn Fm.	Sandstones, mudstones, and coal that overtop major structures and record sedimentation along meandering rivers that flowed east to west.
Sedimentation during strike-slip faulting			
Chumstick basin	49 to ca. 46 Ma	Clark Canyon Mbr., Nahahum Canyon Mbr., and Tumwater Canyon Mbr. of the Chumstick Fm.	Sandstones, conglomerates, and mudstones that record extremely high sediment accumulation rates (up to 7 m/kyr), and have evidence for syn-depositional faulting.
Bimodal volcanism			
No regional name	49.9 to ???	Upper Naches Fm., Barlow Pass volcanics, Basalt of Frost Mountain, Teanaway Fm.	Dominantly basaltic flows with interbedded rhyolites and fluvial sedimentary rock.
Swauk basin			
Upper Swauk basin	51.3 to > 49.9 Ma	Higgins Mtn. unit of the SE Chuckanut Fm., Sperry Pk. unit of the SE Chuckanut Fm., Swauk Fm. above Silver Pass Mbr., possibly the Guye Mbr. of the Naches Fm.	Sandstones, conglomerates, and mudstones that dominantly record E or NE directed paleoflow, and contain conglomerate clasts likely sourced from the western and eastern mélange belts.
Silver Pass volcanics	ca. 51.5 – 51 Ma	Taneum Fm., Silver Pass Volcanic Mbr.	Andesitic to rhyolitic volcanic rocks of unknown tectonic setting.
Lower Swauk basin	≤ 59.9 to 51.3 Ma	Swauk Fm. below Silver Pass Mbr., Manastash Fm., Coal Mtn. unit of the SE Chuckanut Fm., Chuckanut Fm.	Sandstones, conglomerates, and mudstones deposited along SW flowing rivers.

Table A1: CA-ID-TIMS U-Pb Zircon Geochronology Results

Frac.	Dates								Composition			Isotopic Ratios							
	$^{206}Pb/^{238}U^{*}$	2σ abs.	$^{207}Pb/^{235}U^{\dagger}$	2σ abs.	$^{207}Pb/^{206}Pb^{\dagger}$	2σ abs.	% Disc.[§]	Corr. Coef.	Th/ U[=]	Pb_c (pg)[**]	Pb*/ Pb_c[††]	$^{206}Pb/^{204}Pb$[§§]	$^{208}Pb/^{206}Pb$[#]	$^{206}Pb/^{238}U^{*,\#}$	2σ %	$^{207}Pb/^{235}U^{\#}$	2σ %	$^{207}Pb/^{206}Pb^{*,\#}$	2σ %
NC-203																			
z1	57.23	0.32	57.7	4.7	83	190	31.09	0.312	0.43	0.25	2	157	0.138	0.008917	0.57	0.0585	8.3	0.047615	8.1
z2	57.083	0.060	57.15	0.67	63	28	9.69	0.445	0.74	0.20	20	1100	0.238	0.008894	0.11	0.05789	1.2	0.047230	1.2
z3	56.98	0.10	55.4	1.4	-9	59	700.88	0.387	0.38	0.22	8	517	0.121	0.008878	0.18	0.0560	2.5	0.045810	2.5
z4	57.03	0.17	56.9	2.3	54	98	-5.96	0.293	0.47	0.33	5	301	0.150	0.008885	0.30	0.0576	4.2	0.047035	4.1
z5	56.86	0.16	56.3	2.1	34	89	-64.59	0.381	0.50	0.29	5	341	0.161	0.008860	0.28	0.0570	3.8	0.046659	3.7
zl	56.70	0.12	56.8	1.2	64	47	12.00	0.482	0.45	0.31	11	646	0.146	0.008835	0.21	0.0575	2.1	0.047244	2.0
zm	57.10	0.10	55.6	1.4	-6	60	1099.13	0.473	0.34	0.38	10	610	0.109	0.008896	0.18	0.0563	2.6	0.045880	2.5
zn	56.973	0.049	56.92	0.48	58	20	2.63	0.308	0.59	0.30	26	1514	0.188	0.008877	0.086	0.05766	0.87	0.047132	0.85
zo	56.855	0.069	56.82	0.57	59	23	4.22	0.545	0.35	0.44	22	1385	0.112	0.008859	0.12	0.05755	1.0	0.047140	0.98
zp	57.073	0.074	57.13	0.81	63	34	10.13	0.383	0.46	0.60	14	829	0.148	0.008893	0.13	0.05788	1.5	0.047226	1.4
zq	57.15	0.21	59.3	2.9	149	120	61.70	0.320	0.58	0.91	4	240	0.186	0.008905	0.37	0.0601	5.1	0.048972	5.0
zu	57.57	0.22	58.4	3.1	97	120	40.95	0.329	0.59	1.13	4	229	0.189	0.008971	0.38	0.0592	5.4	0.047911	5.3
zv	56.92	0.16	57.5	2.2	84	92	32.08	0.351	0.36	0.57	5	309	0.114	0.008869	0.29	0.0582	4.0	0.047627	3.9
zw	57.023	0.083	57.69	0.97	89	40	36.12	0.367	0.49	0.49	11	681	0.157	0.008885	0.15	0.0585	1.7	0.047741	1.7
zy	56.88	0.40	56.1	5.6	28	240	-106.45	0.405	0.30	0.32	2	138	0.098	0.008862	0.71	0.0568	10	0.046517	10
zz	56.85	0.18	57.1	2.5	71	100	20.29	0.392	0.46	0.41	5	288	0.147	0.008858	0.32	0.0578	4.5	0.047381	4.3
NC-MPE-016																			
z5-1	67.894	0.038	67.94	0.13	73.1	4.1	7.23	0.538	0.31	0.42	150	9341	0.098	0.010588	0.056	0.06920	0.20	0.047427	0.17
z71-1	59.919	0.098	60.7	1.3	94	52	36.46	0.316	0.40	1.03	8	518	0.127	0.009338	0.16	0.0616	2.2	0.047843	2.2
z81-1	69.14	0.16	67.3	2.2	7	78	-845.14	0.264	0.27	0.51	6	404	0.087	0.010784	0.24	0.0686	3.3	0.046141	3.3
NC-190																			
z1	51.313	0.073	51.24	0.79	52	37	2.42	0.370	0.34	0.57	12	750	0.108	0.007992	0.14	0.05176	1.6	0.046998	1.5
z3	51.40	0.14	52.1	1.6	88	74	41.82	0.248	0.44	0.68	6	389	0.141	0.008006	0.27	0.0526	3.2	0.047712	3.1
z4	52.262	0.082	54.22	0.84	146	36	64.28	0.380	0.35	0.40	12	760	0.113	0.00814	0.16	0.05485	1.6	0.048895	1.5
z5	51.291	0.08	51.71	0.79	75	37	31.94	0.239	0.48	0.97	13	784	0.155	0.007988	0.16	0.05224	1.6	0.047454	1.5
z6	51.78	0.13	52.6	1.5	95	67	45.67	0.396	0.33	0.96	7	438	0.105	0.008065	0.26	0.0532	2.9	0.047849	2.8
z7	51.63	0.13	52.1	1.8	76	82	32.27	0.371	0.27	0.65	5	352	0.087	0.008041	0.26	0.0526	3.5	0.047464	3.5
z8	51.364	0.047	51.65	0.51	70	24	26.26	0.281	0.31	0.68	18	1130	0.099	0.008	0.092	0.05219	1.0	0.047334	1.0
z9	51.46	0.14	50.9	1.9	28	91	-83.94	0.331	0.22	0.58	5	324	0.072	0.008015	0.28	0.0514	3.9	0.046514	3.8
z13	51.414	0.061	51.41	0.66	55	31	7.49	0.214	0.32	0.47	15	925	0.102	0.008008	0.12	0.05193	1.3	0.047056	1.3
z14	51.482	0.082	52.15	0.92	87	42	41.15	0.390	0.26	0.38	11	706	0.084	0.008018	0.16	0.05270	1.8	0.047688	1.8
z15	51.84	0.11	52.5	1.4	89	62	41.96	0.350	0.27	0.39	7	451	0.087	0.008074	0.21	0.0531	2.7	0.047726	2.6
NC-MPE-358B																			
z1	76.09	0.11	75.5	1.3	61	41	-24.04	0.379	0.37	0.55	11	700	0.118	0.011874	0.14	0.0772	1.8	0.047201	1.7
z2	52.95	0.33	52.6	5.0	42	230	-26.02	0.331	0.88	0.27	2	142	0.282	0.008248	0.63	0.0532	9.8	0.046813	9.6
z3	51.548	0.042	51.51	0.40	54	18	5.39	0.383	0.28	0.41	25	1593	0.089	0.008028	0.081	0.05204	0.80	0.047033	0.77
z4	89.951	0.093	89.82	0.93	89	25	-1.13	0.305	0.26	0.24	19	1198	0.083	0.014051	0.1	0.0925	1.1	0.047759	1.1
z5	90.97	0.18	89.8	1.8	62	50	-46.68	0.328	0.29	0.29	10	655	0.091	0.014211	0.2	0.0925	2.1	0.047222	2.1
z6	90.156	0.060	90.36	0.28	98.4	6.8	8.52	0.608	0.13	0.35	72	4719	0.042	0.014084	0.067	0.09307	0.32	0.047950	0.29
z7	92.52	0.14	92.2	1.6	87	42	-5.86	0.53	0.27	0.37	11	738	0.087	0.014456	0.15	0.0951	1.9	0.047729	1.8
z8	51.43	0.11	52.1	1.5	88	66	41.99	0.324	0.21	0.66	6	421	0.069	0.008010	0.21	0.0527	2.9	0.047710	2.8
z9	89.71	0.20	89.8	2.6	95	70	5.31	0.291	0.25	0.33	6	411	0.080	0.014014	0.22	0.0925	3	0.047875	3.0
z10	89.312	0.092	89.4	1.0	95	28	6.35	0.339	0.17	0.57	15	975	0.054	0.013951	0.1	0.0921	1.2	0.047886	1.2
z11	89.87	0.47	89.5	6.3	83	170	-7.64	0.33	0.30	0.23	3	184	0.096	0.014039	0.52	0.0922	7.3	0.047650	7.1
z13	93.03	0.37	103.9	4.6	363	100	74.38	0.362	0.15	0.21	4	247	0.047	0.014537	0.4	0.1077	4.7	0.053765	4.5
z14	51.496	0.039	51.16	0.33	40	15	-27.89	0.418	0.18	0.23	31	1998	0.056	0.008020	0.076	0.05168	0.66	0.046751	0.63

NC-MPE-419B																		
z1	51.397	0.091	51.5	1.2	61	56	15.93	0.324	0.43	0.49	8	492	0.138	0.008005	0.18	0.0520	2.4	0.047170	2.4
z3	51.287	0.070	51.45	0.87	63	40	19.36	0.395	0.39	0.31	12	732	0.125	0.007988	0.14	0.05198	1.7	0.047217	1.7
z4	51.315	0.089	50.60	0.87	21	40	-142.13	0.468	0.34	0.44	14	877	0.109	0.007992	0.17	0.05109	1.8	0.046387	1.7
z6	51.277	0.039	50.93	0.36	39	17	-30.31	0.3	0.32	0.25	29	1840	0.103	0.007986	0.076	0.05144	0.72	0.046738	0.70
z7	51.332	0.041	51.35	0.30	57	14	9.49	0.431	0.31	0.25	33	2054	0.101	0.007995	0.079	0.05187	0.60	0.047078	0.57
z9	51.833	0.092	50.5	1.6	-8	79	725.23	0.393	0.36	0.32	7	468	0.115	0.008073	0.18	0.0510	3.3	0.045825	3.3
NC-MPE-420B																		
z1	49.178	0.035	49.23	0.29	56	14	12.61	0.301	0.53	0.20	39	2278	0.168	0.007658	0.072	0.04968	0.61	0.047074	0.59
z3	48.999	0.029	49.044	0.081	55.9	3.7	12.57	0.451	0.31	0.22	164	10241	0.100	0.007630	0.059	0.049486	0.17	0.047060	0.15
z5	49.040	0.035	49.07	0.25	55	12	11.00	0.329	0.50	0.20	39	2328	0.160	0.007636	0.072	0.04952	0.53	0.047049	0.51
NC-MPE-421																		
z1	50.07	0.24	52.4	3.4	166	150	69.82	0.298	0.38	0.91	3	179	0.123	0.007798	0.48	0.0530	6.7	0.049304	6.5
z2	50.21	0.45	52.6	6.6	167	300	70.06	0.309	0.51	0.76	1	103	0.162	0.007819	0.90	0.0532	13	0.049346	13
z3	50.30	0.61	54.2	9.0	236	390	78.74	0.328	0.47	1.14	1	84	0.151	0.007833	1.2	0.0549	17	0.050827	17
z4	49.99	0.26	51.8	3.7	139	170	64.03	0.301	0.45	1.50	2	166	0.144	0.007784	0.52	0.0523	7.4	0.048743	7.3
z5	49.85	0.12	47.2	1.6	-81	85	161.08	0.388	0.34	0.22	6	395	0.110	0.007764	0.24	0.0476	3.5	0.044462	3.5
z7	49.84	0.13	48.6	1.7	-9	83	651.78	0.435	0.43	0.24	6	389	0.138	0.007761	0.26	0.0490	3.5	0.045810	3.4
z9	50.14	0.11	51.0	1.5	94	69	46.71	0.471	0.39	0.19	7	459	0.124	0.007809	0.23	0.0515	3.0	0.047824	2.9
z10	50.001	0.09	50.7	1.2	88	58	43.04	0.324	0.38	0.25	8	479	0.122	0.007787	0.18	0.0512	2.5	0.047696	2.4
NC-MPE-436																		
z1	49.716	0.051	49.47	0.38	42	18	-17.59	0.340	0.31	0.30	28	1784	0.099	0.007742	0.10	0.04993	0.78	0.046792	0.75
z2	49.82	0.12	49.9	1.7	60	81	17.09	0.301	0.41	0.83	5	348	0.132	0.007759	0.24	0.0504	3.5	0.047146	3.4
z3	49.62	0.15	49.8	2.1	65	100	23.82	0.293	0.52	0.89	4	274	0.166	0.007728	0.30	0.0503	4.4	0.047249	4.3
z7	49.677	0.048	49.43	0.47	42	23	-17.91	0.167	0.25	0.25	20	1306	0.081	0.007736	0.098	0.04988	0.97	0.046787	0.96
z9	49.756	0.075	49.60	0.89	46	42	-8.20	0.443	0.68	0.22	13	748	0.218	0.007748	0.15	0.05006	1.8	0.046878	1.8
z11	49.746	0.053	49.93	0.34	63	16	21.67	0.445	0.25	0.21	32	2054	0.080	0.007747	0.11	0.05040	0.70	0.047207	0.66
z12	49.661	0.064	49.21	0.50	32	23	-54.62	0.508	0.20	0.28	25	1603	0.065	0.007733	0.13	0.04966	1.0	0.046590	0.98
NC-MPE-356																		
z5	49.395	0.063	49.48	0.83	58	40	15.26	0.241	0.47	0.40	11	695	0.151	0.007692	0.13	0.04994	1.7	0.047112	1.7
z7	49.55	0.11	49.8	1.6	66	75	24.77	0.343	0.42	0.52	6	383	0.135	0.007716	0.22	0.0503	3.2	0.047260	3.2
z8	49.372	0.077	49.9	1.0	81	48	38.85	0.381	0.41	0.34	10	594	0.132	0.007688	0.16	0.0504	2.1	0.047555	2.0
z9	49.35	0.16	49.0	2.2	35	110	-40.03	0.344	0.51	0.32	4	275	0.162	0.007685	0.32	0.0494	4.6	0.046661	4.5
z10	49.285	0.052	48.77	0.65	28	32	-76.31	0.343	0.49	0.30	16	953	0.155	0.007675	0.11	0.04920	1.4	0.046519	1.3
z11	49.38	0.13	48.5	1.7	12	85	-311.81	0.347	0.44	0.36	6	356	0.139	0.007689	0.26	0.0490	3.6	0.046210	3.5
ED072413-147																		
z1	49.24	0.17	50.7	2.4	123	110	59.91	0.306	0.46	0.90	4	243	0.148	0.007667	0.34	0.0511	4.9	0.048409	4.8
z2	49.17	0.14	49.8	2.0	83	94	41.11	0.308	0.38	1.11	5	296	0.120	0.007656	0.28	0.0502	4.0	0.047608	4.0
z3	49.147	0.058	49.64	0.80	78	39	37.24	0.258	0.41	0.44	12	713	0.131	0.007653	0.12	0.05011	1.7	0.047506	1.6
z4	85.3	1.0	91	14	243	360	64.95	0.303	0.46	1.12	1	84	0.148	0.013326	1.2	0.094	16	0.051021	16
z5	49.08	0.13	49.9	1.9	92	92	46.94	0.306	0.31	0.63	5	310	0.099	0.007642	0.28	0.0503	3.9	0.047786	3.9
z6	49.32	0.24	51.2	3.5	143	160	65.54	0.295	0.47	0.62	3	176	0.151	0.007680	0.49	0.0517	6.9	0.048828	6.8
z7	49.119	0.089	49.5	1.2	70	58	30.14	0.347	0.55	0.51	8	491	0.175	0.007649	0.18	0.0499	2.5	0.047352	2.4
z8	51.42	0.77	60	11	429	420	88.04	0.327	0.45	0.95	1	69	0.143	0.008008	1.5	0.061	19	0.055347	19
NC-MPE-359																		
z1	48.987	0.091	48.9	1.3	50	62	3.08	0.351	0.49	0.44	8	466	0.156	0.007628	0.19	0.0494	2.6	0.046959	2.6
z2	48.95	0.24	49.7	3.5	88	170	44.70	0.301	0.41	0.63	3	175	0.133	0.007622	0.49	0.0501	7.1	0.047710	7
z3	66.34	0.87	75	12	359	380	81.53	0.281	0.39	5.65	1	75	0.123	0.010345	1.3	0.076	17	0.053652	17
z4	49.13	0.74	54	11	270	470	81.85	0.312	0.61	1.88	1	68	0.196	0.007651	1.5	0.054	21	0.051590	20
z5	49.18	0.24	51.2	3.5	149	160	67.16	0.307	0.33	1.55	3	173	0.104	0.007658	0.50	0.0517	7.1	0.048960	6.9
z6	49.13	0.22	50.3	3.2	110	150	55.41	0.332	0.49	0.24	3	206	0.156	0.007651	0.44	0.0508	6.4	0.048152	6.3
z7	49.10	0.29	50.0	4.1	97	190	49.30	0.439	0.40	0.36	2	168	0.129	0.007645	0.59	0.0504	8.4	0.047878	8.2

NC-MPE-359 (Cont'd)																		
z9	48.95	0.1	48.8	1.4	47	70	-4.96	0.322	0.53	0.51	7	407	0.169	0.007623	0.21	0.0493	3	0.046884	2.9
z10	48.931	0.048	48.85	0.54	50	26	1.37	0.385	0.38	0.39	18	1090	0.123	0.007619	0.099	0.04929	1.1	0.046937	1.1
ED062313-035																			
z1	48.548	0.034	48.57	0.22	54	11	10.56	0.295	0.36	0.61	45	2784	0.115	0.007559	0.071	0.04899	0.46	0.047027	0.44
z2	48.76	0.21	50.1	3.1	118	140	58.64	0.303	0.35	1.58	3	195	0.113	0.007592	0.44	0.0505	6.3	0.048302	6.1
z3	48.79	0.26	49.8	3.7	104	180	53.30	0.363	0.35	0.35	2	171	0.112	0.007597	0.54	0.0503	7.6	0.048029	7.5
z4	48.494	0.034	48.33	0.34	45	17	-7.88	0.203	0.45	0.66	31	1855	0.145	0.007551	0.070	0.04875	0.72	0.046847	0.70
z5	48.662	0.044	48.77	0.50	59	25	17.62	0.333	0.38	0.52	18	1130	0.122	0.007577	0.092	0.04921	1.1	0.047122	1.0
z6	48.525	0.032	48.65	0.14	59.5	6.6	18.58	0.349	0.37	0.43	74	4529	0.117	0.007556	0.067	0.04908	0.29	0.047132	0.28
z7	48.510	0.032	48.46	0.34	51	17	4.93	0.208	0.36	0.36	30	1839	0.116	0.007553	0.066	0.04889	0.71	0.046963	0.70
z8	48.541	0.051	48.44	0.62	48	30	-0.71	0.360	0.38	0.47	15	953	0.123	0.007558	0.10	0.04886	1.3	0.046908	1.3
z9	48.531	0.061	48.58	0.79	56	39	12.88	0.330	0.36	0.40	11	723	0.115	0.007557	0.13	0.04901	1.7	0.047055	1.6
NC-MPE-365B																			
z1	48.290	0.046	48.45	0.45	61	22	20.36	0.432	0.56	0.19	24	1392	0.180	0.007519	0.095	0.04887	0.94	0.047159	0.91
z2	48.376	0.036	48.53	0.21	60.7	9.9	20.49	0.351	0.49	0.19	55	3277	0.155	0.007533	0.075	0.04896	0.43	0.047161	0.41
z3	48.41	0.48	49.0	6.9	83	340	42.03	0.321	0.46	0.67	1	97	0.147	0.007538	1.0	0.0495	14	0.047611	14
z4	163.00	0.87	160	11	115	170	-41.18	0.299	0.53	0.52	3	173	0.170	0.025608	0.54	0.171	7.4	0.048325	7.3
z5	68.72	0.39	69.6	5.2	104	180	33.96	0.375	0.51	0.37	3	168	0.163	0.010717	0.57	0.0710	7.8	0.048054	7.6
z6	67.28	0.19	69.0	2.6	132	88	49.15	0.321	0.67	0.44	5	314	0.214	0.010492	0.28	0.0703	3.8	0.048636	3.7
z7	67.82	0.58	70.0	8	148	270	54.12	0.361	0.57	0.30	2	118	0.181	0.010576	0.86	0.0714	12	0.048955	12
STC62-1																			
z2	48.191	0.048	48.35	0.38	61	19	20.56	0.180	0.59	0.41	28	1656	0.190	0.007504	0.10	0.04877	0.80	0.047161	0.79
z3	48.172	0.062	48.06	0.72	47	35	-2.19	0.425	0.38	0.34	13	830	0.120	0.007501	0.13	0.04847	1.5	0.046886	1.5
z4	48.176	0.048	48.06	0.60	47	30	-3.25	0.128	0.49	0.38	16	969	0.155	0.007501	0.10	0.04847	1.3	0.046881	1.3
z6	68.397	0.057	68.28	0.37	68	13	-1.19	0.433	0.40	0.59	39	2361	0.126	0.010667	0.083	0.06956	0.56	0.047318	0.53
z7	48.201	0.059	48.37	0.82	61	41	21.76	0.254	0.43	0.58	11	703	0.138	0.007505	0.12	0.04879	1.7	0.047173	1.7
z8	48.22	0.12	48.6	1.7	72	83	32.91	0.335	0.56	0.67	6	339	0.179	0.007508	0.26	0.0490	3.6	0.047382	3.5
NMNC366-2																			
z1	47.967	0.048	48.07	0.52	58	26	17.33	0.375	0.47	0.88	18	1108	0.150	0.007469	0.1	0.04848	1.1	0.047104	1.1
z2	47.994	0.092	48.1	1.3	57	63	16.06	0.362	0.49	0.98	7	460	0.156	0.007473	0.19	0.0485	2.7	0.047088	2.6
z7	47.984	0.064	48.39	0.77	73	38	34.24	0.375	0.49	0.55	12	756	0.156	0.007471	0.13	0.04881	1.6	0.047400	1.6
z10	47.995	0.038	48.01	0.36	53	17	9.77	0.376	0.52	0.56	27	1619	0.166	0.007473	0.08	0.04842	0.76	0.047010	0.73
z11	48.012	0.043	48.16	0.37	60	18	20.45	0.289	0.43	0.35	25	1514	0.137	0.007476	0.089	0.04858	0.78	0.047148	0.76
z12	47.952	0.036	48.03	0.25	56	12	14.95	0.323	0.60	0.52	40	2288	0.193	0.007466	0.075	0.04844	0.54	0.047076	0.52
ED070113-063																			
z39	47.879	0.040	48.05	0.14	61.4	7	22.13	0.170	0.43	0.38	98	5892	0.136	0.007455	0.083	0.04846	0.30	0.04717	0.29
z69	47.847	0.085	47.1	1.1	16	54	-192.31	0.411	0.46	0.55	10	637	0.146	0.007450	0.18	0.04750	2.3	0.046292	2.2
ED071613-127																			
z08	47.364	0.074	47.06	0.70	36	34	-30.04	0.647	0.48	0.30	15	929	0.152	0.007374	0.16	0.04744	1.5	0.046679	1.4
z99	46.902	0.076	44.29	0.81	-90	44	151.91	0.377	0.31	0.32	10	655	0.099	0.007302	0.16	0.04458	1.9	0.044297	1.8
NC-MPE-015																			
z4-5	48.875	0.065	48.90	0.11	55.0	3.9	11.34	0.687	0.28	0.50	161	10136	0.088	0.007611	0.13	0.04934	0.22	0.047041	0.16
z6-8	49.513	0.029	49.496	0.080	52.4	3.4	5.69	0.578	0.82	0.25	325	17675	0.263	0.007710	0.059	0.049954	0.17	0.047011	0.14
z7-8a	49.18	0.91	58	14	447	530	89.01	0.398	0.45	0.45	1	62	0.145	0.007658	1.9	0.059	24	0.055782	24
z7-8b	48.80	0.11	48.0	1.6	14	79	-241.13	0.317	0.31	0.35	6	370	0.100	0.007600	0.23	0.0484	3.4	0.046249	3.3
NC-MPE-014																			
z3-1	49.010	0.029	49.019	0.089	54.1	3.8	9.64	0.578	0.33	0.36	142	8783	0.107	0.007632	0.059	0.049460	0.19	0.047026	0.16
z13-1	50.132	0.040	50.20	0.31	57	15	11.63	0.248	0.93	0.34	45	2393	0.298	0.007807	0.080	0.05068	0.62	0.047099	0.61
z88-1	47.580	0.028	47.74	0.14	59.8	6.6	20.60	0.359	0.70	0.29	99	5576	0.223	0.007408	0.060	0.04814	0.29	0.047149	0.27

NC-MPE-014 (Cont'd)																		
z93-1	49.258	0.047	49.59	0.60	69	29	29.20	0.278	0.66	0.72	17	996	0.213	0.007670	0.095	0.05005	1.2	0.047342	1.2
NC-MPE-020																		
z3	45.889	0.045	45.85	0.49	48	25	5.31	0.307	0.53	0.86	18	1089	0.170	0.007144	0.099	0.04619	1.1	0.046914	1.1
z4	45.911	0.063	46.28	0.61	70	31	34.95	0.238	0.37	0.98	14	879	0.117	0.007147	0.14	0.04664	1.3	0.047344	1.3
z5	45.932	0.043	45.82	0.38	45	20	-2.95	0.293	0.55	1.03	23	1376	0.175	0.007151	0.094	0.04616	0.86	0.046839	0.83
z6	45.907	0.032	46.09	0.21	60	11	24.07	0.248	0.58	0.39	44	2566	0.186	0.007147	0.070	0.04644	0.47	0.047152	0.46
NC-MPE-417A																		
z1	25.613	0.023	25.58	0.13	32	12	20.69	0.284	0.24	0.91	37	2363	0.078	0.003981	0.090	0.02552	0.53	0.046506	0.51
z2	25.625	0.037	25.95	0.50	66	45	61.15	0.340	0.20	0.82	9	606	0.063	0.003983	0.14	0.02589	2.0	0.047160	1.9
z3	25.662	0.083	26.1	1.2	74	110	65.29	0.300	0.47	1.25	4	253	0.151	0.003989	0.32	0.0260	4.8	0.047338	4.7
z4	25.587	0.027	25.45	0.36	21	33	-22.19	0.318	0.47	0.94	14	867	0.152	0.003977	0.11	0.02538	1.4	0.046303	1.4
z5	25.685	0.094	26.6	1.4	116	120	77.90	0.299	0.39	0.75	3	225	0.126	0.003992	0.37	0.0265	5.3	0.048183	5.2
z6	25.616	0.039	25.91	0.53	62	49	59.15	0.329	0.19	0.91	8	564	0.060	0.003982	0.15	0.02584	2.1	0.047095	2.0
NC-MPE-418																		
z1	24.234	0.025	24.22	0.22	31	22	23.33	0.280	0.45	0.22	30	1793	0.145	0.003766	0.10	0.02414	0.93	0.046498	0.90
z2	24.206	0.018	24.19	0.14	32	14	25.35	0.242	0.36	0.17	39	2392	0.117	0.003762	0.073	0.02411	0.58	0.046507	0.56
z3	24.217	0.015	24.31	0.12	43	11	43.82	0.391	0.35	0.27	41	2527	0.112	0.003764	0.064	0.02423	0.49	0.046713	0.47

* Corrected for initial Th/U disequilibrium using radiogenic ^{208}Pb and $Th/U_{[Magma]}$=2.8±0.5.

† Isotopic dates calculated using the decay constants λ238 = 1.55125E-10 and λ235 = 9.8485E-10 (Jaffey et al. 1971).

§ % discordance = 100 - (100 * ($^{206}Pb/^{238}U$ date) / ($^{207}Pb/^{206}Pb$ date))

‡ Th contents calculated from radiogenic ^{208}Pb and the $^{207}Pb/^{206}Pb$ date of the sample, assuming concordance between U-Th and Pb systems.

** Total mass of common Pb.

†† Ratio of radiogenic Pb (including ^{208}Pb) to common Pb.

§§ Measured ratio corrected for fractionation and spike contribution only.

‡‡ Measured ratios corrected for fractionation, tracer and blank.

Chapter 3

Age and Volcanic Stratigraphy of the Siletzia Terrane in Washington and Vancouver Island

Abstract

Geophysical, geochemical, geochronologic, and stratigraphic observations all suggest that the basalts that underlie western Oregon, western Washington, and southern Vancouver Island form a coherent terrane of Eocene age that is named Siletzia. The total volume of basalt within this terrane is comparable those seen in large igneous provinces, and several lines of evidence suggest that it is an accreted oceanic plateau. However, a thick sequence of turbidites has long been considered to floor the northern part of the terrane and has led to an alternative hypothesis in which the terrane was built on the continental margin during marginal rifting or ridge-trench interaction. We present new high-precision U-Pb zircon dates from silicic tuffs and intrusive rocks throughout northern Siletzia, as well as detrital zircon age spectra and maximum depositional ages for sedimentary rocks within the terrane. Our new dates help clarify the volcanic stratigraphy of northern Siletzia and show that it was emplaced between 53.18 ± 0.17 and 48.364 ± 0.036 Ma, similar to the age and duration of magmatism in central and southern Siletzia. The 'basal' turbidites have maximum depositional ages as young as 44.72 ± 0.21 Ma and are distinctly younger than the rest of northern Siletzia, implying that they were thrust under the terrane at a later date. Importantly, a younger age for these sediments no longer necessitates that Siletzia formed along a rifted margin and we consider our revised stratigraphy to provide support for Siletzia's origin as an accreted oceanic plateau.

Introduction

Siletzia is an Eocene terrane of thick basaltic crust that underlies much of western Washington and Oregon, as well as southern Vancouver Island (Fig. 1A). Seismic studies suggest that the terrane is 20-30 km thick (e.g., Trehu et al., 1994), resulting in a total estimated volume of basalt that is comparable to the volumes emplaced in large igneous provinces (Wells

et al., 2014). Geochronologic and biostratigraphic age constraints support relatively rapid eruption and have led to the hypothesis that Siletzia represents an accreted oceanic plateau, or a chain of seamounts, developed above a hot spot within the Paleogene Pacific basin (Duncan, 1982; Murphy et al, 2003; McCrory and Wilson, 2013; Wells et al., 2014). Such an origin is supported by evidence for regional shortening from Vancouver Island to southern Oregon at ~50 Ma that has been attributed to accretion (Wells et al., 2000; Johnston and Acton, 2003; Eddy et al., 2016), geophysical studies that show that the terrane is connected to subducted oceanic lithosphere imaged in the upper mantle beneath eastern Washington and Oregon (Gao et al., 2011; Schmandt and Humphreys, 2011), and Pb, Sr, Nd, Os, and He isotopic compositions of basalts that suggest that they were derived from isotopically enriched mantle (Pyle et al., 2015). Nevertheless, a thick (1-2 km) sequence of continentally derived turbidites is considered to form the base of the northern part of the terrane in Washington (Tabor and Cady, 1978; Einarsen, 1987; Babcock et al., 1992; Brandon et al., 2014). The presence of these sedimentary rocks suggests that the basalts were erupted on the continental margin and challenges the accretion hypothesis. Combined with the likely presence of the Kula-Farallon-North America, or Resurrection-Farallon-North America, triple-junction near northern Siletzia during the terrane's construction (Groome et al., 2003; Madsen et al., 2006; Ickert et al., 2009; Eddy et al., 2016), these sedimentary rocks have led some researchers to consider Siletzia to have originated as a marginal rift (Wells et al., 1984; Babcock et al, 1992; Brandon et al., 2014) or as forearc magmatism related to triple-junction migration (Haeussler et al., 2003; Madsen et al., 2006).

To better assess the tectonic setting of Siletzia, we have revised the volcanic stratigraphy of the northern part of the terrane using high-precision U-Pb zircon geochronology. We show that the bulk of northern Siletzia was constructed between 53.18 ± 0.17 and 48.364 ± 0.036 Ma, similar to the age and duration over which the basaltic basement in central and southern Siletzia was constructed (e.g., Wells et al., 2014). Maximum depositional ages for the continentally derived turbidites that were previously considered to floor the terrane range between 47.775 ± 0.057 and 44.72 ± 0.21 Ma and demonstrate that these rocks were thrust under the terrane < 44.72 ± 0.21 Ma. The recognition that these rocks are younger than the rest of the basaltic basement that forms northern Siletzia permits the terrane to have been built on oceanic crust and we consider our revised stratigraphy to support Siletzia's origin as an accreted oceanic plateau developed near a triple-junction (e.g., McCrory and Wilson, 2013; Wells et al., 2014).

Northern Siletzia

The northernmost exposures of Siletzia occur in western Washington and southern Vancouver Island (Fig. 1B). On Vancouver Island the terrane is thrust under Mesozoic metasedimentary rocks along the Leech River fault (Fig. 1B: Groome et al., 2003), but its boundary with older terranes is buried under thick sedimentary and volcanic cover in Washington (Fig. 1B). The terrane's western margin is in fault contact with the Olympic Subduction Complex (Fig. 1B), which represents the accretionary prism for this part of the Cascadia subduction zone (e.g., Brandon and Calderwood, 1990).

The thickest exposures of Siletzia occur on the Olympic Peninsula where uplift of the Olympic Subduction Complex has tilted the terrane (Fig. 1C). These exposures are collectively known as the Crescent Fm. and consist of stratigraphic sequences of basalt that are up to ~16.2 km thick, though this thickness is likely a maximum due to the difficulty in recognizing faults in the heavily forested terrain of the Olympic Peninsula (Babcock et al., 1992). The Crescent Fm. is informally split into three units, the Blue Mtn. unit and the lower and upper Crescent Fm. (Tabor and Cady, 1978). The Blue Mtn. unit is in fault contact with the Olympic Subduction Complex and is composed of turbidites and pebble conglomerates that are interbedded with minor basalt (Tabor and Cady, 1978; Einarsen, 1987). The Blue Mtn. unit is ~1-2 km thick around most of the Peninsula, but forms a thick ~6.8 km thick sequence in the northeast (Fig. 1B). A thick section of submarine basalts conformably overlies the Blue Mtn. unit and is known as the Crescent Fm. These basalts transition to shallow marine and subaerial flows up section, and this transition marks an informal boundary between the lower and upper Crescent Fm. Along the Dosewallips River, the Crescent Fm. is estimated to be ~16.2 km thick (8.4 km: lower Crescent Fm. and 7.8 km: upper Crescent Fm.), and represents one of the thickest exposures of basalt on Earth (Babcock et al., 1992). The Crescent Fm. is overlain by rocks that belong to a thick marine forearc sedimentary sequence that ranges in age from the middle Eocene to the Miocene. On the northern Olympic Peninsula these rocks unconformably overlie the Crescent Fm., but on the eastern and southern parts of the Peninsula they are conformable (Babcock et al., 1994).

There are three other major outcrop areas in northern Siletzia; the Metchosin complex on Vancouver Island, the Bremerton complex within the Puget Sound region, and the Black Hills basalts near Olympia (Fig. 1B). The Metchosin complex has a partial ophiolite stratigraphy (e.g.,

Massey, 1986) and was thrust under Cretaceous metasedimentary rocks along the Leech River fault during the early to middle Eocene (Fig. 1B: Groome et al., 2003). It consists of a basal section of gabbro, diorite, and plagiogranite overlain by a thin sheeted dike complex and ~2.5 km of basalt flows that transition from submarine to subaerial up section (Massey, 1986). The lower part of the complex is not exposed, and seismic data shows that it is truncated by underthrust sedimentary rock (Clowes et al., 1987). Oligocene sedimentary rocks unconformably overlie the Metchosin complex (Massey et al., 2005). The Bremerton complex also has a partial ophiolite stratigraphy and consists of a lower section of gabbro and plagiogranite overlain by a thin section of sheeted dikes and <1.4 km of basalt flows that transition from submarine to subaerial up section (Clark, 1989). Gravity and magnetic surveys suggest that ultramafic rocks may exist immediately below these exposures (Haeussler and Clark, 2000) and would indicate a nearly complete ophiolite stratigraphy. The complex is cut by a series of hornblende dacite dikes (Tepper et al., 2004) that mark the end of volcanism in this area. The Black Hills basalts are composed of >600 m of mixed submarine and subaerial basalt flows conformably overlain by middle to late Eocene sedimentary rocks (Globerman et al., 1982).

U-Pb Zircon Geochronology

Previous geochronology from northern Siletzia largely consists of whole rock K-Ar and $^{40}Ar/^{39}Ar$ dates (Duncan, 1982; Clark, 1989; Babcock et al., 1992; Babcock et al., 1994; Hirsch, and Babcock 2009; Polenz et al., 2011; Polenz et al., 2012). These data have helped establish that northern Siletzia is early Eocene in age, but they are relatively imprecise and largely prevent fine temporal correlations between isolated outcrop areas. Furthermore, the variable metamorphism (Timpa et al., 2005; Hirsch and Babcock, 2009) and alteration of basalts and gabbros within northern Siletzia make it difficult to unambiguously interpret whole rock K-Ar and $^{40}Ar/^{39}Ar$ dates as crystallization ages. U-Pb zircon geochronology circumvents these problems, but existing data is limited to detrital zircon dates from the Blue Mtn. unit (Wells et al., 2014), and U-Pb zircon dates of 52 ± 2 Ma and 50.4 ± 0.6 Ma for gabbros within the Metchosin complex and Bremerton complex, respectively (Massey, 1986; Haeussler and Clark, 2000).

We present 11 new U-Pb zircon chemical abrasion-isotope dilution-thermal ionization mass spectrometry (CA-ID-TIMS) dates from throughout northern Siletzia that better help

constrain the regional volcanic stratigraphy. The methods for this procedure are slightly modified from Mattinson (2005) and are described in detail in Eddy et al. (2016). All isotopic ratios were measured on either the VG Sector 54 or Isotopx X62 thermal ionization mass spectrometers at the Massachusetts Institute of Technology and the data are presented in Table A1. We use the $^{206}Pb/^{238}U$ date for all of our interpretations because it offers the most precise date for rocks of this age, and we correct for preferential exclusion of ^{230}Th during zircon crystallization using the $[Th/U]_{zircon}$ and assuming a $[Th/U]_{magma} = 2.8$ for silicic tuffs (e.g., Machlus et al., 2015) or a $[Th/U]_{magma} = 3.2$ for mafic intrusive rocks (e.g., Gale et al., 2013) with an arbitrarily assigned uncertainty of ± 1 (2σ). We assume that zircon does not incorporate Pb during its crystallization and that all measured common Pb (Pb_c) is from laboratory contamination. We correct for this contamination using the measured mass of ^{204}Pb and a laboratory Pb_c isotopic composition of $^{206}Pb/^{204}Pb = 18.145833 \pm 0.475155$ (1σ abs.), $^{207}Pb/^{204}Pb = 15.303903 \pm 0.295535$ (1σ abs.), and $^{208}Pb/^{204}Pb = 37.107788 \pm 0.875051$ (1σ abs.), calculated from 149 procedural blanks measured in the MIT isotope geochemistry lab. Samples were spiked with the EARTHTIME ^{205}Pb-^{233}U-^{235}U isotopic tracer (Condon et al., 2015; McLean et al., 2015) and all data reduction was done on the U-Pb_REDUX software package (Bowring et al., 2011) using the U decay constants presented in Jaffey et al. (1971). Our preferred date for each sample is presented in Table 1 and the data is shown as traditional concordia plots in Figure A1. With the exception of a single xeno- or antecrystic grain in CR-MPE-003, zircons from all igneous samples have age dispersion within the 2σ variability of the mean square weighted deviation (MSWD: Wendt and Carl, 1991). Therefore, all of our preferred dates for igneous samples represent weighted means. Uncertainties are reported in the format ± X/Y/Z in Table 1., where X represents the analytical uncertainty, Y includes uncertainty in the isotopic tracer calibration, and Z represents the full uncertainty and includes uncertainty in the ^{238}U decay constant. However, other references to dates within the text only report the analytical uncertainty.

Detrital zircons were analyzed from four sandstones by laser ablation-inductively coupled plasma-mass spectrometry (LA-ICP-MS) on a Thermo-Fisher Element 2 at the Arizona LaserChron Center. The methods for these analyses follow those in Ibanez et al. (2015) and Pullen et al. (*in prep*) and all isotopic data is presented in Tables A2, A3, A4, and A5. To obtain maximum depositional ages for the sandstones, we removed some of the youngest grains identified during LA-ICP-MS analysis and dated them by CA-ID-TIMS. These dates are

presented in Table A1 and the youngest grain dated by CA-ID-TIMS for each sample is reported in Table 1 as a maximum depositional age.

Results

Blue Mtn. unit and Crescent Fm.

We sampled two composite sections through the Crescent Fm.: one along the Dungeness River and adjacent areas in the northwestern Olympic Peninsula, and one between lakes Cushman and Wynoochee in the southern part of the Olympic Peninsula (Fig. 1B). The Dungeness River section is through the thickest part of the Blue Mtn. unit (Fig. 2), which we estimate to be ~6.8 km thick based on the cross sections of Cady et al. (1972). Higher in the section, a sequence of subaerial basalts is in fault contact with the Blue Mtn. unit along the Boundary Creek fault (Figs. 1B and 2). These basalts are mapped as part of the upper Crescent Fm., have an exposed thickness < 1 km, and are unconformably overlain by marine sedimentary rocks (Schasse et al., 1998). We dated four samples from this composite section. Two sandstone samples from the base of the Blue Mtn. unit (CR-MPE-020 and CR-MPE-022) have maximum depositional ages of 44.72 ± 0.21 and 45.15 ± 0.21 Ma (Fig. 2), while a sandstone sample from the top of the Blue Mtn. unit has a maximum depositional age of 46.428 ± 0.048 Ma (Fig 2). A rhyolite (HS-11-13-97-8) from the upper Crescent Fm. is 51.424 ± 0.027 Ma (Fig. 2), is significantly older than the Blue Mtn. unit, and implies that stratigraphic continuity is not maintained across the Boundary Creek fault.

Our second sampling transect was through the area between Lake Cushman and Lake Wynoochee (Fig. 1B). In this area the Blue Mtn. unit is ~1 km thick and the overlying Crescent Fm. has a total thickness of ~11 km (Fig. 2). Mapping by Ken Clark (personal communication) has shown that the boundary between the lower and upper Crescent Fm. in this area is marked by an angular unconformity (Fig. 2) that is slightly higher in the section than the boundary mapped by Tabor and Cady (1978). Using this revised stratigraphy the lower Crescent Fm. is ~6.5 km thick and the upper Crescent Fm. is ~3.5 km thick. We dated five samples from this area: a sample of sandstone from the Blue Mtn. unit (CR-MPE-015), two silicic tuffs (KC-176.1 and KC-226) within the lower Crescent Fm., a silicic tuff (KC-300) from near the top of the upper Crescent Fm., and a gabbro (CR-MPE-024) that intrudes near the boundary between the lower

and upper Crescent Fm. (Table 1). Dates for the three tuffs follow stratigraphic order and show that much of this part of the Crescent Fm. was erupted between 53.18 ± 0.17 and 48.624 ± 0.023 Ma (Fig. 2). The 48.364 ± 0.036 Ma age of the gabbro is also consistent with the established stratigraphy. However, a maximum depositional age of 47.775 ± 0.057 Ma for the sandstone within the Blue Mtn. unit is significantly younger than the overlying rocks and implies that a thrust fault lies between CR-MPE-015 and KC-176.1 (Fig. 2).

Metchosin Complex

We dated three intrusive samples from the Metchosin complex on southern Vancouver Island (Fig. 1B). A diorite (CR-MPE-004B) gave a date of 51.115 ± 0.070 Ma, a plagiogranite (CR-MPE-007) gave a date of 50.986 ± 0.023 Ma, and a gabbro (CR-MPE-010A) gave a date of 51.176 ± 0.023 Ma (Fig. 3). These dates are in good agreement with the previously published date of 52 ± 2 Ma for a gabbro within the complex (Massey, 1986), and we consider these dates to constrain the age of volcanism in this area to ~51 Ma since the complex is considered to have formed in an extensional environment similar to those at mid-ocean ridges (Massey, 1986).

Bremerton Complex

Two samples were dated from the Bremerton complex (Fig. 1B). A sample of pegmatitic gabbro from the base of the partial ophiolite stratigraphy gave a date of 50.075 ± 0.016 Ma and overlaps within uncertainty with a previously published 50.4 ± 0.6 Ma U-Pb zircon date from leucogabbro (Haeussler and Clark, 2000). Like the Metchosin complex, we consider this date to be representative of the volcanism in this area due to the partial ophiolite stratigraphy of the complex. A hornblende dacite dike gave a date of 48.209 ± 0.057 Ma and provides a minimum age constraint for the construction of the partial ophiolite stratigraphy since similar dacite dikes cut the entire complex (Fig. 3: Clark, 1989).

Black Hills Basalts

We dated a thin (~1 cm) bentonite (CR-MPE-017B) within a thin sedimentary interbed in the lower to middle Black Hills basalts (Fig. 3). The bentonite gave a date of 49.729 ± 0.014 Ma and provides the first U-Pb date for rocks in this area.

Discussion

Volcanic Stratigraphy of Northern Siletzia

The oldest rocks in northern Siletzia are submarine basalt flows in the lower Crescent Fm. that are as old as 53.18 ± 0.17 Ma. Basalt continued to be erupted in the Crescent Fm. until 48.364 ± 0.036 Ma and led to the emplacement of up to 6 km of basalt in the southern Olympic Peninsula (Fig. 2). During this time the Crescent Fm. rose to a shallow marine or subaerial setting. Wells et al. (2014) interpreted this change to represent the emergence of a thick volcanic edifice. However, we note that a possible angular unconformity in the southern Olympic Peninsula (Fig. 2) may indicate that tectonic uplift played a role in this transition. Volcanism occurred over a similar duration in the areas adjacent the Crescent Fm. (Fig. 3). Both the Metchosin and Bremerton complexes were emplaced between 51.176 ± 0.023 Ma and 50.075 ± 0.016 Ma and also record a transition to subaerial eruption (Fig. 3). Likewise, the Black Hills basalts were emplaced during this time and similarly record mixed shallow marine and subaerial basalt flows. Collectively, these rocks form the exposed basaltic basement of Siletzia in this area and record voluminous volcanism between 53.18 ± 0.17 Ma and 48.364 ± 0.036 Ma (Fig. 5). The end of widespread and voluminous magmatism occurred after 48.364 ± 0.036 Ma and is marked by subsidence of the terrane below sea level and initial deposition of marine forearc sedimentary rocks.

The Blue Mtn. unit has long been considered the lowermost part of the Crescent Fm. (e.g., Tabor and Cady, 1978). Nevertheless, our maximum depositional ages for these rocks are distinctly younger than the rest of northern Siletzia (Fig. 2) and demonstrate that they were thrust under the terrane after their < 44.72 ± 0.21 Ma deposition. Along the northern part of the Olympic Peninsula the Boundary Creek fault has juxtaposed the Blue Mtn. unit with older rocks of the upper Crescent Fm. (Figs. 1B and 2), and while no continuation of this fault has been mapped along the eastern or southern parts of the Peninsula we suggest that through going thrust faults must exist based on a 46.3 ± 1.2 Ma date for a detrital zircon in the Blue Mtn. unit in the Dosewallips River area (Wells et al., 2014) and a 47.775 ± 0.057 Ma maximum depositional age for the Blue Mtn. unit on the southern part of the Peninsula. Interestingly, conformable contacts between the Blue Mtn. unit and submarine basalt (e.g., Einarsen, 1987) suggest that an unknown thickness of the lower Crescent Fm. is also < 44.72 ± 0.21 Ma in age. On the northern part of the

Peninsula the entire sequence of submarine basalts that is currently mapped as the lower Crescent Fm. lies below the Boundary Creek fault and may be younger than previously thought (Fig. 1B). On the eastern and southern parts of the Peninsula the thickness of these younger basalts is unconstrained.

Einarsen (1987) interpreted the Blue Mtn. unit as a submarine fan deposited along the North American margin and our new maximum depositional ages for the unit suggest that it may have formed a distal part of the forearc sedimentary sequence that overlies the upper Crescent Fm. Einarsen (1987) considered the source of these sediments to be uplifted Mesozoic rocks on Vancouver Island and in the San Juan Islands, as well as the Jurassic-Eocene Coast Mountain Batholith on the basis of sandstone petrology. Fig. 4 shows a composite probability density function for the 956 detrital zircons that were analyzed from the Blue Mtn. unit in this study. It shows peaks during the Eocene, Cretaceous, and Jurassic that correspond to major periods of magmatism within the Coast Mountain Batholith (Gehrels et al., 2009) and the youngest three peaks closely correspond to period of pluton construction in the southernmost part of the Coast Mountain Batholith in Washington (Miller et al., 2009). These observations support Einarsen (1987)'s interpretation of a sediment source in these areas. Small, but significant, peaks occur at ~1380 and between 1600 and 1800 Ma (Fig. 4) and closely correspond to those that Dumitru et al. (2016) attributed to erosion of the Mesoproterozoic Belt Group in Idaho and Montana.

Comparison to Southern Siletzia

The structure of southern Siletzia is remarkably similar to northern Siletzia, with a thick basaltic basement overlain by marine and deltaic sedimentary rocks (Wells et al., 2014). Only a few U-Pb dates are available for the basement in these areas. In central and northern Oregon, two U-Pb zircon dates from the top of the basaltic basement bracket a transition from submarine to subaerial eruption between 52 ± 1 and 49.0 ± 0.8 Ma and $^{40}Ar/^{39}Ar$ dates for the underlying basalts are as old as 54 Ma (Wells et al., 2014). These ages are similar to those in northern Siletzia and imply that the eruptions that constructed Siletzia occurred simultaneously (Fig. 5) over at least 350 km. The southernmost part of Siletzia, near Roseburg, OR, dominantly consists of submarine basalt flows dated between 56 and 53 Ma using whole rock $^{40}Ar/^{39}Ar$ (Wells et al., 2014). These dates suggest that it is the oldest exposed portion part of the terrane (Fig. 5).

Thick deltaic and marine sedimentary rocks overlie Siletzia in Oregon and southern Washington. These rocks are interbedded with basalts and gabbro that form distinct volcanic centers that are between 49 and 35 Ma in age (Fig. 5: Wells et al., 2014). Some of these volcanic centers contain isotopic evidence for melting 'plume-like' mantle (Chan et al., 2012), and others contain alkaline basalts or basalts with OIB-like geochemistry (Wells et al., 2014). These characteristics have led to speculation that hotspot volcanism played a roll in their development (Chan et al., 2012; Wells et al., 2014).

Tectonic Setting

The tectonic setting of Siletzia has been a longstanding problem, with debate centering on whether it represents an accreted oceanic terrane (Duncan, 1982; Murphy et al., 2003; McCrory and Wilson, 2013; Wells et al., 2014) or a rifted margin (Babcock et al., 1992; Brandon et al., 2014). One of the most compelling arguments for an origin as a rifted margin was the inferred stratigraphic position of the Blue Mtn. unit at the base of the terrane in Washington (e.g., Cady, 1975; Tabor and Cady, 1978; Einarsen, 1987; Babcock et al., 1992). However, our new U-Pb zircon geochronology demonstrates that these rocks were thrust under the rest of the terrane after 44.72 ± 0.21 Ma (Fig. 2). Given that the oldest rocks within Siletzia are submarine basalts (Fig. 5), combined with the evidence for regional shortening at ~50 Ma in Oregon and Washington (Wells et al., 2000; Wells et al., 2014; Eddy et al., 2016) and geophysical evidence linking Siletzia to tomographic images of subducted oceanic lithosphere under eastern Washington and Oregon (Gao et al., 2011; Schmandt and Humphreys, 2011), we prefer an origin as an accreted oceanic terrane. Several authors have suggested that the terrane represents an oceanic plateau, or series of oceanic islands, developed above a hotspot, consistent with the projected Eocene position of a long-lived Yellowstone hotspot near western Oregon (Duncan, 1982; Murphy et al., 2003; McCrory and Wilson, 2013; Wells et al., 2014). Such an origin would explain the great volume of basalt within Siletzia (e.g., Wells et al., 2014) and we suggest that our data is compatible with its construction immediately prior to and coeval with its attempted subduction based on the 51.3-49.3 Ma age regional shortening in central and western Washington that Eddy et al. (2016).

The Bremerton and Metchosin complexes may represent the basement onto which Siletzia was built as their partial ophiolite stratigraphy suggests that they were emplaced in

tectonic setting similar to that at oceanic spreading centers (Massey, 1986; Clark, 1989). Nevertheless, the age of these complexes is younger than the oldest rocks within the Olympic Peninsula and would imply that a spreading center lay between the Crescent Fm. and the North American margin immediately prior to Siletzia's accretion (Fig. 6). Plate reconstructions require that the Kula-Farallon, and possibly the Resurrection-Farallon, spreading ridge(s) intersected North America during the Paleogene (e.g., Atwater, 1970; Engebretson et al., 1985; Haeussler et al., 2003; Madsen et al., 2006), and several lines of evidence suggest that one of these ridges intersected North America near southern Vancouver Island and western Washington; including the presence of geochemically anomalous forearc and backarc magmatism from ~51-49 Ma (Cowan, 2003; Groome et al., 2003; Madsen et al., 2003; Ickert et al., 2009) and initiation, or acceleration, of dextral strike-slip faulting in Washington immediately following Siletzia's accretion (Eddy et al., 2016). Therefore, we follow McCrory and Wilson (2013) and Wells et al. (2014) and consider Siletzia to have been erupted near a triple-junction. In this model, northern Siletzia represents part of the Kula (or Resurrection) plate, while all of central and southern Siletzia represents a captured piece of the Farallon plate (Fig. 6: Duncan, 1982; McCrory and Wilson, 2013). Construction of an oceanic plateau on extremely young oceanic crust may also explain why Siletzia jammed the subduction zone rather than subducting since oceanic plateaus that are broad, thick, and young can exert a buoyancy force that equals or exceeds slab pull (e.g., Cloos et al., 1993; Arrial and Billen, 2013).

After Siletzia's accretion, continued interaction between the Yellowstone hotspot and the North American margin may have led to continued forearc magmatism as represented by the ~49-35 Ma volcanic centers in the southern Washington and Oregon forearc (e.g., Wells et al., 2014). The basalts interbedded with and immediately overlying the < 44.72 ± 0.21 Ma Blue Mtn. unit are likely also a manifestation of this process (Fig. 6).

Conclusions

Our new U-Pb zircon dates from throughout northern Siletzia place new constraints on the timing and duration of terrane's construction. They show that much of the terrane was built between .53.18 ± 0.17 and 48.364 ± 0.036 Ma, similar to the duration and age of magmatism in central and southern Siletzia. The thick section of turbidites that has long been considered to floor the terrane are considerably younger and were thrust under the rest of the terrane < 44.72 ±

0.21 Ma along with an unknown thickness of submarine basalt. We consider this revised volcanic stratigraphy to be consistent with Siletzia's development as an oceanic plateau that developed near an oceanic spreading ridge immediately prior to accretion.

References

Arrial, P., and Billen, M.I., 2013, Influence of geometry and eclogitization on oceanic plateau subduction: Earth and Planetary Science Letters, v. 363, p. 34-43, doi: 10.1016/j.epsl.2012.12.011.

Atwater, T., 1970, Implications of plate tectonics for the Cenozoic tectonic evolution of western North America: Geological Society of America Bulletin, v. 81, p. 3513-3536, doi: 10.1130/0016-7606(1970)81[3513:IOPTFT]2.0.CO;2.

Babcock, R.S., Burmester, R.R., Engebretson, D.C., Warnock, A.C., Clark, K.P., 1992, A rifted margin origin for the Crescent basalts and related rocks in the northern Coast Range Volcanic Province, Washington and British Columbia: Journal of Geophysical Research, v. 97, p. 6799-6821, doi: 10.1029/91JB02926.

Babcock, R.S., Suczek, C.A., and Engebretson, D.C., 1994, The Crescent "Terrane", Olympic Peninsula and Southern Vancouver Island: Washington Division of Geology and Earth Resources Bulletin, v. 80, p. 141-157.

Brandon, M.T., and Calderwood, A.R., 1990, High-pressure metamorphism and uplift of the Olympic subduction complex: Geology, v. 18, p. 1252-1255, doi: 10.1130/0091-7613(1990)018<1252:HPMAUO>2.3.CO;2.

Brandon, M.T., Hourigan, J., Garver, J.I., 2014, New evidence for backarc basin interpretation for Eocene Coast Range Terrane: Geological Society of America Abstracts with Programs, v. 46, n. 6, p. 657.

Bowring, J.F., McLean, N.M., and Bowring, S.A., 2011, Engineering cyber infrastructure for U-Pb geochronology: Tripoli and U-Pb_Redux: Geochemistry, Geophysics, and Geosystems, v. 12, doi: 10.1029/2010GC003479.

Cady, W.M., 1975, Tectonic setting of the Tertiary volcanic rocks of the Olympic Peninsula, Washington: Journal of Research of the U.S. Geological Survey, v. 5, p. 573-582.

Cady, W.M., Tabor, R.W., MacLeod, N.S., and Sorensen, M.L., 1972, Geologic map of the Tyler Peak quadrangle, Clallam and Jefferson counties, Washington: U.S. Geological Survey, scale 1:62,000, 1 sheet.

Chan, C.F., Tepper, J.H., and Nelson, B.K., 2012, Petrology of the Grays River volcanics, southwest Washington: plume-influenced slab window magmatism in the Cascadia forearc: Geological Society of America Bulletin, v. 124, p. 1324-1338, doi: 10.1130/B30576.1.

Clark, K.P., 1989, The stratigraphy and geochemistry of the Crescent Formation basalts and the bedrock geology of associated igneous rocks near Bremerton Washington [MS thesis]: Western Washington University, 171 p.

Cloos, M., 1993, Lithospheric buoyancy and collisional orogenesis: subduction of oceanic plateaus, continental margins, island arcs, spreading ridges, and seamounts: Geological Society of America Bulletin, v. 105, p. 715-737, doi: 10.1130/0016-7606(1993)105<0715:LBACOS>2.3.CO;2.

Clowes, R.M., Brandon, M.T., Green, A.G., Yorath, C.J., Sutherland, A., Kanasewich, E.R., and Spencer, C., 1987, LITHOPROBE-southern Vancouver Island: Cenozoic subduction complex imaged by deep seismic reflections: Canadian Journal of Earth Science, v. 24, p. 31-51, doi: 10.1139/e87-004.

Condon, D.J., Schoene, B., McLean, N.M., Bowring, S.A., and Parrish, R.R., 2015, Metrology and traceability of U-Pb isotope dilution geochronology (EARTHTIME tracer calibration part I): Geochimica et Cosmochimica Acta, v. 164, p. 464-480, doi: 10.1016/j.gca.2015.05.026.

Cowan, D.S., 2003, Revisiting the Baranof-Leech River hypothesis for early Tertiary coastwise transport of the Chugach-Prince William terrane: Earth and Planetary Science Letters, v. 213, p. 463-475, doi: 10.1016/S0012-821X(03)00300-5.

Dragovich, J.D., Logan, R.L., Schasse, H.W., Walsh, T.J., Lingley Jr., W.S., Norman, D.K., Gerstel, W.J., Lapen, T.J., Schuster, E., and Meyers, K.D., 2002, Geologic map of Washington-northwest quadrant: Washington Department of Natural Resources Geologic Map GM-50, scale 1:250,000, 3 sheets, 72 p. text.

Dumitru, T.A., Elder, W.P., Hourigan, J.K., Chapman, A.D., Graham, S.A., 2016, Four Cordilleran paleorivers that connected Sevier thrust zones in Idaho to depocenters in

California, Washington, Wyoming, and, indirectly, Alaska: Geology, v. 44, p. 75-78, doi: 10.1130/G37286.1.

Duncan, R.A., 1982, A captured island chain in the coast range of Oregon and Washington: Journal of Geophysical Research, v. 87, p. 827-837, doi: 10.1029/JB087iB13p10827.

Eddy, M.P., Bowring, S.A., Umhoefer, P.J., Miller, R.B., McLean, N.M., and Donaghy, E.E., 2016, High-resolution temporal and stratigraphic record of Siletzia's accretion and triple junction migration from nonmarine sedimentary basins in central and western Washington: Geological Society of America Bulletin, v. 128, p. 425-441, doi: 10.1130/B31335.1.

Einarsen, J.M., 1987, The petrography and tectonic significance of the Blue Mountain unit, Olympic Peninsula, Washington [M.S. Thesis]: Bellingham, Western Washington University, 175 p.

Engebretson, D.C., Cox, A., and Gordon, R.G., 1985, Relative motions between oceanic and continental plates in the Pacific basin: Geological Society of America Special Papers, v. 206, p. 1-60, doi: 10.1130/SPE206-p1.

Gale, A., Dalton, C.A., Langmuir, C.H., Su, Y., and Schilling, J., 2013, The mean composition of ocean ridge basalts: Geochemistry, Geophysics, Geosystems, v. 14, p. 489-518, doi: 10.1029/2012GC004334.

Gao, H., Humphreys, E.D., Yao, H., and van der Hilts, R.D., 2011, Crust and lithosphere structure of the northwestern U.S. with ambient noise tomography: terrane accretion and Cascade arc development: Earth and Planetary Science Letters, v. 304, p. 202-211, doi: 10.1016/j.epsl.2011.01.033.

Gehrels, G., Rusmore, M., Woodsworth, G., Crawford, M., Andronicos, C., Hollister, L., Patchett, J., Ducea, M., Butler, R., Klepeis, K., Davidson, C., Friedman, R., Haggart, J., Mahoney, B., Crawford, W., Pearson, D., and Girardi, J., 2009, U-Th-Pb geochronology of the Coast Mountains batholith in north-coastal British Columbia: constraints on age and tectonic evolution: Geological Society of America, v. 121, p. 1341-1361, doi: 10.1130/B26404.1.

Globerman, B.R., Beck Jr., M.E., and Duncan, R.A., 1982, Paleomagnetism and tectonic significance of Eocene basalts from the Black Hills, Washington Coast Range:

Geological Society of America Bulletin, v. 93, p. 1151-1159, doi: 10.1130/0016-7606(1982)93<1151:PATSOE>2.0.CO;2.

Groome, W.G., Thorkelson, D.J., Friedman, R.M., Mortensen, J.K., Massey, N.W.D., Marschall, D.D., and Layer, P.W., 2003, Magmatic and tectonic history of the Leech River Complex, Vancouver Island, British Columbia: evidence for ridge-trench intersection and accretion of the Crescent Terrane, *in* Sisson, V.B., Roeske, S.M., and Pavlis, T.L., eds., Geology of a transpressional orogen developed during ridge-trench interaction along the North Pacific margin: Boulder, Colorado, Geological Society of America Special Paper 371, p. 327-353, doi: 10.1130/0-8137-2371-X.327.

Haeussler, P.J., Bradley, D.C., Wells, R.E., Miller, M.L., 2003, Life and death of the Resurrection plate: evidence for its existence and subduction in the northeastern Pacific in Paleocene-Eocene time: Geological Society of America Bulletin, v., 115, p. 867-880, doi: 10.1130/0016-7606(2003)115<0867:LADOTR>2.0.CO;2.

Haeussler, P.J., and Clark, K.P., 2000, Geologic map of the Wildcat Lake 7.5' quadrangle, Kitsap and Mason counties Washington: U.S. Geological Survey, scale 1:24,000, 1 sheet.

Hirsch, D.M., and Babcock, R.S., 2009, Spatially heterogeneous burial and high-P/T metamorphism in the Crescent Formation, Olympic Peninsula, Washington: American Mineralogist, v. 94, p. 1103-1110, doi: 10.2138/am.2009.3187.

Ibanez-Mejia, M., Pullen, A., Arenstein, J., Gehrels, G.E., Valley, J., Ducea, M.N., Mora, A.R., Pecha, M., and Ruiz, J., 2015, Unraveling crustal growth and reworking processes in complex zircons from orogenic lower-crust: the Proterozoic Putumayo Orogen of Amazonia: Precambrian Research, v. 267, p. 285-310, doi: 10.1016/j.precamres.2015.06.014.

Ickert, R.B., Thorkelson, D.J., Marshall, D.D., and Ullrich, T.D., 2009, Eocene adakitic volcanism in southern British Columbia: remelting of arc basalt above a slab window: Tectonophysics, v. 464, p. 164-185, doi: 10.1016/j.tecto.2007.10.007.

Jaffey, A.H., Flynn, K.F., Glendenin, L.E., Bentley, W.C., Essling, A.M., 1971, Precision measurement of half-lives and specific activities of 235U and 38U: Physical Review C, v. 4, p. 1889-1906, doi: 10.1103/PhysRevC.4.1889.

Johnston, S.T., and Acton, S., 2003, The Eocene southern Vancouver Island Orocline – a response to seamount accretion and the cause of fold-and-thrust belt and extensional

basin formation: Tectonophysics, v. 365, p. 165-183, doi: 10.1016/S0040-1951(03)00021-0.

Ludwig, K.R., 2003, Using Isoplot/Ex, version 3.00: a geochronological toolkit for Microsoft Excel: Berkeley Geochronology Center Special Publication 4, 71 p.

Machlus, M.L., Ramezani, J., Bowring, S.A., Hemming, S.R., Tsukui, K., and Clyde, W.C., 2015, A strategy for cross-calibrating U-Pb chronology and astrochronology of sedimentary sequences: an example from the Green River Formation, Wyoming, USA: Earth and Planetary Science Letters, v. 413, p. 70-78, doi: 10.1016/j.epsl.2014.12.009.

Madsen, J.K., Thorkelson, D.J., Friedman, R.M., and Marshall, D.D., 2006, Cenozoic to recent plate configurations in the Pacific Basin: ridge subduction and slab window magmatism in western North America: Geosphere, v. 2, p. 11-34, doi: 10.1130/GES00020.1.

Massey, N.W.D., 1986, Metchosin igneous complex, southern Vancouver Island: ophiolite stratigraphy developed in an emergent island setting: Geology, v. 14, p. 602-605, doi: 10.1130/0091-7613(1986)14<602:MICSVI>2.0.CO;2.

Mattinson, J.M., 2005, Zircon U-Pb chemical abrasion ("CA-TIMS") method: combined annealing and multi-step partial dissolution analysis for improved precision and accuracy of zircon ages: Chemical Geology, v. 220, p. 47-66, doi: 10.1016/j.chemgeo.2005.03.011.

Massey, N.W., MacIntyre, D.G., Desjardins, P.J., and Cooney, R.T., 2005, Geology of British Columbia: BC Ministry of Energy, Mines, and Petroleum Resources Geoscience Map 2005-3, scale 1:1,000,000, 3 sheets.

McCrory, P.A., and Wilson, D.S., 2013, A kinematic model for the formation of the Siletz-Crescent forearc terrane by capture of coherent fragments of the Farallon and Resurrection plates: Tectonics, v. 32, p. 718-736, doi: 10.1002/tect.20045.

McLean, N.M., Condon, D.J., Schoene, B., and Bowring, S.A., 2015, Evaluating uncertainties in the calibration of isotopic reference materials and multi-element isotopic tracers (EARTHTIME tracer calibration part II): Geochimica et Cosmochimica Acta, v. 164, p. 481-501, doi: 10.1016/j.gca.2015.02.040.

Miller, R.B., Paterson, S.R., and Matzel, J.P., 2009, Plutonism at different crustal levels: Insights from the ~5–40 km (paleodepth) North Cascades crustal section, Washington, *in* Miller, R.B., and Snoke, A.W., eds., Crustal Cross Sections from the Western North American

Cordillera and Elsewhere: Implications for Tectonic and Petrologic Processes: Geological Society of America Special Paper 456, p. 125–149, doi: 10.1130/2009.2456(05).

Murphy, J.B., Hynes, A.J., Johnston, S.T., and Keppie, J.D., 2003, Reconstructing the ancestral Yellowstone plume from accreted seamounts and its relationship to flat slab subduction: Tectonophysics, v. 365, p. 185-194, doi: 10.1016/S0040-1951(03)00022-2.

Pyle, D.G., Duncan, R.A., Wells, R.E., Graham, D.W., Hanan, B.B., Harrison, B.K., and Haileab, B., 2015, Longevity of Yellowstone hotspot volcanism: isotopic evidence linking the Siletzia LIP (56 Ma) and early Columbia River Basalt Group (17 Ma) mantle sources: Abstract V31E-3060 presented at 2015 Fall Meeting, AGU, San Francisco, California, 14-18 December.

Schasse, H.W., and Logan, R.L., 1998, Geologic map of the Sequim 7.5-minute quadrangle, Clallam County, Washington: Washington Division of Geology and Earth Resources Open File Report 98-7, scale 1:24,000, 1 sheet.

Schmandt, B., and Humphreys, E., 2011, Seismically imaged relict slab from the 55 Ma Siletzia accretion to the northwest United States: Geology, v. 39, p. 175-178, doi: 10.1130/G31558.1.

Tabor, R.W., and Cady, W.M., 1978, The structure of the Olympic Mountains, Washington: analysis of a subduction zone: U.S. Geological Survey Professional Paper 1033, 38 p.

Tabor, R.W., and Cady, W.M., 1978, Geologic map of the Olympic Peninsula, Washington: U.S. Geological Survey, scale 1:125,000, 2 sheets.

Tepper, J.H., Clark, K.P., Asmerom, Y., and McIntosh, W.C., 2004, Eocene adakites in the Cascadia forearc: implications for the position of the Kula-Farallon ridge: Geological Society of America Abstracts with Programs, v. 36, n. 4, p. 69.

Timpa, S., Gillis, K.M., and Canil, D., 2005, Accretion-related metamorphism of the Metchosin Igneous Complex, southern Vancouver Island, British Columbia: Canadian Journal of Earth Sciences, v. 42, p. 1467-1479, doi: 10.1139/e05-043.

Trehu, A.M., Asudeh, I., Brocher, T.M., Luetgert, J.H., Mooney, W.D., Nabelek, J.L., and Nakamura, Y., 1994, Crustal architecture of the Cascadia forearc: Science, v. 266, p. 237-243, doi: 10.1126/science.266.5183.237.

Walsh, T.J., Korosec, M.A., Phillips, W.M., Logan, R.L., and Schasse, H.W., 1987, Geologic map of Washington-southwest quadrant: Washington Division of Geology and Earth Resources Geologic Map GM-34, scale 1:250,000, 2 sheets, 28 p. text.

Wells, R.E., Engebretson, D.C., Snavely Jr., P.D., and Coe, R.S., 1984, Cenozoic plate motions and the volcano-tectonic evolution of western Oregon and Washington: Tectonics, v. 3, p. 275-294, doi: 10.1029/TC003i002p00275.

Wells, R.E., Jayko, A.S., Niem, A.R., Black, G., Wiley, T., Baldwin, E., Molenaar, K.M., Wheeler, K.L., DuRoss, C.B., and Givler, R.W., 2000, Geologic map and database of the Roseburg 30 x 60' quadrangle, Douglas and Coos Counties, Oregon: U.S. Geological Survey, scale 1:100,000, 2 sheets, 55 p. text.

Wells, R.E., Bukry, D., Friedman, R., Pyle, D., Duncan, R., Haeussler, P., and Wooden, J., 2014, Geologic history of Siletzia, a large igneous province in the Oregon and Washington Coast Range: correlation to the geomagnetic polarity time scale and implications for a long-lived Yellowstone hotspot: Geosphere, v. 10, p. 692-719, doi: 10.1130/GES01018.1.

Wendt, I., and Carl, C., 1991, The statistical distribution of the mean squared weighted deviation: Chemical Geology, v. 86, p. 275-285, doi: 10.1016/0168-9622(91)90010-T.

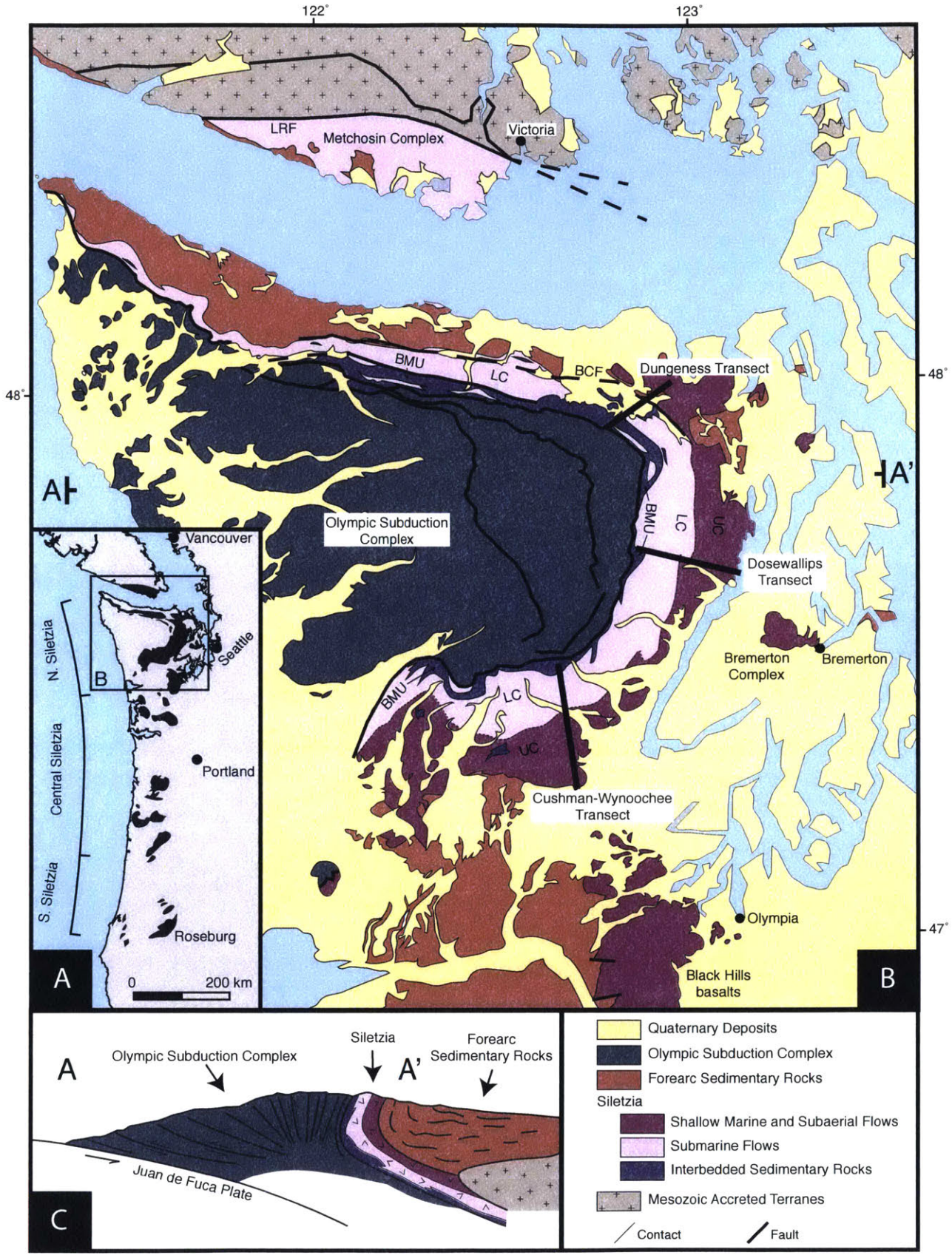
122°
123°
48°
47°
LRF
Metchosin Complex
Victoria
BMU
LC
BCF
Dungeness Transect
A
A'
Olympic Subduction Complex
UC
Dosewallips Transect
Bremerton Complex
Bremerton
Cushman-Wynoochee Transect
Olympia
Black Hills basalts
B
Vancouver
N. Siletzia
Central Siletzia
S. Siletzia
Seattle
Portland
Roseburg
0
200 km
Siletzia
Forearc Sedimentary Rocks
Juan de Fuca Plate
C
Quaternary Deposits
Olympic Subduction Complex
Forearc Sedimentary Rocks
Siletzia
Shallow Marine and Subaerial Flows
Submarine Flows
Interbedded Sedimentary Rocks
Mesozoic Accreted Terranes
Contact
Fault

Figure 1: (A) Exposed portions of Siletzia (black) within western Oregon and Washington and southern Vancouver Island. The regional distinctions made in this paper between northern, central, and southern Siletzia are also shown. **(B)** Simplified geologic map of the Olympic Peninsula and surrounding area modified from Tabor and Cady (1978), Walsh et al. (1987), Dragovich et al. (2002), and Massey et al. (2005). Abbreviations are: Blue Mountain unit (BMU), lower Crescent Fm. (LC), upper Crescent Fm. (UC), Boundary Creek fault (BCF), and Leech River fault (LRF). In this figure we follow Tabor and Cady (1978) and show the upper Crescent Fm. on the southern Olympic Peninsula as largely subaerial. However, Clark (unpublished mapping) has shown that significant portions are submarine. **(C)** Cartoon E-W cross section through the Olympic Peninsula modified from Tabor and Cady (1978).

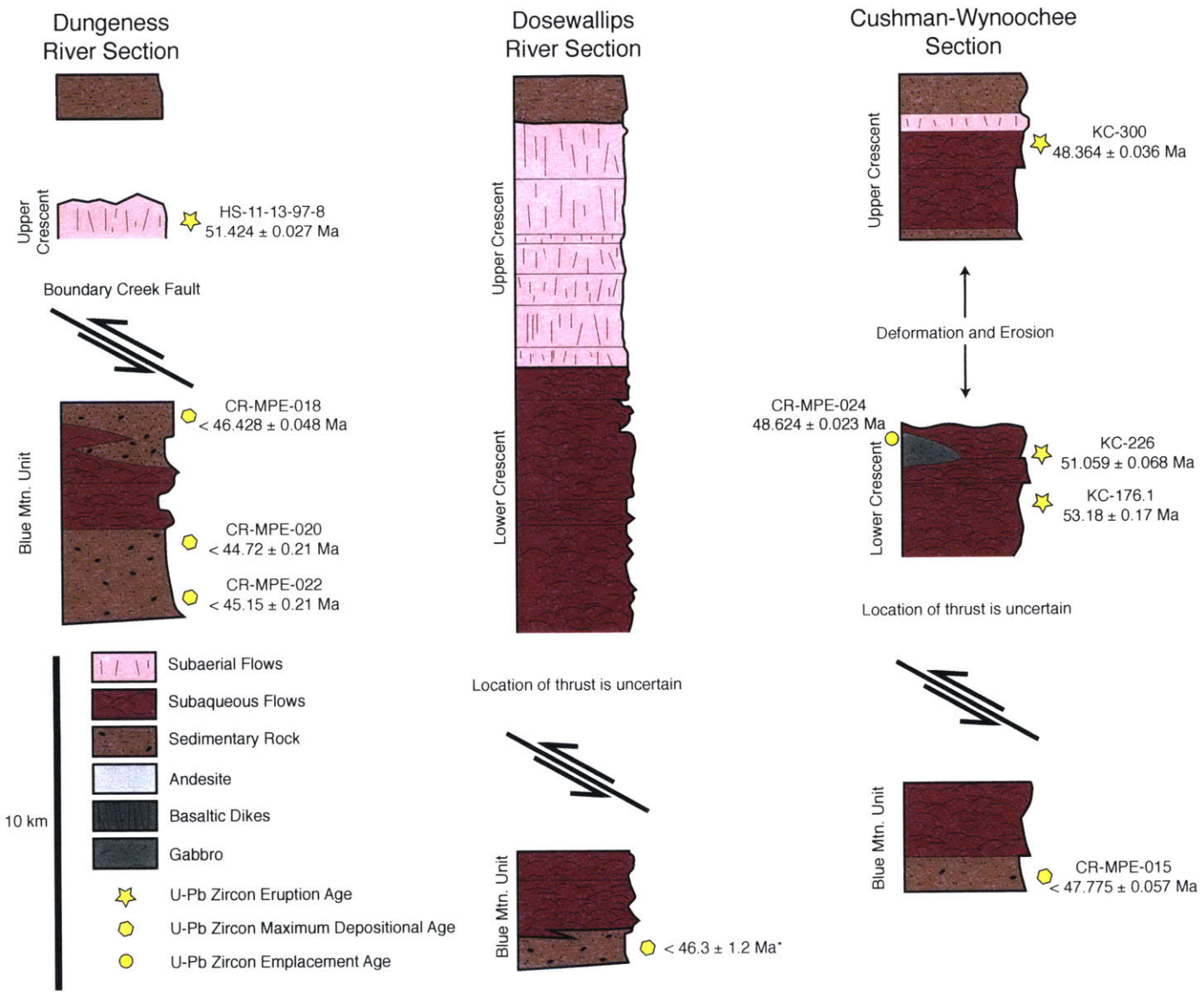
Dungeness River Section
Upper Crescent
HS-11-13-97-8
51.424 ± 0.027 Ma
Boundary Creek Fault
Blue Mtn. Unit
CR-MPE-018
< 46.428 ± 0.048 Ma
CR-MPE-020
< 44.72 ± 0.21 Ma
CR-MPE-022
< 45.15 ± 0.21 Ma
10 km
Subaerial Flows
Subaqueous Flows
Sedimentary Rock
Andesite
Basaltic Dikes
Gabbro
U-Pb Zircon Eruption Age
U-Pb Zircon Maximum Depositional Age
U-Pb Zircon Emplacement Age
Dosewallips River Section
Upper Crescent
Lower Crescent
Location of thrust is uncertain
Blue Mtn. Unit
< 46.3 ± 1.2 Ma*
Cushman-Wynoochee Section
Upper Crescent
KC-300
48.364 ± 0.036 Ma
Deformation and Erosion
CR-MPE-024
48.624 ± 0.023 Ma
Lower Crescent
KC-226
51.059 ± 0.068 Ma
KC-176.1
53.18 ± 0.17 Ma
Location of thrust is uncertain
Blue Mtn. Unit
CR-MPE-015
< 47.775 ± 0.057 Ma

Figure 2: Stratigraphic sections for the Dungeness River, Dosewallips River, and Lake Cushman-Wynoochie transects showing the locations of dated samples. Thicknesses are estimated from Cady et al. (1972) for the Dungeness River transect and from unpublished mapping by K. Clark for the Lake Cushman-Wynoochie transect. The column for the Dosewallips section is modified from Babcock et al. (1992). All dates are from this study with the exception of a U-Pb detrital zircon date from Wells et al. (2014) denoted by a *.

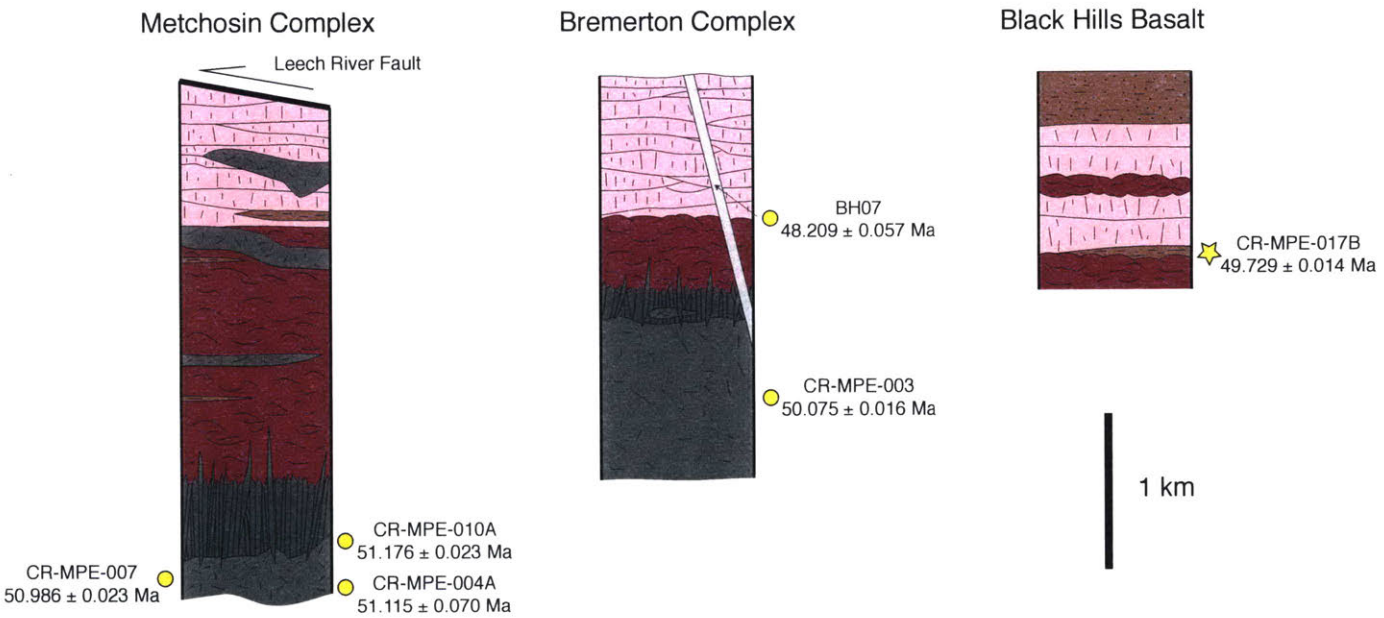

Figure 3: Generalized sections through the Metchosin complex, Bremerton complex, and Black Hills basalts showing thicknesses and the locations of dated samples. The sections for the Metchosin complex and Bremerton complex are modified from Massey et al. (1986) and Clark (1989) respectively. All dates are from this study and all symbols and colors are the same as Fig. 2.

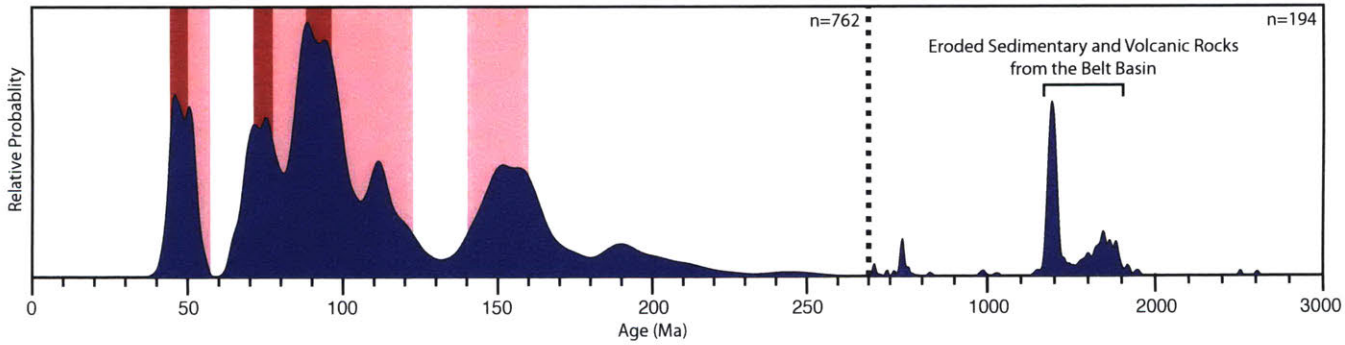

Figure 4: Probability density function of 956 detrital zircons from the Blue Mountain unit generated using Isoplot (Ludwig, 2003). The main periods of Mesozoic and Paleogene magmatism in the Coast Mountain Batholith (Gehrels et al., 2009) are shown in pink, while major periods of pluton construction in the North Cascades are shown in red (Miller et al., 2009). A sharp at ~1380 Ma and a broad peak from 1600 to 1800 Ma closely correspond to the expected ages of zircon eroded from uplifted Proterozoic sedimentary rocks in the Belt basin (Dumitru et al., 2016).

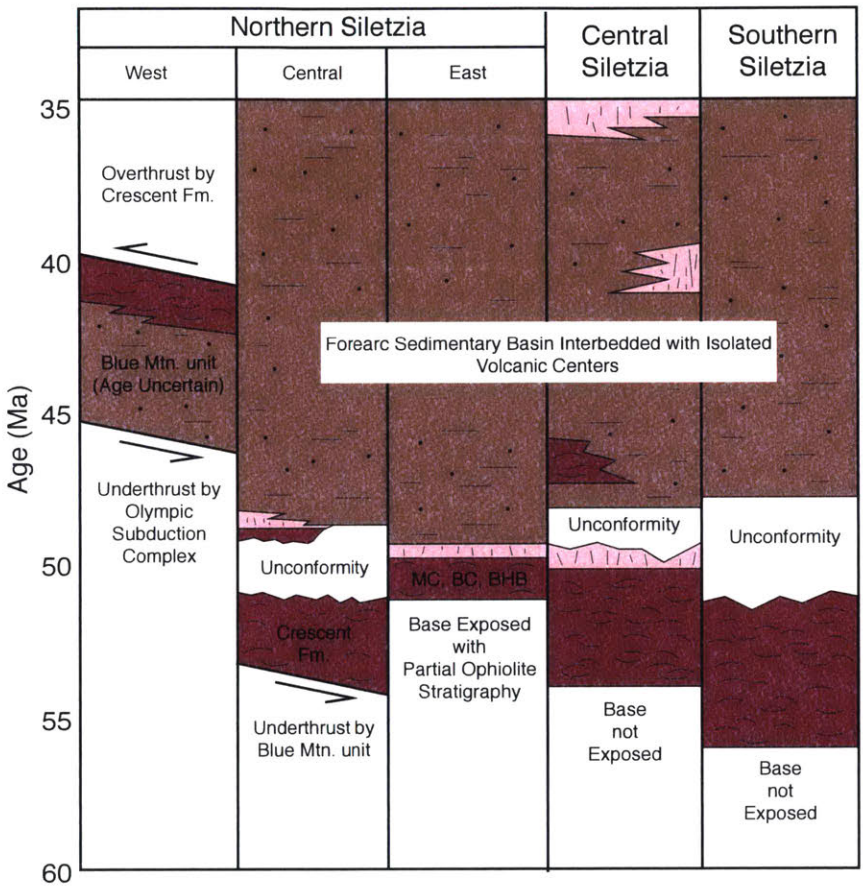

Figure 5: Temporal correlations between magmatism in northern, central, and southern Siletzia. See Fig. 1A for our divisions between these areas. All of the ages for the units in northern Siletzia are based on the geochronology presented in this work. The temporal history of magmatism and sedimentation in central and southern Siletzia is from Wells et al. (2014). Abbreviations are MC: Metchosin complex, BC: Bremerton Complex, BHB: Black Hills basalts.

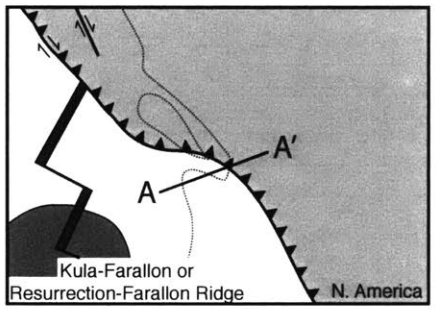

> 53 Ma

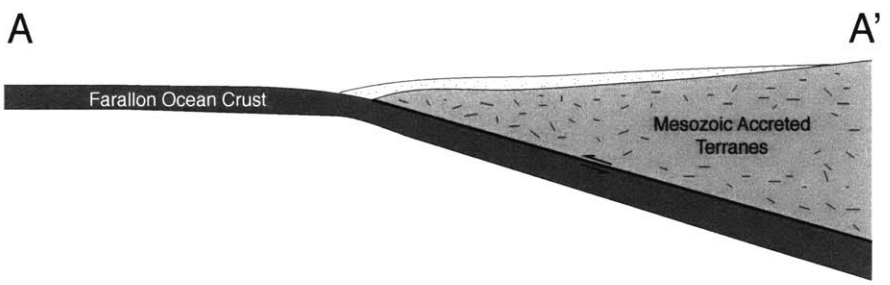

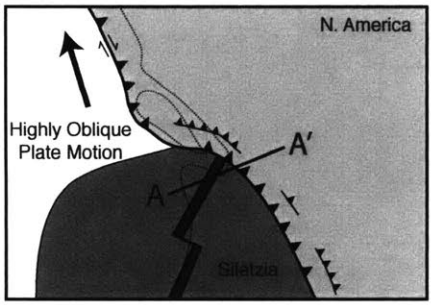

~ 51-48 Ma

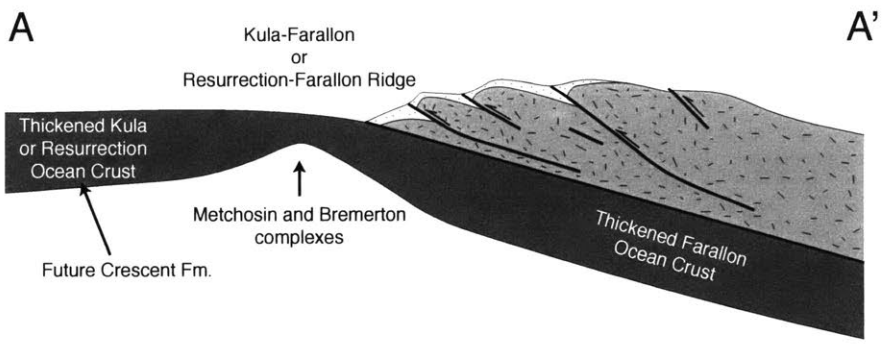

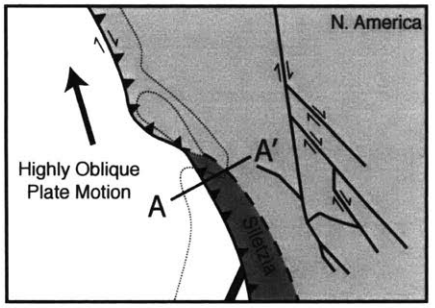

< 44.7 Ma

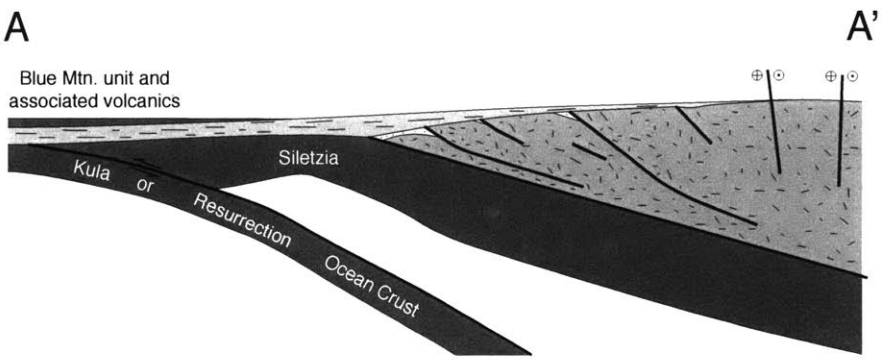

Figure 6 (*on previous page*)**:** Proposed reconstruction for development and accretion of northern Siletzia. Prior to 53 Ma ocean crust of normal thickness belonging to the Farallon plate was subducting at the latitude of Washington. From 53-48 Ma a plateau developed along the Kula-Farallon or Resurrection-Farallon ridge and jammed the subduction zone during its attempted subduction leading to regional shortening. After 44.7 Ma the Blue Mtn. unit was deposited as a distal part of a regional depositional system. Interbedded and overlying basalts may represent continued interaction between the Yellowstone hotspot and the North American margin. Maps are modified from Eddy et al. (2016).

Figure A1: Traditional concordia plots for U-Pb CA-ID-TIMS data. Dates are Th-corrected $^{206}Pb/^{238}U$ dates.

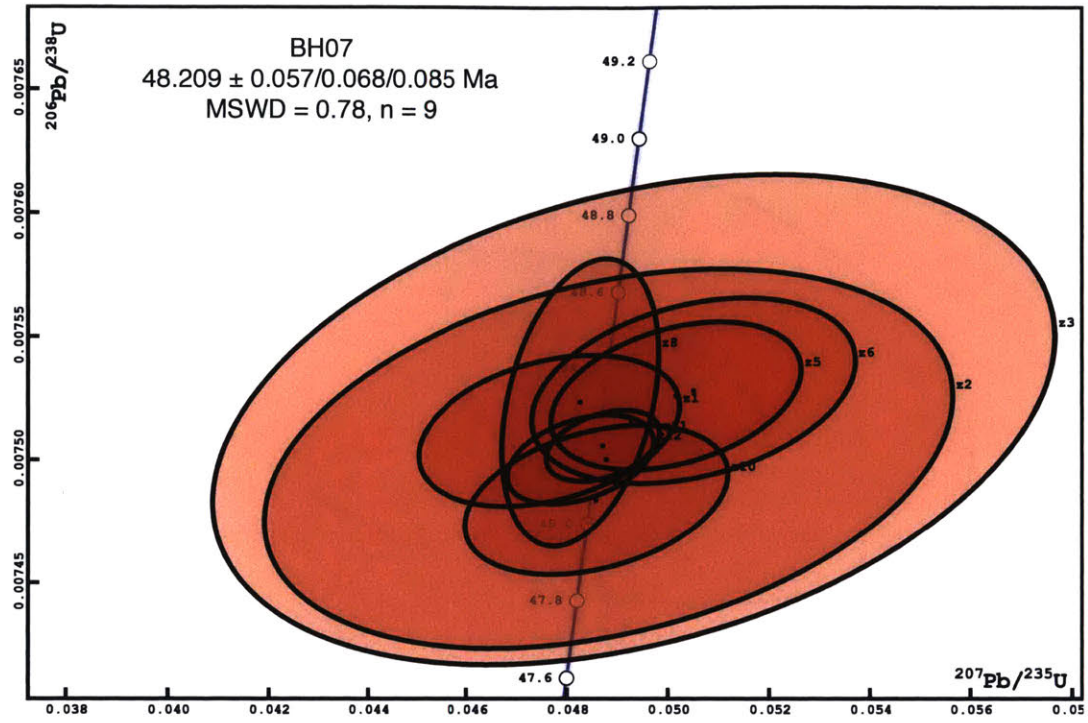

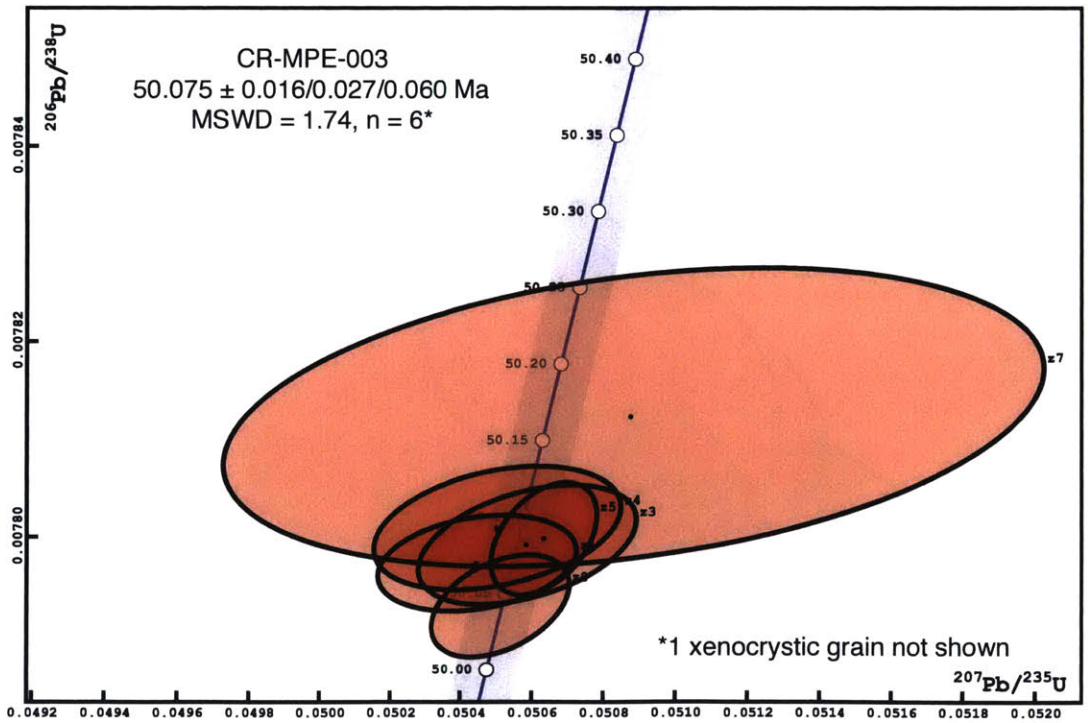

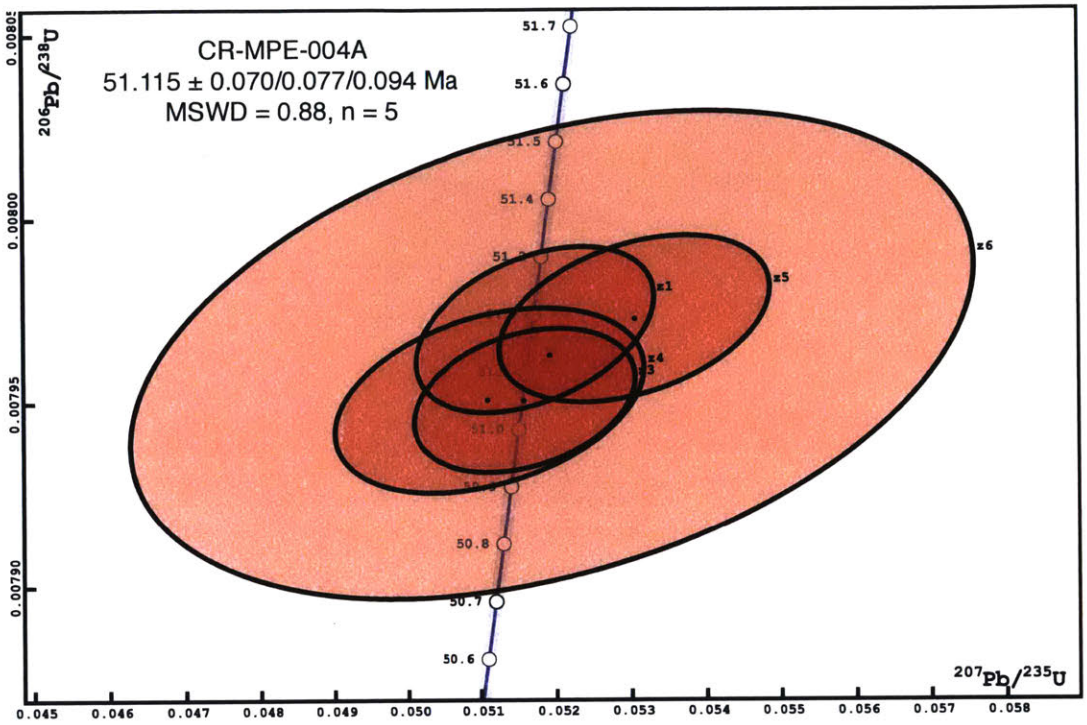
CR-MPE-004A
51.115 ± 0.070/0.077/0.094 Ma
MSWD = 0.88, n = 5
206Pb/238U
207Pb/235U
51.7
51.6
51.5
51.4
50.8
50.7
50.6
z1
z2
z3
z4
z5
z6
0.00805
0.00800
0.00795
0.00790
0.045
0.046
0.047
0.048
0.049
0.050
0.051
0.052
0.053
0.054
0.055
0.056
0.057
0.058

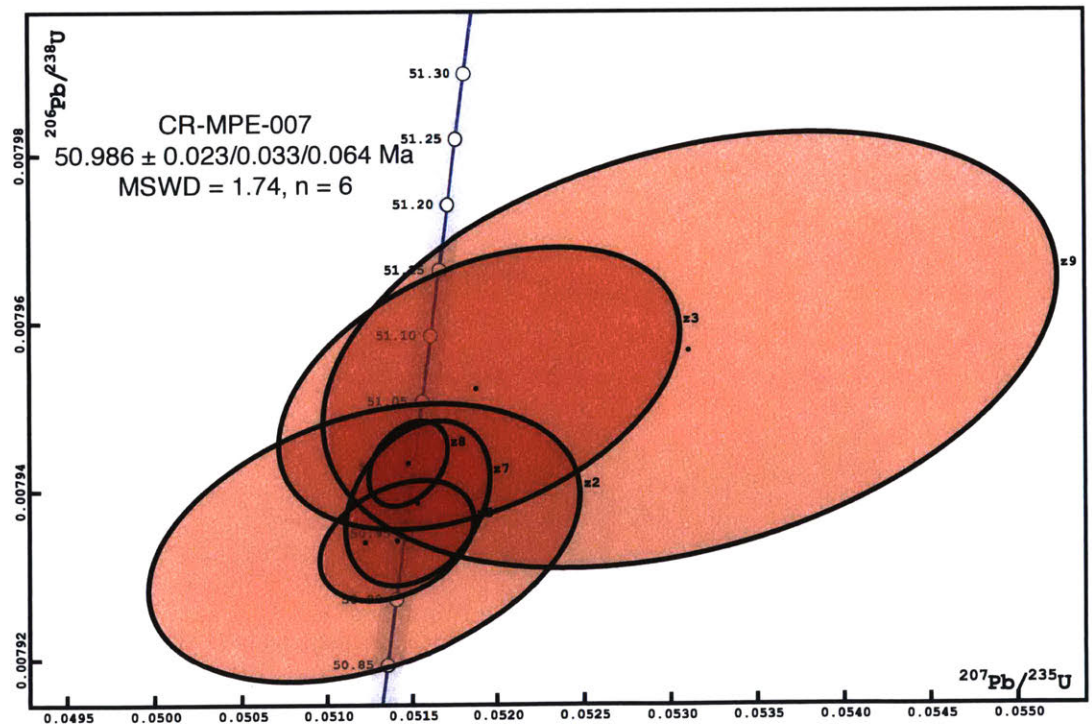
CR-MPE-007
50.986 ± 0.023/0.033/0.064 Ma
MSWD = 1.74, n = 6
206Pb/238U
207Pb/235U
51.30
51.25
51.20
51.10
50.85
z2
z3
z7
z9
0.00798
0.00796
0.00794
0.00792
0.0495
0.0500
0.0505
0.0510
0.0515
0.0520
0.0525
0.0530
0.0535
0.0540
0.0545
0.0550

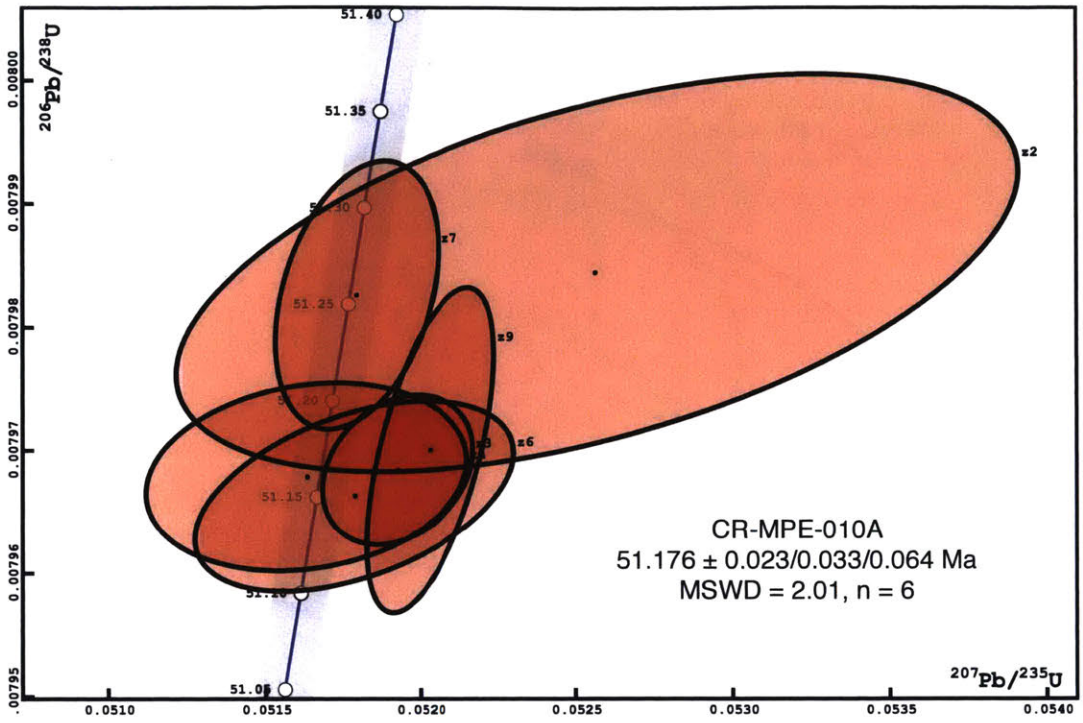
CR-MPE-010A
51.176 ± 0.023/0.033/0.064 Ma
MSWD = 2.01, n = 6
$^{206}Pb/^{238}U$
$^{207}Pb/^{235}U$

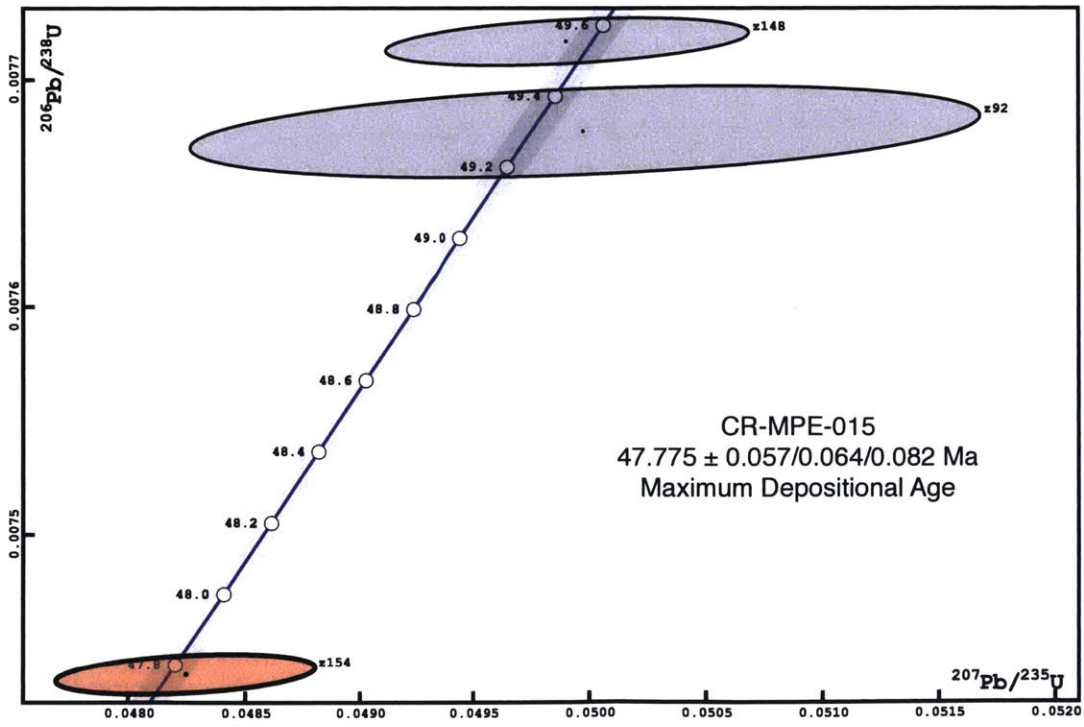
CR-MPE-015
47.775 ± 0.057/0.064/0.082 Ma
Maximum Depositional Age
$^{206}Pb/^{238}U$
$^{207}Pb/^{235}U$

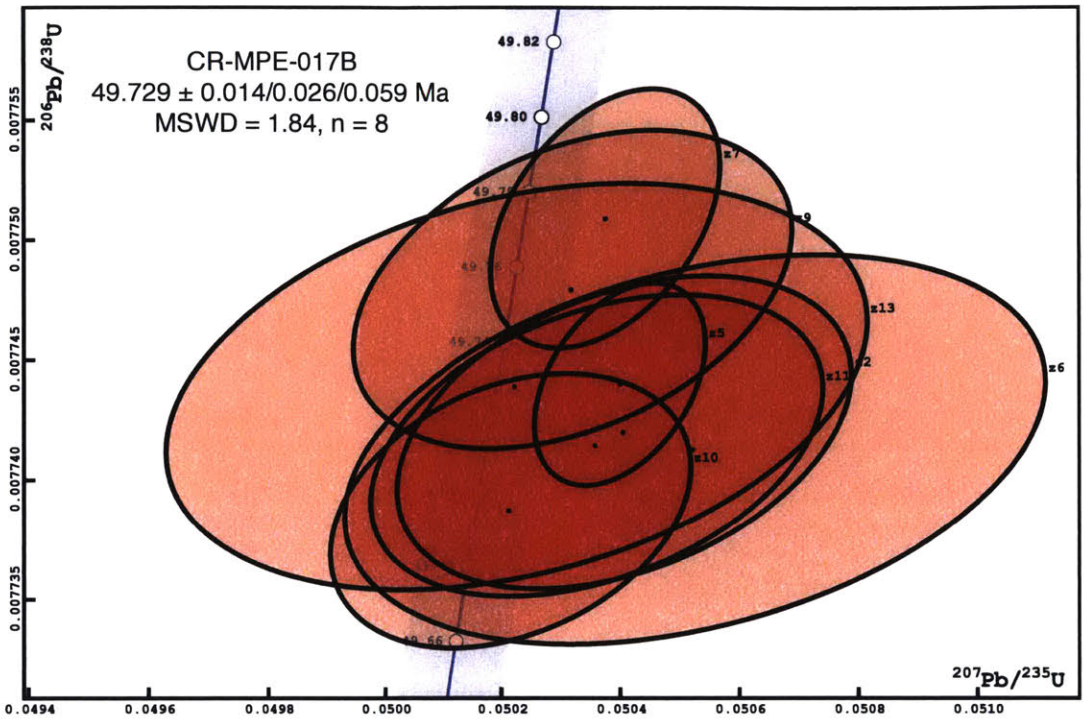
CR-MPE-017B
49.729 ± 0.014/0.026/0.059 Ma
MSWD = 1.84, n = 8
206Pb/238U
207Pb/235U
49.82
49.80
49.66
z7
z9
z13
z5
z6
z10
0.007755
0.007750
0.007745
0.007740
0.007735
0.0494
0.0496
0.0498
0.0500
0.0502
0.0504
0.0506
0.0508
0.0510

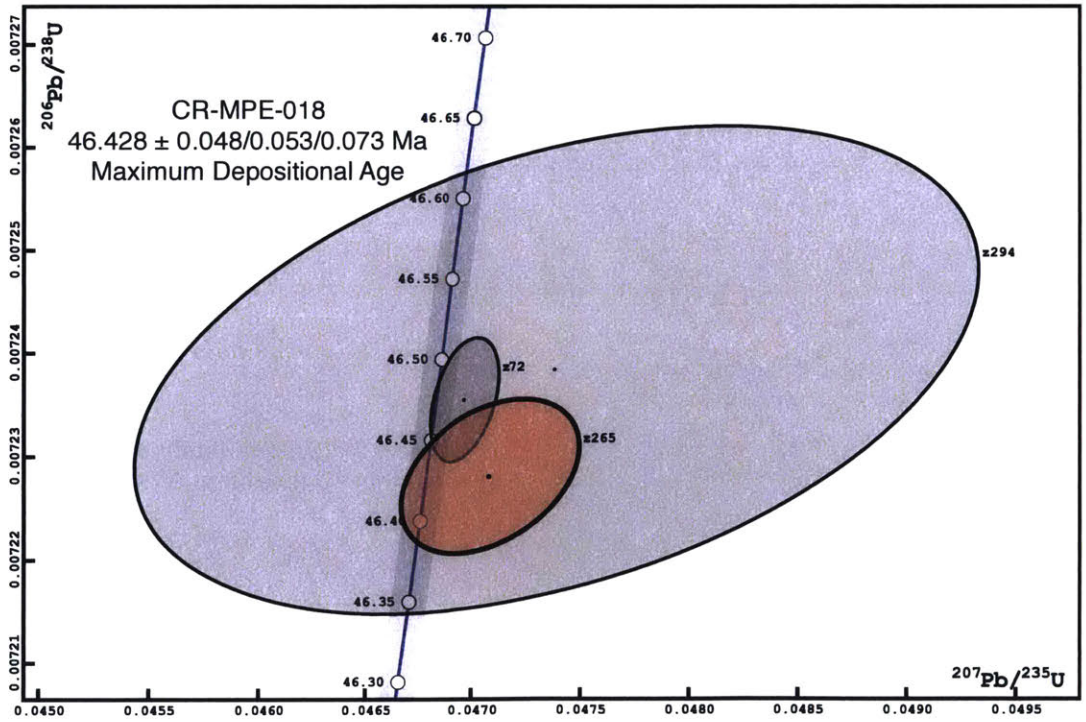
CR-MPE-018
46.428 ± 0.048/0.053/0.073 Ma
Maximum Depositional Age
206Pb/238U
207Pb/235U
46.70
46.65
46.60
46.55
46.50
46.45
46.4
46.35
46.30
z294
z72
z265
0.00727
0.00726
0.00725
0.00724
0.00723
0.00722
0.00721
0.0450
0.0455
0.0460
0.0465
0.0470
0.0475
0.0480
0.0485
0.0490
0.0495

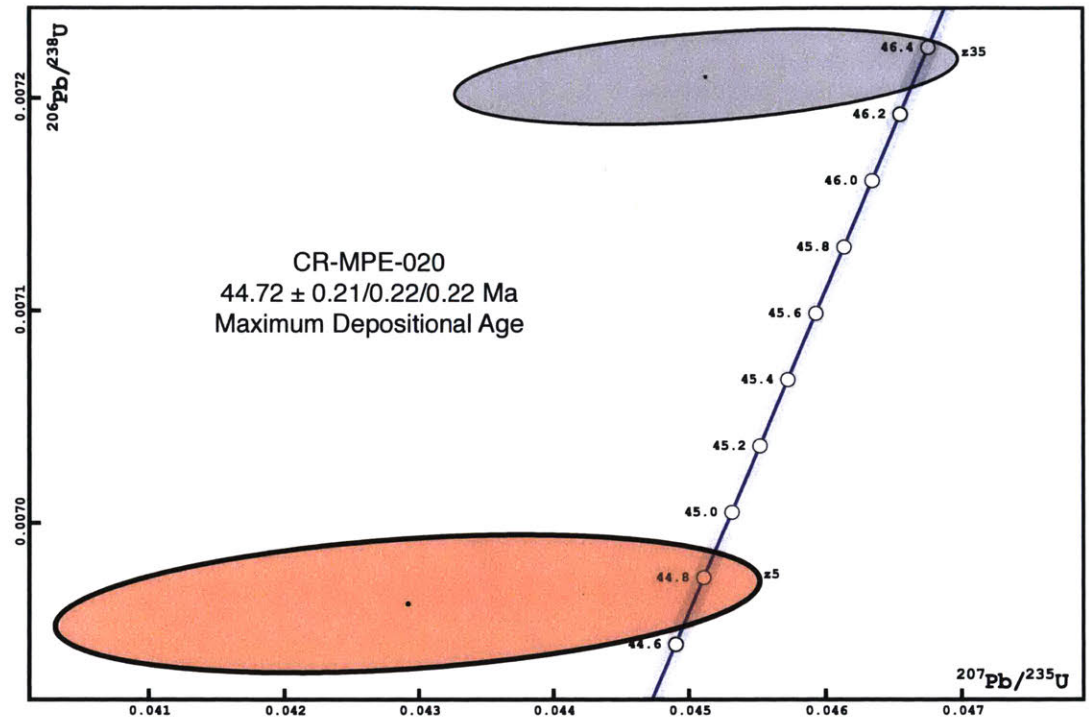
CR-MPE-020
44.72 ± 0.21/0.22/0.22 Ma
Maximum Depositional Age
206Pb/238U
207Pb/235U
0.0072
0.0071
0.0070
0.041
0.042
0.043
0.044
0.045
0.046
0.047
46.4
46.2
46.0
45.8
45.6
45.4
45.2
45.0
44.8
44.6
x35
x5

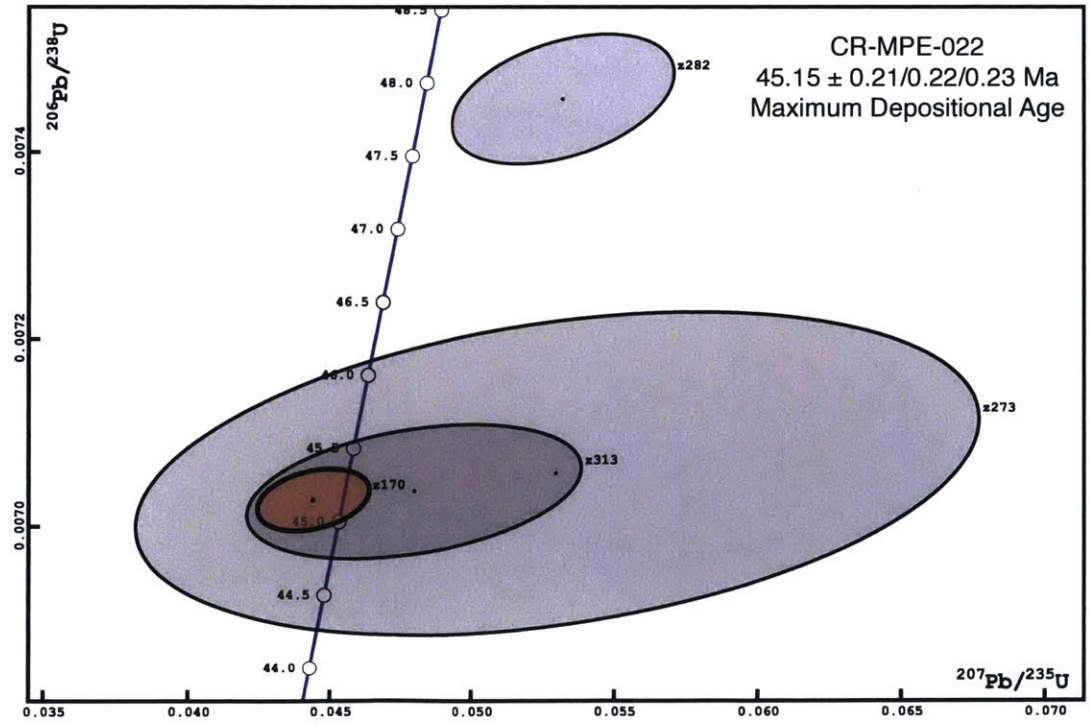
CR-MPE-022
45.15 ± 0.21/0.22/0.23 Ma
Maximum Depositional Age
206Pb/238U
207Pb/235U
0.0074
0.0072
0.0070
0.035
0.040
0.045
0.050
0.055
0.060
0.065
0.070
48.0
47.5
47.0
46.5
46.0
45.5
45.0
44.5
44.0
x282
x273
x313
x170

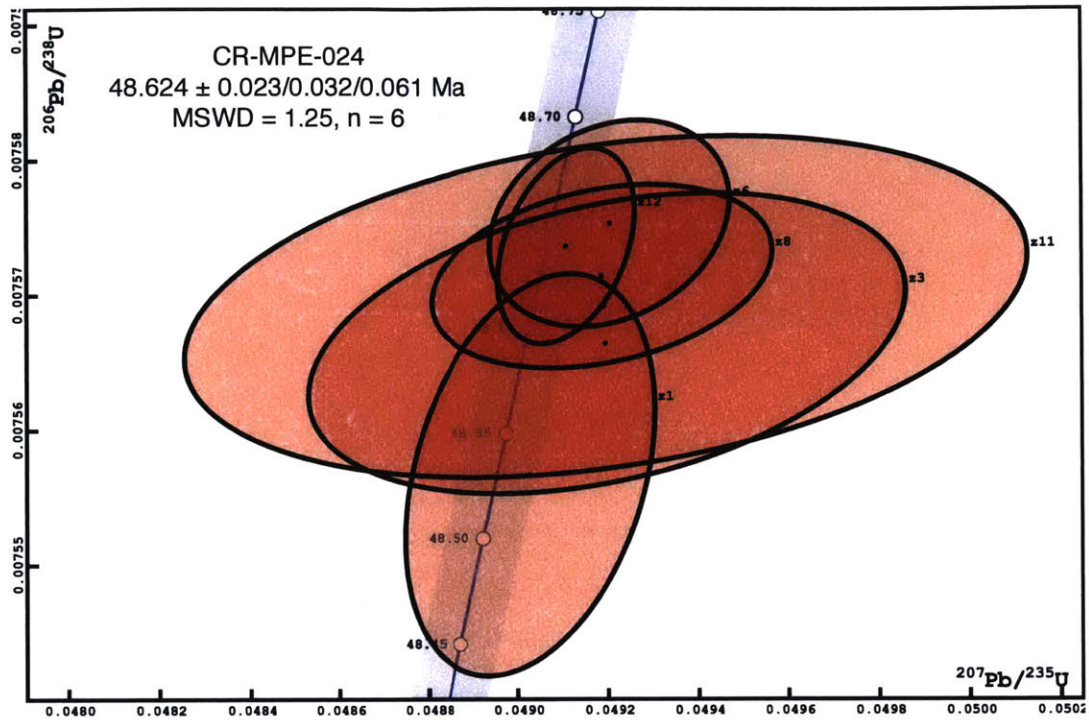
CR-MPE-024
48.624 ± 0.023/0.032/0.061 Ma
MSWD = 1.25, n = 6
$^{206}Pb/^{238}U$
$^{207}Pb/^{235}U$
48.70
48.50
z1
z3
z8
z11
0.00755
0.00756
0.00757
0.00758
0.0480
0.0482
0.0484
0.0486
0.0488
0.0490
0.0492
0.0494
0.0496
0.0498
0.0500

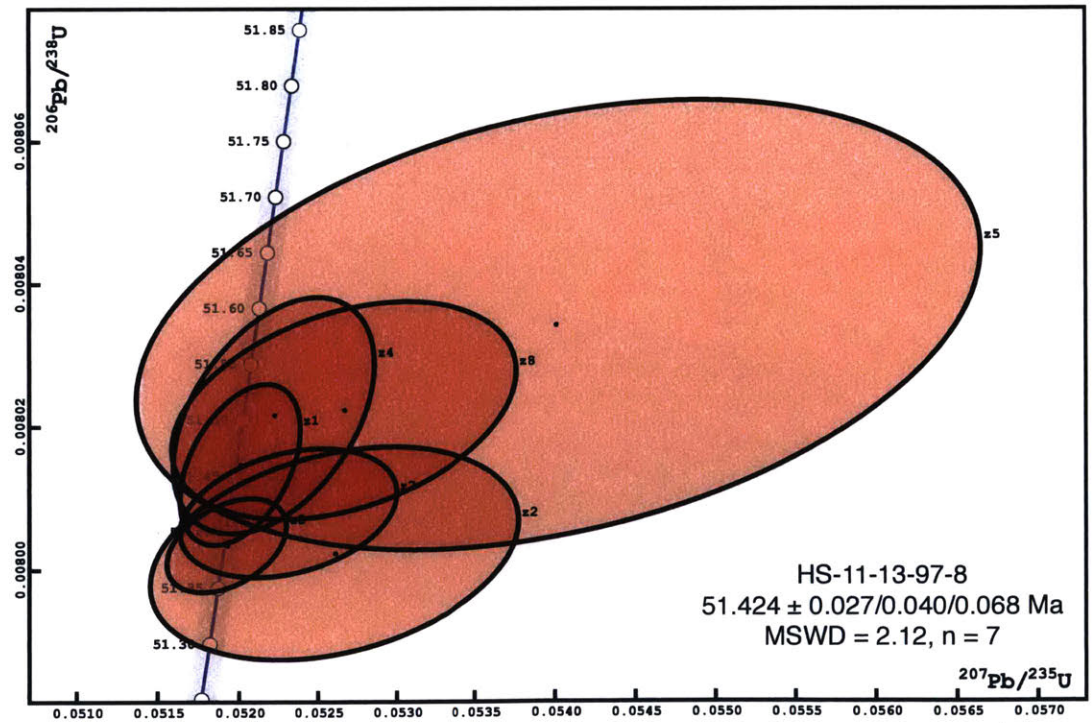
HS-11-13-97-8
51.424 ± 0.027/0.040/0.068 Ma
MSWD = 2.12, n = 7
$^{206}Pb/^{238}U$
$^{207}Pb/^{235}U$
51.85
51.80
51.75
51.70
51.60
z1
z2
z4
z5
z8
0.00800
0.00802
0.00804
0.00806
0.0510
0.0515
0.0520
0.0525
0.0530
0.0535
0.0540
0.0545
0.0550
0.0555
0.0560
0.0565
0.0570

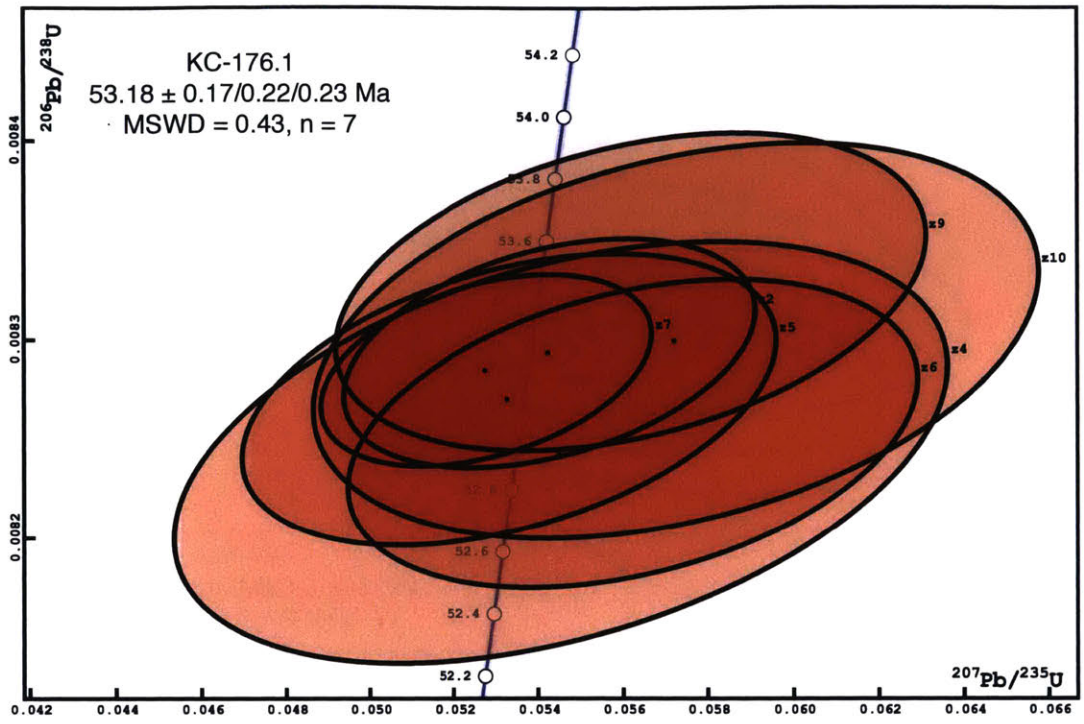
KC-176.1
53.18 ± 0.17/0.22/0.23 Ma
MSWD = 0.43, n = 7
206Pb/238U
207Pb/235U
54.2
54.0
53.8
53.6
52.6
52.4
52.2
z9
z10
z7
z5
z4
z6
0.0084
0.0083
0.0082
0.042
0.044
0.046
0.048
0.050
0.052
0.054
0.056
0.058
0.060
0.062
0.064
0.066

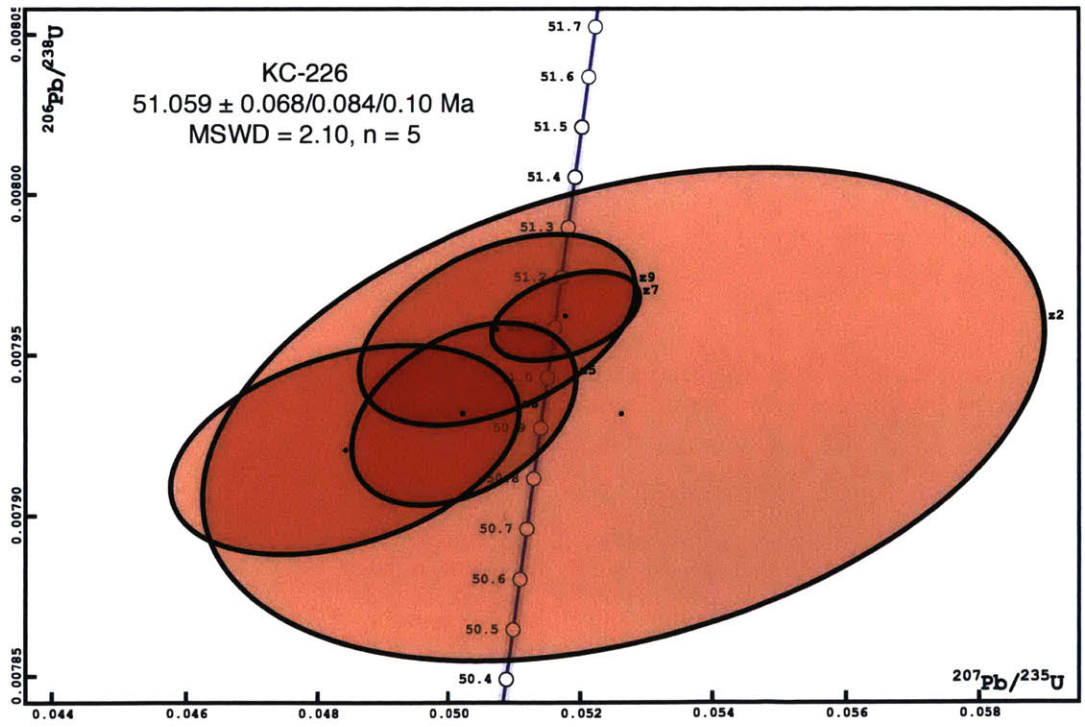
KC-226
51.059 ± 0.068/0.084/0.10 Ma
MSWD = 2.10, n = 5
206Pb/238U
207Pb/235U
51.7
51.6
51.5
51.4
51.3
50.7
50.6
50.5
50.4
z9
z7
z2
0.00800
0.00795
0.00790
0.00785
0.044
0.046
0.048
0.050
0.052
0.054
0.056
0.058

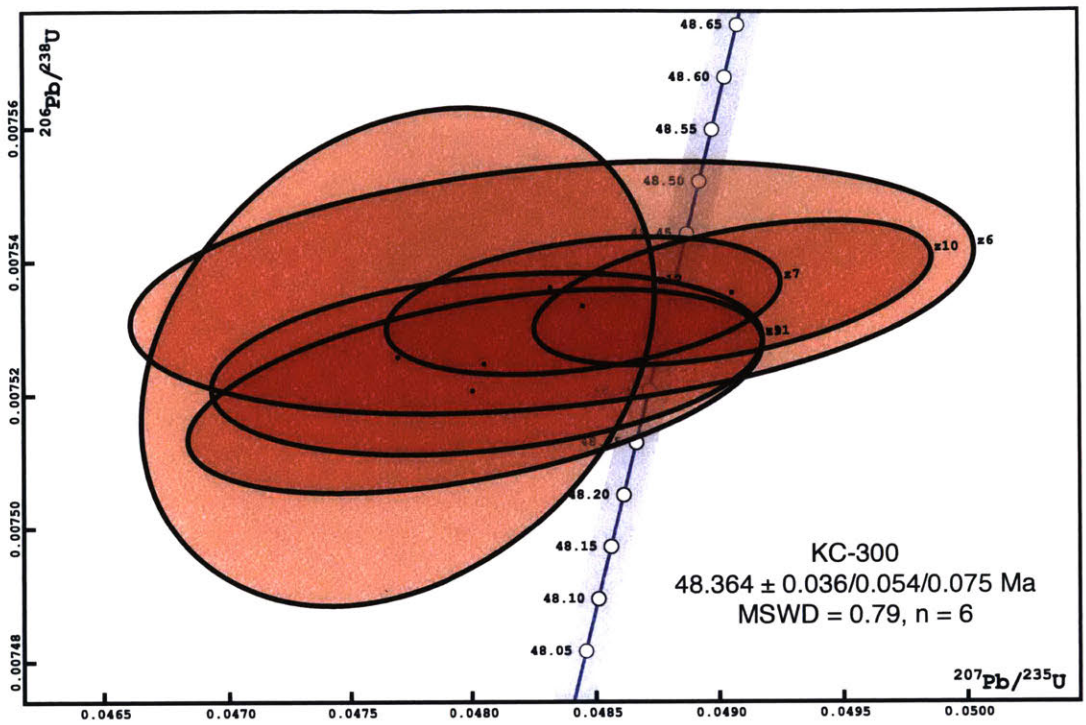
$^{206}Pb/^{238}U$
0.00756
0.00754
0.00752
0.00750
0.00748
48.65
48.60
48.55
48.50
48.20
48.15
48.10
48.05
x10
x6
x7
x1
KC-300
48.364 ± 0.036/0.054/0.075 Ma
MSWD = 0.79, n = 6
$^{207}Pb/^{235}U$
0.0465
0.0470
0.0475
0.0480
0.0485
0.0490
0.0495
0.0500

Table 1: U-Pb Zircon CA-ID-TIMS Geochronology Results

Sample	Lat. (°N)	Long. (°W)	Lithology	Th-corrected $^{206}Pb/^{238}U$ Date (Ma)*, †	Interpretation
Metchosin complex					
CR-MPE-004A	48.33886	123.71416	Quartz Diorite	51.115 ± 0.070/0.077/0.094 (MSWD=0.88, n=5)	
CR-MPE-007	48.35397	123.68497	Plagiogranite	50.986 ± 0.023/0.033/0.064 (MSWD=1.74, n=6)	Emplacement age
CR-MPE-010A	48.37499	123.75426	Gabbro	51.176 ± 0.023/0.033/0.064 (MSWD=2.01, n=6)	Emplacemnt age
Bremerton complex					
CR-MPE-003	47.59377	122.79125	Gabbro	50.075 ± 0.016/0.027/0.060 (MSWD=1.74, n=6)	Emplacement age
BH07	47.53390	122.78248	Andesitic Dike	48.209 ± 0.057/0.068/0.085 (MSWD=0.78, n=9)	
Black Hills basalt					
CR-MPE-017B	47.13748	123.14439	Silicic tuff	49.729 ± 0.014/0.026/0.059 (MSWD=1.84, n=8)	Eruption age
Blue Mountain unit					
CR-MPE-015	47.51211	123.34895	Sandstone	47.775 ± 0.057/0.064/0.082	MDA#
CR-MPE-018	47.97032	123.11235	Sandstone	46.428 ± 0.048/0.053/0.073	MDA#
CR-MPE-020	47.89255	123.12283	Sandstone	44.72 ± 0.21 /0.22 /0.22	MDA#
CR-MPE-022	47.94748	123.22704	Sandstone	45.15 ± 0.21 /0.22 /0.23	MDA#
Crescent Formation					
KC-176.1§	47.46661	123.28426	Silicic tuff	53.18 ± 0.17 /0.22 /0.23 (MSWD=0.43, n=7)	Eruption age
KC-226§	47.44855	123.28672	Silicic tuff	51.059 ± 0.068/0.084/0.10 (MSWD=2.10, n=5)	Eruption age
HS-11-13-97-8§	48.00833	123.12056	Rhyolite	51.424 ± 0.027/0.040/0.068 (MSWD=2.12, n=7)	Eruption age
KC-300§	47.29864	123.38645	Silicic tuff	48.364 ± 0.036/0.054/0.075 (MSWD=0.79, n=6)	Eruption age
CR-MPE-024	47.38776	123.60406	Gabbro	48.624 ± 0.023/0.032/0.061 (MSWD=1.25, n=6)	Emplacement age

* Th correction was done using $[Th/U]_{Magma}=2.8 \pm 1$ (2σ) for silicic volcanic rocks and $[Th/U]_{Magma}=3.2 \pm 1$ (2σ) for gabbro, quartz diorite, and plagiogranite.

† Uncertainties are reported in the format ±X/Y/Z where X is the analytical uncertainty, Y includes uncertainty in the EARTHTIME ^{205}Pb-^{235}U-^{238}U isotopic tracer and Z includes uncertainty in the ^{238}U decay constant.

§ Latitude and longitude for these samples is estimated from marked positions on 1:24,000-scale topographic maps. All other samples were collected with a GPS.

MDA – Maximum depositional age

TABLE A1: CA-ID-TIMS U-Pb ZIRCON GEOCHRONOLOGY RESULTS

Frac.	Dates $^{206}Pb/^{238}U^{*,\dagger}$	2σ abs.	$^{207}Pb/^{235}U^{\dagger}$	2σ abs.	$^{207}Pb/^{206}Pb^{*,\dagger}$	2σ abs.	% Disc.§	Corr. Coef.	Composition Th/U#	Pb_c (pg)**	Pb*/Pb_c††	Isotopic Ratios $^{206}Pb/^{204}Pb$§§	$^{208}Pb/^{206}Pb$##	$^{206}Pb/^{238}U^{*,\#\#}$	2σ %	$^{207}Pb/^{235}U$##	2σ %	$^{207}Pb/^{206}Pb^{*,\#\#}$	2σ %
BH07																			
z1	48.24	0.20	47.2	2.5	-3	130	-2518	0.336	0.39	0.32	4.2	278	0.125	0.007512	0.41	0.0476	5.5	0.046012	5.3
z2	48.17	0.49	48.4	6.6	58	330	23	0.333	0.49	1.80	1.6	112	0.158	0.007500	1.0	0.0488	14	0.047195	14
z3	48.27	0.64	48.8	8.1	77	400	40	0.340	0.63	0.77	1.3	93	0.202	0.007516	1.3	0.0493	17	0.047568	17
z5	48.33	0.19	49.7	2.4	116	110	60	0.356	0.54	1.02	4.4	277	0.172	0.007526	0.40	0.0502	4.9	0.048364	4.8
z6	48.35	0.24	50.0	3.1	132	150	65	0.328	0.53	2.12	3.3	210	0.168	0.007528	0.50	0.0505	6.3	0.048686	6.2
z8	48.32	0.37	47.9	1.5	25	73	-63	0.341	0.57	0.47	9.8	592	0.182	0.007523	0.78	0.0483	3.2	0.046552	3.0
z10	48.06	0.19	48.2	2.5	53	120	17	0.349	0.57	0.48	4.2	261	0.182	0.007484	0.41	0.0486	5.4	0.047105	5.2
z11	48.204	0.092	48.3	1.1	53	54	16	0.384	0.50	0.31	9.7	594	0.160	0.007506	0.19	0.0487	2.3	0.047096	2.2
z12	48.17	0.12	47.9	1.4	33	70	-29	0.389	0.53	0.63	7.7	473	0.171	0.007500	0.24	0.0483	3.0	0.046699	2.9
CR-MPE-003																			
z1	50.070	0.031	49.97	0.27	45	13	-1	0.275	0.70	0.25	48.4	2751	0.225	0.007797	0.063	0.05045	0.56	0.046943	0.54
z3	50.082	0.039	50.11	0.30	51	14	9	0.431	0.79	0.21	44.9	2499	0.253	0.007799	0.078	0.05059	0.61	0.047062	0.58
z4	50.093	0.040	50.03	0.34	47	16	1	0.349	0.77	0.22	39.9	2230	0.247	0.007801	0.081	0.05050	0.69	0.046973	0.67
z5	50.086	0.037	50.15	0.14	53.4	6.4	13	0.441	0.83	0.44	109.2	5994	0.265	0.007800	0.074	0.05063	0.29	0.047104	0.27
z6	50.64	0.18	50.8	2.3	57	110	18	0.381	0.70	1.40	5.0	301	0.225	0.007887	0.36	0.0513	4.6	0.047180	4.5
z7	50.165	0.098	50.4	1.1	61	52	23	0.326	0.76	1.07	10.2	586	0.244	0.007812	0.20	0.0509	2.3	0.047253	2.2
z8	50.042	0.033	50.03	0.19	49.7	8.6	7	0.429	0.68	0.35	70.0	3992	0.218	0.007793	0.067	0.05051	0.38	0.047030	0.36
CR-MPE-004A																			
z1	51.17	0.14	51.2	1.5	52	71	10	0.405	0.51	0.42	7.5	465	0.162	0.007970	0.28	0.0517	3.1	0.047085	3.0
z3	51.05	0.12	51.1	1.4	52	67	9	0.318	0.52	0.75	7.8	482	0.165	0.007951	0.25	0.0516	2.9	0.047070	2.8
z4	51.05	0.16	50.6	2.0	29	95	-52	0.356	0.55	0.50	5.6	348	0.175	0.007951	0.32	0.0511	4.1	0.046632	4.0
z5	51.19	0.14	52.5	1.7	112	78	56	0.381	0.80	0.49	6.9	396	0.257	0.007973	0.28	0.0531	3.4	0.048288	3.3
z6	51.13	0.42	51.4	5.5	64	250	26	0.372	0.48	0.40	2.0	138	0.153	0.007963	0.83	0.0519	11	0.047318	11
CR-MPE-007																			
z2	50.94	0.11	50.7	1.2	40	57	-17	0.349	1.14	0.71	10.4	548	0.364	0.007934	0.21	0.0512	2.5	0.046846	2.4
z3	51.06	0.11	51.4	1.1	66	52	27	0.407	0.53	0.27	10.7	648	0.169	0.007952	0.21	0.0519	2.3	0.047344	2.2
z5	50.945	0.046	50.91	0.44	49	21	4	0.354	0.91	0.24	29.6	1606	0.291	0.007934	0.090	0.05141	0.89	0.047019	0.86
z7	50.973	0.063	51.03	0.41	53	19	10	0.330	1.18	0.30	36.9	1878	0.376	0.007939	0.12	0.05154	0.83	0.047105	0.80
z8	51.003	0.032	50.97	0.22	49	10	5	0.367	0.64	0.28	53.4	3084	0.205	0.007943	0.064	0.05148	0.45	0.047024	0.43
z9	51.09	0.17	52.5	2.1	119	92	58	0.335	1.08	0.29	6.0	329	0.344	0.007957	0.33	0.0531	4.0	0.048430	3.9
CR-MPE-010A																			
z2	51.27	0.10	52.0	1.3	87	59	43	0.517	0.87	0.26	11.4	638	0.277	0.007984	0.20	0.0526	2.6	0.047768	2.5
z3	51.164	0.039	51.40	0.24	63	11	22	0.285	1.10	0.32	55.1	2848	0.351	0.007968	0.076	0.05193	0.47	0.047284	0.45
z4	51.161	0.049	51.12	0.50	49	24	3	0.185	0.88	0.32	26.7	1459	0.282	0.007968	0.096	0.05164	1.0	0.047022	0.99
z6	51.151	0.049	51.27	0.50	57	23	15	0.466	0.97	0.37	25.8	1382	0.309	0.007966	0.097	0.05179	0.99	0.047170	0.95
z7	51.255	0.069	51.28	0.26	52	11	8	0.353	0.91	0.51	58.3	3147	0.291	0.007983	0.14	0.05180	0.51	0.047081	0.48
z9	51.174	0.085	51.50	0.20	66.9	7.8	27	0.599	1.39	0.30	113.4	5471	0.445	0.007970	0.17	0.05203	0.40	0.047371	0.33
CR-MPE-015																			
z92	49.30	0.13	49.5	1.7	60	79	23	0.354	0.46	0.61	6.3	395	0.146	0.007677	0.26	0.0500	3.4	0.047230	3.3
z148	49.555	0.067	49.44	0.76	44	37	-2	0.393	0.38	0.45	14.2	892	0.121	0.007717	0.14	0.04990	1.6	0.046919	1.5
z154	47.775	0.057	47.84	0.54	51	27	15	0.354	0.36	0.20	19.9	1246	0.115	0.007439	0.12	0.04825	1.2	0.047063	1.1
CR-MPE-017B																			
z2	49.716	0.042	49.93	0.37	60	18	24	0.375	0.33	0.91	27.6	1738	0.106	0.007742	0.084	0.05040	0.76	0.047240	0.73
z5	49.729	0.027	49.93	0.14	59.4	6.4	23	0.413	0.33	0.33	77.3	4834	0.107	0.007744	0.055	0.05040	0.29	0.047223	0.27
z6	49.711	0.052	50.05	0.57	66	27	30	0.353	0.33	0.30	17.8	1130	0.106	0.007741	0.11	0.05052	1.2	0.047355	1.1

z7	49.773	0.035	49.90	0.19	56.2	8.6	18	0.420	0.36	0.32	59.9	3718	0.116	0.007751	0.070	0.05038	0.38	0.047158	0.36
z9	49.754	0.042	49.85	0.36	54	17	16	0.379	0.35	0.36	29.6	1851	0.112	0.007748	0.086	0.05032	0.74	0.047122	0.71
z10	49.695	0.037	49.75	0.30	52	14	13	0.322	0.35	0.36	36.9	2304	0.113	0.007739	0.074	0.05021	0.61	0.047080	0.59
z11	49.712	0.040	49.89	0.37	58	17	21	0.384	0.34	0.84	28.6	1801	0.107	0.007741	0.081	0.05036	0.76	0.047200	0.73
z13	49.728	0.054	49.76	0.57	51	27	11	0.325	0.32	0.49	18.2	1157	0.104	0.007744	0.11	0.05022	1.2	0.047057	1.1
CR-MPE-018																			
z72	46.475	0.039	46.60	0.16	53.2	7.6	20	0.412	0.37	0.18	69.5	4302	0.120	0.007235	0.083	0.04697	0.34	0.047099	0.32
z265	46.428	0.048	46.71	0.40	61	20	30	0.394	0.42	0.25	27.5	1689	0.134	0.007228	0.10	0.04708	0.88	0.047263	0.84
z294	46.49	0.15	47.0	1.9	73	95	40	0.409	0.54	0.22	5.7	351	0.174	0.007238	0.33	0.0474	4.1	0.047497	4.0
CR-MPE-020																			
z5	44.72	0.21	42.7	2.5	-71	140	167	0.330	0.41	0.33	3.8	251	0.132	0.006962	0.47	0.0429	6.1	0.044734	5.9
z35	46.31	0.14	44.8	1.8	-35	97	255	0.372	0.40	0.34	5.5	356	0.127	0.007210	0.31	0.0451	4.1	0.045411	4.0
CR-MPE-022																			
z170	45.15	0.21	44.1	1.9	-12	100	736	0.314	0.42	0.27	5.1	327	0.136	0.007029	0.47	0.0444	4.5	0.045837	4.3
z273	45.3	1.1	52	14	389	610	88	0.337	0.64	0.51	0.7	58	0.205	0.007057	2.4	0.053	28	0.054452	27
z282	47.89	0.45	52.6	3.8	275	160	83	0.404	0.55	0.39	3.5	222	0.178	0.007457	0.93	0.0532	7.3	0.051778	7.0
z313	45.21	0.46	47.6	5.7	168	280	74	0.356	0.46	0.53	1.7	120	0.147	0.007037	1.0	0.0480	12	0.049442	12
CR-MPE-024																			
z1	48.530	0.095	48.60	0.27	52	13	-2	0.422	5.66	0.23	100.1	2529	1.805	0.007557	0.20	0.04903	0.57	0.047075	0.54
z3	48.593	0.071	48.76	0.64	57	31	17	0.380	2.41	0.24	26.1	1046	0.770	0.007566	0.15	0.04920	1.4	0.047176	1.3
z6	48.650	0.049	48.77	0.26	55	12	10	0.381	3.54	0.31	75.9	2515	1.131	0.007575	0.10	0.04921	0.54	0.047131	0.52
z8	48.625	0.043	48.75	0.37	55	18	15	0.338	2.11	0.50	41.0	1725	0.673	0.007571	0.090	0.04919	0.77	0.047138	0.75
z11	48.610	0.081	48.76	0.91	56	44	16	0.323	2.30	0.40	17.7	728	0.736	0.007569	0.17	0.04919	1.9	0.047156	1.9
z12	48.639	0.046	48.68	0.15	50.7	6.9	4	0.513	3.09	0.30	151.6	5358	0.987	0.007574	0.096	0.04911	0.31	0.047049	0.29
HS-11-13-97-8																			
z1	51.460	0.072	51.49	0.36	53	16	9	0.442	0.55	0.21	36.6	2166	0.177	0.008015	0.14	0.05201	0.72	0.047089	0.67
z2	51.381	0.095	52.1	1.1	84	51	42	0.311	0.50	0.21	10.7	653	0.161	0.008002	0.19	0.0526	2.2	0.047706	2.2
z3	51.388	0.042	51.40	0.36	52	16	9	0.418	0.59	0.20	33.6	1971	0.189	0.008003	0.082	0.05193	0.72	0.047078	0.68
z4	51.50	0.11	51.69	0.61	60	27	20	0.438	0.53	0.20	25.9	1548	0.170	0.008022	0.21	0.05223	1.2	0.047243	1.1
z5	51.59	0.20	53.4	2.5	136	110	63	0.339	0.53	0.72	4.3	269	0.169	0.008034	0.39	0.0540	4.9	0.048776	4.8
z7	51.417	0.058	51.78	0.66	69	30	29	0.315	0.58	0.24	17.0	1011	0.186	0.008008	0.11	0.05232	1.3	0.047406	1.3
z8	51.509	0.097	52.1	1.0	80	47	39	0.365	0.54	0.26	11.0	667	0.174	0.008022	0.19	0.0527	2.1	0.047641	2.0
KC-176.1																			
z2	53.24	0.37	53.6	4.7	71	210	29	0.380	0.50	0.22	2.5	167	0.158	0.008293	0.70	0.0542	9.0	0.047458	8.7
z4	52.92	0.68	53.9	8.8	96	390	47	0.413	0.42	0.28	1.3	98	0.134	0.008243	1.3	0.0545	17	0.047958	16
z5	53.09	0.47	52.7	6.1	35	280	-35	0.407	0.41	0.18	1.9	135	0.131	0.008270	0.89	0.0533	12	0.046743	12
z6	52.98	0.50	55.5	6.5	166	270	69	0.356	0.46	0.33	1.8	126	0.148	0.008253	0.94	0.0562	12	0.049408	12
z7	53.19	0.31	52.2	3.8	7	170	-378	0.386	0.48	0.31	3.3	218	0.153	0.008285	0.58	0.0528	7.4	0.046201	7.2
z9	53.44	0.51	55.5	6.7	144	280	64	0.356	0.40	0.26	1.7	122	0.129	0.008324	0.96	0.0561	12	0.048944	12
z10	53.28	0.64	56.5	8.2	195	340	73	0.352	0.58	0.93	1.4	99	0.185	0.008299	1.2	0.0572	15	0.050017	15
KC-226																			
z2	50.93	0.49	52.1	6.1	105	280	53	0.341	0.61	0.53	1.8	123	0.196	0.007932	0.97	0.0526	12	0.048139	12
z5	50.93	0.18	49.8	1.6	-6	79	2784	0.380	0.55	0.27	7.8	478	0.177	0.007932	0.36	0.0502	3.4	0.045951	3.3
z7	51.123	0.089	51.3	1.1	58	50	17	0.428	0.68	0.21	11.8	689	0.219	0.007962	0.17	0.0518	2.2	0.047189	2.1
z8	50.86	0.21	48.0	2.6	-92	130	158	0.361	0.62	0.19	4.5	276	0.199	0.007920	0.41	0.0484	5.5	0.044361	5.4
z9	51.10	0.19	50.3	2.0	10	96	-253	0.439	0.54	0.21	6.0	369	0.174	0.007958	0.37	0.0507	4.1	0.046264	4.0
KC-300																			
z6	48.40	0.12	47.9	1.7	24	83	-72	0.296	0.57	0.18	7.3	443	0.182	0.007536	0.25	0.0483	3.5	0.046523	3.5
z7	48.381	0.066	48.04	0.78	31	39	-40	0.355	0.96	0.16	16.1	871	0.308	0.007533	0.14	0.04845	1.7	0.046666	1.6
z9	48.326	0.087	47.7	1.1	14	55	-160	0.279	0.53	0.17	10.3	629	0.168	0.007525	0.18	0.0481	2.3	0.046338	2.3

z10	48.394	0.069	48.63	0.78	60	37	25	0.494	0.41	0.20	15.2	944	0.132	0.007535	0.14	0.04906	1.6	0.047237	1.6
z11	48.300	0.097	47.6	1.1	13	56	-172	0.478	0.42	0.16	10.0	627	0.136	0.007521	0.20	0.0480	2.4	0.046318	2.3
z12	48.33	0.24	47.3	1.0	-4	51	-13084	0.264	0.46	0.24	11.5	709	0.149	0.007526	0.50	0.0477	2.2	0.045987	2.1

* Corrected for initial Th/U disequilibrium using radiogenic ^{208}Pb and $Th/U_{[Magma]} = 3.2 \pm 1$ (2σ) for mafic intrusive rocks and $Th/U_{[Magma]} = 2.8 \pm 1$ (2σ) for silicic volcanic rocks.
† Isotopic dates calculated using the decay constants λ238 = 1.55125E-10 and λ235 = 9.8485E-10 (Jaffey et al. 1971).
§ % discordance = 100 - (100 * ($^{206}Pb/^{238}U$ date) / ($^{207}Pb/^{206}Pb$ date))
# Th contents calculated from radiogenic ^{208}Pb and the $^{207}Pb/^{206}Pb$ date of the sample, assuming concordance between U-Th and Pb systems.
** Total mass of common Pb.
†† Ratio of radiogenic Pb (including ^{208}Pb) to common Pb.
§§ Measured ratio corrected for fractionation and spike contribution only.
Measured ratios corrected for fractionation, tracer and blank.

TABLE A2: LA-ICP-MS U-Pb Zircon Geochronology Results for CR-MPE-015

Zircon #	Composition U (ppm)	$^{206}Pb/^{204}Pb$	U/Th	$^{206}Pb/^{207}Pb$	2σ (%)	$^{207}Pb/^{235}U$	2σ (%)	$^{206}Pb/^{238}U$	2σ (%)	Corr.	Ages $^{206}Pb/^{238}U$	2σ (Ma)	$^{207}Pb/^{235}U$	2σ (Ma)	$^{206}Pb/^{207}Pb$	2σ (Ma)	Best Age	2σ (Ma)
238	324	450	2.0	63.2456	109.7	0.0155	109.7	0.0071	1.9	0.02	45.7	0.9	15.6	17.0	0.0	0.0	45.7	0.9
67	142	490	3.1	58.6431	18.4	0.0173	18.6	0.0073	2.7	0.15	47.2	1.3	17.4	3.2	0.0	1222.5	47.2	1.3
285	412	3023	2.1	22.9459	2.1	0.0445	3.1	0.0074	2.3	0.75	47.6	1.1	44.2	1.3	134.3	51.1	47.6	1.1
287	909	14296	2.6	21.3650	1.1	0.0478	2.2	0.0074	1.9	0.87	47.6	0.9	47.4	1.0	39.3	25.6	47.6	0.9
266	514	11528	1.5	21.3895	1.5	0.0481	2.5	0.0075	2.0	0.81	47.9	1.0	47.7	1.2	36.6	35.0	47.9	1.0
154	320	35321	2.8	20.0969	1.8	0.0513	3.1	0.0075	2.5	0.81	48.0	1.2	50.8	1.5	183.7	42.8	48.0	1.2
12	498	6941	2.3	21.3657	1.6	0.0485	3.1	0.0075	2.7	0.86	48.3	1.3	48.1	1.5	39.3	38.0	48.3	1.3
83	839	9379	1.9	21.6584	1.4	0.0479	2.5	0.0075	2.1	0.84	48.4	1.0	47.5	1.2	6.6	32.7	48.4	1.0
71	197	799	2.5	33.5249	7.7	0.0313	8.0	0.0076	2.4	0.29	48.9	1.2	31.3	2.5	1176.5	237.6	48.9	1.2
19	795	16677	2.2	20.5334	1.1	0.0514	1.8	0.0076	1.4	0.80	49.1	0.7	50.9	0.9	133.5	25.5	49.1	0.7
64	296	1250	4.2	25.4372	8.7	0.0416	9.0	0.0077	2.3	0.26	49.3	1.1	41.4	3.6	395.9	226.6	49.3	1.1
151	992	22952	1.8	20.5780	1.1	0.0518	2.0	0.0077	1.6	0.82	49.7	0.8	51.3	1.0	128.4	26.8	49.7	0.8
65	1231	7894	1.5	21.5274	1.0	0.0500	2.3	0.0078	2.0	0.89	50.1	1.0	49.6	1.1	21.2	25.0	50.1	1.0
22	295	2807	5.7	22.7128	3.3	0.0476	4.0	0.0078	2.1	0.54	50.3	1.1	47.2	1.8	109.1	82.3	50.3	1.1
250	1159	9601	2.0	21.6775	0.9	0.0499	2.0	0.0078	1.7	0.89	50.4	0.9	49.4	0.9	4.5	21.3	50.4	0.9
92	1744	287588	1.7	20.6294	1.0	0.0526	2.1	0.0079	1.8	0.87	50.5	0.9	52.0	1.1	122.5	24.2	50.5	0.9
45	1037	4823	0.9	20.1891	3.0	0.0537	3.8	0.0079	2.4	0.62	50.5	1.2	53.2	2.0	173.1	70.0	50.5	1.2
148	1013	21091	1.7	20.8164	1.2	0.0522	2.1	0.0079	1.8	0.82	50.6	0.9	51.7	1.1	101.2	28.7	50.6	0.9
280	2242	16653	1.4	19.6113	1.4	0.0555	3.0	0.0079	2.7	0.88	50.7	1.3	54.9	1.6	240.4	32.4	50.7	1.3
244	1443	9247	1.8	21.8872	1.2	0.0498	2.2	0.0079	1.9	0.84	50.8	1.0	49.3	1.1	18.8	29.4	50.8	1.0
237	830	142752	2.8	18.8728	1.5	0.0579	2.4	0.0079	1.9	0.79	50.9	1.0	57.1	1.3	328.2	33.0	50.9	1.0
225	1245	66489	0.8	20.9016	0.9	0.0523	2.0	0.0079	1.8	0.90	50.9	0.9	51.7	1.0	91.5	21.3	50.9	0.9
74	1025	19339	2.0	20.8641	1.0	0.0524	2.2	0.0079	2.0	0.89	51.0	1.0	51.9	1.1	95.8	23.7	51.0	1.0
50	223	1886	2.1	25.8981	9.0	0.0423	9.3	0.0079	2.3	0.25	51.0	1.2	42.0	3.8	442.9	238.1	51.0	1.2
241	1140	22172	1.4	20.7764	1.0	0.0529	2.1	0.0080	1.8	0.87	51.2	0.9	52.3	1.1	105.7	24.8	51.2	0.9
289	986	45255	2.7	20.5538	1.1	0.0536	2.7	0.0080	2.5	0.91	51.3	1.3	53.0	1.4	131.1	26.0	51.3	1.3
78	511	4128	1.1	22.6662	1.5	0.0488	2.8	0.0080	2.4	0.85	51.5	1.2	48.3	1.3	104.0	36.4	51.5	1.2
25	634	4085	2.7	22.1322	1.6	0.0502	2.4	0.0081	1.8	0.74	51.7	0.9	49.7	1.2	45.7	39.9	51.7	0.9
59	1243	13747	2.2	21.1436	1.1	0.0526	2.3	0.0081	2.0	0.88	51.8	1.1	52.0	1.2	64.2	26.6	51.8	1.1
307	1969	19380	1.3	20.8238	0.9	0.0535	2.1	0.0081	1.9	0.91	51.9	1.0	52.9	1.1	100.3	20.7	51.9	1.0
72	991	9159	1.3	19.6399	2.4	0.0568	2.8	0.0081	1.5	0.55	51.9	0.8	56.1	1.5	237.0	54.3	51.9	0.8
145	1210	10021	2.0	21.6674	1.5	0.0518	2.4	0.0081	1.9	0.78	52.3	1.0	51.3	1.2	5.6	36.6	52.3	1.0
179	284	1816	1.9	16.3571	5.9	0.0688	6.3	0.0082	2.3	0.37	52.4	1.2	67.6	4.1	644.0	126.6	52.4	1.2
103	2512	47363	0.8	21.1657	0.8	0.0532	1.7	0.0082	1.4	0.87	52.4	0.8	52.6	0.9	61.7	19.9	52.4	0.8
203	775	19075	1.1	20.8354	1.2	0.0541	2.8	0.0082	2.5	0.90	52.5	1.3	53.5	1.5	99.0	29.3	52.5	1.3
262	2715	18772	1.1	21.5391	0.8	0.0525	1.7	0.0082	1.5	0.88	52.7	0.8	52.0	0.9	19.9	19.8	52.7	0.8
251	1261	53071	1.5	20.7298	0.9	0.0555	1.8	0.0083	1.6	0.88	53.6	0.9	54.9	1.0	111.0	20.3	53.6	0.9
139	1076	23563	3.0	21.3880	0.9	0.0539	1.9	0.0084	1.7	0.88	53.6	0.9	53.3	1.0	36.7	22.0	53.6	0.9
196	1623	17409	1.7	21.1553	0.9	0.0546	2.5	0.0084	2.3	0.94	53.8	1.3	54.0	1.3	62.9	20.5	53.8	1.3
60	2080	16444	0.8	21.3889	1.1	0.0549	2.0	0.0085	1.7	0.85	54.6	0.9	54.2	1.1	36.6	25.2	54.6	0.9
31	1924	45961	1.8	20.9385	0.9	0.0562	1.8	0.0085	1.5	0.86	54.8	0.8	55.5	0.9	87.4	21.2	54.8	0.8
308	2522	25799	3.6	21.4311	0.8	0.0563	1.6	0.0087	1.4	0.87	56.1	0.8	55.6	0.8	31.9	18.7	56.1	0.8
311	182	6300	4.0	20.5165	1.7	0.0683	2.9	0.0102	2.3	0.79	65.2	1.5	67.1	1.9	135.4	41.0	65.2	1.5
300	278	4388	5.7	21.7823	3.9	0.0702	4.4	0.0111	2.0	0.46	71.1	1.4	68.9	2.9	7.2	93.8	71.1	1.4
216	500	14574	3.2	21.1109	1.4	0.0727	1.9	0.0111	1.3	0.68	71.3	0.9	71.2	1.3	67.9	32.9	71.3	0.9
305	413	4636	4.1	21.0580	2.1	0.0734	2.8	0.0112	1.9	0.68	71.9	1.4	72.0	2.0	73.8	49.6	71.9	1.4
100	479	8822	3.7	21.0515	1.2	0.0741	2.1	0.0113	1.8	0.82	72.5	1.3	72.5	1.5	74.6	28.8	72.5	1.3
256	190	641	1.6	37.8121	18.0	0.0418	18.1	0.0115	2.4	0.13	73.5	1.8	41.6	7.4	1564.6	610.2	73.5	1.8
98	190	3587	3.0	22.0041	4.1	0.0727	4.7	0.0116	2.5	0.52	74.4	1.8	71.2	3.3	31.7	98.4	74.4	1.8
222	170	917	2.6	28.7694	2.1	0.0556	3.1	0.0116	2.3	0.74	74.4	1.7	55.0	1.6	727.9	57.7	74.4	1.7
87	214	3555	3.1	21.1486	3.9	0.0760	4.4	0.0117	2.2	0.49	74.7	1.6	74.4	3.2	63.6	92.1	74.7	1.6
122	303	7220	2.2	20.6466	1.5	0.0779	2.2	0.0117	1.6	0.72	74.8	1.2	76.2	1.6	120.5	36.2	74.8	1.2
299	308	1896	2.4	23.8274	9.5	0.0675	9.8	0.0117	2.3	0.24	74.8	1.7	66.4	6.3	228.4	240.0	74.8	1.7

276	481	3724	3.0	21.2390	1.9	0.0759	2.6	0.0117	1.8	0.70	74.9	1.4	74.3	1.9	53.5	45.2	74.9	1.4
117	322	6178	5.2	21.5015	2.0	0.0755	2.8	0.0118	2.0	0.71	75.4	1.5	73.9	2.0	24.0	47.3	75.4	1.5
230	152	2533	2.8	22.3185	2.6	0.0731	3.6	0.0118	2.4	0.69	75.8	1.8	71.6	2.5	66.2	63.1	75.8	1.8
259	906	28941	2.5	20.9031	1.0	0.0780	1.7	0.0118	1.3	0.80	75.8	1.0	76.3	1.2	91.4	23.5	75.8	1.0
297	125	3345	4.2	22.3391	3.4	0.0731	4.7	0.0118	3.3	0.70	75.9	2.5	71.6	3.3	68.4	82.8	75.9	2.5
96	458	61937	2.4	20.1977	0.9	0.0810	2.0	0.0119	1.8	0.89	76.1	1.4	79.1	1.6	172.1	21.6	76.1	1.4
113	149	1459	3.9	25.0701	2.2	0.0657	3.5	0.0120	2.7	0.77	76.6	2.1	64.6	2.2	358.2	57.6	76.6	2.1
231	156	1406	4.9	22.5407	2.5	0.0733	3.3	0.0120	2.1	0.65	76.8	1.6	71.9	2.3	90.4	61.1	76.8	1.6
85	241	955	5.5	28.1403	12.5	0.0588	12.7	0.0120	2.4	0.19	76.9	1.8	58.0	7.2	666.5	344.8	76.9	1.8
109	436	17650	3.6	20.2699	1.2	0.0820	2.1	0.0121	1.7	0.81	77.3	1.3	80.1	1.6	163.7	28.5	77.3	1.3
116	374	5047	7.2	21.5584	1.7	0.0773	3.3	0.0121	2.9	0.87	77.4	2.2	75.6	2.4	17.7	39.9	77.4	2.2
119	376	5251	2.0	19.9583	3.3	0.0835	3.9	0.0121	2.0	0.52	77.4	1.6	81.4	3.0	199.8	76.7	77.4	1.6
310	492	17459	3.3	21.0225	1.0	0.0795	2.2	0.0121	2.0	0.89	77.7	1.5	77.7	1.6	77.8	23.4	77.7	1.5
227	136	3295	4.0	22.4864	5.4	0.0744	6.0	0.0121	2.6	0.43	77.7	2.0	72.9	4.2	84.5	131.8	77.7	2.0
220	273	6589	5.7	21.9344	1.7	0.0763	2.8	0.0121	2.2	0.78	77.8	1.7	74.7	2.0	24.0	41.8	77.8	1.7
127	432	53500	4.7	20.7252	1.0	0.0811	2.4	0.0122	2.2	0.90	78.1	1.7	79.2	1.8	111.6	24.4	78.1	1.7
232	465	3863	3.4	21.6974	3.2	0.0777	4.1	0.0122	2.5	0.61	78.3	1.9	76.0	3.0	2.3	77.8	78.3	1.9
274	420	31494	4.8	21.1268	1.5	0.0799	2.8	0.0122	2.4	0.86	78.4	1.9	78.0	2.1	66.1	34.7	78.4	1.9
99	242	25231	3.3	19.8739	1.8	0.0849	2.8	0.0122	2.1	0.75	78.4	1.6	82.8	2.2	209.7	42.4	78.4	1.6
46	582	14100	2.4	20.8133	1.0	0.0813	2.5	0.0123	2.3	0.92	78.7	1.8	79.4	1.9	101.6	23.2	78.7	1.8
66	500	5877	2.7	19.2571	2.9	0.0886	3.5	0.0124	1.9	0.55	79.3	1.5	86.2	2.9	282.3	66.8	79.3	1.5
111	308	4599	3.2	21.4970	2.1	0.0800	3.1	0.0125	2.3	0.73	79.9	1.8	78.2	2.3	24.5	50.9	79.9	1.8
37	206	11994	3.2	20.0106	1.6	0.0861	3.1	0.0125	2.7	0.85	80.0	2.1	83.8	2.5	193.8	38.3	80.0	2.1
89	452	18549	3.4	20.5130	1.3	0.0841	2.1	0.0125	1.7	0.79	80.2	1.3	82.0	1.7	135.8	30.8	80.2	1.3
292	93	9582	3.0	19.3741	2.7	0.0898	3.9	0.0126	2.9	0.73	80.8	2.3	87.3	3.3	268.4	61.2	80.8	2.3
101	392	39510	2.0	16.5485	4.0	0.1052	4.5	0.0126	2.0	0.45	80.9	1.6	101.6	4.3	618.9	86.2	80.9	1.6
58	295	4965	3.1	20.9707	2.4	0.0831	3.3	0.0126	2.3	0.70	81.0	1.8	81.1	2.5	83.7	55.8	81.0	1.8
209	405	5798	6.9	21.6011	1.4	0.0807	2.2	0.0126	1.7	0.77	81.0	1.3	78.8	1.6	13.0	33.5	81.0	1.3
57	492	16928	6.0	20.7617	1.4	0.0843	2.2	0.0127	1.8	0.79	81.3	1.4	82.2	1.8	107.4	32.3	81.3	1.4
173	690	17303	1.9	20.6313	1.3	0.0850	3.1	0.0127	2.8	0.90	81.5	2.2	82.9	2.4	122.3	30.7	81.5	2.2
191	591	40271	7.8	20.6058	1.2	0.0852	2.5	0.0127	2.2	0.87	81.6	1.7	83.1	2.0	125.2	28.7	81.6	1.7
213	227	93802	3.8	20.4430	1.7	0.0859	2.7	0.0127	2.1	0.78	81.6	1.7	83.7	2.2	143.8	39.6	81.6	1.7
294	378	20536	3.3	18.2180	1.4	0.0983	2.1	0.0130	1.6	0.77	83.2	1.4	95.2	1.9	407.8	30.7	83.2	1.4
202	481	5767	3.6	21.2547	1.5	0.0845	2.4	0.0130	1.9	0.79	83.4	1.6	82.3	1.9	51.7	36.0	83.4	1.6
152	363	2988	3.1	22.4362	5.7	0.0801	6.0	0.0130	2.0	0.33	83.5	1.7	78.3	4.6	79.0	139.6	83.5	1.7
172	284	13132	3.8	21.0796	2.0	0.0856	3.8	0.0131	3.2	0.85	83.8	2.7	83.4	3.0	71.4	48.2	83.8	2.7
38	311	12965	2.5	20.3324	1.8	0.0888	2.8	0.0131	2.2	0.78	83.8	1.8	86.4	2.3	156.5	41.2	83.8	1.8
13	818	36525	3.1	20.1785	0.8	0.0896	2.2	0.0131	2.1	0.94	84.0	1.8	87.2	1.9	174.3	18.1	84.0	1.8
186	271	1286	3.3	26.7397	15.2	0.0683	15.4	0.0132	2.2	0.14	84.8	1.8	67.1	10.0	527.8	410.0	84.8	1.8
178	325	8830	1.7	21.0989	1.6	0.0865	2.4	0.0132	1.8	0.76	84.8	1.5	84.3	1.9	69.2	37.0	84.8	1.5
1	270	5676	3.3	20.7571	1.7	0.0880	2.5	0.0132	1.9	0.74	84.8	1.6	85.6	2.1	107.9	40.5	84.8	1.6
273	616	179900	2.7	19.5370	1.3	0.0936	2.2	0.0133	1.8	0.82	85.0	1.5	90.9	1.9	249.2	29.5	85.0	1.5
296	178	19354	2.2	20.6496	1.9	0.0889	3.2	0.0133	2.6	0.82	85.2	2.2	86.5	2.7	120.2	43.7	85.2	2.2
156	308	3449	1.7	22.0189	1.8	0.0835	2.7	0.0133	2.0	0.74	85.3	1.7	81.4	2.1	33.3	43.5	85.3	1.7
254	99	19616	1.8	18.9532	3.3	0.0970	4.3	0.0133	2.8	0.65	85.4	2.4	94.0	3.9	318.5	73.9	85.4	2.4
44	282	3233	3.0	22.5414	1.5	0.0816	2.8	0.0133	2.3	0.84	85.4	2.0	79.6	2.1	90.5	37.7	85.4	2.0
195	329	2406	2.9	21.5975	3.2	0.0852	4.0	0.0133	2.4	0.59	85.5	2.0	83.0	3.2	13.4	77.8	85.5	2.0
163	440	4905	2.8	21.5107	1.4	0.0856	2.1	0.0134	1.6	0.76	85.5	1.4	83.4	1.7	23.0	33.1	85.5	1.4
134	308	36126	2.1	20.2793	1.4	0.0908	2.3	0.0134	1.8	0.80	85.5	1.5	88.3	1.9	162.6	31.7	85.5	1.5
48	119	947	2.7	30.1339	3.5	0.0612	4.5	0.0134	2.8	0.62	85.7	2.3	60.3	2.6	859.2	101.0	85.7	2.3
314	260	8107	3.1	20.9146	2.0	0.0883	3.1	0.0134	2.3	0.75	85.8	2.0	85.9	2.5	90.1	48.0	85.8	2.0
255	310	21808	5.5	20.4779	1.6	0.0904	2.6	0.0134	2.0	0.79	86.0	1.7	87.9	2.2	139.8	36.6	86.0	1.7
272	293	8080	4.2	17.6843	1.5	0.1047	3.1	0.0134	2.7	0.87	86.0	2.3	101.1	3.0	473.9	34.0	86.0	2.3
291	200	3328	4.6	22.3375	2.8	0.0830	3.4	0.0134	1.9	0.57	86.1	1.6	80.9	2.6	68.3	67.8	86.1	1.6
201	335	22805	3.9	20.8862	1.3	0.0889	2.5	0.0135	2.2	0.86	86.2	1.9	86.5	2.1	93.2	30.9	86.2	1.9
301	122	4749	5.6	21.2990	2.9	0.0872	3.8	0.0135	2.4	0.64	86.3	2.1	84.9	3.1	46.7	69.5	86.3	2.1
131	273	2948	2.2	21.8094	3.0	0.0853	3.8	0.0135	2.4	0.62	86.4	2.0	83.1	3.0	10.1	71.8	86.4	2.0
61	204	4322	2.5	21.2602	2.5	0.0878	3.3	0.0135	2.2	0.66	86.7	1.9	85.4	2.7	51.1	59.7	86.7	1.9

114	706	9163	1.3	20.0835	1.3	0.0929	2.6	0.0135	2.3	0.87	86.7	2.0	90.2	2.3	185.3	29.9	86.7	2.0
283	228	3867	3.8	22.6290	1.5	0.0826	2.5	0.0136	2.0	0.79	86.8	1.7	80.6	2.0	100.0	37.9	86.8	1.7
41	462	83120	3.6	20.5532	1.3	0.0910	2.5	0.0136	2.2	0.86	86.9	1.9	88.5	2.1	131.2	30.5	86.9	1.9
258	346	7259	2.0	20.9517	1.7	0.0893	2.8	0.0136	2.2	0.78	86.9	1.9	86.9	2.3	85.9	41.2	86.9	1.9
164	121	31447	3.8	20.1119	2.2	0.0931	3.7	0.0136	3.0	0.81	86.9	2.6	90.4	3.2	182.0	50.6	86.9	2.6
245	177	7234	2.3	21.5523	1.8	0.0869	3.3	0.0136	2.7	0.84	87.0	2.4	84.6	2.7	18.4	42.9	87.0	2.4
112	202	3051	4.7	22.7934	2.3	0.0822	3.4	0.0136	2.5	0.74	87.0	2.2	80.2	2.6	117.8	56.3	87.0	2.2
211	134	14024	2.8	20.4808	2.6	0.0915	4.1	0.0136	3.3	0.79	87.1	2.8	88.9	3.5	139.5	60.0	87.1	2.8
125	364	99605	1.5	16.2712	4.0	0.1152	4.5	0.0136	2.1	0.46	87.1	1.8	110.7	4.7	655.3	85.8	87.1	1.8
24	351	4891	1.4	21.2723	1.8	0.0887	2.8	0.0137	2.2	0.78	87.6	1.9	86.3	2.3	49.7	42.7	87.6	1.9
106	200	89296	2.0	19.1445	2.5	0.0985	3.4	0.0137	2.3	0.68	87.6	2.0	95.4	3.1	295.7	57.0	87.6	2.0
198	630	7326	2.7	21.5650	1.2	0.0878	2.0	0.0137	1.6	0.81	87.9	1.4	85.4	1.6	17.0	27.7	87.9	1.4
88	225	3198	1.9	22.8692	2.1	0.0829	3.0	0.0137	2.1	0.70	88.0	1.8	80.9	2.3	126.0	52.6	88.0	1.8
278	2109	73675	2.9	20.7394	0.7	0.0916	1.8	0.0138	1.6	0.92	88.3	1.4	89.0	1.5	109.9	16.9	88.3	1.4
93	342	6381	3.5	21.2262	1.3	0.0897	2.2	0.0138	1.8	0.80	88.4	1.5	87.2	1.9	54.9	32.0	88.4	1.5
260	286	16832	1.8	20.3111	1.4	0.0937	2.5	0.0138	2.1	0.83	88.4	1.8	91.0	2.2	159.0	32.4	88.4	1.8
234	327	9221	4.8	21.0743	1.3	0.0903	2.2	0.0138	1.7	0.80	88.4	1.5	87.8	1.8	72.0	31.4	88.4	1.5
157	870	11609	2.4	21.2618	0.9	0.0897	2.0	0.0138	1.8	0.89	88.5	1.6	87.2	1.7	50.9	22.4	88.5	1.6
55	165	11510	2.2	20.7751	2.1	0.0918	3.8	0.0138	3.2	0.84	88.6	2.8	89.2	3.2	105.9	48.4	88.6	2.8
28	187	3840	4.6	21.2945	2.3	0.0898	3.4	0.0139	2.6	0.75	88.8	2.3	87.3	2.9	47.2	54.6	88.8	2.3
236	413	6989	3.0	21.1617	1.5	0.0904	2.5	0.0139	2.0	0.79	88.8	1.7	87.8	2.1	62.1	36.9	88.8	1.7
261	242	1038	2.2	29.2308	17.9	0.0654	18.0	0.0139	2.2	0.12	88.8	1.9	64.4	11.2	772.5	507.7	88.8	1.9
315	466	7707	1.2	21.1803	1.3	0.0905	2.3	0.0139	2.0	0.84	89.0	1.8	88.0	2.0	60.0	30.0	89.0	1.8
81	168	1299	2.5	24.8654	3.2	0.0771	3.9	0.0139	2.2	0.57	89.0	1.9	75.4	2.8	337.0	82.0	89.0	1.9
84	287	15571	3.4	16.7649	4.1	0.1144	4.9	0.0139	2.7	0.55	89.0	2.4	110.0	5.1	590.9	88.6	89.0	2.4
140	557	19005	2.8	20.8738	1.1	0.0919	2.2	0.0139	1.9	0.86	89.1	1.7	89.3	1.9	94.7	26.7	89.1	1.7
165	188	7920	2.3	20.8424	2.1	0.0921	3.2	0.0139	2.4	0.76	89.1	2.2	89.5	2.8	98.2	50.1	89.1	2.2
187	134	2498	1.8	17.3313	4.4	0.1109	5.4	0.0139	3.1	0.57	89.2	2.7	106.8	5.5	518.3	97.6	89.2	2.7
110	264	6539	1.8	20.6865	1.7	0.0930	2.8	0.0139	2.2	0.80	89.3	2.0	90.3	2.4	116.0	40.2	89.3	2.0
275	628	6871	3.4	21.1182	1.2	0.0912	2.2	0.0140	1.8	0.83	89.5	1.6	88.7	1.9	67.0	29.2	89.5	1.6
271	595	11261	2.7	20.9613	1.2	0.0921	2.2	0.0140	1.9	0.84	89.7	1.7	89.5	1.9	84.7	28.9	89.7	1.7
136	115	1177	2.4	26.1601	2.7	0.0739	3.9	0.0140	2.8	0.71	89.7	2.5	72.3	2.7	469.5	72.6	89.7	2.5
17	360	14338	4.4	20.6318	1.4	0.0942	2.5	0.0141	2.1	0.84	90.2	1.9	91.4	2.2	122.2	32.1	90.2	1.9
42	202	4143	2.4	19.7818	4.3	0.0983	5.0	0.0141	2.5	0.51	90.3	2.3	95.2	4.5	220.4	98.9	90.3	2.3
39	194	2347	3.9	23.8130	2.3	0.0818	3.3	0.0141	2.4	0.72	90.4	2.1	79.8	2.5	226.9	57.2	90.4	2.1
219	442	17361	2.8	19.1105	1.9	0.1019	3.9	0.0141	3.5	0.88	90.4	3.1	98.6	3.7	299.7	42.8	90.4	3.1
9	235	8911	3.4	20.4702	2.0	0.0957	3.0	0.0142	2.3	0.76	90.9	2.1	92.8	2.7	140.7	46.3	90.9	2.1
242	280	36805	2.0	19.9416	1.5	0.0984	2.9	0.0142	2.5	0.85	91.1	2.2	95.3	2.6	201.8	35.0	91.1	2.2
33	89	1228	3.1	26.6472	3.8	0.0737	4.9	0.0143	3.0	0.62	91.2	2.7	72.3	3.4	518.5	102.4	91.2	2.7
206	80	3068	3.1	16.2417	3.8	0.1211	4.7	0.0143	2.8	0.59	91.3	2.6	116.1	5.2	659.2	81.8	91.3	2.6
47	3658	38164	1.1	21.2088	0.8	0.0929	1.7	0.0143	1.5	0.88	91.4	1.4	90.2	1.5	56.9	19.2	91.4	1.4
169	393	14835	3.2	20.1963	1.3	0.0978	2.6	0.0143	2.2	0.86	91.7	2.0	94.7	2.3	172.2	30.8	91.7	2.0
137	415	27603	2.4	19.3243	2.0	0.1022	2.8	0.0143	1.9	0.67	91.7	1.7	98.8	2.6	274.3	47.0	91.7	1.7
68	85	3023	3.6	21.9568	2.9	0.0903	4.0	0.0144	2.8	0.70	92.0	2.5	87.8	3.4	26.4	69.5	92.0	2.5
282	301	7407	1.6	20.9832	1.5	0.0945	2.6	0.0144	2.1	0.81	92.1	1.9	91.7	2.3	82.3	36.2	92.1	1.9
128	611	64187	2.2	19.8990	1.3	0.0997	2.1	0.0144	1.7	0.79	92.1	1.6	96.5	2.0	206.8	30.3	92.1	1.6
135	386	23616	7.4	20.3839	1.7	0.0976	3.0	0.0144	2.5	0.83	92.3	2.3	94.6	2.7	150.6	40.0	92.3	2.3
279	262	5039	3.0	21.0276	3.4	0.0948	3.9	0.0145	2.0	0.51	92.6	1.9	92.0	3.5	77.2	80.6	92.6	1.9
226	645	8239	4.3	21.1418	1.3	0.0944	2.1	0.0145	1.7	0.78	92.6	1.5	91.6	1.9	64.4	31.3	92.6	1.5
77	163	9908	5.0	20.8278	1.7	0.0960	3.5	0.0145	3.1	0.87	92.8	2.8	93.1	3.1	99.9	40.7	92.8	2.8
181	157	1523	3.2	24.9135	3.2	0.0804	4.0	0.0145	2.5	0.62	92.9	2.3	78.5	3.0	342.0	81.3	92.9	2.3
2	135	7479	3.7	19.8777	2.6	0.1010	3.8	0.0146	2.9	0.75	93.2	2.6	97.7	3.6	209.2	59.2	93.2	2.6
221	107	41266	3.0	16.7475	4.0	0.1201	5.1	0.0146	3.1	0.61	93.4	2.8	115.2	5.5	593.1	87.4	93.4	2.8
16	495	9719	3.8	20.6199	1.3	0.0981	2.5	0.0147	2.2	0.86	93.8	2.0	95.0	2.3	123.6	30.2	93.8	2.0
62	508	10022	4.4	20.9324	1.3	0.0966	2.5	0.0147	2.1	0.86	93.9	2.0	93.6	2.2	88.1	29.8	93.9	2.0
252	49	735	3.3	34.7704	8.8	0.0582	9.5	0.0147	3.7	0.39	93.9	3.4	57.4	5.3	1290.5	278.0	93.9	3.4
215	176	39397	4.2	19.9019	2.2	0.1021	3.2	0.0147	2.3	0.71	94.3	2.1	98.7	3.0	206.4	51.5	94.3	2.1
257	517	5078	1.7	21.5004	1.3	0.0947	2.2	0.0148	1.7	0.79	94.5	1.6	91.8	1.9	24.2	31.8	94.5	1.6

79	111	2770	2.7	22.8266	2.6	0.0893	3.6	0.0148	2.5	0.70	94.6	2.3	86.8	3.0	121.4	62.9	94.6	2.3
124	340	13264	3.4	20.1530	1.4	0.1011	2.5	0.0148	2.1	0.83	94.6	1.9	97.8	2.3	177.2	32.3	94.6	1.9
161	199	18219	2.6	21.0043	1.7	0.0971	2.9	0.0148	2.3	0.81	94.6	2.2	94.1	2.6	79.9	40.8	94.6	2.2
146	138	2500	2.6	22.4603	7.0	0.0910	7.4	0.0148	2.6	0.35	94.8	2.5	88.4	6.3	81.7	170.5	94.8	2.5
208	551	15487	1.0	20.6063	1.1	0.0993	2.2	0.0148	1.9	0.86	95.0	1.8	96.2	2.0	125.1	26.0	95.0	1.8
102	330	18375	5.3	20.3191	1.4	0.1009	2.2	0.0149	1.8	0.79	95.2	1.7	97.6	2.1	158.1	32.2	95.2	1.7
49	240	28471	2.6	19.4642	1.4	0.1054	2.7	0.0149	2.3	0.85	95.2	2.2	101.7	2.6	257.8	32.4	95.2	2.2
20	177	3956	2.3	22.1181	2.2	0.0928	3.2	0.0149	2.3	0.72	95.3	2.2	90.1	2.7	44.2	53.4	95.3	2.2
183	292	1072	2.8	28.7868	7.9	0.0714	8.3	0.0149	2.3	0.28	95.3	2.2	70.0	5.6	729.6	221.5	95.3	2.2
52	719	51673	4.3	20.3614	0.7	0.1011	2.2	0.0149	2.0	0.94	95.5	1.9	97.8	2.0	153.2	17.5	95.5	1.9
162	456	5970	3.5	20.2191	1.4	0.1022	2.8	0.0150	2.5	0.87	95.9	2.3	98.8	2.7	169.6	32.4	95.9	2.3
248	3116	89752	0.0	20.4511	0.8	0.1013	3.3	0.0150	3.2	0.97	96.1	3.0	97.9	3.0	142.9	17.9	96.1	3.0
298	645	45310	4.0	20.2682	1.1	0.1023	2.1	0.0150	1.8	0.85	96.2	1.7	98.9	2.0	163.9	26.6	96.2	1.7
210	253	1216	4.8	25.4822	15.7	0.0815	15.9	0.0151	2.1	0.13	96.4	2.0	79.6	12.1	400.5	412.5	96.4	2.0
29	202	16814	3.1	20.5433	1.8	0.1014	2.8	0.0151	2.2	0.78	96.7	2.1	98.1	2.6	132.3	41.1	96.7	2.1
204	280	320341	2.1	19.9562	1.1	0.1045	2.6	0.0151	2.3	0.91	96.8	2.2	100.9	2.5	200.1	25.4	96.8	2.2
188	406	17628	2.1	20.3636	1.5	0.1024	2.4	0.0151	1.9	0.78	96.8	1.8	99.0	2.2	152.9	35.0	96.8	1.8
70	205	1356	3.7	24.4333	1.8	0.0858	2.6	0.0152	1.9	0.72	97.3	1.8	83.6	2.1	292.1	46.7	97.3	1.8
8	254	5426	2.8	16.0867	4.2	0.1305	4.8	0.0152	2.4	0.50	97.4	2.3	124.6	5.6	679.7	88.8	97.4	2.3
147	715	27836	2.7	20.3578	0.9	0.1032	2.0	0.0152	1.7	0.89	97.5	1.7	99.8	1.9	153.6	20.4	97.5	1.7
5	281	37351	2.4	19.8073	1.2	0.1061	2.7	0.0152	2.4	0.89	97.6	2.3	102.4	2.6	217.5	27.6	97.6	2.3
126	334	5866	2.4	21.0215	1.4	0.1002	2.3	0.0153	1.9	0.80	97.7	1.8	96.9	2.1	77.9	32.9	97.7	1.8
246	303	9306	1.8	20.6556	1.7	0.1020	2.5	0.0153	1.9	0.75	97.7	1.8	98.6	2.4	119.5	39.3	97.7	1.8
30	424	9385	2.3	19.7046	1.5	0.1072	2.6	0.0153	2.1	0.82	98.0	2.0	103.4	2.5	229.5	33.7	98.0	2.0
207	499	17772	2.9	20.3493	1.1	0.1040	2.6	0.0153	2.4	0.91	98.2	2.3	100.4	2.5	154.6	25.9	98.2	2.3
182	1569	120949	2.2	19.3837	1.5	0.1091	2.9	0.0153	2.5	0.86	98.2	2.4	105.2	2.9	267.2	34.7	98.2	2.4
26	459	9502	1.7	20.4466	1.3	0.1035	2.9	0.0153	2.6	0.89	98.2	2.5	100.0	2.8	143.4	31.5	98.2	2.5
150	404	129791	1.7	20.5839	1.2	0.1028	2.2	0.0154	1.8	0.84	98.2	1.8	99.4	2.0	127.7	27.6	98.2	1.8
309	78	3963	2.4	21.2526	3.0	0.0997	4.0	0.0154	2.6	0.65	98.3	2.5	96.5	3.7	51.9	72.5	98.3	2.5
18	322	10224	2.1	20.3747	1.1	0.1042	2.6	0.0154	2.3	0.90	98.5	2.3	100.7	2.5	151.7	25.9	98.5	2.3
190	299	17703	2.4	20.9424	1.3	0.1014	2.3	0.0154	1.9	0.83	98.5	1.9	98.1	2.1	86.9	30.4	98.5	1.9
263	123	1822	3.4	22.7814	2.7	0.0933	4.3	0.0154	3.3	0.77	98.6	3.2	90.5	3.7	116.5	67.7	98.6	3.2
14	380	49435	2.1	20.4862	1.1	0.1038	1.9	0.0154	1.6	0.83	98.7	1.6	100.3	1.8	138.9	25.4	98.7	1.6
218	168	4971	2.2	19.2376	1.5	0.1106	2.6	0.0154	2.1	0.82	98.7	2.1	106.5	2.6	284.6	34.3	98.7	2.1
36	275	3602	2.2	22.4243	1.8	0.0953	3.3	0.0155	2.8	0.84	99.1	2.7	92.4	2.9	77.7	43.7	99.1	2.7
233	88	904	3.6	30.4923	2.7	0.0705	3.8	0.0156	2.7	0.70	99.7	2.7	69.2	2.6	893.3	79.3	99.7	2.7
193	725	19891	3.8	20.5901	0.9	0.1044	2.0	0.0156	1.7	0.88	99.7	1.7	100.8	1.9	127.0	21.7	99.7	1.7
270	332	9551	2.7	20.3042	1.4	0.1060	2.4	0.0156	2.0	0.82	99.8	2.0	102.3	2.4	159.8	33.0	99.8	2.0
167	643	30860	2.2	20.3614	1.1	0.1075	2.3	0.0159	2.0	0.88	101.5	2.0	103.6	2.2	153.2	25.0	101.5	2.0
205	270	2160	3.0	22.3785	7.8	0.0978	8.1	0.0159	2.0	0.25	101.5	2.1	94.8	7.3	72.7	191.5	101.5	2.1
43	115	7948	2.3	20.9885	2.3	0.1051	3.0	0.0160	1.9	0.65	102.3	2.0	101.5	2.9	81.7	54.1	102.3	2.0
120	437	1392	5.3	23.6695	10.8	0.0934	11.2	0.0160	2.9	0.26	102.5	2.9	90.7	9.7	211.7	271.2	102.5	2.9
82	319	37882	3.0	19.0797	1.6	0.1162	2.6	0.0161	2.1	0.79	102.8	2.1	111.6	2.8	303.4	36.1	102.8	2.1
3	482	21786	2.3	20.5420	1.2	0.1086	2.7	0.0162	2.4	0.90	103.4	2.5	104.7	2.7	132.5	28.1	103.4	2.5
54	242	2264	2.7	6.7088	15.7	0.3366	17.2	0.0164	6.9	0.40	104.7	7.2	294.6	43.9	2335.1	270.3	104.7	7.2
95	178	11475	2.5	20.4557	1.5	0.1135	2.9	0.0168	2.5	0.85	107.7	2.7	109.2	3.0	142.4	36.2	107.7	2.7
76	57	1646	3.4	17.9194	5.4	0.1297	6.3	0.0169	3.3	0.52	107.7	3.5	123.8	7.4	444.6	119.8	107.7	3.5
132	253	1884	5.8	23.1343	7.5	0.1009	7.8	0.0169	2.2	0.29	108.2	2.4	97.6	7.3	154.6	186.0	108.2	2.4
11	417	12341	2.0	20.8710	1.1	0.1127	2.3	0.0171	2.0	0.87	109.1	2.2	108.4	2.4	95.0	26.6	109.1	2.2
200	175	3119	7.0	19.8864	2.0	0.1199	3.0	0.0173	2.3	0.74	110.5	2.5	115.0	3.3	208.2	47.3	110.5	2.5
105	757	32953	1.8	19.8342	1.2	0.1205	2.3	0.0173	2.0	0.85	110.8	2.1	115.5	2.5	214.3	27.5	110.8	2.1
267	222	3224	1.9	21.7161	5.2	0.1110	5.6	0.0175	1.9	0.34	111.7	2.1	106.9	5.6	0.2	125.8	111.7	2.1
217	626	17367	1.4	20.9396	0.9	0.1152	2.0	0.0175	1.7	0.89	111.8	1.9	110.7	2.1	87.2	21.6	111.8	1.9
32	637	20839	1.7	20.5727	1.1	0.1180	2.2	0.0176	1.9	0.88	112.5	2.1	113.2	2.3	129.0	24.8	112.5	2.1
6	127	5339	2.5	21.2385	2.0	0.1143	3.4	0.0176	2.7	0.80	112.5	3.0	109.9	3.5	53.5	48.3	112.5	3.0
277	556	10247	1.8	18.6461	1.9	0.1303	2.8	0.0176	2.1	0.74	112.6	2.3	124.3	3.3	355.6	42.4	112.6	2.3
192	359	9584	44.9	20.2589	1.2	0.1199	2.0	0.0176	1.6	0.80	112.6	1.8	115.0	2.2	165.0	28.8	112.6	1.8
177	270	10536	2.9	21.0828	1.2	0.1166	2.2	0.0178	1.8	0.84	113.9	2.1	112.0	2.3	71.0	27.5	113.9	2.1

73	165	5927	4.2	21.1785	3.1	0.1163	3.5	0.0179	1.6	0.46	114.1	1.8	111.7	3.7	60.3	74.3	114.1	1.8
180	291	23013	2.7	19.7048	1.5	0.1269	2.5	0.0181	2.0	0.81	115.8	2.4	121.3	2.9	229.4	33.9	115.8	2.4
229	118	2693	4.3	22.1075	4.3	0.1140	5.0	0.0183	2.5	0.51	116.8	2.9	109.6	5.2	43.0	104.2	116.8	2.9
155	133	4424	4.1	20.7620	2.1	0.1220	3.2	0.0184	2.4	0.76	117.3	2.8	116.9	3.5	107.4	49.2	117.3	2.8
293	588	21278	1.5	20.4463	0.9	0.1241	2.0	0.0184	1.8	0.89	117.5	2.1	118.7	2.3	143.5	21.4	117.5	2.1
144	239	282528	1.7	19.8602	1.4	0.1283	2.5	0.0185	2.0	0.81	118.0	2.3	122.6	2.8	211.2	33.4	118.0	2.3
7	123	4636	2.3	21.0038	2.1	0.1225	3.4	0.0187	2.7	0.78	119.2	3.2	117.4	3.8	79.9	50.9	119.2	3.2
138	463	23662	1.6	20.1807	1.3	0.1277	2.3	0.0187	1.9	0.83	119.3	2.3	122.0	2.7	174.0	30.2	119.3	2.3
185	175	2987	2.2	20.4578	2.9	0.1266	3.7	0.0188	2.4	0.64	120.0	2.8	121.0	4.3	142.1	67.6	120.0	2.8
306	87	1536	1.4	25.0032	11.9	0.1043	12.3	0.0189	3.2	0.26	120.7	3.8	100.7	11.8	351.3	308.5	120.7	3.8
35	513	11812	2.0	20.4636	0.9	0.1285	2.0	0.0191	1.7	0.89	121.8	2.1	122.8	2.3	141.4	21.0	121.8	2.1
290	1579	41636	2.6	20.4216	0.7	0.1290	1.8	0.0191	1.7	0.93	122.0	2.0	123.2	2.1	146.3	15.6	122.0	2.0
129	140	6288	2.4	19.8892	1.2	0.1346	2.6	0.0194	2.3	0.88	124.0	2.9	128.3	3.2	207.9	29.0	124.0	2.9
312	594	12539	3.1	20.5292	1.0	0.1309	2.0	0.0195	1.8	0.88	124.4	2.2	124.9	2.4	134.0	22.8	124.4	2.2
130	242	43529	2.0	20.0972	1.3	0.1374	2.1	0.0200	1.6	0.78	127.8	2.1	130.7	2.6	183.7	30.8	127.8	2.1
189	149	2998	2.2	20.8915	5.1	0.1332	5.7	0.0202	2.5	0.43	128.8	3.1	127.0	6.8	92.7	121.9	128.8	3.1
86	62	3578	2.6	20.5122	3.5	0.1364	4.9	0.0203	3.4	0.69	129.5	4.3	129.8	5.9	135.9	82.1	129.5	4.3
141	184	4648	2.1	21.0345	2.0	0.1338	3.2	0.0204	2.5	0.79	130.3	3.3	127.5	3.8	76.5	47.1	130.3	3.3
97	239	4973	2.7	21.3860	1.4	0.1333	2.5	0.0207	2.1	0.84	131.9	2.8	127.0	3.0	36.9	33.3	131.9	2.8
168	456	5000	2.0	21.0926	1.0	0.1408	2.3	0.0215	2.0	0.90	137.4	2.8	133.7	2.8	69.9	22.8	137.4	2.8
264	530	237152	3.0	19.8863	0.9	0.1499	2.7	0.0216	2.5	0.94	137.9	3.5	141.8	3.6	208.2	22.0	137.9	3.5
313	228	10716	2.4	20.1698	1.4	0.1518	2.8	0.0222	2.5	0.87	141.6	3.4	143.5	3.8	175.3	32.7	141.6	3.4
121	552	34268	1.7	20.1515	1.0	0.1520	2.1	0.0222	1.9	0.88	141.6	2.6	143.7	2.8	177.4	23.2	141.6	2.6
281	72	24810	2.1	19.0391	2.3	0.1612	4.1	0.0223	3.5	0.84	141.9	4.9	151.8	5.8	308.2	51.5	141.9	4.9
302	226	1824	1.8	23.1389	5.5	0.1331	5.8	0.0223	1.9	0.32	142.4	2.6	126.8	7.0	155.1	137.3	142.4	2.6
184	126	8517	1.4	20.6487	1.5	0.1498	3.1	0.0224	2.7	0.87	143.0	3.9	141.7	4.1	120.3	35.9	143.0	3.9
56	244	49059	1.9	19.4796	1.1	0.1602	3.1	0.0226	2.9	0.93	144.3	4.1	150.9	4.3	255.9	25.0	144.3	4.1
304	245	18019	3.2	20.1390	1.1	0.1568	2.4	0.0229	2.1	0.89	146.0	3.1	147.9	3.3	178.8	25.9	146.0	3.1
239	274	2377	1.9	22.0326	1.4	0.1434	2.6	0.0229	2.2	0.85	146.0	3.2	136.1	3.3	34.8	33.0	146.0	3.2
94	454	12278	3.0	20.5924	1.0	0.1537	2.5	0.0230	2.2	0.91	146.3	3.2	145.2	3.3	126.7	24.1	146.3	3.2
228	144	6188	1.8	20.7427	1.7	0.1527	2.8	0.0230	2.2	0.80	146.4	3.3	144.3	3.8	109.6	39.6	146.4	3.3
214	328	39856	2.5	19.6378	1.2	0.1623	2.3	0.0231	2.0	0.86	147.4	2.9	152.8	3.3	237.3	26.9	147.4	2.9
197	262	24726	2.7	20.0311	1.5	0.1593	2.5	0.0231	2.1	0.82	147.4	3.0	150.1	3.5	191.4	33.8	147.4	3.0
295	231	30721	1.4	20.0972	1.1	0.1590	2.7	0.0232	2.5	0.92	147.7	3.6	149.8	3.8	183.7	25.5	147.7	3.6
265	323	13850	1.6	20.5697	1.4	0.1554	3.0	0.0232	2.7	0.89	147.8	3.9	146.7	4.1	129.3	32.3	147.8	3.9
149	83	4673	2.4	21.5444	2.0	0.1492	3.0	0.0233	2.3	0.76	148.5	3.4	141.2	4.0	19.3	47.5	148.5	3.4
269	168	5980	1.8	19.0468	2.9	0.1692	3.7	0.0234	2.2	0.61	148.9	3.3	158.7	5.4	307.4	66.2	148.9	3.3
243	306	5356	1.9	20.7991	1.2	0.1558	2.3	0.0235	1.9	0.84	149.8	2.9	147.1	3.1	103.2	29.1	149.8	2.9
10	223	10050	2.3	20.4849	1.8	0.1607	2.7	0.0239	2.1	0.75	152.1	3.1	151.3	3.9	139.1	42.9	152.1	3.1
23	703	13595	1.2	20.6554	0.9	0.1600	2.3	0.0240	2.1	0.91	152.7	3.1	150.7	3.2	119.5	22.2	152.7	3.1
4	223	10321	2.6	17.7657	2.9	0.1864	3.9	0.0240	2.5	0.66	153.0	3.9	173.6	6.2	463.8	64.3	153.0	3.9
159	124	3525	4.7	21.3470	2.2	0.1559	3.4	0.0241	2.6	0.76	153.8	4.0	147.1	4.7	41.4	53.1	153.8	4.0
123	103	2153	2.3	22.0014	3.4	0.1550	4.3	0.0247	2.6	0.61	157.5	4.1	146.3	5.9	31.4	82.8	157.5	4.1
158	400	32285	2.4	20.1326	1.1	0.1702	2.9	0.0248	2.7	0.93	158.2	4.3	159.6	4.3	179.6	25.7	158.2	4.3
108	165	6478	2.4	20.7530	2.2	0.1658	3.1	0.0250	2.2	0.71	158.9	3.5	155.8	4.5	108.4	52.4	158.9	3.5
240	760	15422	1.2	20.5891	0.8	0.1676	2.3	0.0250	2.2	0.94	159.3	3.4	157.3	3.4	127.1	18.6	159.3	3.4
175	308	8219	2.1	20.3935	1.1	0.1698	2.5	0.0251	2.3	0.90	159.9	3.6	159.2	3.7	149.5	25.7	159.9	3.6
166	154	5478	2.9	19.0651	1.9	0.1830	3.0	0.0253	2.4	0.78	161.1	3.8	170.7	4.8	305.2	43.8	161.1	3.8
63	912	23048	1.7	20.5008	0.8	0.1717	1.9	0.0255	1.7	0.92	162.5	2.8	160.9	2.8	137.2	17.9	162.5	2.8
80	471	7683	1.2	19.5494	2.4	0.1820	3.0	0.0258	1.7	0.57	164.2	2.8	169.7	4.6	247.7	55.9	164.2	2.8
174	520	126998	3.6	20.2409	0.9	0.1788	2.1	0.0262	1.8	0.89	167.0	3.0	167.0	3.2	167.1	21.9	167.0	3.0
171	152	19860	4.4	20.1871	1.4	0.1837	3.1	0.0269	2.8	0.90	171.1	4.7	171.3	4.8	173.3	31.6	171.1	4.7
115	452	55742	3.2	19.8239	1.0	0.1917	2.3	0.0276	2.1	0.91	175.3	3.7	178.1	3.8	215.5	22.6	175.3	3.7
286	390	17562	2.5	19.0746	2.1	0.2259	3.1	0.0312	2.3	0.73	198.4	4.5	206.8	5.9	304.0	49.0	198.4	4.5
235	123	3090	3.6	21.4417	1.8	0.2011	3.7	0.0313	3.3	0.88	198.5	6.4	186.0	6.3	30.7	43.2	198.5	6.4
143	123	14443	2.7	19.5111	1.4	0.2236	2.4	0.0316	2.0	0.83	200.8	4.0	204.9	4.5	252.2	31.6	200.8	4.0
104	189	9926	1.4	19.4133	2.5	0.2253	3.4	0.0317	2.4	0.69	201.4	4.8	206.4	6.4	263.7	57.0	201.4	4.8
194	156	4850	3.2	20.7634	1.5	0.2109	3.2	0.0318	2.8	0.88	201.6	5.6	194.3	5.6	107.2	35.0	201.6	5.6

118	188	14563	2.0	19.9535	1.3	0.2198	2.7	0.0318	2.4	0.88	201.9	4.7	201.8	4.9	200.4	29.1	201.9	4.7
21	339	19948	2.0	20.0160	0.9	0.2204	2.6	0.0320	2.4	0.93	203.0	4.8	202.2	4.7	193.2	21.7	203.0	4.8
69	887	52843	1.2	19.8127	0.8	0.2306	2.1	0.0331	2.0	0.92	210.2	4.1	210.7	4.1	216.8	19.2	210.2	4.1
303	101	6288	2.5	19.6256	2.8	0.2367	3.8	0.0337	2.6	0.68	213.6	5.4	215.7	7.3	238.7	63.9	213.6	5.4
153	58	15075	2.4	19.9249	2.1	0.2343	3.8	0.0339	3.1	0.82	214.7	6.5	213.7	7.2	203.7	49.3	214.7	6.5
51	72	4165	3.2	20.7894	2.3	0.2283	4.3	0.0344	3.7	0.85	218.2	7.8	208.8	8.1	104.3	54.1	218.2	7.8
40	147	6273	2.5	20.0493	1.0	0.2456	2.3	0.0357	2.0	0.89	226.2	4.5	223.0	4.6	189.2	23.7	226.2	4.5
90	94	5164	3.6	18.9384	1.6	0.2722	3.3	0.0374	2.9	0.87	236.6	6.7	244.5	7.2	320.3	36.4	236.6	6.7
247	376	15819	1.8	19.9402	0.8	0.2636	2.1	0.0381	1.9	0.93	241.1	4.6	237.5	4.4	201.9	18.4	241.1	4.6
268	102	43646	3.2	18.6972	1.2	0.2944	2.7	0.0399	2.5	0.90	252.3	6.1	262.0	6.3	349.4	26.1	252.3	6.1
176	183	24993	2.3	11.1830	0.7	3.0203	2.2	0.2450	2.1	0.95	1412.5	26.7	1412.8	16.9	1413.2	13.6	1413.2	13.6
249	766	69429	1.7	10.9515	0.6	3.0671	2.1	0.2436	2.0	0.96	1405.5	25.4	1424.5	16.0	1453.1	10.5	1453.1	10.5
288	139	72395	0.5	10.4875	0.7	3.3995	2.9	0.2586	2.8	0.97	1482.6	37.0	1504.3	22.7	1535.0	13.9	1535.0	13.9
142	656	291956	2.2	10.1137	0.6	3.7100	1.8	0.2721	1.7	0.94	1551.6	23.0	1573.5	14.2	1603.0	11.6	1603.0	11.6
199	1596	443141	3.3	9.9208	0.8	4.2274	2.2	0.3042	2.0	0.93	1712.0	30.2	1679.4	17.8	1638.8	15.1	1638.8	15.1
27	334	51349	2.5	9.8819	0.8	3.4468	2.1	0.2470	1.9	0.92	1423.1	24.6	1515.1	16.4	1646.1	14.8	1646.1	14.8
223	340	808358	2.5	9.4978	0.6	4.4253	2.3	0.3048	2.2	0.97	1715.2	33.7	1717.1	19.2	1719.3	10.8	1719.3	10.8
107	260	875251	2.2	9.4792	0.5	4.3839	1.9	0.3014	1.9	0.97	1698.2	27.7	1709.3	15.8	1722.9	8.8	1722.9	8.8
91	1045	460776	18.3	9.3714	0.9	4.1386	2.9	0.2813	2.8	0.96	1597.9	39.9	1662.0	24.1	1743.9	15.8	1743.9	15.8
224	232	34350	2.4	9.2863	0.5	4.5583	2.2	0.3070	2.2	0.97	1726.0	32.9	1741.7	18.6	1760.6	9.5	1760.6	9.5
284	577	3233714	2.8	9.2819	0.5	4.4824	1.7	0.3017	1.6	0.95	1700.0	24.4	1727.7	14.3	1761.5	10.0	1761.5	10.0

TABLE A3: LA-ICP-MS U-Pb Zircon Geochronology Results for CR-MPE-018

Zircon #	Composition U (ppm)	$^{206}Pb/^{204}Pb$	U/Th	$^{208}Pb/^{207}Pb$	2σ (%)	$^{207}Pb/^{235}U$	2σ (%)	$^{206}Pb/^{238}U$	2σ (%)	Corr.	Ages $^{206}Pb/^{238}U$	2σ (Ma)	$^{207}Pb/^{235}U$	2σ (Ma)	$^{206}Pb/^{207}Pb$	2σ (Ma)	Best Age	2σ (Ma)
308	98	445	3.0	66.4435	8.1	0.0140	8.5	0.0068	2.7	0.31	43.4	1.1	14.1	1.2	0.0	0.0	43.4	1.1
72	140	618	1.9	40.5176	34.2	0.0233	34.4	0.0069	3.0	0.09	44.1	1.3	23.4	8.0	1804.6	1252.9	44.1	1.3
246	71	728	3.5	28.6751	9.7	0.0331	10.4	0.0069	3.7	0.36	44.2	1.6	33.0	3.4	718.7	272.1	44.2	1.6
294	60	615	1.6	31.6505	8.4	0.0301	9.5	0.0069	4.3	0.46	44.4	1.9	30.1	2.8	1002.5	250.3	44.4	1.9
245	192	2448	2.8	21.7972	3.9	0.0438	4.6	0.0069	2.5	0.54	44.5	1.1	43.5	2.0	8.8	93.4	44.5	1.1
216	285	2231	1.6	23.4292	2.6	0.0407	3.5	0.0069	2.4	0.68	44.5	1.1	40.5	1.4	186.1	64.4	44.5	1.1
62	375	4388	2.1	21.6975	1.6	0.0444	2.7	0.0070	2.1	0.80	44.9	1.0	44.1	1.2	2.2	39.0	44.9	1.0
265	179	4711	1.7	22.7867	4.6	0.0423	5.5	0.0070	2.9	0.54	44.9	1.3	42.1	2.3	117.1	113.9	44.9	1.3
148	141	1391	1.7	25.4382	3.3	0.0379	4.1	0.0070	2.4	0.59	45.0	1.1	37.8	1.5	396.0	86.1	45.0	1.1
131	70	429	3.0	51.3433	11.4	0.0188	12.0	0.0070	4.0	0.33	45.1	1.8	19.0	2.3	2753.7	515.2	45.1	1.8
236	82	880	2.7	36.4384	8.3	0.0266	8.7	0.0070	2.7	0.31	45.1	1.2	26.6	2.3	1441.5	272.5	45.1	1.2
218	120	2992	2.5	23.3436	3.3	0.0415	4.7	0.0070	3.3	0.71	45.2	1.5	41.3	1.9	177.0	82.0	45.2	1.5
74	96	941	1.3	28.7367	21.3	0.0339	21.5	0.0071	2.7	0.13	45.4	1.2	33.8	7.2	724.7	600.8	45.4	1.2
264	248	6851	1.6	20.7151	2.7	0.0470	3.4	0.0071	2.1	0.61	45.4	0.9	46.6	1.5	112.7	63.4	45.4	0.9
292	216	4211	1.7	21.4692	2.8	0.0454	3.5	0.0071	2.1	0.59	45.4	0.9	45.1	1.6	27.7	67.9	45.4	0.9
23	52	355	2.2	118.4783	68.9	0.0082	69.0	0.0071	3.5	0.05	45.5	1.6	8.3	5.7	0.0	739.7	45.5	1.6
241	48	512	2.8	45.4295	24.1	0.0215	24.3	0.0071	3.2	0.13	45.5	1.4	21.6	5.2	2235.4	969.6	45.5	1.4
306	153	1349	1.9	28.0730	5.7	0.0349	6.2	0.0071	2.3	0.38	45.7	1.1	34.9	2.1	659.9	156.8	45.7	1.1
225	92	1425	1.5	23.8906	6.0	0.0411	6.9	0.0071	3.5	0.50	45.8	1.6	40.9	2.8	235.1	151.8	45.8	1.6
117	124	1408	3.6	26.0950	3.4	0.0378	4.3	0.0071	2.7	0.62	45.9	1.2	37.6	1.6	462.9	90.0	45.9	1.2
122	83	646	2.4	31.3826	37.1	0.0316	37.2	0.0072	3.2	0.09	46.2	1.5	31.6	11.6	977.4	1124.8	46.2	1.5
118	23	2111	2.4	22.7046	6.6	0.0440	8.5	0.0072	5.4	0.64	46.5	2.5	43.7	3.6	108.2	161.5	46.5	2.5
253	200	27297	1.5	21.2714	2.0	0.0472	3.3	0.0073	2.6	0.79	46.8	1.2	46.9	1.5	49.8	48.4	46.8	1.2
213	284	5083	2.0	21.3435	2.3	0.0474	3.1	0.0073	2.0	0.66	47.1	1.0	47.0	1.4	41.7	55.1	47.1	1.0
235	24	412	3.6	70.2383	38.5	0.0144	39.0	0.0073	5.8	0.15	47.2	2.7	14.5	5.6	0.0	1019.5	47.2	2.7
269	502	18079	2.8	20.9854	1.7	0.0488	2.7	0.0074	2.1	0.78	47.7	1.0	48.3	1.3	82.0	39.9	47.7	1.0
99	342	84110	1.9	19.9689	2.1	0.0515	3.2	0.0075	2.4	0.75	47.9	1.2	51.0	1.6	198.6	49.8	47.9	1.2
220	354	3708	1.9	21.9216	4.8	0.0473	5.4	0.0075	2.5	0.46	48.3	1.2	46.9	2.5	22.6	115.9	48.3	1.2
183	56	3738	2.7	22.9718	4.1	0.0453	5.3	0.0075	3.3	0.63	48.5	1.6	45.0	2.3	137.1	101.5	48.5	1.6
69	773	9122	2.8	21.0761	1.2	0.0502	2.6	0.0077	2.3	0.89	49.3	1.1	49.7	1.3	71.8	28.1	49.3	1.1
219	22	589	2.8	43.7517	16.2	0.0242	16.7	0.0077	4.2	0.25	49.4	2.1	24.3	4.0	2088.6	622.4	49.4	2.1
64	275	7924	2.8	21.0872	2.1	0.0510	2.9	0.0078	2.0	0.69	50.1	1.0	50.5	1.4	70.5	50.6	50.1	1.0
263	139	4388	3.7	21.5884	3.1	0.0632	4.1	0.0099	2.7	0.66	63.5	1.7	62.2	2.5	14.4	74.0	63.5	1.7
132	263	16039	2.3	20.4772	1.5	0.0679	2.7	0.0101	2.2	0.84	64.7	1.4	66.7	1.7	139.9	34.2	64.7	1.4
130	347	2093	1.8	23.1989	7.9	0.0602	8.1	0.0101	2.1	0.25	64.9	1.3	59.3	4.7	161.5	195.6	64.9	1.3
67	91	1956	2.6	25.3839	3.0	0.0564	4.6	0.0104	3.5	0.76	66.6	2.3	55.7	2.5	390.4	78.3	66.6	2.3
188	128	1597	2.4	24.9872	3.2	0.0577	4.0	0.0104	2.4	0.60	67.0	1.6	56.9	2.2	349.6	82.6	67.0	1.6
24	199	3827	2.8	19.4588	2.5	0.0748	3.6	0.0106	2.6	0.72	67.7	1.7	73.2	2.5	258.4	57.3	67.7	1.7
250	174	3011	2.2	23.5956	4.9	0.0621	5.6	0.0106	2.7	0.48	68.1	1.8	61.1	3.3	203.8	123.9	68.1	1.8
7	398	4145	7.7	22.1494	1.5	0.0671	3.1	0.0108	2.7	0.87	69.2	1.9	66.0	2.0	47.6	37.6	69.2	1.9
100	180	2776	2.1	23.5329	6.5	0.0633	7.0	0.0108	2.4	0.34	69.3	1.6	62.3	4.2	197.2	164.0	69.3	1.6
119	155	3297	1.9	18.7188	3.2	0.0796	4.2	0.0108	2.7	0.64	69.3	1.9	77.8	3.1	346.8	73.2	69.3	1.9
297	638	11089	2.7	21.9655	1.1	0.0679	2.2	0.0108	1.8	0.85	69.4	1.3	66.7	1.4	27.4	27.4	69.4	1.3
2	507	14684	1.8	20.8974	1.4	0.0723	2.4	0.0110	2.0	0.83	70.2	1.4	70.9	1.7	92.0	32.0	70.2	1.4
152	268	1792	1.5	24.8372	1.4	0.0612	3.1	0.0110	2.7	0.89	70.7	1.9	60.4	1.8	334.1	36.0	70.7	1.9
163	78	4156	1.8	21.8053	2.5	0.0698	3.6	0.0110	2.6	0.72	70.7	1.8	68.5	2.4	9.7	60.2	70.7	1.8
39	104	1969	1.8	24.0260	3.6	0.0634	4.6	0.0110	2.9	0.63	70.8	2.0	62.4	2.8	249.4	90.3	70.8	2.0
21	300	18611	2.4	20.0399	1.5	0.0760	2.9	0.0110	2.5	0.85	70.8	1.7	74.4	2.1	190.4	35.7	70.8	1.7
135	150	2216	2.1	21.7538	3.0	0.0713	3.7	0.0112	2.1	0.57	72.1	1.5	69.9	2.5	4.0	73.2	72.1	1.5
272	176	4469	2.0	21.5836	1.9	0.0722	3.3	0.0113	2.7	0.82	72.5	1.9	70.8	2.3	14.9	45.8	72.5	1.9
51	339	9902	2.5	20.6349	1.6	0.0756	2.5	0.0113	2.0	0.77	72.5	1.4	74.0	1.8	121.9	38.2	72.5	1.4
105	177	10025	1.3	20.5110	2.3	0.0763	3.5	0.0113	2.6	0.75	72.7	1.9	74.6	2.5	136.0	54.1	72.7	1.9
49	222	1719	0.9	24.1958	2.6	0.0648	3.3	0.0114	2.0	0.61	72.9	1.5	63.8	2.1	267.2	67.1	72.9	1.5

96	341	3055	2.6	21.6103	5.5	0.0727	6.0	0.0114	2.5	0.42	73.0	1.8	71.2	4.1	11.9	131.5	73.0	1.8
249	629	793187	1.6	20.9763	1.4	0.0754	3.0	0.0115	2.7	0.89	73.5	2.0	73.8	2.1	83.0	32.8	73.5	2.0
65	103	6231	1.1	18.6078	3.8	0.0852	4.8	0.0115	2.8	0.60	73.7	2.1	83.0	3.8	360.2	85.9	73.7	2.1
243	480	24615	1.9	19.5591	1.6	0.0819	2.6	0.0116	2.1	0.79	74.5	1.5	80.0	2.0	246.5	36.7	74.5	1.5
37	119	1916	1.3	25.2199	3.0	0.0636	4.5	0.0116	3.4	0.76	74.5	2.5	62.6	2.7	373.6	76.7	74.5	2.5
90	377	9186	2.4	21.3258	1.7	0.0756	2.6	0.0117	2.0	0.76	75.0	1.5	74.0	1.8	43.7	40.4	75.0	1.5
177	61	1122	1.6	23.9980	3.6	0.0673	4.4	0.0117	2.6	0.59	75.1	2.0	66.2	2.8	246.4	90.2	75.1	2.0
20	400	7538	1.4	20.0793	1.5	0.0806	2.7	0.0117	2.2	0.82	75.2	1.6	78.7	2.0	185.8	35.9	75.2	1.6
81	167	3334	2.1	19.1233	3.2	0.0847	4.3	0.0117	2.8	0.66	75.2	2.1	82.5	3.4	298.2	72.5	75.2	2.1
252	371	6336	1.8	21.5805	2.8	0.0756	3.4	0.0118	2.0	0.57	75.8	1.5	74.0	2.4	15.2	67.3	75.8	1.5
208	382	112481	1.9	19.3451	2.0	0.0844	3.0	0.0118	2.2	0.74	75.9	1.7	82.2	2.4	271.8	46.3	75.9	1.7
224	382	13924	2.1	21.1294	1.4	0.0790	2.4	0.0121	1.9	0.81	77.5	1.5	77.2	1.8	65.8	33.1	77.5	1.5
170	327	1598	4.1	24.7303	7.6	0.0676	7.8	0.0121	2.0	0.26	77.7	1.5	66.5	5.0	323.0	194.2	77.7	1.5
313	220	6611	1.8	19.9592	1.6	0.0844	2.8	0.0122	2.3	0.82	78.3	1.8	82.3	2.2	199.7	36.7	78.3	1.8
114	398	14289	1.7	20.3417	1.4	0.0829	2.5	0.0122	2.1	0.83	78.4	1.6	80.9	1.9	155.4	31.8	78.4	1.6
260	133	760	2.5	11.5867	11.2	0.1467	11.9	0.0123	3.7	0.32	79.0	2.9	139.0	15.4	1345.0	217.9	79.0	2.9
6	48	706	2.2	36.9530	27.6	0.0475	27.9	0.0127	3.7	0.13	81.5	3.0	47.1	12.8	1487.7	928.7	81.5	3.0
270	378	10314	3.3	21.1126	1.8	0.0831	3.4	0.0127	2.9	0.86	81.5	2.3	81.1	2.6	67.7	41.7	81.5	2.3
57	142	2778	2.2	15.7688	4.3	0.1127	4.7	0.0129	1.8	0.39	82.5	1.5	108.4	4.8	722.2	91.6	82.5	1.5
185	92	1602	1.3	23.6804	3.3	0.0755	6.7	0.0130	5.8	0.87	83.1	4.8	73.9	4.8	212.8	82.7	83.1	4.8
222	364	64425	2.6	20.8722	1.5	0.0857	2.4	0.0130	1.9	0.79	83.1	1.6	83.5	2.0	94.9	35.3	83.1	1.6
25	745	9079	2.2	20.3419	1.2	0.0890	2.8	0.0131	2.5	0.90	84.1	2.1	86.5	2.3	155.4	29.2	84.1	2.1
212	99	7799	1.8	20.4971	2.2	0.0891	3.7	0.0132	3.0	0.81	84.8	2.5	86.7	3.1	137.6	50.6	84.8	2.5
158	256	4435	1.5	21.4719	1.5	0.0853	2.7	0.0133	2.3	0.83	85.0	1.9	83.1	2.2	27.4	36.4	85.0	1.9
303	222	4406	1.3	22.2125	2.1	0.0831	3.1	0.0134	2.3	0.75	85.7	2.0	81.0	2.4	54.6	50.0	85.7	2.0
40	89	1437	2.4	24.0153	4.7	0.0777	5.8	0.0135	3.4	0.59	86.6	2.9	75.9	4.2	248.2	118.3	86.6	2.9
285	790	19698	1.6	21.2322	1.1	0.0882	2.4	0.0136	2.2	0.89	87.0	1.9	85.9	2.0	54.2	25.9	87.0	1.9
153	246	2496	5.0	23.3887	1.9	0.0802	3.0	0.0136	2.4	0.78	87.1	2.1	78.4	2.3	181.8	47.0	87.1	2.1
32	109	4620	2.1	21.1011	2.0	0.0901	3.4	0.0138	2.8	0.82	88.2	2.4	87.6	2.9	68.9	47.0	88.2	2.4
29	84	141637	2.5	18.2516	4.3	0.1042	5.5	0.0138	3.5	0.63	88.3	3.0	100.7	5.3	403.6	96.6	88.3	3.0
11	303	11846	7.4	21.4505	1.5	0.0892	2.8	0.0139	2.4	0.84	88.8	2.1	86.7	2.3	29.8	36.9	88.8	2.1
78	127	4125	2.0	22.3285	2.4	0.0865	3.4	0.0140	2.5	0.73	89.7	2.2	84.2	2.8	67.3	57.8	89.7	2.2
267	526	145346	0.8	21.0503	1.2	0.0918	2.2	0.0140	1.8	0.84	89.7	1.6	89.2	1.9	74.7	28.5	89.7	1.6
266	1181	10624	4.2	20.5376	1.2	0.0950	2.5	0.0142	2.2	0.88	90.6	2.0	92.2	2.2	133.0	28.1	90.6	2.0
210	1111	43544	20.9	20.5745	1.0	0.0952	2.1	0.0142	1.8	0.87	91.0	1.6	92.4	1.8	128.8	24.0	91.0	1.6
112	31	813	1.7	34.9803	9.0	0.0560	10.1	0.0142	4.6	0.46	91.0	4.2	55.4	5.4	1309.6	285.3	91.0	4.2
305	320	1494	2.3	22.8786	3.3	0.0862	3.8	0.0143	1.9	0.50	91.5	1.7	84.0	3.1	127.0	82.5	91.5	1.7
290	357	11537	2.1	21.2826	1.4	0.0933	2.7	0.0144	2.3	0.85	92.2	2.1	90.6	2.3	48.5	33.9	92.2	2.1
68	607	37394	2.6	20.2518	1.2	0.0983	2.1	0.0144	1.8	0.84	92.4	1.6	95.2	1.9	165.8	27.4	92.4	1.6
108	206	2465	1.8	15.7756	6.6	0.1262	7.2	0.0144	2.9	0.40	92.4	2.7	120.7	8.2	721.3	140.5	92.4	2.7
110	807	135645	1.6	20.5767	0.9	0.0972	2.2	0.0145	1.9	0.90	92.8	1.8	94.2	1.9	128.5	22.0	92.8	1.8
13	652	242907	1.9	20.1637	1.4	0.0995	2.8	0.0146	2.4	0.86	93.2	2.3	96.3	2.6	176.0	33.3	93.2	2.3
174	240	15870	3.1	20.3217	2.0	0.0992	3.3	0.0146	2.6	0.79	93.5	2.4	96.0	3.0	157.8	47.6	93.5	2.4
52	118	4394	2.7	20.8193	4.0	0.0970	4.8	0.0146	2.7	0.56	93.7	2.5	94.0	4.3	100.9	95.0	93.7	2.5
162	838	85876	1.8	20.9211	1.5	0.0966	3.2	0.0147	2.8	0.88	93.8	2.6	93.7	2.9	89.3	35.6	93.8	2.6
273	309	6726	3.0	21.4498	1.6	0.0944	2.5	0.0147	1.9	0.76	93.9	1.8	91.6	2.2	29.8	38.1	93.9	1.8
56	149	3843	2.5	22.5751	2.6	0.0898	3.6	0.0147	2.6	0.71	94.1	2.4	87.3	3.0	94.2	62.7	94.1	2.4
133	1243	1960974	7.7	20.5080	0.8	0.0991	1.6	0.0147	1.4	0.88	94.3	1.3	95.9	1.5	136.4	17.8	94.3	1.3
121	162	4707	3.1	21.9751	1.8	0.0932	3.1	0.0149	2.6	0.82	95.1	2.4	90.5	2.7	28.5	43.8	95.1	2.4
164	1757	208706	13.2	20.6817	0.8	0.0997	2.0	0.0149	1.8	0.92	95.6	1.8	96.5	1.8	116.5	18.8	95.6	1.8
276	965	163572	4.8	20.6163	0.8	0.1002	2.2	0.0150	2.1	0.93	95.8	2.0	96.9	2.0	124.0	18.8	95.8	2.0
35	245	887	1.2	32.0915	6.6	0.0655	7.1	0.0152	2.4	0.34	97.6	2.3	64.4	4.4	1043.7	199.2	97.6	2.3
143	771	36498	2.7	20.2824	1.0	0.1040	1.8	0.0153	1.5	0.83	97.8	1.5	100.4	1.8	162.3	24.2	97.8	1.5
199	140	4524	1.6	21.2189	3.1	0.0998	3.8	0.0154	2.3	0.61	98.3	2.3	96.6	3.5	55.7	73.0	98.3	2.3
211	881	14846	1.7	20.6190	1.4	0.1030	2.6	0.0154	2.2	0.85	98.5	2.2	99.5	2.5	123.7	31.9	98.5	2.2
30	282	7502	2.5	21.3665	1.5	0.0996	2.5	0.0154	2.0	0.79	98.7	1.9	96.4	2.3	39.2	37.0	98.7	1.9
87	462	12192	4.0	20.7776	1.3	0.1028	2.4	0.0155	2.0	0.85	99.1	2.0	99.4	2.2	105.6	29.8	99.1	2.0
124	1309	157320	2.5	20.5056	0.8	0.1045	2.4	0.0155	2.3	0.95	99.4	2.2	100.9	2.3	136.6	18.4	99.4	2.2

230	658	60042	2.2	20.4911	1.2	0.1048	2.7	0.0156	2.4	0.89	99.6	2.4	101.2	2.6	138.3	28.8	99.6	2.4
42	261	7445	1.9	21.3575	2.3	0.1011	3.5	0.0157	2.6	0.74	100.1	2.6	97.8	3.2	40.2	55.9	100.1	2.6
315	331	2308	3.0	23.4524	4.5	0.0921	5.0	0.0157	2.3	0.45	100.2	2.3	89.5	4.3	188.6	111.5	100.2	2.3
102	267	7090	2.0	21.1155	1.5	0.1035	2.8	0.0159	2.4	0.85	101.4	2.4	100.0	2.7	67.3	35.5	101.4	2.4
147	290	23226	2.0	20.9057	1.6	0.1060	2.3	0.0161	1.7	0.73	102.7	1.7	102.3	2.2	91.1	36.8	102.7	1.7
165	121	6083	2.0	20.7946	1.9	0.1079	3.2	0.0163	2.5	0.80	104.0	2.6	104.0	3.1	103.7	45.2	104.0	2.6
50	281	7141	2.2	21.2575	1.9	0.1058	2.9	0.0163	2.2	0.75	104.3	2.2	102.1	2.8	51.3	45.7	104.3	2.2
76	208	2148	1.4	23.7388	1.8	0.0950	2.9	0.0164	2.3	0.78	104.6	2.3	92.1	2.6	219.0	45.9	104.6	2.3
83	136	255	1.5	3.1994	50.1	0.7154	50.6	0.0166	7.4	0.15	106.1	7.8	547.9	217.6	3533.6	1446.1	106.1	7.8
191	183	2026	2.6	22.3406	4.0	0.1028	4.9	0.0167	2.8	0.57	106.5	3.0	99.4	4.7	68.6	98.9	106.5	3.0
149	161	5532	1.5	21.1495	2.0	0.1087	3.1	0.0167	2.4	0.78	106.6	2.6	104.8	3.1	63.5	46.7	106.6	2.6
172	201	3797	2.1	21.9626	2.0	0.1051	3.2	0.0167	2.4	0.78	107.1	2.6	101.5	3.0	27.1	48.1	107.1	2.6
4	415	4541	3.2	21.5114	1.2	0.1077	2.7	0.0168	2.5	0.90	107.4	2.6	103.8	2.7	22.9	29.3	107.4	2.6
281	648	986537	2.1	20.4486	1.1	0.1134	2.5	0.0168	2.3	0.91	107.5	2.4	109.1	2.6	143.2	24.7	107.5	2.4
196	471	6174	1.2	21.2674	1.0	0.1097	2.2	0.0169	2.0	0.90	108.1	2.1	105.7	2.2	50.2	23.3	108.1	2.1
86	1016	43393	3.6	20.5751	0.8	0.1138	2.3	0.0170	2.1	0.93	108.6	2.3	109.4	2.4	128.7	19.1	108.6	2.3
113	788	13820	10.2	20.7501	1.0	0.1129	2.2	0.0170	2.0	0.89	108.6	2.1	108.6	2.3	108.7	23.7	108.6	2.1
190	184	21671	2.5	19.4337	1.5	0.1207	2.6	0.0170	2.1	0.82	108.7	2.3	115.7	2.8	261.4	33.8	108.7	2.3
254	117	3303	3.6	22.4095	2.5	0.1055	3.7	0.0171	2.7	0.74	109.6	3.0	101.8	3.6	76.1	61.7	109.6	3.0
228	103	2651	3.2	14.8485	3.3	0.1606	5.8	0.0173	4.7	0.82	110.6	5.2	151.3	8.1	848.5	67.8	110.6	5.2
271	263	12173	1.6	20.4590	1.1	0.1168	2.9	0.0173	2.6	0.93	110.8	2.9	112.2	3.0	142.0	24.9	110.8	2.9
126	283	883369	1.4	20.3166	1.2	0.1179	2.6	0.0174	2.3	0.88	111.0	2.5	113.1	2.8	158.4	28.7	111.0	2.5
84	416	4052	1.7	22.0786	1.6	0.1095	2.6	0.0175	2.1	0.79	112.0	2.3	105.5	2.6	39.9	39.1	112.0	2.3
85	78	5687	2.4	21.9560	2.9	0.1115	4.3	0.0178	3.1	0.73	113.4	3.5	107.3	4.3	26.3	70.7	113.4	3.5
28	108	3182	4.0	21.6376	4.8	0.1132	5.6	0.0178	2.8	0.51	113.6	3.2	108.9	5.7	8.9	114.7	113.6	3.2
44	842	76204	1.6	20.2764	0.8	0.1212	2.0	0.0178	1.8	0.92	113.9	2.1	116.2	2.2	163.0	18.4	113.9	2.1
115	129	14594	2.3	19.8400	1.7	0.1262	3.2	0.0182	2.7	0.84	116.0	3.1	120.7	3.6	213.7	39.6	116.0	3.1
107	408	14755	1.5	20.7349	1.1	0.1215	2.8	0.0183	2.6	0.92	116.7	3.0	116.5	3.1	110.5	25.6	116.7	3.0
89	351	10957	2.5	20.9653	1.8	0.1204	3.5	0.0183	3.1	0.86	117.0	3.5	115.5	3.9	84.3	42.4	117.0	3.5
274	115	3507	1.5	22.5588	2.2	0.1145	3.3	0.0187	2.5	0.75	119.6	3.0	110.1	3.5	92.4	53.9	119.6	3.0
311	491	56875	1.6	17.7437	1.1	0.1464	2.7	0.0188	2.5	0.91	120.3	2.9	138.7	3.5	466.5	24.3	120.3	2.9
18	272	285580	2.3	20.0394	1.4	0.1322	2.6	0.0192	2.2	0.85	122.7	2.7	126.1	3.1	190.4	31.9	122.7	2.7
268	393	117754	1.0	20.2458	1.0	0.1445	2.6	0.0212	2.4	0.93	135.3	3.2	137.0	3.3	166.5	22.5	135.3	3.2
8	361	100637	0.5	19.8736	1.1	0.1487	2.7	0.0214	2.5	0.91	136.7	3.4	140.7	3.6	209.7	26.2	136.7	3.4
227	129	2326	1.9	23.4529	7.7	0.1279	8.1	0.0218	2.5	0.30	138.7	3.4	122.2	9.3	188.6	192.7	138.7	3.4
287	515	38156	3.1	20.4924	0.9	0.1480	2.6	0.0220	2.4	0.93	140.2	3.3	140.1	3.4	138.1	21.4	140.2	3.3
19	407	11930	2.5	20.5699	1.4	0.1484	2.4	0.0221	2.0	0.83	141.2	2.8	140.5	3.2	129.3	32.5	141.2	2.8
184	113	9505	3.2	20.4347	1.6	0.1504	2.8	0.0223	2.3	0.82	142.2	3.2	142.3	3.7	144.8	37.9	142.2	3.2
146	148	7941	4.0	20.4711	1.4	0.1509	2.7	0.0224	2.3	0.86	142.9	3.2	142.7	3.6	140.6	32.7	142.9	3.2
233	89	29102	2.0	19.6825	1.7	0.1572	3.0	0.0224	2.5	0.83	143.0	3.5	148.2	4.1	232.0	38.5	143.0	3.5
242	84	5081	4.4	20.4926	2.1	0.1511	3.5	0.0225	2.9	0.81	143.2	4.0	142.9	4.7	138.1	48.5	143.2	4.0
166	1359	21819	8.9	15.8729	2.5	0.1985	4.4	0.0229	3.6	0.82	145.7	5.2	183.9	7.4	708.2	54.0	145.7	5.2
3	71	1167	2.3	25.0600	2.9	0.1264	4.3	0.0230	3.1	0.72	146.4	4.4	120.9	4.9	357.1	76.2	146.4	4.4
66	208	7368	1.7	20.3210	1.6	0.1570	3.3	0.0231	2.9	0.88	147.4	4.2	148.1	4.5	157.9	36.5	147.4	4.2
93	59	2054	2.5	22.6804	3.1	0.1416	4.1	0.0233	2.7	0.64	148.5	3.9	134.5	5.2	105.6	77.5	148.5	3.9
15	596	54660	1.9	20.2691	0.8	0.1588	2.0	0.0233	1.9	0.92	148.7	2.7	149.6	2.8	163.8	18.1	148.7	2.7
142	37	910	3.2	19.3904	9.6	0.1662	10.7	0.0234	4.6	0.43	148.9	6.8	156.1	15.5	266.5	221.4	148.9	6.8
203	89	28055	2.4	19.6666	2.2	0.1641	3.3	0.0234	2.4	0.74	149.2	3.6	154.3	4.7	233.9	50.8	149.2	3.6
82	127	3691	2.1	21.7254	3.1	0.1486	3.9	0.0234	2.3	0.60	149.2	3.5	140.7	5.1	0.8	75.1	149.2	3.5
63	222	10800	2.4	20.3604	1.1	0.1590	2.4	0.0235	2.1	0.89	149.6	3.2	149.8	3.3	153.3	25.1	149.6	3.2
109	60	86934	1.8	19.9309	2.3	0.1625	4.4	0.0235	3.7	0.84	149.7	5.4	152.9	6.2	203.1	54.2	149.7	5.4
9	110	8896	2.5	18.7361	3.1	0.1735	4.2	0.0236	2.9	0.69	150.2	4.3	162.4	6.3	344.7	69.4	150.2	4.3
54	225	3566	2.7	21.0697	1.4	0.1545	2.5	0.0236	2.0	0.82	150.4	3.0	145.8	3.3	72.5	33.3	150.4	3.0
295	618	35348	4.2	18.8237	1.4	0.1733	3.4	0.0237	3.1	0.91	150.7	4.7	162.3	5.1	334.1	31.5	150.7	4.7
175	269	10645	3.3	20.8316	1.6	0.1568	2.5	0.0237	1.9	0.77	150.9	2.9	147.9	3.5	99.5	37.8	150.9	2.9
91	42	25550	2.8	20.7619	3.4	0.1582	4.8	0.0238	3.4	0.72	151.8	5.2	149.2	6.7	107.4	79.4	151.8	5.2
77	163	2513	2.1	22.6278	1.6	0.1454	2.8	0.0239	2.3	0.83	152.0	3.5	137.9	3.6	99.9	38.6	152.0	3.5
180	317	32675	2.5	20.4314	1.2	0.1613	2.4	0.0239	2.1	0.87	152.3	3.1	151.8	3.4	145.1	27.5	152.3	3.1

288	96	4327	2.3	20.9444	3.4	0.1575	4.3	0.0239	2.6	0.61	152.4	4.0	148.5	5.9	86.7	80.0	152.4	4.0
221	174	10247	1.3	20.4897	1.7	0.1615	3.3	0.0240	2.8	0.85	152.9	4.2	152.0	4.6	138.5	40.4	152.9	4.2
261	31	1919	2.3	24.0811	4.1	0.1374	5.3	0.0240	3.4	0.64	152.9	5.1	130.7	6.5	255.2	102.9	152.9	5.1
238	124	2776	2.2	22.1687	2.5	0.1497	3.6	0.0241	2.6	0.71	153.3	3.9	141.6	4.8	49.8	61.7	153.3	3.9
70	42	2112	2.5	23.3473	3.1	0.1426	5.2	0.0242	4.1	0.80	153.8	6.3	135.4	6.5	177.4	77.5	153.8	6.3
128	460	50801	0.8	20.2763	1.2	0.1645	2.6	0.0242	2.4	0.90	154.1	3.6	154.6	3.8	163.0	26.9	154.1	3.6
247	68	7771	2.5	19.8578	2.3	0.1680	3.7	0.0242	2.9	0.78	154.1	4.5	157.7	5.5	211.5	54.0	154.1	4.5
38	199	59810	1.5	19.9804	1.2	0.1675	2.8	0.0243	2.6	0.91	154.6	3.9	157.3	4.1	197.3	27.7	154.6	3.9
155	97	2827	1.6	21.5693	1.6	0.1552	3.1	0.0243	2.7	0.86	154.7	4.1	146.5	4.2	16.5	37.8	154.7	4.1
88	352	9496	1.9	20.3332	1.2	0.1652	2.3	0.0244	2.0	0.85	155.2	3.1	155.3	3.4	156.5	28.7	155.2	3.1
10	412	41984	1.8	20.3028	1.2	0.1659	2.2	0.0244	1.9	0.85	155.6	2.8	155.9	3.2	160.0	26.9	155.6	2.8
296	201	8868	3.5	20.0107	1.2	0.1693	2.8	0.0246	2.5	0.90	156.5	3.9	158.8	4.1	193.8	28.2	156.5	3.9
95	95	4642	1.6	21.0280	2.9	0.1612	4.1	0.0246	2.9	0.71	156.6	4.5	151.7	5.8	77.2	69.2	156.6	4.5
139	106	315316	2.5	19.9559	1.7	0.1701	3.3	0.0246	2.8	0.85	156.8	4.3	159.5	4.8	200.1	39.9	156.8	4.3
12	230	5308	2.1	17.9386	3.5	0.1895	7.6	0.0247	6.7	0.89	157.0	10.4	176.2	12.2	442.2	77.9	157.0	10.4
258	100	4100	2.7	21.2268	4.1	0.1602	5.1	0.0247	3.1	0.61	157.1	4.9	150.9	7.2	54.8	97.0	157.1	4.9
104	215	2692	2.0	18.9819	3.9	0.1795	4.3	0.0247	1.8	0.42	157.3	2.8	167.6	6.6	315.1	88.5	157.3	2.8
280	157	9638	2.0	20.4242	1.7	0.1668	2.9	0.0247	2.4	0.82	157.3	3.7	156.6	4.2	146.0	39.0	157.3	3.7
307	358	6627	1.4	20.9984	1.0	0.1623	2.2	0.0247	2.0	0.89	157.4	3.0	152.7	3.1	80.5	24.1	157.4	3.0
48	416	9187	1.5	19.4349	2.5	0.1754	3.2	0.0247	2.0	0.63	157.4	3.1	164.1	4.8	261.2	56.4	157.4	3.1
101	260	23895	1.5	20.1086	1.1	0.1697	2.5	0.0248	2.3	0.89	157.6	3.5	159.2	3.7	182.4	26.7	157.6	3.5
312	338	55246	2.3	19.5745	1.1	0.1745	2.2	0.0248	1.9	0.86	157.7	3.0	163.3	3.3	244.7	25.6	157.7	3.0
197	182	5573	2.3	20.4502	2.4	0.1676	3.6	0.0249	2.7	0.74	158.2	4.2	157.3	5.3	143.0	57.1	158.2	4.2
98	186	2383	2.9	22.7668	7.2	0.1505	7.6	0.0249	2.5	0.32	158.3	3.8	142.4	10.1	114.9	178.0	158.3	3.8
257	222	14053	2.4	20.3209	1.4	0.1695	2.4	0.0250	2.0	0.81	159.1	3.1	159.0	3.6	157.9	33.0	159.1	3.1
129	340	14871	1.8	19.9329	1.4	0.1737	3.0	0.0251	2.7	0.89	159.8	4.2	162.6	4.5	202.8	31.6	159.8	4.2
189	490	117490	1.5	20.0659	0.9	0.1728	2.3	0.0252	2.1	0.92	160.1	3.3	161.9	3.4	187.3	20.9	160.1	3.3
215	258	8333	1.8	20.3704	1.2	0.1708	2.4	0.0252	2.1	0.87	160.7	3.3	160.1	3.5	152.2	27.5	160.7	3.3
92	115	5107	2.0	20.7973	2.3	0.1682	3.4	0.0254	2.6	0.75	161.5	4.1	157.9	5.0	103.4	53.8	161.5	4.1
237	279	4613	1.2	21.1409	1.2	0.1667	2.3	0.0256	1.9	0.85	162.7	3.1	156.6	3.3	64.5	28.0	162.7	3.1
298	378	7837	2.0	20.9076	1.9	0.1697	2.9	0.0257	2.2	0.76	163.8	3.5	159.2	4.2	90.9	44.3	163.8	3.5
186	134	1486	3.2	24.5568	12.5	0.1447	12.7	0.0258	2.4	0.19	164.0	3.9	137.2	16.3	305.0	320.0	164.0	3.9
140	108	2471	1.9	22.5760	1.9	0.1578	3.2	0.0258	2.5	0.80	164.4	4.1	148.7	4.4	94.3	46.3	164.4	4.1
244	168	11380	1.8	20.7270	1.4	0.1721	2.7	0.0259	2.3	0.85	164.6	3.7	161.2	4.0	111.4	32.6	164.6	3.7
16	62	13413	2.8	20.6854	2.6	0.1729	3.9	0.0259	2.9	0.74	165.1	4.7	161.9	5.8	116.1	61.7	165.1	4.7
195	2416	1051791	4.7	20.2855	0.7	0.1800	2.6	0.0265	2.5	0.96	168.5	4.2	168.0	4.1	161.9	16.7	168.5	4.2
45	647	65325	1.8	19.9731	1.1	0.1835	2.5	0.0266	2.2	0.89	169.1	3.7	171.1	3.9	198.1	25.8	169.1	3.7
304	275	17086	1.4	19.9916	1.2	0.1842	2.6	0.0267	2.3	0.88	169.9	3.8	171.7	4.1	196.0	28.6	169.9	3.8
301	811	86870	1.8	20.1410	0.9	0.1896	2.1	0.0277	1.9	0.90	176.1	3.3	176.3	3.4	178.6	21.0	176.1	3.3
150	111	4076	10.5	20.7334	2.0	0.1846	3.1	0.0278	2.4	0.77	176.5	4.2	172.0	5.0	110.6	47.4	176.5	4.2
194	98	17376	2.6	20.1968	1.7	0.1903	3.5	0.0279	3.0	0.86	177.2	5.2	176.9	5.6	172.2	40.8	177.2	5.2
47	127	5025	2.1	21.1590	1.5	0.1868	3.3	0.0287	2.9	0.89	182.2	5.3	173.9	5.3	62.4	36.3	182.2	5.3
79	173	4436	2.8	21.1117	1.6	0.1875	3.4	0.0287	3.0	0.89	182.4	5.4	174.5	5.4	67.8	37.1	182.4	5.4
251	256	7138	2.4	20.4317	1.1	0.1943	2.2	0.0288	1.9	0.87	183.0	3.4	180.3	3.6	145.1	25.3	183.0	3.4
201	332	8754	2.0	20.3610	1.2	0.1962	2.5	0.0290	2.1	0.86	184.1	3.8	181.9	4.1	153.2	29.2	184.1	3.8
202	349	21235	1.4	19.9131	1.3	0.2011	2.7	0.0290	2.3	0.88	184.5	4.2	186.0	4.5	205.1	29.4	184.5	4.2
205	323	38423	1.6	19.5172	1.3	0.2056	2.5	0.0291	2.2	0.86	184.9	4.0	189.9	4.4	251.5	29.7	184.9	4.0
286	101	106828	2.7	19.0572	1.7	0.2115	2.7	0.0292	2.1	0.79	185.7	3.9	194.8	4.8	306.1	38.0	185.7	3.9
214	331	32712	2.1	19.5820	1.0	0.2087	2.4	0.0296	2.2	0.91	188.3	4.1	192.5	4.3	243.9	23.2	188.3	4.1
198	511	28645	2.3	20.2026	1.1	0.2025	2.6	0.0297	2.4	0.91	188.5	4.5	187.3	4.5	171.5	24.8	188.5	4.5
283	326	15062	2.7	19.7791	1.2	0.2075	2.4	0.0298	2.1	0.88	189.1	3.9	191.4	4.2	220.7	26.8	189.1	3.9
239	217	6214	2.2	20.6991	1.4	0.1984	3.2	0.0298	2.9	0.90	189.2	5.4	183.8	5.4	114.5	33.1	189.2	5.4
240	334	53551	2.3	19.7364	1.1	0.2113	2.6	0.0302	2.3	0.90	192.0	4.4	194.6	4.6	225.8	26.2	192.0	4.4
36	410	74246	3.0	19.9661	0.9	0.2092	2.3	0.0303	2.1	0.92	192.4	4.0	192.9	4.1	198.9	21.2	192.4	4.0
154	333	29125	3.9	20.1099	0.9	0.2080	1.8	0.0303	1.6	0.87	192.7	3.0	191.9	3.2	182.2	21.4	192.7	3.0
207	130	4201	1.5	14.0754	6.6	0.3029	7.7	0.0309	4.0	0.52	196.3	7.7	268.7	18.2	958.7	135.2	196.3	7.7
27	217	18768	2.4	20.0300	0.9	0.2148	2.6	0.0312	2.4	0.94	198.1	4.7	197.6	4.6	191.5	20.5	198.1	4.7
46	68	2681	4.8	20.2637	2.9	0.2233	4.1	0.0328	2.9	0.71	208.2	6.0	204.7	7.7	164.4	67.9	208.2	6.0

59	105	2301	3.1	21.5943	1.7	0.2168	3.2	0.0340	2.7	0.84	215.3	5.7	199.3	5.7	13.7	41.1	215.3	5.7
248	60	7678	3.9	19.7335	1.7	0.2697	3.7	0.0386	3.2	0.89	244.1	7.8	242.4	7.9	226.1	39.4	244.1	7.8
171	66	3193	3.3	20.4440	2.4	0.3285	3.5	0.0487	2.6	0.73	306.6	7.8	288.4	8.9	143.7	56.6	306.6	7.8
156	366	27712	1.8	19.2923	1.1	0.3591	2.4	0.0502	2.1	0.90	316.0	6.6	311.5	6.4	278.1	24.3	316.0	6.6
71	828	32261	4.5	11.0911	1.1	0.6548	6.3	0.0527	6.2	0.99	330.9	20.0	511.4	25.2	1429.0	20.1	330.9	20.0
200	127	38054	1.4	17.9774	1.0	0.4765	2.3	0.0621	2.1	0.91	388.5	7.7	395.6	7.4	437.4	21.4	388.5	7.7
169	106	8630	2.4	17.7227	0.9	0.5907	2.4	0.0759	2.3	0.94	471.8	10.3	471.3	9.2	469.1	19.1	471.8	10.3
141	36	9809	2.3	17.7819	1.7	0.5953	3.9	0.0768	3.5	0.90	476.9	16.2	474.3	14.8	461.7	37.3	476.9	16.2
275	98	11148	2.2	17.7996	1.0	0.5965	3.2	0.0770	3.0	0.95	478.2	14.0	475.0	12.2	459.5	22.5	478.2	14.0
289	166	9179	2.6	17.7682	1.1	0.5996	2.5	0.0773	2.3	0.91	479.8	10.7	477.0	9.7	463.5	23.5	479.8	10.7
179	202	6377	2.4	17.4226	1.1	0.6467	3.3	0.0817	3.1	0.94	506.3	15.3	506.4	13.2	506.8	23.9	506.3	15.3
157	654	40494	9.1	16.5451	0.7	0.6958	1.9	0.0835	1.8	0.93	516.9	8.9	536.3	8.0	619.4	15.5	516.9	8.9
111	33	15837	0.4	16.5125	1.4	0.7337	4.5	0.0879	4.2	0.95	542.9	22.0	558.7	19.1	623.6	30.7	542.9	22.0
33	143	26300	1.8	13.4719	0.9	1.7931	2.3	0.1752	2.1	0.92	1040.7	19.9	1042.9	14.7	1047.7	18.0	1047.7	18.0
5	1279	242846	1.7	11.9480	0.8	2.6610	2.3	0.2306	2.1	0.94	1337.6	25.9	1317.7	16.9	1285.5	15.5	1285.5	15.5
41	1219	254551	12.0	11.6799	1.4	2.4340	3.3	0.2062	3.1	0.91	1208.4	33.6	1252.7	24.1	1329.5	26.8	1329.5	26.8
80	123	9751	1.1	11.6391	1.0	2.5684	3.1	0.2168	2.9	0.94	1265.0	33.1	1291.7	22.4	1336.3	20.3	1336.3	20.3
217	179	245101	2.6	11.5880	0.6	2.5127	2.4	0.2112	2.3	0.97	1235.1	26.0	1275.7	17.4	1344.8	11.9	1344.8	11.9
277	329	33048	2.3	11.5810	0.7	2.7027	2.2	0.2270	2.1	0.94	1318.8	25.1	1329.2	16.5	1346.0	14.2	1346.0	14.2
187	631	228105	2.4	11.5779	0.8	2.7452	2.4	0.2305	2.3	0.94	1337.2	27.2	1340.8	17.9	1346.5	15.8	1346.5	15.8
43	382	266535	4.6	11.5639	0.6	2.6641	2.1	0.2234	2.0	0.95	1300.0	23.3	1318.6	15.3	1348.8	12.2	1348.8	12.2
22	277	216279	2.7	11.5622	0.8	2.7335	2.2	0.2292	2.1	0.94	1330.4	25.1	1337.6	16.6	1349.1	14.8	1349.1	14.8
256	357	206559	3.5	11.5555	0.8	2.7254	2.1	0.2284	1.9	0.93	1326.1	23.1	1335.4	15.5	1350.2	15.2	1350.2	15.2
14	282	44344	2.9	11.5554	0.7	2.8312	1.8	0.2373	1.7	0.93	1372.5	20.8	1363.8	13.6	1350.3	12.9	1350.3	12.9
299	625	1653734	5.0	11.5246	0.8	2.9233	2.1	0.2443	1.9	0.92	1409.2	24.4	1388.0	15.9	1355.4	16.0	1355.4	16.0
193	413	74368	0.7	11.5222	0.9	2.5962	2.6	0.2170	2.4	0.94	1265.8	27.6	1299.6	18.7	1355.8	16.5	1355.8	16.5
125	554	8060961	3.6	11.5124	0.6	2.6311	2.0	0.2197	1.9	0.95	1280.2	21.5	1309.4	14.4	1357.4	11.9	1357.4	11.9
26	257	135280	2.6	11.5107	0.8	2.6659	2.6	0.2226	2.5	0.95	1295.4	29.3	1319.1	19.3	1357.7	15.0	1357.7	15.0
255	195	73464	2.3	11.5090	0.8	2.2816	2.9	0.1905	2.8	0.96	1123.8	28.6	1206.6	20.4	1358.0	15.4	1358.0	15.4
181	198	100223	2.7	11.4896	0.6	2.7750	1.8	0.2312	1.7	0.94	1341.0	20.6	1348.8	13.6	1361.3	12.4	1361.3	12.4
284	464	177719	6.1	11.4878	0.6	2.4179	2.2	0.2015	2.1	0.96	1183.1	22.8	1247.9	15.8	1361.6	12.1	1361.6	12.1
223	471	182072	5.9	11.4616	0.8	2.8285	2.4	0.2351	2.3	0.95	1361.3	28.3	1363.1	18.2	1365.9	14.8	1365.9	14.8
116	664	230928	5.4	11.4616	0.6	2.9215	6.0	0.2429	5.9	1.00	1401.5	74.9	1387.5	45.2	1366.0	11.1	1366.0	11.1
282	438	118341	4.9	11.4579	0.7	2.6837	2.8	0.2230	2.7	0.97	1297.8	31.4	1324.0	20.4	1366.6	13.5	1366.6	13.5
262	150	26636	2.3	11.4576	0.7	2.7671	2.7	0.2299	2.6	0.97	1334.2	30.9	1346.7	19.8	1366.6	13.4	1366.6	13.4
226	178	16522	1.9	11.4565	0.9	2.8782	2.7	0.2391	2.5	0.94	1382.3	31.4	1376.2	20.1	1366.8	16.8	1366.8	16.8
182	647	126849	5.8	11.4523	0.8	2.7569	2.2	0.2290	2.0	0.94	1329.2	24.5	1343.9	16.2	1367.5	14.6	1367.5	14.6
314	668	1101268	4.7	11.4496	0.7	2.6630	2.1	0.2211	2.0	0.94	1287.9	23.0	1318.2	15.4	1368.0	13.6	1368.0	13.6
94	819	800551	5.5	11.4470	0.7	2.7507	2.0	0.2284	1.8	0.93	1326.0	21.9	1342.3	14.6	1368.4	13.9	1368.4	13.9
167	563	228718	1.5	11.4377	0.6	2.7277	1.9	0.2263	1.8	0.96	1314.9	21.8	1336.0	14.2	1370.0	10.6	1370.0	10.6
279	701	917934	1.2	11.4349	0.6	2.8186	1.5	0.2338	1.4	0.92	1354.2	16.6	1360.5	11.0	1370.4	10.8	1370.4	10.8
291	94	87242	1.1	11.4259	0.7	2.7845	2.8	0.2307	2.7	0.96	1338.4	32.4	1351.4	20.8	1372.0	14.2	1372.0	14.2
106	137	63234	1.3	11.4073	0.8	2.8181	2.2	0.2331	2.0	0.93	1351.0	24.9	1360.4	16.4	1375.1	15.2	1375.1	15.2
134	491	311122	6.1	11.4070	0.6	2.7928	2.1	0.2310	2.0	0.95	1340.0	23.9	1353.6	15.5	1375.1	12.3	1375.1	12.3
168	350	104567	3.7	11.4019	0.8	2.7723	2.1	0.2293	1.9	0.92	1330.6	22.8	1348.1	15.5	1376.0	16.1	1376.0	16.1
120	508	304221	4.9	11.3968	0.7	2.8254	2.1	0.2335	1.9	0.94	1353.0	23.7	1362.3	15.4	1376.9	13.1	1376.9	13.1
97	707	412971	2.5	11.3719	0.8	2.7483	2.6	0.2267	2.4	0.94	1317.0	28.7	1341.6	19.0	1381.1	16.3	1381.1	16.3
55	428	84298	1.8	11.3688	0.7	2.8629	2.4	0.2361	2.3	0.95	1366.2	27.9	1372.2	18.0	1381.6	14.2	1381.6	14.2
53	395	425948	2.7	11.3683	0.9	2.8441	2.4	0.2345	2.3	0.94	1358.0	27.9	1367.3	18.3	1381.7	16.4	1381.7	16.4
209	510	11054662	7.7	11.3675	0.7	2.7938	2.2	0.2303	2.1	0.95	1336.2	25.4	1353.9	16.5	1381.8	12.7	1381.8	12.7
300	576	241057	3.5	11.3527	0.6	2.7450	1.7	0.2260	1.5	0.92	1313.6	18.3	1340.7	12.4	1384.3	12.3	1384.3	12.3
234	643	2540422	14.3	11.3456	0.8	2.6727	2.1	0.2199	2.0	0.93	1281.5	23.2	1320.9	15.8	1385.5	14.6	1385.5	14.6
61	447	830696	2.9	11.3448	0.7	2.7764	2.1	0.2284	2.0	0.94	1326.3	24.0	1349.2	15.9	1385.7	14.0	1385.7	14.0
73	453	281242	4.1	11.3118	0.7	2.7642	2.2	0.2268	2.1	0.95	1317.6	25.3	1345.9	16.7	1391.2	13.7	1391.2	13.7
58	298	283782	5.2	11.2949	0.7	2.7522	2.3	0.2255	2.2	0.95	1310.7	26.4	1342.7	17.5	1394.1	14.0	1394.1	14.0
178	208	44491	1.2	11.0087	0.6	3.1088	2.0	0.2482	1.9	0.95	1429.3	24.6	1434.9	15.5	1443.2	12.3	1443.2	12.3
137	228	43932	1.4	10.8334	0.7	3.0898	2.4	0.2428	2.3	0.95	1401.1	28.4	1430.2	18.2	1473.7	13.8	1473.7	13.8
259	481	145447	9.9	10.6955	0.7	3.3504	2.1	0.2599	1.9	0.94	1489.3	25.5	1492.9	16.0	1498.0	13.6	1498.0	13.6

31	186	867586	1.1	10.4016	0.7	3.5561	2.6	0.2683	2.5	0.96	1532.0	34.1	1539.8	20.7	1550.5	14.1	1550.5	14.1
302	1318	267695	3.0	10.3458	0.7	3.6282	2.3	0.2722	2.2	0.95	1552.2	29.8	1555.7	18.2	1560.6	13.8	1560.6	13.8
75	1006	329282	3.7	10.1871	0.7	3.8978	1.7	0.2880	1.6	0.91	1631.4	22.7	1613.2	13.9	1589.5	13.1	1589.5	13.1
310	577	2101949	0.6	10.1723	0.6	3.6771	1.9	0.2713	1.8	0.94	1547.3	24.5	1566.4	15.1	1592.2	12.1	1592.2	12.1
151	549	933298	3.9	9.8863	0.7	4.0175	2.7	0.2881	2.6	0.96	1631.8	37.2	1637.7	21.7	1645.3	13.0	1645.3	13.0
123	274	70083	1.5	9.8447	0.7	3.8337	2.3	0.2737	2.2	0.96	1559.7	30.7	1599.8	18.7	1653.1	12.6	1653.1	12.6
145	425	177048	2.6	9.8035	0.9	3.9317	2.4	0.2795	2.3	0.93	1589.1	31.7	1620.2	19.6	1660.9	16.5	1660.9	16.5
229	129	164535	3.0	9.6859	1.0	4.1883	2.8	0.2942	2.6	0.93	1662.6	38.0	1671.7	22.8	1683.2	18.4	1683.2	18.4
278	106	168655	3.3	9.6845	0.8	4.2124	2.4	0.2959	2.3	0.95	1670.8	34.2	1676.4	20.1	1683.5	14.1	1683.5	14.1
206	159	93116	2.6	9.6681	0.6	3.5951	2.4	0.2521	2.3	0.97	1449.2	29.6	1548.4	18.7	1686.6	10.2	1686.6	10.2
231	303	420981	0.7	9.6665	0.8	4.1119	2.2	0.2883	2.1	0.93	1632.9	29.9	1656.7	18.3	1686.9	15.4	1686.9	15.4
204	467	415138	3.4	9.6593	0.6	4.2421	2.6	0.2972	2.5	0.97	1677.3	36.8	1682.2	21.1	1688.3	11.6	1688.3	11.6
17	144	84684	2.2	9.5621	1.0	4.3859	2.6	0.3042	2.4	0.93	1711.9	36.7	1709.7	21.7	1706.9	17.7	1706.9	17.7
103	158	199443	1.7	9.4301	0.7	4.4046	2.1	0.3012	2.0	0.94	1697.5	29.8	1713.2	17.6	1732.5	13.1	1732.5	13.1
127	604	164964	0.6	9.3801	0.8	4.5712	2.5	0.3110	2.3	0.94	1745.6	35.7	1744.0	20.6	1742.2	14.8	1742.2	14.8
161	639	196956	4.1	9.1925	0.9	4.6046	2.6	0.3070	2.4	0.94	1725.9	36.7	1750.1	21.6	1779.1	16.7	1779.1	16.7
160	348	121400	3.1	9.1220	0.7	4.7798	2.0	0.3162	1.8	0.94	1771.3	28.3	1781.4	16.4	1793.2	12.6	1793.2	12.6
60	266	30382	2.2	8.6723	0.7	5.0987	2.2	0.3207	2.1	0.94	1793.1	33.0	1835.9	19.0	1884.7	13.5	1884.7	13.5
309	306	10775941	4.5	8.6259	1.0	4.5510	2.1	0.2847	1.8	0.87	1615.1	26.3	1740.3	17.6	1894.4	18.8	1894.4	18.8
293	201	70652	1.1	5.7190	0.6	12.0740	2.2	0.5008	2.1	0.96	2617.3	45.5	2610.2	20.7	2604.6	10.6	2604.6	10.6

TABLE A4: LA-ICP-MS U-Pb Zircon Geochronology Results for CR-MPE-020

Zircon #	Composition U (ppm)	$^{206}Pb/^{204}Pb$	U/Th	$^{206}Pb/^{207}Pb$	2σ (%)	$^{207}Pb/^{235}U$	2σ (%)	$^{206}Pb/^{238}U$	2σ (%)	Corr.	Ages $^{206}Pb/^{238}U$	2σ (Ma)	$^{207}Pb/^{235}U$	2σ (Ma)	$^{206}Pb/^{207}Pb$	2σ (Ma)	Best Age	2σ (Ma)
5	28	965	2.5	21.5441	11.3	0.0407	12.2	0.0064	4.6	0.38	40.8	1.9	40.5	4.8	19.3	271.8	40.8	1.9
35	83	5934	2.4	22.1285	3.1	0.0455	4.2	0.0073	2.8	0.66	46.9	1.3	45.2	1.8	45.3	76.6	46.9	1.3
42	246	829	2.4	34.2769	12.8	0.0299	12.9	0.0074	2.1	0.16	47.8	1.0	29.9	3.8	1245.5	401.4	47.8	1.0
7	108	3398	1.6	23.3742	2.3	0.0637	4.0	0.0108	3.3	0.82	69.2	2.3	62.7	2.4	180.2	57.1	69.2	2.3
13	230	1834	2.2	25.7672	10.8	0.0607	11.1	0.0113	2.6	0.23	72.7	1.8	59.8	6.4	429.6	283.7	72.7	1.8
12	135	15744	2.7	20.5607	1.7	0.0860	3.5	0.0128	3.1	0.88	82.1	2.5	83.8	2.8	130.3	39.5	82.1	2.5
41	2238	50194	8.7	20.6549	0.8	0.0907	1.9	0.0136	1.8	0.92	87.0	1.5	88.2	1.6	119.6	17.8	87.0	1.5
26	330	48288	2.7	21.0165	1.4	0.0904	2.7	0.0138	2.3	0.85	88.2	2.0	87.9	2.3	78.5	33.7	88.2	2.0
29	2005	435077	3.1	20.9790	1.0	0.0929	2.3	0.0141	2.1	0.91	90.5	1.9	90.2	2.0	82.7	23.0	90.5	1.9
23	620	17843	3.6	21.6199	1.2	0.0907	2.3	0.0142	1.9	0.84	91.0	1.7	88.1	1.9	10.9	29.8	91.0	1.7
14	116	10164	1.2	21.7049	2.2	0.0908	3.5	0.0143	2.7	0.77	91.5	2.4	88.2	3.0	1.4	54.1	91.5	2.4
48	199	43604	1.6	21.0747	1.6	0.0940	3.2	0.0144	2.8	0.87	91.9	2.6	91.2	2.8	71.9	38.5	91.9	2.6
6	189	4035	3.3	22.9791	1.2	0.0874	2.4	0.0146	2.0	0.85	93.3	1.9	85.1	2.0	137.9	30.9	93.3	1.9
27	329	9229	2.1	21.1797	1.2	0.0955	2.6	0.0147	2.3	0.88	93.9	2.1	92.6	2.3	60.1	29.5	93.9	2.1
47	801	31963	2.0	21.1281	1.0	0.0962	2.0	0.0147	1.8	0.87	94.4	1.6	93.3	1.8	65.9	23.8	94.4	1.6
31	328	6435	1.8	16.4264	5.2	0.1359	5.8	0.0162	2.5	0.44	103.5	2.6	129.4	7.0	634.9	111.9	103.5	2.6
34	250	3080	2.6	22.6064	2.9	0.1053	3.5	0.0173	1.9	0.54	110.4	2.0	101.7	3.3	97.6	71.6	110.4	2.0
37	962	50980	6.0	20.3711	0.8	0.1178	1.9	0.0174	1.7	0.91	111.2	1.9	113.1	2.0	152.1	18.2	111.2	1.9
17	76	2100	1.6	22.9654	2.5	0.1113	3.8	0.0185	2.8	0.75	118.4	3.3	107.1	3.8	136.4	61.8	118.4	3.3
49	476	15162	1.6	20.5803	1.4	0.1250	2.7	0.0187	2.3	0.85	119.2	2.7	119.6	3.1	128.1	34.0	119.2	2.7
20	187	138408	2.3	17.2221	3.6	0.1585	6.2	0.0198	5.0	0.81	126.4	6.3	149.4	8.6	532.2	79.5	126.4	6.3
43	75	6011	3.5	20.9300	1.9	0.1453	2.7	0.0221	2.0	0.73	140.7	2.8	137.8	3.5	88.3	44.1	140.7	2.8
15	46	9585	2.5	21.2036	2.3	0.1441	4.0	0.0222	3.3	0.81	141.3	4.5	136.7	5.1	57.4	55.6	141.3	4.5
18	71	5824	3.4	21.3857	1.8	0.1463	3.0	0.0227	2.4	0.81	144.6	3.5	138.6	3.9	37.0	42.2	144.6	3.5
10	41	1090	3.9	25.0904	10.4	0.1268	10.7	0.0231	2.5	0.23	147.0	3.6	121.2	12.2	360.3	269.7	147.0	3.6
30	74	120419	1.7	20.9789	2.0	0.1524	3.8	0.0232	3.2	0.85	147.8	4.7	144.0	5.1	82.7	48.1	147.8	4.7
16	96	4552	2.1	21.1863	2.6	0.1534	3.7	0.0236	2.5	0.69	150.1	3.8	144.9	5.0	59.4	62.9	150.1	3.8
33	317	10592	2.0	18.6349	2.2	0.1762	3.1	0.0238	2.2	0.70	151.8	3.3	164.8	4.8	356.9	50.2	151.8	3.3
3	142	20916	2.6	20.0700	1.1	0.1637	2.3	0.0238	2.0	0.88	151.8	3.0	153.9	3.3	186.8	25.0	151.8	3.0
4	157	751	1.6	8.2266	9.4	0.4056	9.8	0.0242	2.6	0.27	154.1	4.0	345.7	28.7	1979.2	168.2	154.1	4.0
1	284	21358	3.2	20.4981	1.2	0.1664	2.5	0.0247	2.1	0.87	157.5	3.3	156.3	3.6	137.5	28.9	157.5	3.3
11	397	19193	1.4	20.5645	1.1	0.1712	2.2	0.0255	2.0	0.88	162.5	3.1	160.4	3.3	129.9	25.1	162.5	3.1
24	188	1168	1.4	27.0909	2.2	0.1384	3.2	0.0272	2.3	0.71	173.0	3.9	131.6	3.9	562.9	60.4	173.0	3.9
8	2191	348757	19.0	11.8924	1.0	2.2435	3.3	0.1935	3.2	0.95	1140.4	33.0	1194.8	23.3	1294.6	19.8	1294.6	19.8
46	130	35425	2.2	11.5169	0.7	2.7939	2.2	0.2334	2.1	0.94	1352.2	25.7	1353.9	16.7	1356.7	14.4	1356.7	14.4
25	782	497741	2.2	11.4327	0.6	2.7692	2.1	0.2296	2.0	0.95	1332.5	23.6	1347.3	15.3	1370.8	11.8	1370.8	11.8
22	223	379931	1.3	11.4014	0.7	2.5767	2.2	0.2131	2.1	0.95	1245.1	23.5	1294.0	16.1	1376.1	13.6	1376.1	13.6
28	568	107591	1.4	11.3975	0.6	2.8566	1.8	0.2361	1.7	0.95	1366.6	21.3	1370.6	13.8	1376.7	11.3	1376.7	11.3
36	385	391676	3.3	11.3771	0.7	2.8296	2.6	0.2335	2.5	0.96	1352.7	30.5	1363.4	19.5	1380.2	13.6	1380.2	13.6
44	578	590902	3.1	11.3670	0.5	2.8202	1.9	0.2325	1.9	0.97	1347.6	22.9	1360.9	14.6	1381.9	9.6	1381.9	9.6
21	199	170727	2.0	11.3652	0.7	2.5063	2.7	0.2066	2.6	0.97	1210.6	29.0	1273.9	19.8	1382.2	13.6	1382.2	13.6
2	351	345631	1.5	11.2893	0.7	2.9005	2.3	0.2375	2.2	0.96	1373.6	27.1	1382.1	17.3	1395.1	12.8	1395.1	12.8
19	424	194643	3.0	11.2614	0.6	2.8887	1.9	0.2359	1.8	0.95	1365.6	22.0	1379.0	14.3	1399.8	11.8	1399.8	11.8
39	848	609078	3.7	10.2126	0.7	3.3740	2.4	0.2499	2.3	0.95	1438.0	29.7	1498.4	19.0	1584.8	14.0	1584.8	14.0
32	72	590374	1.2	10.0072	1.1	3.7015	2.7	0.2686	2.5	0.92	1533.9	34.4	1571.7	21.9	1622.7	19.8	1622.7	19.8
40	780	345760	34.1	10.0018	0.9	3.8098	2.8	0.2764	2.6	0.94	1573.0	36.6	1594.8	22.4	1623.7	17.3	1623.7	17.3
45	127	86411	0.7	9.7426	0.8	4.0337	2.3	0.2850	2.2	0.94	1616.6	31.0	1641.0	18.9	1672.4	15.0	1672.4	15.0
38	531	109955	2.1	9.7040	0.6	4.0138	2.1	0.2825	2.0	0.96	1603.9	28.0	1637.0	16.7	1679.8	10.7	1679.8	10.7
9	505	1256846	1.3	9.6445	0.7	4.1805	2.2	0.2924	2.1	0.95	1653.6	31.1	1670.2	18.4	1691.1	12.8	1691.1	12.8
5	28	965	2.5	21.5441	11.3	0.0407	12.2	0.0064	4.6	0.38	40.8	1.9	40.5	4.8	19.3	271.8	40.8	1.9
35	83	5934	2.4	22.1285	3.1	0.0455	4.2	0.0073	2.8	0.66	46.9	1.3	45.2	1.8	45.3	76.6	46.9	1.3
42	246	829	2.4	34.2769	12.8	0.0299	12.9	0.0074	2.1	0.16	47.8	1.0	29.9	3.8	1245.5	401.4	47.8	1.0
7	108	3398	1.6	23.3742	2.3	0.0637	4.0	0.0108	3.3	0.82	69.2	2.3	62.7	2.4	180.2	57.1	69.2	2.3

13	230	1834	2.2	25.7672	10.8	0.0607	11.1	0.0113	2.6	0.23	72.7	1.8	59.8	6.4	429.6	283.7	72.7	1.8
12	135	15744	2.7	20.5607	1.7	0.0860	3.5	0.0128	3.1	0.88	82.1	2.5	83.8	2.8	130.3	39.5	82.1	2.5
41	2238	50194	8.7	20.6549	0.8	0.0907	1.9	0.0136	1.8	0.92	87.0	1.5	88.2	1.6	119.6	17.8	87.0	1.5
26	330	48288	2.7	21.0165	1.4	0.0904	2.7	0.0138	2.3	0.85	88.2	2.0	87.9	2.3	78.5	33.7	88.2	2.0
29	2005	435077	3.1	20.9790	1.0	0.0929	2.3	0.0141	2.1	0.91	90.5	1.9	90.2	2.0	82.7	23.0	90.5	1.9
23	620	17843	3.6	21.6199	1.2	0.0907	2.3	0.0142	1.9	0.84	91.0	1.7	88.1	1.9	10.9	29.8	91.0	1.7
14	116	10164	1.2	21.7049	2.2	0.0908	3.5	0.0143	2.7	0.77	91.5	2.4	88.2	3.0	1.4	54.1	91.5	2.4
48	199	43604	1.6	21.0747	1.6	0.0940	3.2	0.0144	2.8	0.87	91.9	2.6	91.2	2.8	71.9	38.5	91.9	2.6
6	189	4035	3.3	22.9791	1.2	0.0874	2.4	0.0146	2.0	0.85	93.3	1.9	85.1	2.0	137.9	30.9	93.3	1.9
27	329	9229	2.1	21.1797	1.2	0.0955	2.6	0.0147	2.3	0.88	93.9	2.1	92.6	2.3	60.1	29.5	93.9	2.1
47	801	31963	2.0	21.1281	1.0	0.0962	2.0	0.0147	1.8	0.87	94.4	1.6	93.3	1.8	65.9	23.8	94.4	1.6
31	328	6435	1.8	16.4264	5.2	0.1359	5.8	0.0162	2.5	0.44	103.5	2.6	129.4	7.0	634.9	111.9	103.5	2.6
34	250	3080	2.6	22.6064	2.9	0.1053	3.5	0.0173	1.9	0.54	110.4	2.0	101.7	3.3	97.6	71.6	110.4	2.0
37	962	50980	6.0	20.3711	0.8	0.1178	1.9	0.0174	1.7	0.91	111.2	1.9	113.1	2.0	152.1	18.2	111.2	1.9
17	76	2100	1.6	22.9654	2.5	0.1113	3.8	0.0185	2.8	0.75	118.4	3.3	107.1	3.8	136.4	61.8	118.4	3.3
49	476	15162	1.6	20.5803	1.4	0.1250	2.7	0.0187	2.3	0.85	119.2	2.7	119.6	3.1	128.1	34.0	119.2	2.7
20	187	138408	2.3	17.2221	3.6	0.1585	6.2	0.0198	5.0	0.81	126.4	6.3	149.4	8.6	532.2	79.5	126.4	6.3
43	75	6011	3.5	20.9300	1.9	0.1453	2.7	0.0221	2.0	0.73	140.7	2.8	137.8	3.5	88.3	44.1	140.7	2.8
15	46	9585	2.5	21.2036	2.3	0.1441	4.0	0.0222	3.3	0.81	141.3	4.5	136.7	5.1	57.4	55.6	141.3	4.5
18	71	5824	3.4	21.3857	1.8	0.1463	3.0	0.0227	2.4	0.81	144.6	3.5	138.6	3.9	37.0	42.2	144.6	3.5
10	41	1090	3.9	25.0904	10.4	0.1268	10.7	0.0231	2.5	0.23	147.0	3.6	121.2	12.2	360.3	269.7	147.0	3.6
30	74	120419	1.7	20.9789	2.0	0.1524	3.8	0.0232	3.2	0.85	147.8	4.7	144.0	5.1	82.7	48.1	147.8	4.7
16	96	4552	2.1	21.1863	2.6	0.1534	3.7	0.0236	2.5	0.69	150.1	3.8	144.9	5.0	59.4	62.9	150.1	3.8
33	317	10592	2.0	18.6349	2.2	0.1762	3.1	0.0238	2.2	0.70	151.8	3.3	164.8	4.8	356.9	50.2	151.8	3.3
3	142	20916	2.6	20.0700	1.1	0.1637	2.3	0.0238	2.0	0.88	151.8	3.0	153.9	3.3	186.8	25.0	151.8	3.0
4	157	751	1.6	8.2266	9.4	0.4056	9.8	0.0242	2.6	0.27	154.1	4.0	345.7	28.7	1979.2	168.2	154.1	4.0
1	284	21358	3.2	20.4981	1.2	0.1664	2.5	0.0247	2.1	0.87	157.5	3.3	156.3	3.6	137.5	28.9	157.5	3.3
11	397	19193	1.4	20.5645	1.1	0.1712	2.2	0.0255	2.0	0.88	162.5	3.1	160.4	3.3	129.9	25.1	162.5	3.1
24	188	1168	1.4	27.0909	2.2	0.1384	3.2	0.0272	2.3	0.71	173.0	3.9	131.6	3.9	562.9	60.4	173.0	3.9
8	2191	348757	19.0	11.8924	1.0	2.2435	3.3	0.1935	3.2	0.95	1140.4	33.0	1194.8	23.3	1294.6	19.8	1294.6	19.8
46	130	35425	2.2	11.5169	0.7	2.7939	2.2	0.2334	2.1	0.94	1352.2	25.7	1353.9	16.7	1356.7	14.4	1356.7	14.4
25	782	497741	2.2	11.4327	0.6	2.7692	2.1	0.2296	2.0	0.95	1332.5	23.6	1347.3	15.3	1370.8	11.8	1370.8	11.8
22	223	379931	1.3	11.4014	0.7	2.5767	2.2	0.2131	2.1	0.95	1245.1	23.5	1294.0	16.1	1376.1	13.6	1376.1	13.6
28	568	107591	1.4	11.3975	0.6	2.8566	1.8	0.2361	1.7	0.95	1366.6	21.3	1370.6	13.8	1376.7	11.3	1376.7	11.3
36	385	391676	3.3	11.3771	0.7	2.8296	2.6	0.2335	2.5	0.96	1352.7	30.5	1363.4	19.5	1380.2	13.6	1380.2	13.6
44	578	590902	3.1	11.3670	0.5	2.8202	1.9	0.2325	1.9	0.97	1347.6	22.9	1360.9	14.6	1381.9	9.6	1381.9	9.6
21	199	170727	2.0	11.3652	0.7	2.5063	2.7	0.2066	2.6	0.97	1210.6	29.0	1273.9	19.8	1382.2	13.6	1382.2	13.6
2	351	345631	1.5	11.2893	0.7	2.9005	2.3	0.2375	2.2	0.96	1373.6	27.1	1382.1	17.3	1395.1	12.8	1395.1	12.8
19	424	194643	3.0	11.2614	0.6	2.8887	1.9	0.2359	1.8	0.95	1365.6	22.0	1379.0	14.3	1399.8	11.8	1399.8	11.8
39	848	609078	3.7	10.2126	0.7	3.3740	2.4	0.2499	2.3	0.95	1438.0	29.7	1498.4	19.0	1584.8	14.0	1584.8	14.0
32	72	590374	1.2	10.0072	1.1	3.7015	2.7	0.2686	2.5	0.92	1533.9	34.4	1571.7	21.9	1622.7	19.8	1622.7	19.8
40	780	345760	34.1	10.0018	0.9	3.8098	2.8	0.2764	2.6	0.94	1573.0	36.6	1594.8	22.4	1623.7	17.3	1623.7	17.3
45	127	86411	0.7	9.7426	0.8	4.0337	2.3	0.2850	2.2	0.94	1616.6	31.0	1641.0	18.9	1672.4	15.0	1672.4	15.0
38	531	109955	2.1	9.7040	0.6	4.0138	2.1	0.2825	2.0	0.96	1603.9	28.0	1637.0	16.7	1679.8	10.7	1679.8	10.7
9	505	1256846	1.3	9.6445	0.7	4.1805	2.2	0.2924	2.1	0.95	1653.6	31.1	1670.2	18.4	1691.1	12.8	1691.1	12.8

TABLE A5: LA-ICP-MS U-Pb Zircon Geochronology Results for CR-MPE-022

Zircon #	Composition U (ppm)	$^{206}Pb/^{204}Pb$	U/Th	$^{206}Pb/^{207}Pb$	2σ (%)	$^{207}Pb/^{235}U$	2σ (%)	$^{206}Pb/^{238}U$	2σ (%)	Corr.	Ages $^{206}Pb/^{238}U$	2σ (Ma)	$^{207}Pb/^{235}U$	2σ (Ma)	$^{206}Pb/^{207}Pb$	2σ (Ma)	Best Age	2σ (Ma)
94	172	605	2.4	41.2234	3.6	0.0219	5.3	0.0065	3.8	0.72	42.0	1.6	22.0	1.1	1866.8	131.6	42.0	1.6
313	333	2283	1.2	23.1893	4.2	0.0391	4.7	0.0066	2.1	0.44	42.2	0.9	38.9	1.8	160.5	104.5	42.2	0.9
217	44	441	2.3	38.1448	28.5	0.0249	28.9	0.0069	4.6	0.16	44.3	2.0	25.0	7.1	1594.2	983.8	44.3	2.0
70	140	1535	2.2	24.3420	3.8	0.0395	5.1	0.0070	3.4	0.68	44.8	1.5	39.4	2.0	282.5	95.6	44.8	1.5
99	118	3606	2.5	20.5982	3.9	0.0470	4.8	0.0070	2.8	0.59	45.1	1.3	46.7	2.2	126.1	91.1	45.1	1.3
273	222	2796	1.5	21.7387	6.2	0.0449	6.5	0.0071	2.2	0.34	45.5	1.0	44.6	2.9	2.3	148.6	45.5	1.0
170	163	5669	2.4	22.2455	3.1	0.0442	4.2	0.0071	2.9	0.68	45.9	1.3	44.0	1.8	58.2	75.7	45.9	1.3
185	176	1687	1.9	23.9539	3.5	0.0412	4.1	0.0072	2.2	0.53	46.0	1.0	41.0	1.7	241.8	88.6	46.0	1.0
35	127	18023	2.5	21.3674	3.4	0.0469	4.9	0.0073	3.5	0.72	46.6	1.6	46.5	2.2	39.1	81.2	46.6	1.6
172	515	5683	0.9	21.6214	1.8	0.0464	3.0	0.0073	2.4	0.81	46.7	1.1	46.1	1.4	10.7	42.8	46.7	1.1
282	63	754	1.7	24.3106	6.1	0.0416	7.3	0.0073	4.0	0.55	47.1	1.9	41.4	3.0	279.2	155.7	47.1	1.9
108	62	3765	3.2	21.8800	4.3	0.0463	5.4	0.0073	3.2	0.60	47.2	1.5	45.9	2.4	18.0	104.4	47.2	1.5
40	52	619	1.7	31.6420	7.5	0.0324	8.6	0.0074	4.2	0.49	47.7	2.0	32.3	2.7	1001.7	223.3	47.7	2.0
45	50	10128	2.1	22.9422	4.1	0.0452	6.0	0.0075	4.4	0.74	48.3	2.1	44.9	2.6	133.9	100.5	48.3	2.1
57	935	13667	1.7	22.4801	1.6	0.0463	3.0	0.0075	2.6	0.85	48.5	1.3	45.9	1.4	83.8	38.8	48.5	1.3
163	110	2251	2.9	26.2498	9.4	0.0401	10.0	0.0076	3.3	0.33	49.0	1.6	39.9	3.9	478.5	250.1	49.0	1.6
83	239	2270	2.0	8.2689	18.0	0.1275	19.0	0.0076	6.2	0.33	49.1	3.1	121.9	21.9	1970.0	323.1	49.1	3.1
266	46	1579	2.4	20.4150	5.7	0.0527	7.1	0.0078	4.2	0.60	50.1	2.1	52.1	3.6	147.1	133.4	50.1	2.1
305	96	11581	1.6	17.2134	3.8	0.0627	5.2	0.0078	3.5	0.68	50.3	1.7	61.7	3.1	533.3	82.9	50.3	1.7
11	40	81009	2.2	21.8396	5.0	0.0511	7.1	0.0081	5.0	0.71	52.0	2.6	50.6	3.5	13.5	121.6	52.0	2.6
237	252	10503	2.3	21.8253	2.2	0.0513	2.8	0.0081	1.8	0.63	52.1	0.9	50.8	1.4	11.9	53.2	52.1	0.9
262	246	2277	3.2	23.6307	2.4	0.0589	3.0	0.0101	1.9	0.63	64.8	1.2	58.1	1.7	207.6	59.5	64.8	1.2
233	88	752	3.7	35.0082	5.3	0.0398	6.1	0.0101	2.8	0.47	64.8	1.8	39.6	2.4	1312.1	170.3	64.8	1.8
79	368	5673	1.4	16.1578	3.5	0.0878	4.4	0.0103	2.6	0.59	66.0	1.7	85.5	3.6	670.3	75.3	66.0	1.7
151	244	4053	3.0	20.7804	2.8	0.0696	3.7	0.0105	2.5	0.66	67.3	1.6	68.3	2.5	105.3	66.6	67.3	1.6
42	1575	10803	4.4	21.0883	1.1	0.0692	2.2	0.0106	2.0	0.88	67.8	1.3	67.9	1.5	70.4	25.4	67.8	1.3
309	287	66067	2.3	20.8149	1.7	0.0706	2.8	0.0107	2.2	0.79	68.3	1.5	69.3	1.9	101.3	40.5	68.3	1.5
244	451	4312	1.4	22.5306	1.9	0.0654	3.1	0.0107	2.4	0.78	68.6	1.6	64.4	1.9	89.3	47.2	68.6	1.6
168	220	4426	2.0	20.9534	3.0	0.0705	4.1	0.0107	2.7	0.67	68.7	1.9	69.1	2.7	85.7	72.2	68.7	1.9
143	217	20191	1.6	21.2157	1.9	0.0696	2.8	0.0107	2.0	0.74	68.7	1.4	68.3	1.8	56.1	44.4	68.7	1.4
141	481	7219	2.0	21.4649	1.6	0.0693	2.7	0.0108	2.2	0.81	69.2	1.5	68.0	1.8	28.1	37.7	69.2	1.5
187	339	98248	2.0	21.3942	1.9	0.0696	2.7	0.0108	1.9	0.72	69.2	1.3	68.3	1.8	36.0	44.6	69.2	1.3
247	254	6809	2.4	21.1147	2.1	0.0707	3.3	0.0108	2.6	0.77	69.4	1.8	69.4	2.2	67.5	50.1	69.4	1.8
213	934	30963	2.6	21.2794	1.0	0.0702	2.3	0.0108	2.0	0.90	69.5	1.4	68.9	1.5	48.9	23.7	69.5	1.4
195	133	5699	1.5	21.6195	2.3	0.0691	3.4	0.0108	2.5	0.74	69.5	1.8	67.9	2.3	10.9	55.4	69.5	1.8
221	162	2200	1.7	24.1847	3.2	0.0618	4.2	0.0108	2.8	0.66	69.5	1.9	60.9	2.5	266.0	80.4	69.5	1.9
112	394	2370	2.7	23.6650	3.0	0.0633	3.6	0.0109	2.0	0.55	69.7	1.4	62.4	2.2	211.2	75.4	69.7	1.4
212	541	65955	2.0	20.8287	1.6	0.0722	2.4	0.0109	1.8	0.75	69.9	1.3	70.8	1.6	99.8	37.9	69.9	1.3
104	681	82110	8.0	20.4212	1.3	0.0745	2.0	0.0110	1.6	0.78	70.7	1.1	72.9	1.4	146.4	29.4	70.7	1.1
33	344	4526	2.0	21.9085	2.7	0.0695	3.3	0.0110	1.9	0.58	70.8	1.3	68.2	2.1	21.1	64.4	70.8	1.3
145	142	1775	2.3	24.9644	5.6	0.0614	6.2	0.0111	2.7	0.44	71.3	1.9	60.5	3.7	347.3	144.2	71.3	1.9
84	293	1111	1.6	28.8093	8.3	0.0533	8.7	0.0111	2.3	0.27	71.3	1.7	52.7	4.4	731.7	233.5	71.3	1.7
272	510	54915	1.5	21.2937	1.3	0.0721	2.4	0.0111	2.1	0.86	71.4	1.5	70.7	1.7	47.3	30.0	71.4	1.5
188	175	61972	2.1	21.0879	2.2	0.0731	3.3	0.0112	2.4	0.73	71.6	1.7	71.6	2.3	70.5	53.0	71.6	1.7
171	643	24207	1.3	21.0154	1.3	0.0740	1.8	0.0113	1.3	0.71	72.3	0.9	72.5	1.3	78.6	30.6	72.3	0.9
91	145	5851	2.8	21.5547	3.1	0.0722	4.4	0.0113	3.1	0.71	72.4	2.3	70.8	3.0	18.1	73.6	72.4	2.3
242	188	87830	2.1	21.6705	2.2	0.0722	3.4	0.0113	2.6	0.76	72.8	1.9	70.8	2.3	5.2	52.2	72.8	1.9
249	359	7355	2.5	21.2782	1.5	0.0736	2.6	0.0114	2.2	0.83	72.9	1.6	72.2	1.8	49.0	34.7	72.9	1.6
186	282	16435	1.9	20.5668	1.7	0.0764	2.5	0.0114	1.8	0.73	73.1	1.3	74.8	1.8	129.7	40.0	73.1	1.3
82	213	2119	2.1	24.6519	1.9	0.0648	3.1	0.0116	2.5	0.80	74.3	1.9	63.8	1.9	314.9	47.9	74.3	1.9
199	493	16341	2.3	21.3301	1.6	0.0755	2.5	0.0117	2.0	0.78	74.9	1.5	73.9	1.8	43.2	38.3	74.9	1.5
206	179	9892	1.8	20.1483	2.1	0.0801	2.9	0.0117	2.0	0.70	75.0	1.5	78.2	2.2	177.8	48.7	75.0	1.5
211	374	809	1.8	35.2998	24.6	0.0458	24.7	0.0117	2.3	0.09	75.1	1.7	45.4	11.0	1338.6	795.1	75.1	1.7

34	1075	407510	0.8	19.9548	1.3	0.0814	2.2	0.0118	1.7	0.80	75.5	1.3	79.5	1.7	200.2	29.9	75.5	1.3
158	172	3191	1.3	15.2857	5.0	0.1082	5.8	0.0120	2.9	0.51	76.8	2.2	104.3	5.7	787.9	104.5	76.8	2.2
92	213	3527	3.0	23.5096	3.4	0.0713	4.4	0.0122	2.8	0.64	77.9	2.2	69.9	3.0	194.7	85.3	77.9	2.2
150	682	11723	5.5	21.6392	1.4	0.0791	2.1	0.0124	1.6	0.75	79.5	1.2	77.3	1.5	8.7	32.8	79.5	1.2
218	1036	6317	2.6	20.1206	1.7	0.0879	4.3	0.0128	3.9	0.92	82.2	3.2	85.6	3.5	181.0	40.0	82.2	3.2
299	396	8114	2.4	20.5277	1.5	0.0868	3.1	0.0129	2.7	0.88	82.8	2.2	84.5	2.5	134.1	35.0	82.8	2.2
161	958	11224	2.0	21.4825	1.3	0.0850	4.0	0.0132	3.7	0.94	84.8	3.2	82.8	3.2	26.2	31.2	84.8	3.2
315	205	2800	1.9	22.3330	1.9	0.0829	3.4	0.0134	2.8	0.82	86.0	2.4	80.9	2.6	67.8	47.5	86.0	2.4
119	157	2141	2.6	24.7784	2.7	0.0751	4.1	0.0135	3.0	0.74	86.4	2.6	73.5	2.9	328.0	69.6	86.4	2.6
274	1038	20920	2.7	21.3362	1.1	0.0884	1.9	0.0137	1.6	0.82	87.6	1.4	86.0	1.6	42.5	26.1	87.6	1.4
27	459	3514	5.1	22.8850	1.9	0.0826	2.8	0.0137	2.0	0.74	87.8	1.8	80.6	2.1	127.7	45.9	87.8	1.8
306	196	2629	1.0	23.0081	2.3	0.0822	3.4	0.0137	2.5	0.74	87.8	2.2	80.2	2.6	141.0	57.3	87.8	2.2
24	1299	47593	12.9	20.9367	0.8	0.0909	2.3	0.0138	2.1	0.94	88.3	1.9	88.3	1.9	87.6	18.1	88.3	1.9
208	870	2178	1.8	19.1355	5.8	0.0997	6.1	0.0138	2.0	0.33	88.5	1.8	96.5	5.7	296.8	132.4	88.5	1.8
270	669	13393	2.6	21.1392	1.4	0.0903	2.5	0.0138	2.0	0.82	88.6	1.8	87.8	2.1	64.7	33.7	88.6	1.8
49	300	17594	1.3	20.1539	1.9	0.0951	3.0	0.0139	2.3	0.77	89.0	2.0	92.3	2.6	177.1	43.7	89.0	2.0
204	217	22160	2.7	21.3619	1.9	0.0899	3.2	0.0139	2.5	0.79	89.2	2.2	87.4	2.6	39.7	45.9	89.2	2.2
142	1027	19589	6.7	20.3905	1.4	0.0942	2.5	0.0139	2.1	0.83	89.2	1.8	91.4	2.2	149.9	32.4	89.2	1.8
81	1972	90761	3.6	21.2082	0.9	0.0910	1.9	0.0140	1.7	0.89	89.6	1.5	88.4	1.6	56.9	20.5	89.6	1.5
209	1520	93454	5.3	20.8100	1.0	0.0939	2.3	0.0142	2.1	0.90	90.8	1.9	91.2	2.0	101.9	24.0	90.8	1.9
260	856	11425	1.9	21.2720	1.4	0.0920	2.5	0.0142	2.0	0.83	90.8	1.8	89.4	2.1	49.8	32.7	90.8	1.8
232	1005	13341	3.1	21.4518	1.0	0.0914	2.5	0.0142	2.3	0.92	91.1	2.1	88.9	2.1	29.6	23.3	91.1	2.1
285	165	2325	1.6	23.9122	2.5	0.0827	3.7	0.0143	2.8	0.74	91.8	2.5	80.7	2.9	237.4	62.5	91.8	2.5
277	1169	200810	2.6	21.2774	1.0	0.0930	2.2	0.0144	2.0	0.89	91.9	1.8	90.3	1.9	49.1	24.5	91.9	1.8
135	1551	19440	2.0	20.5807	1.7	0.0962	2.7	0.0144	2.1	0.79	91.9	2.0	93.2	2.4	128.1	39.1	91.9	2.0
126	429	3964	2.0	21.7995	1.3	0.0913	2.2	0.0144	1.8	0.82	92.4	1.7	88.7	1.9	9.1	30.9	92.4	1.7
230	597	5635	3.9	22.1892	2.2	0.0897	3.0	0.0144	2.0	0.69	92.4	1.9	87.2	2.5	52.0	52.4	92.4	1.9
8	289	3694	1.6	11.6082	10.3	0.1741	10.6	0.0147	2.5	0.24	93.8	2.3	163.0	16.0	1341.4	199.5	93.8	2.3
12	575	8487	3.7	20.7983	1.8	0.0975	2.7	0.0147	1.9	0.73	94.2	1.8	94.5	2.4	103.2	43.1	94.2	1.8
265	2341	21436	6.4	20.9939	0.8	0.0968	2.1	0.0147	2.0	0.93	94.3	1.9	93.8	1.9	81.1	18.8	94.3	1.9
216	416	8611	4.2	20.9219	1.4	0.0972	2.3	0.0147	1.9	0.81	94.4	1.8	94.2	2.1	89.2	32.3	94.4	1.8
23	659	53529	2.6	20.7163	1.1	0.0983	2.6	0.0148	2.3	0.90	94.5	2.2	95.2	2.3	112.6	26.6	94.5	2.2
289	2479	30254	4.8	21.2316	0.8	0.0962	1.8	0.0148	1.6	0.90	94.8	1.5	93.3	1.6	54.3	18.7	94.8	1.5
15	2787	65870	23.0	20.8970	0.6	0.0981	1.5	0.0149	1.3	0.90	95.1	1.3	95.0	1.3	92.0	15.3	95.1	1.3
205	710	21491	10.4	21.1266	1.1	0.0971	2.1	0.0149	1.8	0.85	95.2	1.7	94.1	1.9	66.1	26.3	95.2	1.7
124	236	4479	2.4	17.6280	4.0	0.1168	4.7	0.0149	2.5	0.52	95.5	2.3	112.1	5.0	480.9	88.3	95.5	2.3
184	578	25176	3.1	21.1259	1.3	0.0975	2.2	0.0149	1.8	0.82	95.6	1.7	94.4	2.0	66.2	30.2	95.6	1.7
179	540	12992	3.4	20.7406	1.7	0.0993	2.9	0.0149	2.3	0.81	95.6	2.2	96.1	2.7	109.8	40.6	95.6	2.2
214	770	6649	2.0	21.6076	1.5	0.0956	2.4	0.0150	1.8	0.78	95.9	1.8	92.7	2.1	12.3	36.0	95.9	1.8
259	1006	8498	2.0	21.7451	1.1	0.0954	2.2	0.0150	1.8	0.85	96.3	1.8	92.5	1.9	3.0	27.5	96.3	1.8
3	827	11144	1.5	21.3223	1.1	0.0979	2.0	0.0151	1.7	0.83	96.9	1.6	94.9	1.9	44.1	27.3	96.9	1.6
194	651	26713	5.9	21.1494	1.1	0.0988	2.2	0.0152	1.9	0.87	97.0	1.8	95.7	2.0	63.6	25.6	97.0	1.8
239	673	17573	4.4	21.4192	1.0	0.0988	2.4	0.0153	2.2	0.91	98.2	2.1	95.7	2.2	33.2	23.5	98.2	2.1
102	380	1364	1.6	26.7952	2.0	0.0792	2.9	0.0154	2.1	0.73	98.4	2.1	77.4	2.2	533.4	54.2	98.4	2.1
275	1261	17360	1.8	21.4655	1.0	0.0994	2.1	0.0155	1.9	0.88	99.0	1.8	96.2	1.9	28.1	24.3	99.0	1.8
287	455	35207	2.0	20.2421	1.2	0.1057	2.2	0.0155	1.9	0.85	99.2	1.8	102.0	2.1	166.9	27.2	99.2	1.8
254	346	4110	2.1	22.5601	4.3	0.0956	4.9	0.0156	2.4	0.50	100.0	2.4	92.7	4.4	92.5	104.8	100.0	2.4
53	346	2504	2.0	23.4012	1.3	0.0923	2.5	0.0157	2.1	0.84	100.2	2.1	89.7	2.1	183.1	33.6	100.2	2.1
132	366	25024	5.3	20.8447	1.4	0.1038	2.3	0.0157	1.8	0.80	100.4	1.8	100.3	2.2	98.0	32.2	100.4	1.8
293	472	13785	2.1	21.3085	1.3	0.1021	2.2	0.0158	1.8	0.80	100.9	1.8	98.7	2.1	45.7	32.3	100.9	1.8
48	1319	110588	2.0	20.6933	0.8	0.1071	2.1	0.0161	1.9	0.92	102.8	2.0	103.3	2.0	115.2	19.2	102.8	2.0
1	644	17323	1.3	21.2995	1.2	0.1043	2.3	0.0161	2.0	0.85	103.1	2.0	100.8	2.2	46.7	29.0	103.1	2.0
152	297	1802	2.1	25.0166	10.5	0.0894	10.9	0.0162	2.7	0.25	103.8	2.7	87.0	9.0	352.6	272.3	103.8	2.7
311	209	2462	2.7	22.8133	3.1	0.0981	3.7	0.0162	2.1	0.56	103.8	2.2	95.0	3.4	120.0	75.9	103.8	2.2
80	263	9319	2.9	21.2946	1.7	0.1057	2.2	0.0163	1.5	0.67	104.3	1.6	102.0	2.2	47.2	40.0	104.3	1.6
207	338	17247	2.2	21.6142	1.5	0.1044	2.6	0.0164	2.1	0.82	104.7	2.2	100.8	2.5	11.5	35.9	104.7	2.2
296	356	13131	3.3	20.5325	1.2	0.1108	2.3	0.0165	2.0	0.85	105.5	2.1	106.7	2.4	133.6	28.8	105.5	2.1
20	541	47226	2.5	20.7684	1.0	0.1107	2.5	0.0167	2.3	0.92	106.6	2.4	106.6	2.5	106.7	23.8	106.6	2.4

41	505	23029	4.3	20.6003	0.8	0.1121	2.0	0.0168	1.8	0.92	107.1	1.9	107.9	2.0	125.8	18.1	107.1	1.9
116	119	7791	1.8	21.1927	2.4	0.1113	3.5	0.0171	2.5	0.72	109.3	2.7	107.1	3.5	58.7	57.8	109.3	2.7
304	531	18855	2.3	20.8721	1.3	0.1137	2.4	0.0172	2.0	0.85	110.0	2.2	109.3	2.5	94.9	29.9	110.0	2.2
46	391	31942	2.7	21.5289	1.5	0.1107	2.1	0.0173	1.5	0.72	110.5	1.7	106.6	2.2	21.0	35.6	110.5	1.7
87	519	6354	2.5	21.7259	1.1	0.1097	2.6	0.0173	2.4	0.91	110.5	2.6	105.7	2.6	0.9	26.5	110.5	2.6
181	451	51925	2.3	20.4652	1.3	0.1167	2.5	0.0173	2.2	0.85	110.7	2.4	112.0	2.7	141.3	31.3	110.7	2.4
144	342	33125	1.5	21.0695	1.4	0.1135	2.7	0.0173	2.3	0.85	110.9	2.5	109.2	2.8	72.6	33.5	110.9	2.5
22	402	2529	2.5	23.0250	6.8	0.1042	7.2	0.0174	2.1	0.30	111.2	2.4	100.6	6.9	142.8	169.8	111.2	2.4
136	550	921849	3.3	20.5362	1.3	0.1173	2.4	0.0175	2.1	0.85	111.6	2.3	112.6	2.6	133.1	29.8	111.6	2.3
88	257	3976	2.0	20.6609	1.9	0.1167	3.0	0.0175	2.3	0.78	111.7	2.6	112.1	3.2	118.9	44.1	111.7	2.6
222	374	4256	5.1	22.6876	1.9	0.1063	2.6	0.0175	1.9	0.71	111.8	2.1	102.6	2.6	106.4	46.2	111.8	2.1
17	236	1750	4.8	24.5831	10.7	0.0981	10.8	0.0175	2.0	0.18	111.8	2.2	95.0	9.8	307.7	273.4	111.8	2.2
292	173	2144	1.8	24.2103	1.9	0.1004	2.9	0.0176	2.2	0.75	112.7	2.5	97.2	2.7	268.7	49.1	112.7	2.5
77	250	6817	2.9	21.7838	1.7	0.1117	2.9	0.0176	2.4	0.82	112.8	2.7	107.5	3.0	7.3	40.9	112.8	2.7
131	253	7764	1.7	21.3954	1.6	0.1140	2.7	0.0177	2.1	0.80	113.0	2.4	109.6	2.8	35.9	38.6	113.0	2.4
56	398	39299	3.0	20.7044	1.3	0.1180	2.1	0.0177	1.6	0.79	113.2	1.8	113.2	2.2	113.9	29.7	113.2	1.8
155	449	68316	4.1	20.2983	1.4	0.1216	2.9	0.0179	2.5	0.88	114.4	2.9	116.5	3.2	160.5	32.6	114.4	2.9
101	111	167705	3.8	19.3492	2.6	0.1291	3.8	0.0181	2.8	0.73	115.7	3.2	123.3	4.4	271.3	59.2	115.7	3.2
191	1795	294141	9.2	19.5069	1.4	0.1284	2.8	0.0182	2.4	0.86	116.1	2.8	122.7	3.3	252.7	32.8	116.1	2.8
60	276	2848	2.2	23.1351	1.7	0.1085	2.8	0.0182	2.2	0.79	116.3	2.6	104.6	2.8	154.6	42.5	116.3	2.6
227	203	11342	1.6	20.5531	1.9	0.1222	3.3	0.0182	2.7	0.82	116.3	3.1	117.0	3.6	131.2	43.8	116.3	3.1
279	357	5184	2.9	21.9947	1.3	0.1176	2.6	0.0188	2.3	0.88	119.8	2.7	112.9	2.8	30.6	30.7	119.8	2.7
114	285	6819	2.7	21.0244	1.5	0.1243	2.6	0.0190	2.1	0.83	121.1	2.6	119.0	2.9	77.6	34.5	121.1	2.6
149	108	7158	4.5	21.8990	2.3	0.1196	3.8	0.0190	3.0	0.80	121.3	3.6	114.7	4.1	20.1	55.1	121.3	3.6
236	419	22801	2.4	20.6601	1.2	0.1301	2.7	0.0195	2.4	0.89	124.4	3.0	124.2	3.2	119.0	28.8	124.4	3.0
6	1753	58076	2.6	14.2719	1.2	0.1885	2.5	0.0195	2.2	0.88	124.6	2.7	175.4	4.0	930.4	24.3	124.6	2.7
133	231	15349	4.2	20.5224	1.4	0.1325	2.4	0.0197	2.0	0.81	125.9	2.5	126.4	2.9	134.7	33.4	125.9	2.5
295	137	18745	2.1	20.9738	1.9	0.1334	3.4	0.0203	2.8	0.82	129.5	3.6	127.1	4.1	83.3	45.8	129.5	3.6
307	206	13322	2.3	20.7843	1.8	0.1391	2.7	0.0210	2.0	0.74	133.8	2.6	132.3	3.3	104.8	42.8	133.8	2.6
197	158	1216	2.7	27.5413	2.1	0.1105	3.4	0.0221	2.7	0.78	140.7	3.7	106.4	3.4	607.6	58.0	140.7	3.7
66	368	2315	1.7	24.3993	7.9	0.1295	8.3	0.0229	2.4	0.29	146.0	3.5	123.6	9.7	288.5	202.4	146.0	3.5
261	112	11153	2.0	20.3119	1.7	0.1563	3.0	0.0230	2.5	0.83	146.8	3.6	147.5	4.1	158.9	39.0	146.8	3.6
96	184	4472	2.7	21.7102	2.9	0.1467	3.7	0.0231	2.3	0.61	147.2	3.3	139.0	4.8	0.9	70.8	147.2	3.3
72	697	20116	1.8	20.4781	0.8	0.1557	2.1	0.0231	1.9	0.91	147.3	2.8	146.9	2.8	139.8	19.7	147.3	2.8
93	74	4171	2.9	22.8720	2.3	0.1399	3.7	0.0232	2.9	0.78	147.9	4.2	133.0	4.6	126.3	57.6	147.9	4.2
198	1774	69658	2.9	20.6724	0.8	0.1564	2.1	0.0235	1.9	0.93	149.5	2.8	147.6	2.9	117.6	18.1	149.5	2.8
215	277	5617	3.1	20.6846	1.0	0.1579	1.9	0.0237	1.6	0.85	150.9	2.4	148.8	2.6	116.2	23.5	150.9	2.4
238	148	10502	2.2	20.5349	1.9	0.1594	2.7	0.0237	2.0	0.72	151.3	2.9	150.2	3.8	133.3	43.7	151.3	2.9
85	84	20616	3.1	20.3279	1.9	0.1613	3.3	0.0238	2.7	0.82	151.5	4.1	151.9	4.7	157.1	44.8	151.5	4.1
160	67	2525	2.1	23.1124	2.0	0.1423	3.5	0.0239	2.9	0.82	152.0	4.3	135.1	4.5	152.2	50.0	152.0	4.3
115	188	46365	2.6	20.5268	1.3	0.1604	2.5	0.0239	2.2	0.85	152.2	3.3	151.1	3.6	134.2	30.9	152.2	3.3
140	347	14947	1.3	20.5435	1.4	0.1604	2.5	0.0239	2.2	0.85	152.2	3.2	151.0	3.6	132.3	31.9	152.2	3.2
276	152	12988	2.4	20.5953	1.7	0.1604	2.8	0.0240	2.2	0.80	152.6	3.3	151.0	3.9	126.4	39.6	152.6	3.3
14	136	4308	3.3	20.5254	2.7	0.1610	3.3	0.0240	1.9	0.56	152.7	2.8	151.6	4.7	134.4	64.3	152.7	2.8
264	88	10707	2.6	20.8748	2.1	0.1585	3.9	0.0240	3.3	0.85	152.9	5.1	149.4	5.5	94.6	49.1	152.9	5.1
130	109	65781	3.1	20.3658	2.0	0.1644	3.9	0.0243	3.3	0.85	154.7	5.0	154.6	5.5	152.7	47.4	154.7	5.0
257	273	4801	1.9	21.3396	1.5	0.1583	2.7	0.0245	2.3	0.84	156.0	3.5	149.2	3.8	42.2	34.8	156.0	3.5
21	552	41025	1.7	20.1018	0.8	0.1699	2.2	0.0248	2.1	0.93	157.8	3.2	159.4	3.3	183.2	19.6	157.8	3.2
154	252	1752	1.7	23.8722	10.3	0.1433	10.5	0.0248	2.2	0.21	158.0	3.4	136.0	13.4	233.1	259.7	158.0	3.4
220	95	5064	2.3	21.4007	1.9	0.1600	3.6	0.0248	3.0	0.85	158.1	4.7	150.7	5.0	35.3	45.0	158.1	4.7
76	150	14165	2.8	21.3427	1.5	0.1604	3.3	0.0248	2.9	0.89	158.1	4.6	151.1	4.6	41.8	36.1	158.1	4.6
156	213	1968	2.3	23.5794	9.1	0.1452	9.3	0.0248	1.9	0.21	158.1	3.0	137.7	12.0	202.1	228.2	158.1	3.0
43	249	13268	1.8	20.4023	1.6	0.1681	3.1	0.0249	2.6	0.86	158.4	4.1	157.8	4.5	148.5	36.4	158.4	4.1
271	518	56115	1.8	20.3523	0.9	0.1687	2.1	0.0249	1.9	0.91	158.5	3.0	158.3	3.0	154.2	20.5	158.5	3.0
308	914	109493	1.3	20.3325	1.1	0.1692	2.4	0.0250	2.2	0.90	158.9	3.4	158.8	3.5	156.5	25.1	158.9	3.4
75	267	83598	1.4	20.3290	1.2	0.1693	2.2	0.0250	1.8	0.84	159.0	2.9	158.8	3.2	156.9	27.1	159.0	2.9
253	571	29783	2.3	20.7027	1.0	0.1672	2.3	0.0251	2.1	0.91	159.8	3.3	157.0	3.4	114.1	22.8	159.8	3.3
175	654	44083	1.5	20.0808	0.8	0.1726	2.2	0.0251	2.0	0.94	160.0	3.2	161.7	3.3	185.6	18.0	160.0	3.2

290	430	1944	2.2	23.4150	4.7	0.1483	5.0	0.0252	1.9	0.37	160.4	2.9	140.4	6.6	184.6	116.3	160.4	2.9
90	82	265592	3.0	19.9023	1.9	0.1746	3.6	0.0252	3.1	0.86	160.5	5.0	163.4	5.5	206.4	43.2	160.5	5.0
25	201	18832	4.1	20.4764	1.4	0.1702	3.3	0.0253	3.0	0.91	160.9	4.8	159.6	4.9	140.0	32.0	160.9	4.8
68	602	36479	2.5	20.5100	1.0	0.1704	2.2	0.0253	2.0	0.90	161.3	3.2	159.7	3.3	136.1	23.0	161.3	3.2
122	554	5966	2.8	21.3189	0.7	0.1651	1.9	0.0255	1.7	0.92	162.5	2.8	155.2	2.7	44.5	17.4	162.5	2.8
176	97	12888	2.1	19.9114	1.8	0.1777	4.2	0.0257	3.9	0.91	163.4	6.2	166.1	6.5	205.3	41.2	163.4	6.2
173	457	8541	2.1	20.7602	0.9	0.1714	1.9	0.0258	1.7	0.89	164.3	2.8	160.7	2.9	107.6	20.6	164.3	2.8
29	279	5669	2.3	15.6834	5.0	0.2282	5.7	0.0260	2.7	0.48	165.2	4.4	208.7	10.7	733.7	105.4	165.2	4.4
98	133	4521	1.9	20.8716	1.7	0.1717	3.5	0.0260	3.0	0.87	165.5	5.0	160.9	5.2	94.9	41.0	165.5	5.0
192	380	35184	2.3	20.2674	0.8	0.1781	2.1	0.0262	1.9	0.92	166.6	3.1	166.5	3.2	164.0	19.4	166.6	3.1
36	629	28995	1.1	20.3825	0.8	0.1791	2.3	0.0265	2.2	0.94	168.5	3.6	167.3	3.5	150.8	18.3	168.5	3.6
39	541	15701	1.8	20.4194	0.8	0.1799	2.1	0.0266	1.9	0.92	169.5	3.2	168.0	3.2	146.6	19.1	169.5	3.2
111	1135	68317	10.4	14.2888	1.1	0.2601	3.1	0.0270	2.9	0.94	171.5	5.0	234.8	6.6	927.9	22.5	171.5	5.0
202	32	2174	2.1	24.0872	3.9	0.1555	5.6	0.0272	4.1	0.73	172.7	7.0	146.7	7.7	255.8	97.8	172.7	7.0
64	191	5170	2.3	18.9153	3.1	0.1993	3.8	0.0273	2.2	0.57	173.9	3.8	184.5	6.4	323.1	71.1	173.9	3.8
16	430	15329	1.6	19.1446	1.1	0.1974	2.5	0.0274	2.2	0.89	174.3	3.8	182.9	4.1	295.7	25.9	174.3	3.8
183	139	51282	2.9	20.1213	0.9	0.1880	2.8	0.0274	2.6	0.95	174.5	4.5	175.0	4.5	180.9	20.4	174.5	4.5
300	126	7162	3.2	20.7446	1.5	0.1850	3.3	0.0278	3.0	0.89	177.0	5.2	172.4	5.3	109.3	35.5	177.0	5.2
190	880	61241	1.6	20.1806	0.9	0.2003	2.1	0.0293	1.8	0.89	186.3	3.3	185.4	3.5	174.0	22.1	186.3	3.3
100	326	67278	2.6	20.1805	1.0	0.2008	2.2	0.0294	2.0	0.90	186.7	3.7	185.8	3.8	174.0	23.1	186.7	3.7
251	411	88564	1.8	20.3561	1.1	0.2022	2.2	0.0299	1.9	0.87	189.7	3.6	187.0	3.7	153.8	25.1	189.7	3.6
297	356	520743	2.5	20.3700	1.1	0.2025	2.0	0.0299	1.7	0.85	190.1	3.2	187.3	3.4	152.2	24.6	190.1	3.2
210	134	6583	2.1	21.3849	1.6	0.1932	3.4	0.0300	3.0	0.88	190.3	5.6	179.3	5.6	37.1	39.4	190.3	5.6
203	332	134655	3.0	20.0468	1.0	0.2062	2.4	0.0300	2.2	0.91	190.4	4.1	190.4	4.1	189.5	22.3	190.4	4.1
129	230	5608	2.5	16.5691	4.4	0.2498	4.8	0.0300	1.9	0.39	190.7	3.5	226.5	9.8	616.2	95.9	190.7	3.5
286	104	3589	3.4	21.0473	2.5	0.1990	4.0	0.0304	3.1	0.78	193.0	5.9	184.3	6.7	75.0	58.7	193.0	5.9
165	425	14023	2.4	20.5462	1.0	0.2055	2.4	0.0306	2.2	0.91	194.4	4.2	189.7	4.2	132.0	23.4	194.4	4.2
37	323	20770	1.8	20.0660	1.1	0.2115	2.3	0.0308	2.0	0.87	195.5	3.8	194.8	4.0	187.3	26.2	195.5	3.8
138	746	99850	3.1	19.9859	0.7	0.2139	2.2	0.0310	2.0	0.94	196.8	3.9	196.8	3.9	196.7	17.2	196.8	3.9
63	118	8997	3.5	20.4821	1.7	0.2156	3.6	0.0320	3.1	0.87	203.2	6.2	198.3	6.4	139.4	40.7	203.2	6.2
47	243	5767	2.0	20.9708	1.0	0.2106	2.1	0.0320	1.9	0.89	203.3	3.8	194.1	3.8	83.7	22.9	203.3	3.8
283	225	4869	3.5	21.0576	1.3	0.2157	2.9	0.0329	2.6	0.89	209.0	5.3	198.4	5.2	73.9	31.3	209.0	5.3
288	234	24528	3.0	20.0822	1.0	0.2280	2.3	0.0332	2.0	0.91	210.6	4.2	208.6	4.3	185.4	22.2	210.6	4.2
13	135	9041	3.3	20.4239	1.9	0.2297	3.4	0.0340	2.8	0.83	215.6	6.0	209.9	6.5	146.0	44.5	215.6	6.0
26	88	6550	3.1	20.9456	1.6	0.2276	3.5	0.0346	3.1	0.89	219.1	6.7	208.2	6.6	86.6	38.3	219.1	6.7
280	458	39406	2.1	7.4508	0.6	0.7237	2.1	0.0391	2.0	0.95	247.3	4.8	552.9	8.9	2153.8	11.2	247.3	4.8
110	199	15363	1.7	17.7425	0.9	0.5371	2.3	0.0691	2.1	0.92	430.9	8.9	436.5	8.3	466.6	19.8	430.9	8.9
137	134	38448	1.7	17.7513	1.0	0.5917	2.5	0.0762	2.3	0.92	473.3	10.3	472.0	9.3	465.6	21.7	473.3	10.3
246	727	42950	10.7	17.7989	0.6	0.5965	1.9	0.0770	1.8	0.95	478.2	8.5	475.0	7.4	459.6	13.8	478.2	8.5
139	922	93581	1.0	17.6985	0.6	0.6070	1.8	0.0779	1.7	0.94	483.6	7.8	481.6	6.9	472.1	13.6	483.6	7.8
248	606	51124	1.6	17.6809	0.7	0.6093	1.9	0.0781	1.8	0.94	484.9	8.5	483.1	7.5	474.4	15.1	484.9	8.5
69	269	43754	2.0	17.6516	1.0	0.6121	2.6	0.0784	2.4	0.93	486.3	11.4	484.9	10.1	478.0	21.5	486.3	11.4
52	297	33346	1.6	16.4732	0.8	0.8875	2.3	0.1060	2.1	0.94	649.7	13.3	645.0	10.9	628.8	16.6	649.7	13.3
182	133	17166	1.1	14.0898	0.8	1.4776	2.6	0.1510	2.5	0.95	906.6	21.1	921.3	15.9	956.6	17.2	956.6	17.2
240	98	11248	1.3	14.0050	0.7	1.6296	2.6	0.1655	2.5	0.96	987.4	22.7	981.7	16.2	968.9	13.9	968.9	13.9
58	228	43161	2.6	11.5901	0.6	2.5196	2.5	0.2118	2.4	0.97	1238.4	27.4	1277.7	18.2	1344.5	11.2	1344.5	11.2
59	174	129384	1.6	11.5068	0.8	2.7719	2.5	0.2313	2.4	0.96	1341.5	29.5	1348.0	19.0	1358.4	14.5	1358.4	14.5
78	239	37661	1.3	11.4977	0.7	2.5042	2.3	0.2088	2.2	0.95	1222.5	24.9	1273.2	17.1	1359.9	13.9	1359.9	13.9
148	97	562996	1.3	11.4758	0.7	2.7946	2.4	0.2326	2.3	0.96	1348.1	27.6	1354.1	17.7	1363.6	13.3	1363.6	13.3
301	109	67534	1.9	11.4690	0.8	2.8886	2.5	0.2403	2.3	0.94	1388.2	29.2	1379.0	18.8	1364.7	16.3	1364.7	16.3
73	456	61548	1.6	11.4418	0.6	2.8007	1.9	0.2324	1.8	0.95	1347.1	21.6	1355.7	14.0	1369.3	11.0	1369.3	11.0
128	367	978126	4.0	11.4029	0.6	2.7717	2.0	0.2292	1.9	0.95	1330.4	23.1	1347.9	15.1	1375.8	12.2	1375.8	12.2
5	771	237159	2.5	11.3958	0.6	2.7235	2.0	0.2251	1.9	0.95	1308.7	22.4	1334.9	14.8	1377.0	12.2	1377.0	12.2
200	575	128618	1.8	11.3908	0.6	2.8372	2.3	0.2344	2.2	0.96	1357.5	26.7	1365.4	17.0	1377.9	11.6	1377.9	11.6
134	1945	450197	5.4	11.3882	0.8	3.0313	2.1	0.2504	1.9	0.93	1440.4	24.9	1415.5	15.9	1378.3	15.0	1378.3	15.0
118	616	112125	4.4	11.3848	0.6	2.7661	2.2	0.2284	2.1	0.96	1326.1	25.3	1346.4	16.4	1378.9	12.0	1378.9	12.0
4	411	98389	6.4	11.3598	0.6	2.8234	2.3	0.2326	2.2	0.96	1348.2	27.1	1361.8	17.3	1383.1	11.9	1383.1	11.9
241	1758	860862	5.2	11.3527	0.8	2.7226	2.4	0.2242	2.2	0.94	1303.9	26.2	1334.6	17.6	1384.3	15.7	1384.3	15.7

303	486	458532	1.1	11.3525	0.7	2.8319	1.8	0.2332	1.7	0.93	1351.1	20.3	1364.0	13.5	1384.3	12.7	1384.3	12.7
147	53	17732	2.0	11.3316	0.8	2.5386	3.4	0.2086	3.3	0.97	1221.5	36.8	1283.2	24.8	1387.9	15.6	1387.9	15.6
127	692	445324	11.3	11.3232	0.7	2.7638	2.4	0.2270	2.3	0.96	1318.6	27.6	1345.8	18.0	1389.3	13.0	1389.3	13.0
169	683	172243	7.1	11.3197	0.6	2.8731	1.9	0.2359	1.8	0.94	1365.2	22.0	1374.9	14.3	1389.9	12.0	1389.9	12.0
159	604	121764	3.6	11.3193	0.6	2.7693	2.2	0.2274	2.1	0.96	1320.6	24.8	1347.3	16.0	1390.0	11.0	1390.0	11.0
32	644	133007	12.8	11.3183	0.6	2.7880	2.4	0.2289	2.3	0.97	1328.5	27.7	1352.3	17.8	1390.1	11.8	1390.1	11.8
252	461	309190	3.3	11.3159	0.7	2.7432	2.5	0.2251	2.4	0.96	1308.9	28.3	1340.2	18.5	1390.5	13.4	1390.5	13.4
314	840	256996	6.4	11.3010	0.7	2.9448	2.3	0.2414	2.2	0.96	1393.8	28.2	1393.5	17.8	1393.1	12.8	1393.1	12.8
7	603	178823	7.4	11.2979	0.6	3.0038	2.1	0.2461	2.0	0.96	1418.5	25.2	1408.6	15.7	1393.6	11.3	1393.6	11.3
267	591	80666	4.0	11.2946	0.6	2.9444	1.9	0.2412	1.8	0.95	1392.9	22.3	1393.4	14.2	1394.2	11.6	1394.2	11.6
224	769	131382	3.3	11.2915	0.6	2.7165	1.9	0.2225	1.8	0.95	1294.9	20.9	1333.0	14.0	1394.7	11.8	1394.7	11.8
310	585	150105	2.4	11.2834	0.7	2.7904	2.0	0.2284	1.9	0.93	1325.9	22.3	1353.0	14.9	1396.1	13.9	1396.1	13.9
258	444	1058252	3.0	11.2787	0.6	2.8710	2.2	0.2349	2.1	0.96	1359.9	25.5	1374.3	16.3	1396.9	11.5	1396.9	11.5
178	193	95709	1.9	11.2677	0.8	2.8057	3.0	0.2293	2.9	0.97	1330.7	34.8	1357.1	22.4	1398.7	14.8	1398.7	14.8
19	618	105837	2.4	11.2653	0.7	2.8350	1.8	0.2316	1.7	0.92	1343.0	20.2	1364.9	13.6	1399.1	13.7	1399.1	13.7
268	741	2667453	1.9	11.2633	0.7	2.6436	2.1	0.2160	2.0	0.94	1260.5	22.5	1312.9	15.3	1399.5	13.1	1399.5	13.1
113	555	174753	5.3	11.2564	0.5	2.8328	2.1	0.2313	2.0	0.97	1341.1	24.2	1364.3	15.5	1400.7	9.6	1400.7	9.6
61	92	20001	1.6	11.2522	0.7	3.0519	2.5	0.2491	2.4	0.96	1433.7	30.4	1420.7	18.9	1401.4	13.7	1401.4	13.7
86	921	953303	8.5	11.2479	0.6	2.9182	1.9	0.2381	1.8	0.94	1376.6	21.7	1386.6	14.1	1402.1	12.0	1402.1	12.0
164	372	492722	4.9	11.2262	0.8	2.8616	2.3	0.2330	2.1	0.94	1350.2	26.0	1371.9	17.1	1405.8	15.0	1405.8	15.0
312	833	96687	2.5	11.2227	0.6	2.8733	1.9	0.2339	1.9	0.96	1354.8	22.6	1374.9	14.6	1406.4	11.0	1406.4	11.0
44	773	115372	5.6	11.2153	0.7	2.8888	2.6	0.2350	2.5	0.97	1360.6	30.8	1379.0	19.6	1407.7	12.6	1407.7	12.6
89	360	1389469	3.4	11.2151	0.6	2.7501	2.1	0.2237	2.1	0.96	1301.3	24.4	1342.1	16.0	1407.7	11.1	1407.7	11.1
107	551	464362	3.5	11.2068	0.6	2.8309	1.8	0.2301	1.6	0.94	1335.0	19.9	1363.8	13.2	1409.1	11.5	1409.1	11.5
180	524	158546	3.0	11.2057	0.6	2.8805	2.2	0.2341	2.1	0.96	1356.0	25.6	1376.8	16.3	1409.3	11.0	1409.3	11.0
121	789	293116	3.8	11.2020	0.7	2.8859	2.1	0.2345	2.0	0.95	1357.9	25.0	1378.2	16.1	1409.9	12.4	1409.9	12.4
117	978	1759955	3.2	11.1907	0.7	2.8687	1.9	0.2328	1.8	0.94	1349.3	21.7	1373.7	14.3	1411.9	12.8	1411.9	12.8
225	1010	4740844	22.6	11.1849	0.7	2.7679	2.1	0.2245	1.9	0.95	1305.8	23.0	1346.9	15.4	1412.9	12.9	1412.9	12.9
166	664	138637	2.0	11.1822	0.8	2.8932	2.1	0.2346	1.9	0.92	1358.8	23.7	1380.1	15.8	1413.3	15.3	1413.3	15.3
50	1093	5424270	4.8	11.1590	0.7	2.8061	2.0	0.2271	1.8	0.93	1319.3	22.0	1357.2	14.8	1417.3	13.5	1417.3	13.5
9	1179	208307	5.4	11.1091	0.6	2.7730	2.1	0.2234	2.1	0.96	1299.9	24.2	1348.3	16.0	1425.9	11.8	1425.9	11.8
298	135	118999	2.1	11.0285	0.8	3.0409	2.3	0.2432	2.1	0.94	1403.5	26.7	1417.9	17.2	1439.8	14.7	1439.8	14.7
10	365	439214	0.8	10.9681	0.5	2.8077	1.9	0.2233	1.8	0.96	1299.5	21.3	1357.6	14.1	1450.2	10.0	1450.2	10.0
162	520	383099	1.6	10.8286	0.7	3.1019	1.9	0.2436	1.7	0.92	1405.4	21.8	1433.2	14.4	1474.5	14.0	1474.5	14.0
55	200	52866	1.7	10.7901	0.6	3.0771	2.2	0.2408	2.1	0.97	1390.9	26.4	1427.0	16.7	1481.3	10.8	1481.3	10.8
97	250	65571	1.7	10.6457	0.5	3.3460	2.2	0.2583	2.1	0.97	1481.4	27.6	1491.9	16.8	1506.8	10.2	1506.8	10.2
125	184	30161	4.0	10.5312	0.8	3.4738	2.7	0.2653	2.6	0.96	1517.0	35.2	1521.3	21.4	1527.2	14.4	1527.2	14.4
269	1471	576249	11.8	10.4938	1.0	3.1356	3.0	0.2386	2.8	0.94	1379.7	34.7	1441.5	22.9	1533.9	19.4	1533.9	19.4
256	503	46826	4.5	10.3364	0.9	3.4102	2.4	0.2556	2.3	0.93	1467.5	30.0	1506.7	19.2	1562.3	16.4	1562.3	16.4
74	65	43546	0.6	10.3309	0.8	3.7347	3.5	0.2798	3.4	0.98	1590.5	48.4	1578.8	28.2	1563.3	14.6	1563.3	14.6
71	1067	452239	4.6	10.2330	0.7	3.4494	2.3	0.2560	2.2	0.95	1469.4	29.0	1515.7	18.2	1581.1	13.2	1581.1	13.2
219	873	797692	0.9	10.1381	0.6	3.5520	1.8	0.2612	1.7	0.94	1495.8	23.2	1538.9	14.6	1598.5	11.8	1598.5	11.8
196	431	37991	1.5	10.0501	0.7	3.0778	4.1	0.2243	4.1	0.99	1304.8	48.1	1427.2	31.7	1614.8	13.2	1614.8	13.2
229	165	144988	1.7	9.9697	0.6	4.0440	2.7	0.2924	2.7	0.97	1653.6	38.8	1643.1	22.3	1629.7	11.9	1629.7	11.9
235	474	232036	2.6	9.9218	0.6	3.9037	2.0	0.2809	1.9	0.94	1595.9	26.3	1614.4	15.9	1638.7	12.0	1638.7	12.0
65	2421	354138	2.6	9.9033	0.8	3.5966	2.3	0.2583	2.2	0.94	1481.3	28.9	1548.8	18.5	1642.1	15.0	1642.1	15.0
250	134	34205	1.2	9.8133	0.6	4.0644	2.3	0.2893	2.2	0.97	1637.9	31.7	1647.2	18.5	1659.0	10.8	1659.0	10.8
223	337	16490	3.0	9.7534	0.7	3.9531	2.3	0.2796	2.2	0.96	1589.5	31.0	1624.6	18.7	1670.4	12.5	1670.4	12.5
234	293	63691	3.5	9.7408	0.7	4.1113	2.7	0.2905	2.6	0.97	1643.8	37.8	1656.6	21.9	1672.8	12.1	1672.8	12.1
243	382	316611	4.5	9.6916	0.6	3.9646	1.9	0.2787	1.8	0.95	1584.7	25.9	1627.0	15.7	1682.1	11.0	1682.1	11.0
174	664	745564	3.1	9.6100	0.6	3.7020	2.2	0.2580	2.2	0.96	1479.7	28.4	1571.8	17.9	1697.7	11.2	1697.7	11.2
193	414	12012	5.4	9.6057	0.8	3.6699	1.7	0.2557	1.5	0.88	1467.7	20.1	1564.9	13.9	1698.5	15.1	1698.5	15.1
291	791	174951	3.1	9.6047	0.5	3.8739	1.6	0.2699	1.6	0.95	1540.0	21.5	1608.2	13.3	1698.7	9.1	1698.7	9.1
284	629	405761	2.6	9.5155	0.4	3.9650	1.5	0.2736	1.4	0.95	1559.2	19.8	1627.1	12.1	1715.9	8.2	1715.9	8.2
189	524	461759	6.2	9.4895	0.7	4.4605	2.1	0.3070	2.0	0.94	1725.9	30.4	1723.7	17.7	1720.9	13.3	1720.9	13.3
120	127	96819	1.6	9.4661	0.7	4.2285	2.4	0.2903	2.3	0.96	1643.1	33.7	1679.6	19.9	1725.5	12.7	1725.5	12.7
62	165	127333	2.4	9.4189	0.6	4.6036	2.4	0.3145	2.3	0.96	1762.7	35.9	1749.9	20.1	1734.6	11.8	1734.6	11.8
18	876	981052	1.9	9.4162	0.7	3.9719	1.9	0.2713	1.8	0.93	1547.2	24.4	1628.5	15.6	1735.2	13.2	1735.2	13.2

105	584	260864	2.3	9.3514	0.6	4.4280	1.8	0.3003	1.7	0.93	1692.9	24.7	1717.6	14.8	1747.8	11.9	1747.8	11.9
30	240	53285	1.9	9.3043	0.6	4.2821	2.1	0.2890	2.0	0.96	1636.3	29.2	1689.9	17.4	1757.1	11.1	1757.1	11.1
95	672	331741	2.1	9.2542	0.7	3.9366	2.0	0.2642	1.8	0.94	1511.4	24.8	1621.2	15.9	1766.9	12.4	1766.9	12.4
294	750	1549641	1.9	9.2542	0.7	4.3549	2.3	0.2923	2.2	0.95	1652.9	31.9	1703.8	19.0	1766.9	13.3	1766.9	13.3
106	193	33110	1.4	9.2385	0.7	4.2996	2.8	0.2881	2.7	0.96	1632.0	38.6	1693.3	22.8	1770.0	13.3	1770.0	13.3
146	534	128871	3.4	9.2263	0.6	3.9086	1.9	0.2615	1.8	0.95	1497.7	24.5	1615.5	15.6	1772.4	11.0	1772.4	11.0
109	1224	509698	2.3	9.1040	0.8	4.1087	2.3	0.2713	2.2	0.93	1547.3	29.6	1656.0	18.9	1796.8	15.2	1796.8	15.2
226	96	21805	1.4	8.9434	0.7	4.9692	2.5	0.3223	2.4	0.96	1801.0	37.1	1814.1	20.7	1829.1	11.9	1829.1	11.9
103	501	337799	2.4	8.9398	0.7	4.8666	2.1	0.3155	2.0	0.95	1767.9	31.2	1796.5	17.9	1829.8	12.4	1829.8	12.4
38	781	960188	6.0	8.8987	0.7	4.5106	2.8	0.2911	2.7	0.97	1647.1	39.8	1732.9	23.5	1838.2	12.9	1838.2	12.9
28	429	170037	1.6	6.0724	0.5	10.2706	1.8	0.4523	1.7	0.96	2405.6	34.9	2459.5	16.8	2504.3	8.8	2504.3	8.8

Chapter 4

Rapid assembly and crystallization of a fossil, large-volume, silicic magma chamber

Abstract

The rates at which large-volume, silicic (> 65 wt% SiO2) magma chambers (>40-60% melt) are constructed, as well as their longevity in the upper crust remain controversial. This controversy is due, in part, to a missing record of granitoid plutonic complexes that represent large, fossil, upper-crustal magma chambers. We present new geologic mapping and high-precision U-Pb zircon geochronology from the Eocene Golden Horn batholith (GHB) in Washington, USA. These data reveal that the batholith was constructed as a series of sills over 739 ± 34 k.y. Topographic relief of >2 km permits volume estimates for four of the sills, the largest of which, a >424 km^3 rapakivi granite, was emplaced in 26 ± 25 k.y. at a rate of ca. 0.0125 km^3/a. This rate exceeds the thermally modeled requirements to build large-volume, silicic magma chambers and we suggest that that this unit represents the first fossil magma chamber of this type described in the geologic record.

Introduction

Rhyolites and dacites emplaced during 'supereruptions' demonstrate that large-volumes (>450 km^3) of eruptible silicic magma can exist in the upper crust. However, the timescales over which the magma reservoirs that source these eruptions are built remain controversial. Thermal models suggest that magma emplacement rates need to be >0.003-0.01 km^3/a in order to accumulate enough eruptible magma to supply a 'supereruption' (Annen, 2009; Gelman et al., 2013). Yet, these rates are higher than the time-averaged rates for nearly all well-studied granitoid plutonic complexes (i.e., < 0.001 km^3/a; Glazner et al., 2004). This disparity contradicts evidence that 'supereruptions' are sourced from crystal-rich magma chambers that should be preserved in the geologic record as granitoid plutons (e.g., Bachmann et al., 2007), leading to two end-member hypotheses for magma chamber construction: 1) that long-lived magma

reservoirs that spend the majority of their lifetimes at low melt fraction, can differentiate to form pools of eruptible magma or be rejuvenated through new magma input (Bachmann and Bergantz, 2003, 2004) or 2) that some silicic magma chambers are assembled rapidly and exist ephemerally within the upper crust (e.g., Glazner et al., 2004). However, the plutonic equivalents of rapidly assembled silicic magma chambers have not been described in the geologic record.

Geochronologic studies paired with robust volume estimates for magmatic intrusions provide the most direct means of assessing magma emplacement rates and quantifying crystallization duration (e.g., Matzel et al., 2006; Tappa et al., 2011; Davis et al., 2012; Leuthold et al., 2012; Frazer et al., 2012; Barboni et al., 2015). Nevertheless, the number of such studies is limited. Here we present new mapping and high-precision U-Pb zircon geochronology from the Golden Horn batholith (GHB) in the North Cascades, Washington. These data show that part of the batholith was assembled rapidly and may represent a fossil large-volume (>424 km^3) silicic magma chamber.

Golden Horn Batholith

The 307 km^2 Eocene GHB intrudes Mesozoic sedimentary, volcanic, and plutonic rocks near the southern end of the Coast Plutonic Complex (Fig. 1A). It is dominantly composed of peralkaline and calc-alkaline granite and granodiorite with minor diorite. The presence of a narrow metamorphic aureole, abundant miarolitic cavities, and intrusive breccias all point to emplacement within the upper crust. We estimate a depth of ca. 7-8 km based on GHB granite compositions that plot near the 0.2 GPa water-saturated eutectic in the Qz-Ab-Or system (Fig. 2) and a pressure of 0.25 ± 0.06 GPa calculated using Al-in-hornblende barometry (see Appendix A for methods and results).

Geologic mapping by the authors and Stull (1969) split the GHB into six units: 1) peralkaline granite; 2) hypersolvus granite; 3) rapakivi granite; 4) heterogeneous granite; 5) granodiorite; and 6) diorite (Fig. 1B; see petrographic descriptions in Appendix B). Topographic relief of >2 km gives excellent 3D control on the geometry of these units and shows that they form sheet-like bodies (Fig. 1B and 1C). Volumes were estimated by assuming each sheet had a constant thickness and was tabular across its areal extent. We also include eroded portions of each sheet in areas where we can confidently project units across glacial valleys. The thickness and area used for each estimate is presented in the Appendix B. The peralkaline and hypersolvus

granites are exposed in a down-dropped fault block in the southeastern part of the GHB (Fig. 1B) and we calculate respective volumes of 29 km^3 and 54 km^3 for these units. These volumes are likely minimums because they do not include any parts of these sheets that extended to the northwest, but are now eroded. Indeed, a larger size for the hypersolvus granite is suggested by a <50 m wide (not shown in Fig. 1B) zone of this unit exposed along the western side of the batholith. We assume that the rapakivi granite and heterogeneous granite extend under the entire areal extent of the granitoid portions of the GHB resulting in respective volumes of >424 km^3 and 197 km^3. The volume of the rapakivi granite is a minimum estimate because the top and bottom of the sheet are never exposed within the same fault block (Fig. 1B). Volumes for the diorite and granodiorite were not estimated due to their presumed small volume and/or only limited exposure.

U-Pb Zircon Geochronology

Our volume estimates for the mapped units of the GHB provide an excellent opportunity to estimate magma emplacement rates, and we dated 15 samples using U-Pb zircon chemical abrasion-isotope dilution-thermal ionization mass spectrometry (CA-ID-TIMS) geochronology (Mattinson, 2005) with this goal in mind. The methods used for these analyses are discussed in Appendix D, all measured isotopic data is presented in Table A1), and concordia plots are shown in Fig. A2. We used $^{206}Pb/^{238}U$ dates for all of our interpretations because this chronometer provides the most precise and accurate date for rocks of this age. Reported dates are corrected for initial disequilibrium in the ^{238}U-^{206}Pb decay chain using the measured $[Th/U]_{zircon}$ and the mean ratio of zircon/melt partition coefficients for Th and U (f_{ThU}=0.138) from high-SiO_2 rhyolites erupted from the Yellowstone caldera (Stelten et al., 2015). The 2σ variability in the mean square weighted deviation (MSWD; Wendt and Carl, 1991) of weighted means is used to determine whether analytical uncertainty can account for the observed intra-sample dispersion in zircon dates or whether it represents resolvable age differences in zircon crystallization. With the exception of a single antecrystic grain found in sample NC-MPE-485 (Fig. 3A), which is excluded from our calculations, none of the samples have resolvable age dispersion (Table 1). Therefore, we conclude that the duration of zircon crystallization within each hand sample is equal to or less than our analytical uncertainty (18-34 k.y.). Since all of the analyses used the

same isotopic tracer and decay constants, all discussion of the data uses analytical uncertainty only.

The petrologic significance of zircon dates is dependent on when the melt becomes saturated with this mineral during its crystallization history. Early saturation can result in inherited zircons entrained from the magma's source region or antecrystic zircons that record crystallization at depth prior to transport and emplacement, leading to overestimates of the magma's residence time in the upper crust (Miller et al., 2007; Barboni et al., 2015). Alternatively, late zircon saturation may lead to limited age dispersion that underestimates residence times. CL images of zircons from the GHB do not show inherited cores (Fig. 4), and only one of the dated zircons is demonstrably antecrystic (Fig. 3A), suggesting that the majority of GHB magmas intruded above their zircon saturation temperatures (Miller et al., 2003). However, petrographic observations (Fig. 5) demonstrate that zircon predated or co-crystallized with the major rock-forming minerals in each unit, and we consider the duration of zircon crystallization to approximate the duration of magma crystallization at the emplacement level.

The difference between the oldest and youngest dates within the GHB demonstrates that it was built over at least 739 ± 34 k.y. (Fig. 3A), starting with intrusion of the diorite and followed by under-accretion of the peralkaline granite, hypersolvus granite, rapakivi granite, and granodiorite. Subsequently, the heterogeneous granite intruded along the contact between the rapakivi granite and granodiorite, and a subvolcanic stock of uncertain relationship to the batholith intruded the rapakivi granite (Fig. 1B). Estimates for the duration of magmatism within individual units is reported in Fig. 3A and represent the difference between the weighted mean dates of the oldest and youngest samples.

Magma Chamber Construction and Crystallization

Magma emplacement rates were calculated assuming a constant rate of emplacement over our calculated durations. The durations are of similar magnitude to our analytical uncertainty, resulting in asymmetric probability distributions for rates calculated using Monte Carlo simulations (Fig. 3B: see Appendix E for methods). Given this asymmetry, we report the mode of these simulations as the best estimate for the magma emplacement rate in each unit. The peralkaline (ca. 0.0004 km^3/a), hypersolvus (ca. 0.0012 km^3/a), and heterogeneous granite (ca. 0.0027 km^3/a) span the range of rates seen in other well-studied plutonic complexes (Fig. 6), and

distinct sample dates (Fig. 3A) and sharp internal contacts support the interpretation that these bodies never formed single, large-volume magma chambers. The rapakivi granite, however, has a calculated magma emplacement rate of 0.0125 km^3/a, exceeding the rates required for the construction of large-volume, silicic magma chambers in thermal models (Fig. 3B). While it is possible that our dates for this unit do not span its complete emplacement duration, overlapping zircon dates from five widely spaced samples (Fig. 1B) indicate that melt was simultaneously present throughout much of the sheet. Because we infer that zircon crystallization occurred over a similar interval to that of magma crystallization, we suggest that this unit represents a large, fossil, silicic magma chamber. The 26 ± 25 k.a. duration of magma emplacement and crystallization suggests that this body was an ephemeral feature and is more rapid than the crystallization timescales (>100 k.a.) predicted for silicic magma reservoirs the size of the rapakivi granite at ca. 5-10 km (Gelman et al., 2013). The reasons for such rapid crystallization remain unclear, but may include the relatively short duration of high magma emplacement rates and the evolved nature of the melt (whole rock SiO2 ranges from 73-76 wt%: Stull, 1969).

Extremely high magma emplacement rates are likely trigger eruptions by generating overpressure within a magma chamber (e.g., Degruyter et al., 2016), and this may explain the scarcity of rapidly assembled silicic magma chambers in the plutonic record (e.g., Glazner et al., 2004; Tappa et al., 2011). It is presently unclear whether any part of the GHB is related to an eruption. A series of 9 tuffs in the Chumstick strike-slip basin, ca. 100 km to the south of the GHB, closely match the batholith in age (Eddy et al., 2015), but the geochemical data needed to assess whether any of these tuffs were sourced from the GHB does not exist. Nevertheless, the discovery of extremely high magma emplacement rates in the rapakivi granite of the GHB demonstrates that plutons representing rapidly assembled, large-volume, silicic magma chambers can be preserved in the geologic record under certain circumstances (i.e., when wall rock is pre-heated by previous intrusions), and we anticipate that more such fossil chambers will be discovered in the future.

Conclusions

New geologic mapping and high-precision U-Pb zircon geochronology from the Eocene GHB provide estimates of magma emplacement rates for four out of six map units. The largest unit, a >424 km^3 body of rapakivi granite, was built over 26 ± 25 k.y., implying a magma

emplacement rate of ca. 0.0125 km^3/a. This is the highest rate documented in a granitoid pluton and exceeds the thermally modeled requirements for the development of large, silicic magma chambers. We suggest that this unit represents the first fossil, large-volume, silicic magma chamber described in the geologic record. The continued study and documentation of such chambers will provide unique opportunities to better understand the processes that occur within these chambers and their relationship to large eruptions.

Appendix A: Al-in-Hornblende Barometry

In order to better assess the emplacement depth of the GHB, we calculated pressures for two samples of the rapakivi granite (NC-MPE-086: 48.57338 -120.63071 and NC-MPE-503: 48.64422 -120.75922) using the Al-in-hornblende barometer. This barometer is based on a linear relationship between the intrusion depth of silicic liquids and the total aluminum content (Al_{tot}) in hornblende. However, the silicic liquid must have been saturated with plagioclase, potassium feldspar, biotite, hornblende, titanite, quartz, magnetite or ilmenite, and a fluid phase during final crystallization for accurate pressure determinations. The required mineral assemblage was identified in thin section, and the presence of both magnetite and ilmenite was confirmed using energy dispersive spectrometry (Fig. A1). Hornblende and plagioclase core and rim compositions were measured using a 5 μm spot size on the MIT JEOL-JXA8200 using a 15 kV accelerating voltage and 10 nA beam current. The results are reported in Tables A1 and A2. Pressures were calculated using pairs of plagioclase-hornblende cores and plagioclase-hornblende rims using the calibration of Anderson and Smith (1995). Temperatures were estimated using the Blundy and Holland (1990) plagioclase-hornblende thermometer. All temperature and pressure estimates are reported in Table A3.

The calculated pressures range from 0.05 to 0.30 GPa with an associated uncertainty of 0.06 GPa. Three measurements of hornblende rims give pressures lower than the experimental calibration of the Al-in-hornblende barometer (0.25 GPa: Schmidt, 1992) and hornblende-plagioclase thermometry for these samples gives temperatures below the H_2O-saturated solidus for granitic melts at pressures of <0.5 GPa (Ebadi and Johannes, 1991). Therefore, these results likely do not provide accurate pressure estimates. The remaining measurements give magmatic temperatures and consistent pressures. A mean of these values gives 0.25 ± 0.06 GPa and is at the lower limit of the experimental calibration for the barometer.

Appendix B: Lithologic Descriptions

Peralkaline granite

Misch (1965) first recognized peralkaline granite within the Golden Horn batholith (GHB) and the rock was subsequently described by Stull (1969). It forms a ~400 m thick sheet of leucocratic, medium-grained granite dominantly composed of perthite, quartz, and sodic amphiboles (riebeckite, arfvedsonite) exposed in a down-dropped fault block (72 km^2) in the southeastern portion of the batholith (Fig. 1B and 1C). The presence of dark blue sodic amphibole is diagnostic in the field. Quartz occurs as large (5-10 mm) rounded crystals and in granophyric intergrowths between large grains (Stull, 1969). Miarolitic cavities are abundant within this lithology and range from several millimeters to one meter in diameter. The cavities are filled with diverse minerals, including several unique to the GHB (Boggs, 1984). Dikes of the hypersolvus granite cut the peralkaline granite and establish a relative age relationship between the two lithologies. The normative mineralogy of the peralkaline granite plots near the 0.2 GPa H_2O-saturated eutectic in the Ab-Or-Qz system (Fig. 2).

Hypersolvus granite

Hypersolvus granite was first mapped and described by Stull (1969). It forms two subhorizontal sheets exposed in the southeastern portion of the GHB (Fig. 1B and 1C). The first sheet is only exposed at very high elevations and remains poorly documented and undated. The second sheet is ~750 m thick and is exposed underneath the peralkaline granite. The contact between the two lithologies is sharp and marked by highly weathered hypersolvus granite (Stull, 1969), and the sheet's lower contact with the rapakivi granite appears to be gradational. The hypersolvus granite is primarily composed of perthite, quartz, biotite, and hornblende and is distinguished from the peralkaline granite based on the absence of sodic amphiboles and the presence of biotite. Miarolitic cavities are abundant. The normative mineralogy of the hypersolvus granite plots just below the 0.2 GPa H_2O-saturated eutectic in the Ab-Or-Qz system (Fig. 2). The current areal exposure of this unit is largely restricted to the down-dropped fault block (72 km^2) in the SE of the GHB. However, a thin screen of hypersolvus granite that extends along the west side of the batholith suggests that it may have once covered a larger area.

Nevertheless, we use the 72 km^2 area of the fault block to calculate a minimum volume estimate for the unit and neglect the undated upper hypersolvus sheet in our calculations.

Rapakivi granite

The rapakivi granite was described in detail by Stull (1969, 1978). It is coarse grained and dominantly composed of plagioclase, orthoclase, quartz, and biotite ± hornblende. Perthitic orthoclase mantled with plagioclase (rapakivi texture) is pervasive and is a distinguishing characteristic in the field. Enclaves are common within the rapakivi granite and range from small (<1 cm) clots of mafic minerals to meter-scale, fine-grained enclaves. Mapping shows that the rapakivi granite forms a sheet-like body that extends across most of the batholith (303 km^2) with a minimum thickness of ~1400 m (Fig. 1B and 1C). Smaller, tabular bodies of leucogranite are common at high elevations within the rapakivi granite and may represent segregations of high-SiO_2 melt (Bachmann and Bergantz, 2004; Lee and Morton, 2015) or intrusion of a different melt composition after the rapakivi granite had mostly crystallized. The normative mineralogy of the rapakivi granite plots along a linear array in the Ab-Or-Qz ternary (Fig. 2). This array reflects systematic variations in the chemistry of the rapakivi granite that correlate with each sample's vertical position within the sheet. These variations may reflect the vertical stratification expected to develop as silicic magma chambers differentiate (e.g., Lee and Morton, 2015), suggesting that these whole rock analyses do not represent liquid compositions and precluding their use in depth estimates.

Heterogeneous granite

Heterogeneous granite is exposed in the NW part of the batholith (Fig. 1B and 1C) as a 650-m-thick sheet-like body. Internal contacts are present and range from sharp to gradational, implying that the unit is composed of many individual intrusions. However, we could not split the heterogeneous granite into smaller map units due to poor exposure. The rocks are dominantly leucocratic granites and include both perthite-bearing and two-feldspar varieties. A distinctive, ~100-m-thick, fine-grained biotite granite forms the uppermost part of the heterogeneous granites and is found directly underneath the rapakivi granite over a wide area. We project the heterogeneous granite under the granitoid portions of the batholith (303 km^2) for our volume estimate.

Granodiorite

Granodiorite is exposed at low elevations in the extreme NW of the batholith (Fig. 1B). This map unit is composed of heterogeneous granitoids with a higher color index than the heterogeneous granites. The dominant lithology is a medium-grained hornblende granodiorite that includes some rapakivi-textured feldspars.

Quartz Diorite

A small body of hornblende quartz diorite occurs along the SW boundary of the GHB (Fig. 1B). It is medium grained and includes angular xenoliths of the host rock along its outer margin.

Unnamed Subvolcanic Stock

A subvolcanic rhyolitic stock intrudes the rapakivi granite in the NW of the GHB (Fig. 1B). At lower elevations it is a fine-grained, quartz-rich granite and grades into porphyritic rhyolite at higher elevations. The rhyolite is vesiculated and contains quartz phenocrysts, pieces of pumice, and small angular lithic fragments. Its relationship to the GHB is unclear. However, it must postdate the rapakivi granite based on the intrusive contact between the two units.

Appendix C: Zircon Petrography

Fig. 4 shows representative cathodeluminescence (CL) images of zircon from GHB granitoids. Imaging was done on the JEOL JXA-733 microprobe at the Massachusetts Institute of Technology using a beam current of 10 nA. Oscillatory zoning is common in the zircons and indicates an igneous origin. No resorbed cores were seen in any of the images, supporting our interpretation that the GHB granitoids were emplaced above zircon saturation temperature. However, petrographic observations demonstrate that zircon is included in, and therefore predated or co-crystallized with, the major rock-forming minerals of the granitoid phases of the GHB (Fig. 5). We conclude that zircon became saturated shortly after emplacement in the upper crust and that the duration of zircon crystallization approximates the duration of magma crystallization.

Appendix D: U-Pb Zircon Geochronology Methods

Zircons were separated and dated via chemical abrasion-isotope dilution-thermal ionization mass spectrometry (CA-ID-TIMS) following methods slightly modified from Mattinson (2005) and outlined in Appendix A for Eddy et al. (2016). All of the isotopic measurements were made on the VG Sector 54 thermal ionization mass spectrometer (TIMS) at the Massachusetts Institute of Technology and are presented in Table A4. Pb isotopes were measured by peak hopping on a Daly detector and corrected for fractionation based on repeat analyses of the NBS 981 Pb isotopic standard. U was measured statically on Faraday cups and corrected for fractionation using the known ratio of $^{233}U/^{235}U$ in the EARTHTIME ^{205}Pb-^{233}U-^{235}U isotopic tracer (Condon et al., 2015; McLean et al., 2015). We assume that zircon does not incorporate initial common Pb (Pb_c) during crystallization and that all measured ^{204}Pb arises from laboratory contamination. We correct for this contamination following the procedures outlined in McLean et al. (2011), using a laboratory Pb_c isotopic composition of $^{206}Pb/^{204}Pb$ = 18.145833 ± 0.475155 (1σ abs.), $^{207}Pb/^{204}Pb$ = 15.303903 ± 0.295535 (1σ abs.), and $^{208}Pb/^{204}Pb$ = 37.107788 ± 0.875051 (1σ abs.), calculated from 149 procedural blanks measured in the MIT isotope geochemistry lab between 2009 and 2015. The mass of Pbc measured in all of these procedural blanks is comparable to the range of Pb_c measured in the analyses presented in this paper and provides strong support for the assumption that no Pb_c is incorporated in zircon during crystallization.

The ^{230}Th isotope is a long-lived ($t^{1/2}$ = 75,400 yr) daughter isotope of ^{238}U, and preferential exclusion of Th during zircon crystallization can lead to initial secular disequilibrium. A correction for the resulting deficiency in radiogenic ^{206}Pb is described by McLean (2011) and Ickert et al. (2015) and is dependent on the $[Th/U]_{zircon}$ and $[Th/U]_{melt}$. The $[Th/U]_{zircon}$ is routinely calculated from zircon measurements using radiogenic ^{208}Pb and assuming concordance between the ^{232}Th-^{208}Pb and U-Pb systems. However, the $[Th/U]_{melt}$ is more difficult to constrain. Two potential methods can be used to derive $[Th/U]_{melt}$, 1) assume a $[Th/U]_{melt}$ using whole rock geochemical measurements or an average value for the rock type being investigated, or 2) use partition coefficients ($f_{ThU}=D_{Th}/D_U$) to calculate $[Th/U]_{melt}$ using $[Th/U]_{zircon}$. We compare both methods in Table A5. For the approach using constant $[Th/U]_{melt}$, we use $[Th/U]_{melt}=2.8 \pm 1$ (2σ). This value encompasses the range seen in most igneous rocks (Machlus et al., 2015), and is consistent with whole rock measurements from granites within the

GHB (Tepper, unpublished data). For the constant partition coefficient approach we use f_{ThU} =0.138 (Stelten et al., 2015) for granitic rocks and f_{ThU} =0.33 (Rubatto and Hermann, 2007) for the marginal tonalite/diorite and apply an arbitrary uncertainty of 1(2σ) on the resulting $[Th/U]_{melt}$.

The difference between data corrected using the two methods is minor and does not affect our interpretations of magma emplacement rates. We prefer the use of a constant f_{ThU} because it seems more reasonable that different $[Th/U]_{zircon}$ within a sample is a result of of changing melt composition either due to local depletion of trace elements around crystallizing trace phases or through changes in bulk melt composition due to fractional crystallization. Nevertheless, trace element partitioning between zircon and melt remains poorly constrained. The value used for granites in this paper (f_{ThU} = 0.138) is an average for coexisting zircon and high-SiO_2 melt erupted from Yellowstone (Stelten et al., 2015). These measurements offer an advantage over other datasets that report partition coefficients for zircon and coexisting high-SiO_2 melt in that it uses trace element measurements from zircon surfaces whose ^{238}U-^{230}Th dates are consistent with crystallization immediately prior to or concurrent with eruption. Other studies either lack corresponding age data or inevitably use a $[Th/U]_{zircon}$ calculated from a mixture of interior and surface domains that may not be in equilibrium with the matrix glass. In Fig. A3 we show that the Stelten et al. (2015) value reproduces the range of whole rock Th/U measurements for GHB granites for the typical range of $[Th/U]_{zircon}$ values from our dataset.

Data reduction was done using the U-Pb_Redux software package (Bowring et al., 2011) and used the decay constants for ^{235}U and ^{238}U presented in Jaffey et al. (1971). All isotopic ratios are presented in Table A4 and shown as concordia plots in Fig. A2.

Appendix E: Magma Emplacement Rates

Magma emplacement rates were estimated for the GHB using our volume estimates (with no assigned uncertainty) and durations (Δt) calculated using Monte Carlo simulations with 10^7 iterations. The simulations found the difference between randomly selected dates from normal distributions with a mean value and 2σ variability equal to the weighted mean dates and 2σ uncertainty of our oldest and youngest sample within each unit. In cases where the oldest and youngest samples substantially overlap within uncertainty, we used the absolute value of the calculated difference to prevent negative durations. The distribution of results is shown in Fig.

3B. Fig. 6 compares these results with magma emplacement rates, recalculated using the same technique, from previously published geochronologic data from upper-crustal granitoid plutonic complexes (Table A6). As noted in the text, the rapakivi granite represents the highest magma emplacement rates documented in a granitoid plutonic complex.

References

Anderson, J.L. and Smith, D.R., 1995, The effects of temperature and fo2 on the Al-in-hornblende barometer: American Mineralogist, v. 80, p. 549-559, doi: 10.2138/am-1995-5-615.

Annen, C., 2009, From plutons to magma chambers: thermal constraints on the accumulation of eruptible silicic magma in the upper crust: Earth and Planetary Science Letters, v. 284, p. 409-416, doi: 10.1016/j.epsl.2009.05.006.

Bachmann, O., and Bergantz, G.W., 2003, Rejuvenation of the Fish Canyon magma body: a window into the evolution of large-volume silicic magma systems: Geology, v. 31, p. 789-792, doi: 10.1130/G19764.1.

Bachmann, O., and Bergantz, G.W., 2004, On the origin of crystal-poor rhyolites: extracted from batholithic crystal mushes: Journal of Petrology, v. 45, p. 1565-1582, doi: 10.1093/petrology/egh019.

Bachmann, O., Miller, C.F., and de Silva, S.L., 2007, The volcanic-plutonic connection as a stage for understanding crustal magmatism: Journal of Volcanology and Geothermal Research, v. 167, p. 1-23, doi: 10.1016/j.jvolgeores.2007.08.002.

Barboni, M., Annen, C., and Schoene B., 2015, Evaluating the construction and evolution of upper crustal magma reservoirs with coupled U/Pb zircon geochronology and thermal modeling: A case study from the Mt. Capanne pluton (Elba, Italy): Earth and Planetary Science Letters, v. 432, p. 436-448, doi: 10.1016/j.epsl.2015.09.043.

Blundy, J., and Cashman, K., 2001, Ascent-driven crystallization of dacite magmas at Mount St Helens, 1980-1986: Contributions to Mineralogy and Petrology, v. 140, p. 631-650, doi: 10.1007/s004100000219.

Blundy, J., and Holland, T.J.B., 1990, Calcic amphibole equilibria and a new amphibole-plagioclase geothermometer: Contributions to Mineralogy and Petrology, v. 104, p. 208-224, doi: 10.1007/BF00306444.

Bowring, J.F., McLean, N.M., and Bowring, S.A., 2011, Engineering cyber infrastructure for U-Pb geochronology: Tripoli and U-Pb_Redux: Geochemistry, Geophysics, and Geosystems, v. 12, doi: 10.1029/2010GC003479.

Boggs, R.C., 1984, Mineralogy and geochemistry of the Golden Horn batholith, northern Cascades, Washington [PhD Thesis]: Santa Barbara, University of California, 187 p.

Coleman, D.S., Gray, W., and Glazner, A.F., Rethinking the emplacement and evolution of zoned plutons: geochronologic evidence for incremental assembly of the Tuolumne Intrusive Suite, California: Geological Society of America Bulletin, v. 32, p. 433-436, doi: 10.1130/G20220.1.

Condon, D.J., Schoene, B., McLean, N.M., Bowring, S.A., and Parrish, R.R., 2015, Metrology and traceability of U-Pb isotopic dilution geochronology (EARTHTIME tracer calibration part I): Geochimica et Cosmochimica, v. 164, p 464-480, doi: 10.1016/j.gca.2015.05.026.

Davis, J.W., Coleman, D.S., Gracely, J.T., Gaschnig, R., and Stearns, M., 2012, Magma accumulation rates and thermal histories of plutons of the Sierra Nevada batholith, CA: Contributions to Mineralogy and Petrology, v., 163, p. 449-465, doi: 10.1007/s00410-011-0683-7.

Degruyter, W., Huber, C., Bachmann, O., Cooper, K.M., and Kent, A.J.R., 2016, Magma reservoir response to transient recharge events: the case of Santorini volcano (Greece): Geology, v. 44, p. 23-26, doi: 10.1130/G37333.1.

Eddy, M.P., Bowring, S.A., Umhoefer, P.J., Miller, R.B., McLean, N.M., and Donaghy, E.E., 2015, High-resolution temporal and stratigraphic record of Siletzia's accretion and triple junction migration from nonmarine sedimentary basins in central and western Washington: Geological Society of America Bulletin, doi: 10.1130/B31335.1.

Frazer, R.E., Coleman, D.S., and Mills, R.D., 2014, Zircon U-Pb geochronology of the Mount Givens Granodiorite: Implications for the genesis of large-volumes of eruptible magma: Journal of Geophysical Research Solid Earth, v. 119, p. 2907-2924, doi: 10.1002/2013JB010716.

Gelman, S.E., Gutierrez, F.J., and Bachmann, O., 2013, On the longevity of large upper crustal silicic magma reservoirs: Geology, v. 41, p. 759-762, doi: 10.1130/G34241.1.

Glazner, A.F., Bartley, J.M., Coleman, D.S., Gray, W., and Taylor, R.Z., 2004, Are plutons assembled over millions of years by amalgamation from small magma chambers: GSA Today, v. 14, p.4-11, doi: 10.1130/1052-5173(2004)014<0004:APAOMO>2.0.CO;2.

Haugerud, R.A., and Tabor, R.W., 2009, Geologic map of the North Cascade range, Washington: United States Geological Survey Scientific Investigations Map 2940, scale 1:200,000, 2 sheets, 2 pamphlets, 29 p. and 23 p.

Ickert, R.B., Mundil, R., Magee Jr., C.W., and Mulcahy, S.R., 2015, The U-Th-Pb systematics of zircon from the Bishop Tuff: A case study in challenges to high-precision Pb/U geochronology at the millennial scale: Geochimica et Cosmochimica Acta, v. 168, p. 88-110, doi: 10.1016/j.gca.2015.07.018.

Jaffey, A.H., Flynn, K.F., Glendenin, L.E., Bentley, W.C., Essling, A.M., 1971, Precision measurement of half-lives and specific activities of 235U and 38U: Physical Review C, v. 4, p. 1889-1906, doi: 10.1103/PhysRevC.4.1889.

John, B.E., and Blundy, J.D., 1993, Emplacement-related deformation of granitoid magmas, southern Adamello Massif, Italy: Geological Society of America Bulletin, v. 105, p. 1517-1541, doi: 10.1130/0016-7606(1993)105<1517:ERDOGM>2.3.CO;2.

Lee, C.A., and Morton, D.M., 2015, High silica granites: terminal porosity and crystal settling in shallow magma chambers: Earth and Planetary Science Letters, v. 409, p. 23-31, doi: 10.1016/j.epsl.2014.10.040.

Leuthold, J., Muntener, O., Baumgartner, L.P., Putlitz, B., Ovtcharova, M., and Schaltegger, U., 2012, Time resolved construction of a bimodal laccolith (Torres del Paine, Patagonia): Earth and Planetary Science Letters, v. 325-326, p. 85-92, doi: 10.1016/j.epsl.2012.01.032.

Machlus, M.L., Ramezani, J., Bowring, S.A., Hemming, S.R., Tsukui, K., and Clyde, W.C., 2015, A strategy for cross-calibrating U-Pb chronology and astrochronology of sedimentary sequences: an example from the Green River Formation, Wyoming, USA: Earth and Planetary Sciences, v. 413, p. 70-78, doi:10.1016/j.epsl.2014.12.009.

Mattinson, J.M., 2005, Zircon U-Pb chemical abrasion ("CA-TIMS") method: Combined annealing and multi-step partial dissolution analysis for improved precision and accuracy of zircon ages: Chemical Geology, v. 220, p. 47-66, doi: 10.1016/j.chemgeo.2005.03.011.

Matzel, J.E.P., Bowring, S.A., and Miller, R.B., 2006, Time scales of pluton construction at differing crustal levels: Examples from the Mount Stuart and Tenpeak intrusions, North Cascades, Washington: Geological Society of America Bulletin, v. 118, p. 1412-1430, doi: 10.1130/B25923.1.

McLean, N.M., Bowring, J.F., and Bowring, S.A., 2011, An algorithm for U-Pb isotope dilution data reduction and uncertainty propagation: Geochemistry, Geophysics, Geosystems, v. 12, Q0AA19, doi: 10.1029/2010GC003478.

McLean, N.M., Condon, D.J., Condon, B., and Bowring, S.A., 2015, Evaluating uncertainties in the calibration of isotopic reference materials and multi-element isotopic tracers (EARTHTIME tracer calibration II): Geochimica et Cosmochimica, v. 164, p. 481-501, doi: 10.1016/j.gca.2015.02.040.

McNulty, B.A., Tobish, O.T., Cruden, A.R., and Giler, S., 2000, Multistage emplacement of the Mount Givens pluton, central Sierra Nevada batholith, California: Geological Society of America Bulletin, v. 112, p. 119-135, doi: 10.1130/0016-7606(2000)112<119:MEOTMG>2.0.CO;2.

Memeti, V., Paterson, S., Matzel, J., Mundil, R., and Okaya, D., 2010, Magmatic lobes as "snapshots" of magma chamber growth and evolution in large, composite batholiths: An example from the Tuolumne intrusion, Sierra Nevada, California: Geological Society of America Bulletin, v. 122, p. 1912-1931, doi: 10.1130/B30004.1.

Miller, C.F., McDowell, S.M., and Mapes, R.W., 2003, Hot and cold granites? Implications of zircon saturation temperatures and preservation of inheritance: Geology, v. 31, p. 529-532, doi: 10.1130/0091-7613(2003)031<0529:HACGIO>2.0.CO;2.

Miller, J.S., Matzel, J.E.P., Miller, C.F., Burgess, S.D., and Miller, R.B., 2007, Zircon growth and recycling during the assembly of large, composite arc plutons: Journal of Volcanology and Geothermal Research, v. 167, p. 282-299, doi: 10.1016/j.jvolgeores.2007.04.019.

Miller, R.B., Paterson, S.R., DeBari, S.M., and Whitney, D.L., 2000, North Cascades Cretaceous crustal section: Changing kinematics, rheology, metamorphism, pluton emplacement and petrogenesis from 0 to 40 km depth: in Woodsworth, G.J., et al., eds., Guidebook for geological field trips in southwestern British Columbia and northern Washington: Vancouver, Geological Association of Canada, p. 229-278.

Mills, R.D., and Coleman, D.S., 2013, Temporal and chemical connections between plutons and ignimbrites from the Mount Princeton magmatic center: Contributions to Mineralogy and Petrology, v. 165, p. 961-980, doi: 10.1007/s00410-012-0843-4.

Misch, P., 1965, Alkaline granite amidst the calc-alkaline intrusive suite of the Northern Cascades, Washington: Geological Society of America Special Papers, v. 87, p. 216-217.

Rubatto, D., and Hermann, J., 2007, Experimental zircon/melt and zircon/garnet trace element partitioning and implications for the geochronology of crustal rocks: Chemical Geology, v. 241, p. 38-61, doi: 10.1016/j.chemgeo.2007.01.027.

Schmidt, M.W., 1992, Amphibole composition in tonalite as a function of pressure: an experimental calibration of the Al-in-hornblende barometer: Contributions to Mineralogy and Petrology, v. 110, p. 304-310, doi: 10.1007/BF00310745.

Schoene, B., Schaltegger, U., Brack, P., Latkoczy, C., Stracke, A., and Gunther, D., Rates of magma differentiation and emplacement in a ballooning pluton recorded by U-Pb TIMS-TEA, Adamello batholith, Italy: Earth and Planetary Science Letters, v. 355-356, p. 162-173, doi: 10.1016/j.epsl.2012.08.019.

Stelten, M.E., Cooper, K.M., Vazquez, J.A., Calvert, A.T., and Glessner, J.J.G., 2015, Mechanisms and timescales of generating eruptible rhyolitic magmas at Yellowstone caldera from zircon and sanidine geochronology and geochemistry: Journal of Petrology, v. 56, p. 1607-1642, doi: 10.1093/petrology/egv047.

Stull, R.J., 1969, The geochemistry of the southeastern portion of the Golden Horn batholith, Northern Cascades, Washington [Ph.D. thesis]: Seattle, University of Washington, 127 p.

Stull, R.J., 1978, Mantled feldspars from the Golden Horn batholith, Washington: Lithos, v. 11, p. 243-249, doi: 10.1016/0024-4937(78)90024-5.

Tappa, M.J., Coleman, D.S., Mills, R.D., and Samperton, K.M., 2011, The plutonic record of a silicic ignimbrite from the Latir volcanic field, New Mexico: Geochemistry, Geophysics, Geosystems, v. 12, Q10011, doi: 10.1029/2011GC003700.

Wendt, I., and Carl, C., 1991, The statistical distribution of the mean square weighted deviation: Chemical Geology, v. 86, p. 275-285, doi: 10.1016/0168-9622(91)90010-T.

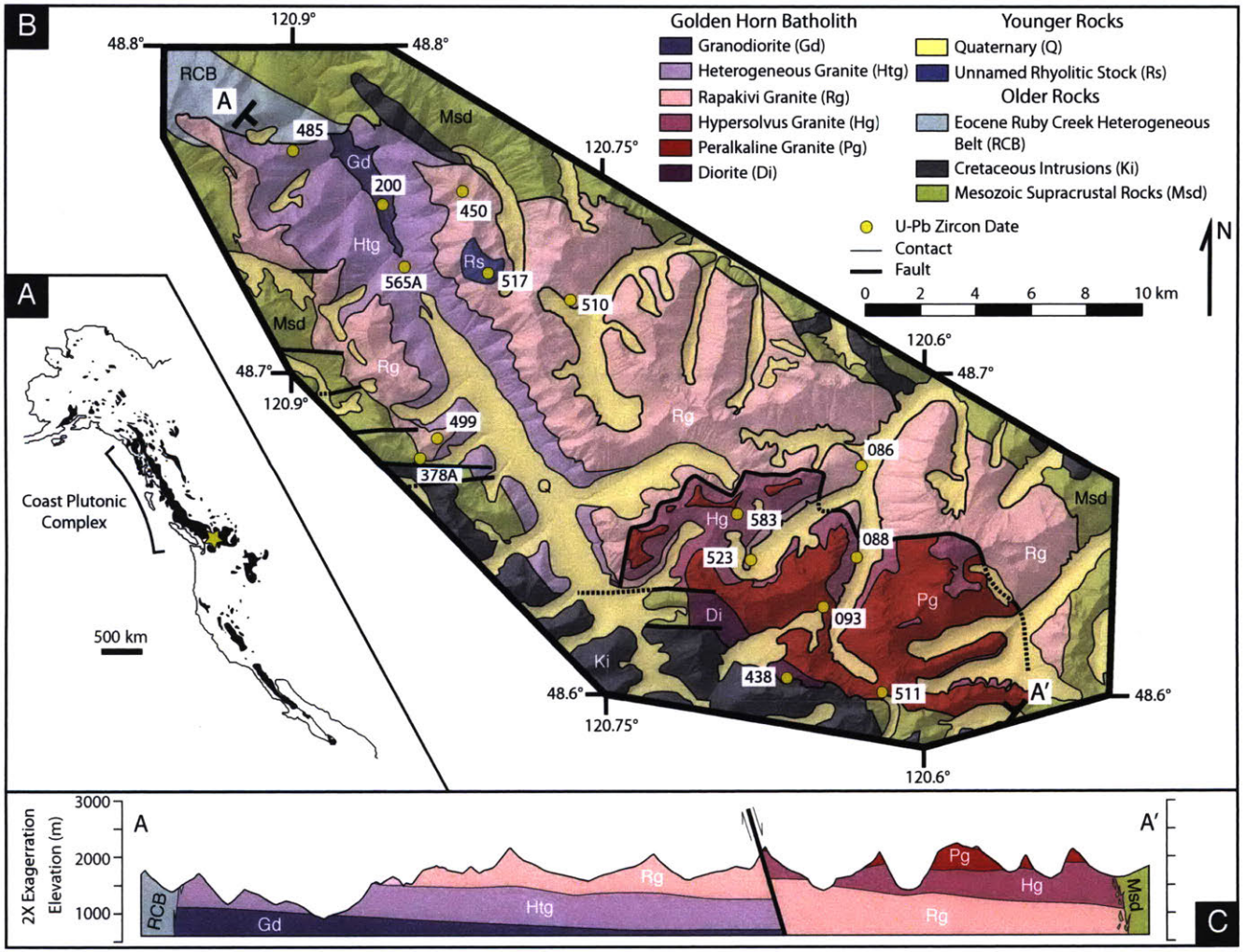

Figure 1: (A) Map modified from Miller et al., 2000 showing the location of the GHB (yellow star) in relation to other Mesozoic and Paleogene plutonic rocks in the North American Cordillera (shown in black). **(B)** Geologic map of the GHB. Internal contacts are based on mapping done by the authors and Stull (1969). External contacts are from Haugerud and Taber (2009). The locations of samples dated by U-Pb zircon geochronology are shown with yellow circles. Sample names are abbreviated such that XXX should be read as NC-MPE-XXX. **(C)** Cross section of the GHB along A-A' showing the sheet-like nature of the mapped units.

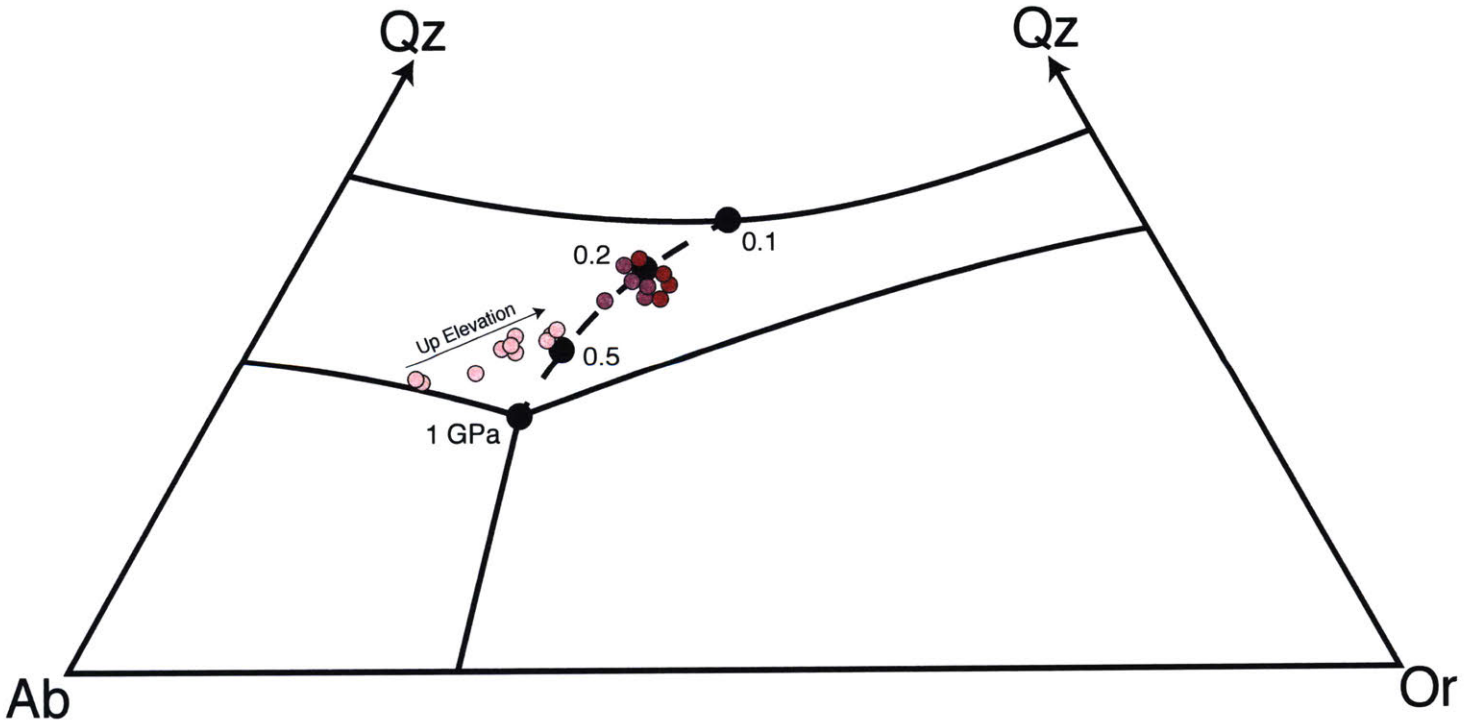

Figure 2: Plot showing the H_2O-saturated eutectic in the quartz (Qz), albite (Ab), orthoclase (Or) system for pressures ranging from 1 to 0.1 GPa (Ebadi and Johannes, 1991). The normative mineralogy for geochemical analyses by Stull (1969) of the peralkaline, hypersolvus, and rapakivi granites are shown and projected using the method of Blundy and Cashman (2001). Compositions for the peralkaline and hypersolvus granites cluster around the 0.2 GPa H_2O-saturated eutectic.

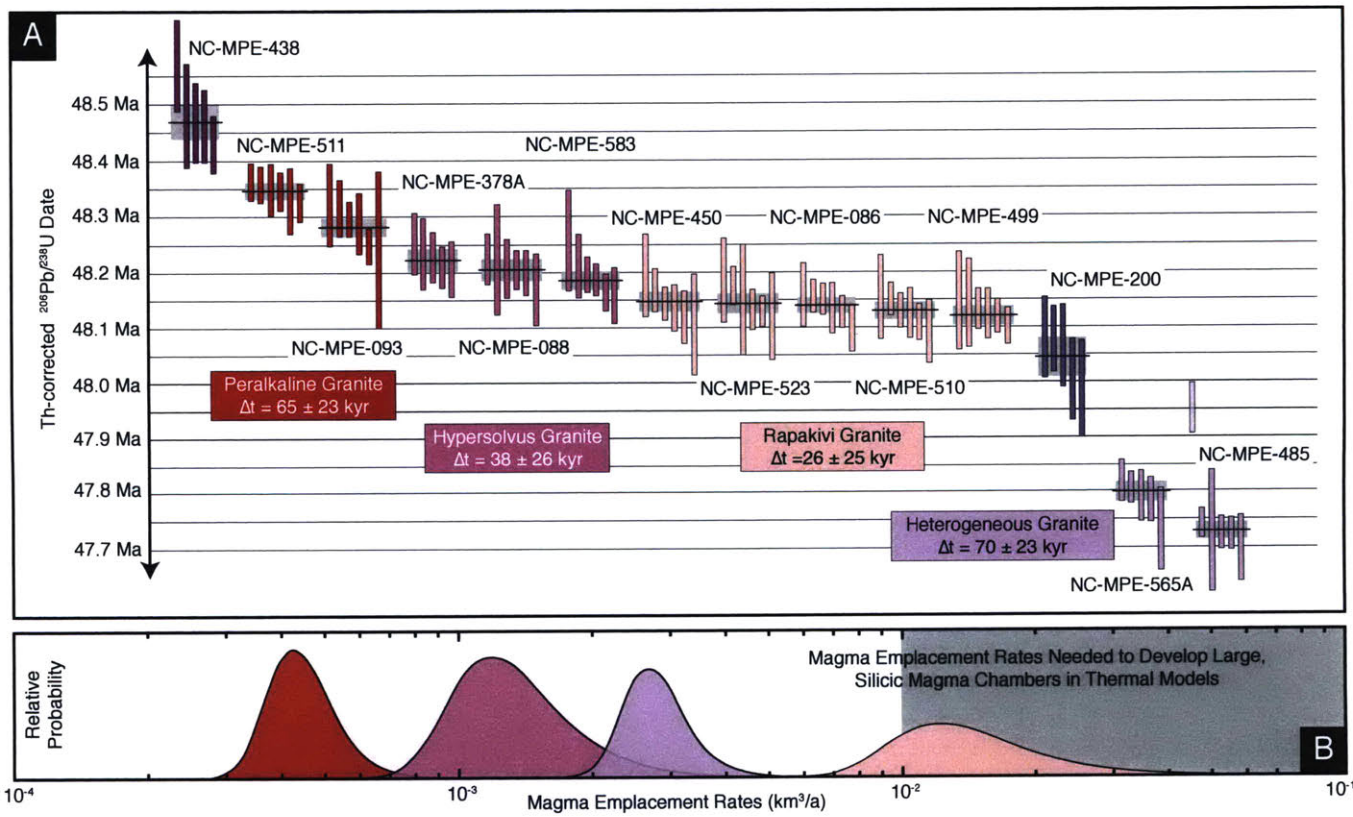

Figure 3: (A) Rank order plot of Th-corrected $^{206}Pb/^{238}U$ zircon dates (bars represent 2σ analytical uncertainty) from the GHB. Colors correspond to map units and are the same as Fig. 1B. Heavy black lines denote the weighted mean date for each sample reported with 2σ analytical uncertainty (gray boxes). For map units with more than one dated sample, we present the duration (Δt) of magmatism calculated using the difference between weighted means of the oldest and youngest samples. **(B)** Relative probability plots for magma emplacement rates within the GHB (colors the same as Fig. 1B) calculated using Monte Carlo simulations (see Appendix E for methods). The heights of the curves are scaled 1X, 5X, 5X, and 30X for the peralkaline, hypersolvus, heterogeneous, and rapakivi granites, respectively, to aid in comparison.

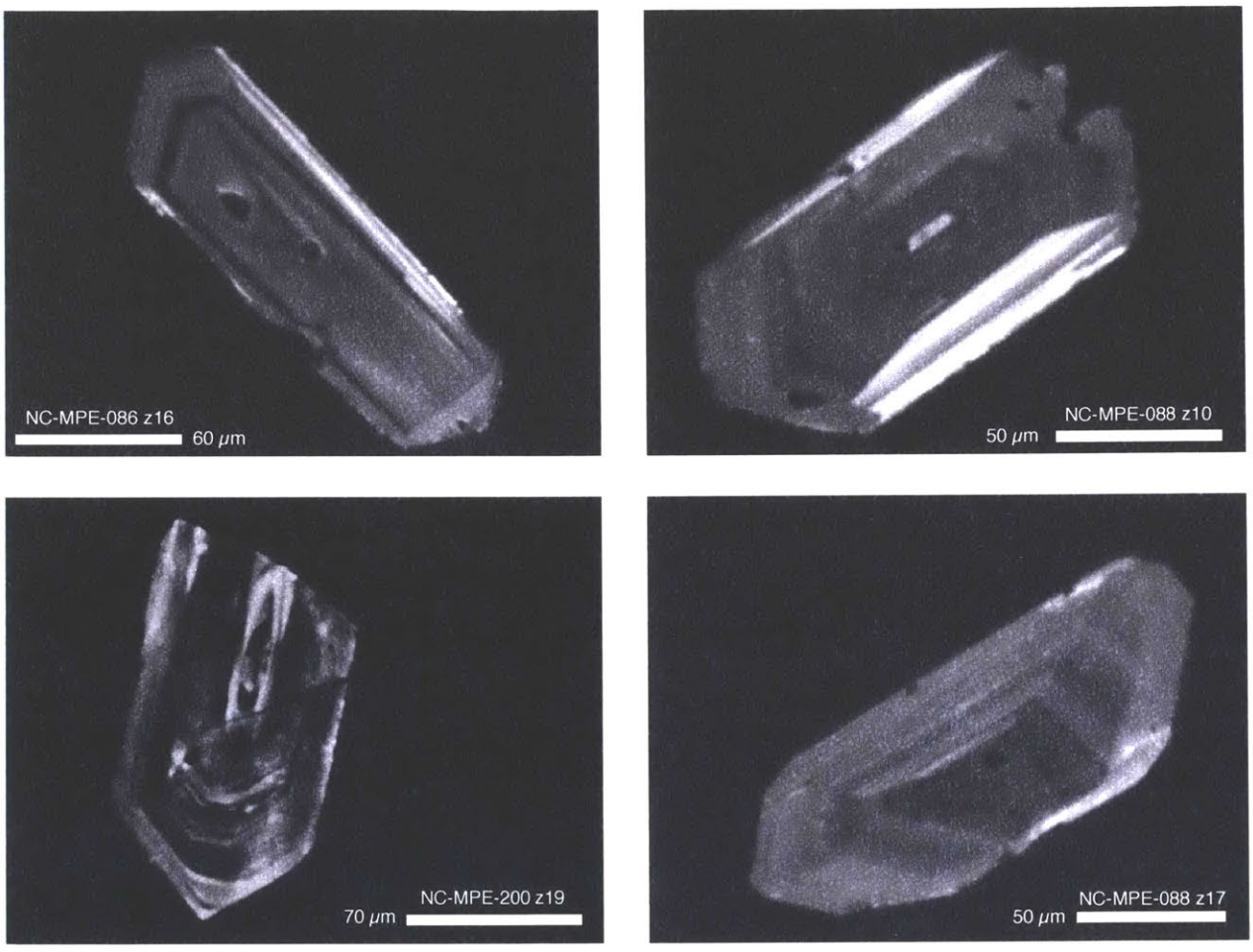

Figure 4: Representative CL images of zircon from granites within the GHB. Oscillatory zoning is clearly seen, indicating an igneous origin. No resorbed cores were seen in any of the images, supporting the inference that GHB magmas intruded above their zircon saturation temperatures.

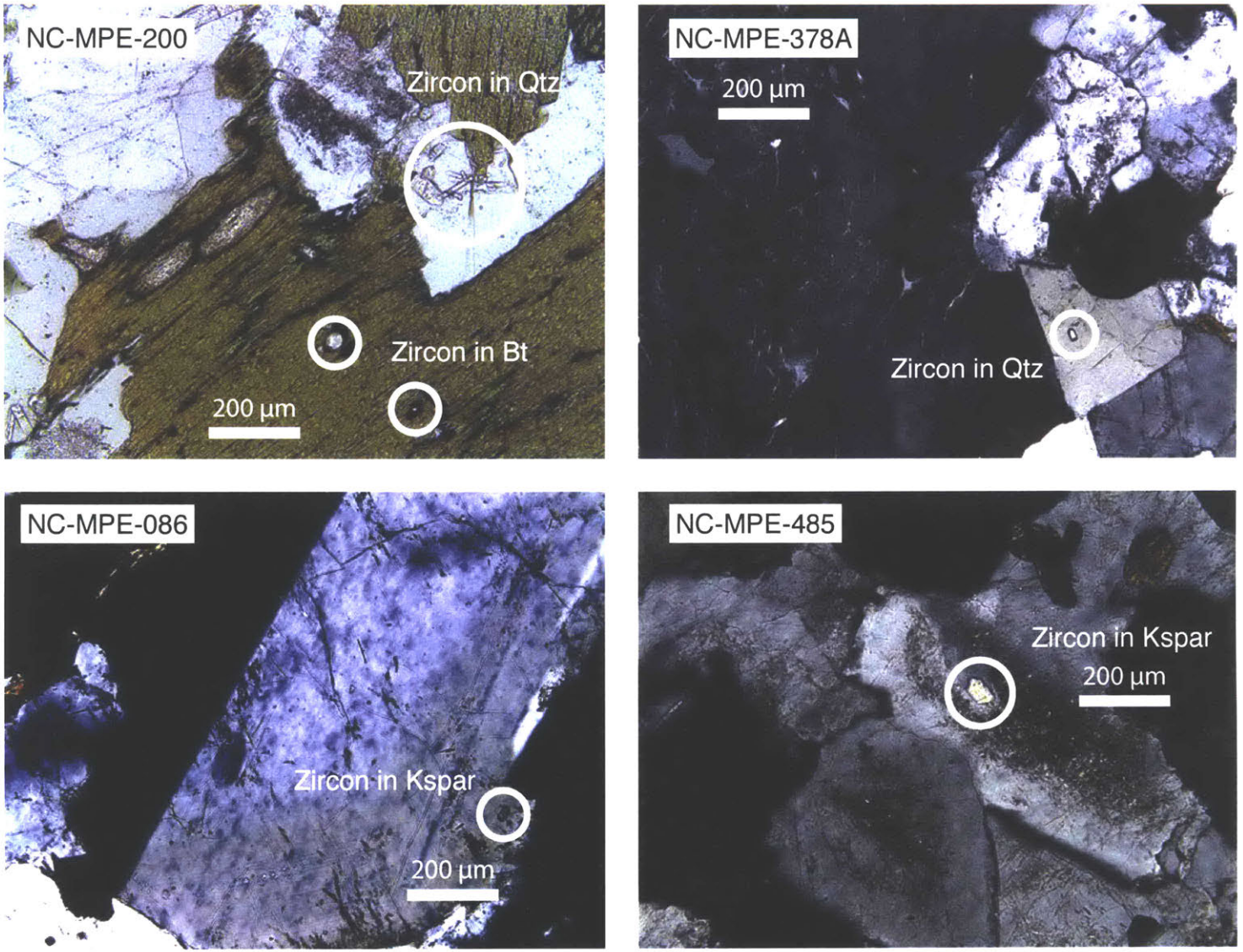

Figure 5: Select photomicrographs showing zircon included in major, rock-forming minerals in the granodiorite (NC-MPE-200), hypersolvus granite (NC-MPE-378A), rapakivi granite (NC-MPE-086), and heterogeneous granite (NC-MPE-485). The photomicrograph for NC-MPE-200 is in plane polarized light, while the others are all in cross-polarized light.

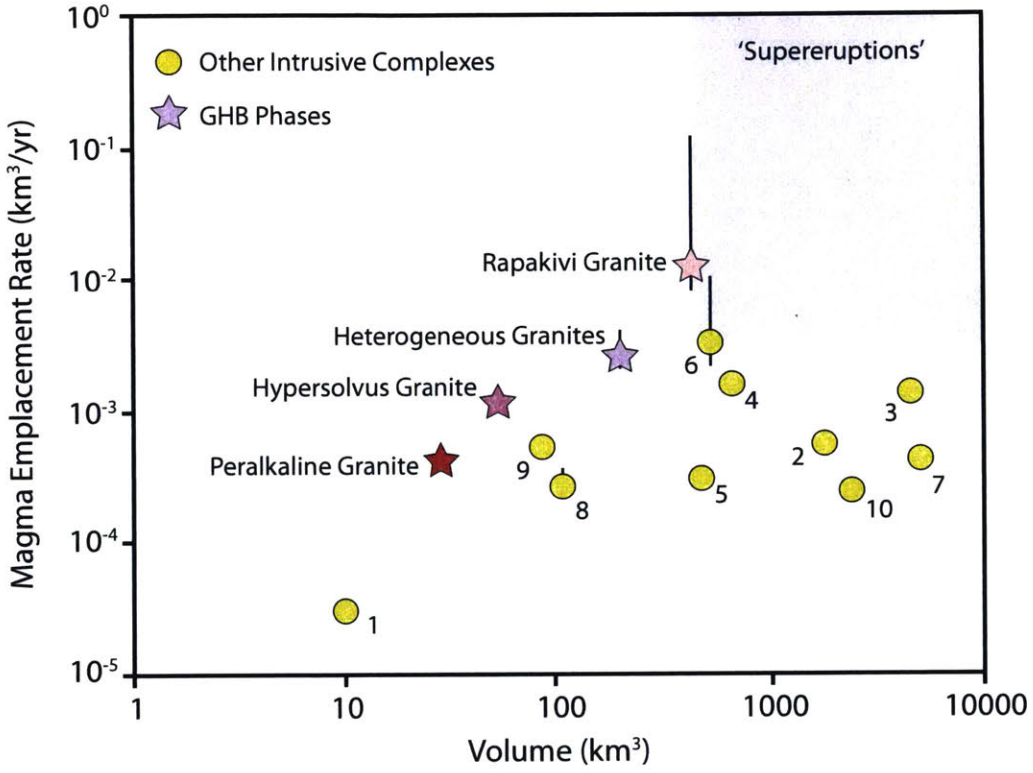

Figure 6: Plot showing volumes and magma emplacement rates for upper crustal granitoid plutons modified from Mills and Coleman (2013) and Frazer et al. (2014). The shaded field represents the rates needed in thermal models to build a large-volume, high-SiO2 magma chamber (Annen, 2009; Gelman et al., 2013). All emplacement rates represent the mode of Monte Carlo simulations and uncertainties represent the 95% confidence interval. Labels correspond to the numbered intrusive complexes in Table A6. Volume estimates are limited to the exposed volume (volume = area x topographic relief) to facilitate comparison to the GHB data.

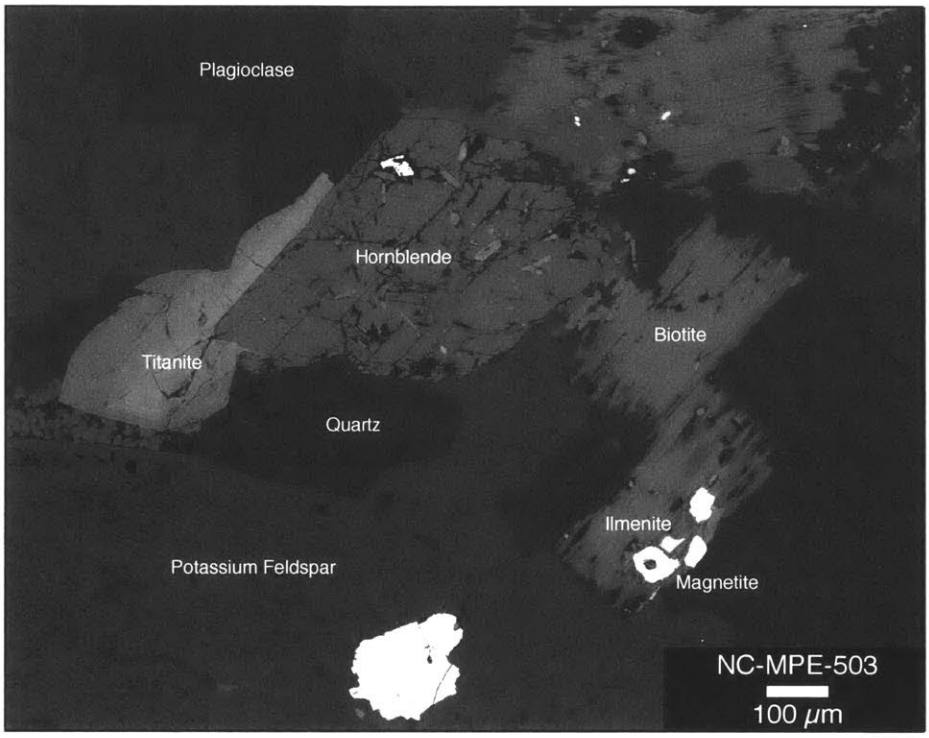

Figure DR2: Back scattered electron (BSE) image of an amphibole in sample NC-MPE-503 from the rapakivi granite of the GHB. The image shows the required assemblage for Al-in-hornblende barometry.

Figure A2: Traditional concordia plots for all dated samples.

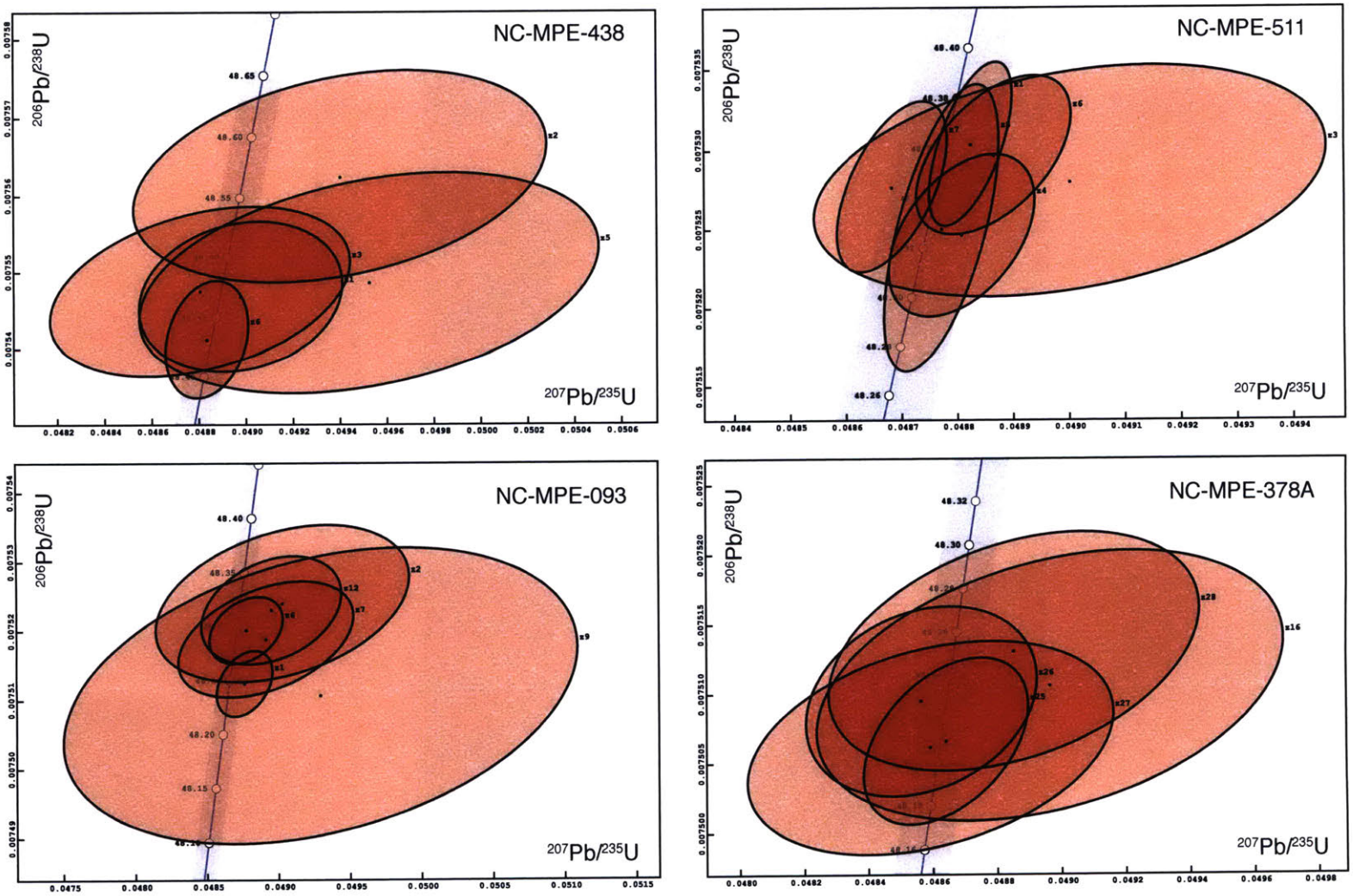

NC-MPE-088
$^{206}Pb/^{238}U$
$^{207}Pb/^{235}U$
NC-MPE-583
$^{206}Pb/^{238}U$
$^{207}Pb/^{235}U$
NC-MPE-450
$^{206}Pb/^{238}U$
$^{207}Pb/^{235}U$
NC-MPE-523
$^{206}Pb/^{238}U$
$^{207}Pb/^{235}U$

NC-MPE-086
$^{206}Pb/^{238}U$
$^{207}Pb/^{235}U$
NC-MPE-510
$^{206}Pb/^{238}U$
$^{207}Pb/^{235}U$
NC-MPE-499
$^{206}Pb/^{238}U$
$^{207}Pb/^{235}U$
NC-MPE-200
$^{206}Pb/^{238}U$
$^{207}Pb/^{235}U$

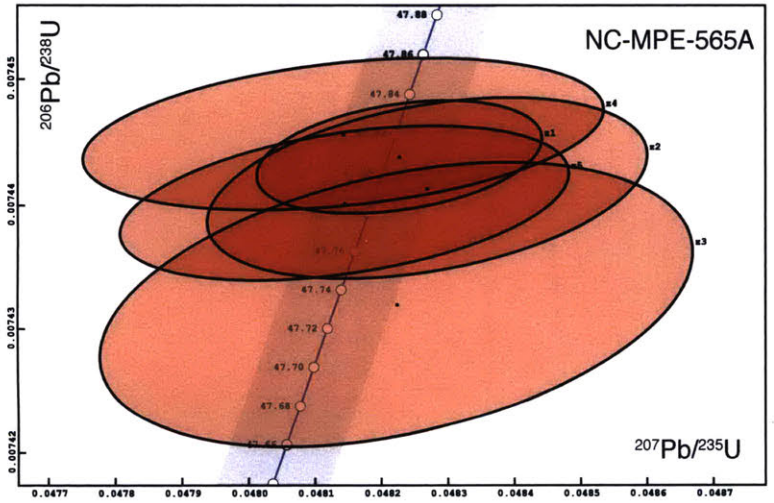
NC-MPE-565A
$^{206}Pb/^{238}U$
$^{207}Pb/^{235}U$
47.88
47.86
47.84
47.74
47.72
47.70
47.68
47.66
0.00745
0.00744
0.00743
0.00742
0.0477
0.0478
0.0479
0.0480
0.0481
0.0482
0.0483
0.0484
0.0485
0.0486
0.0487

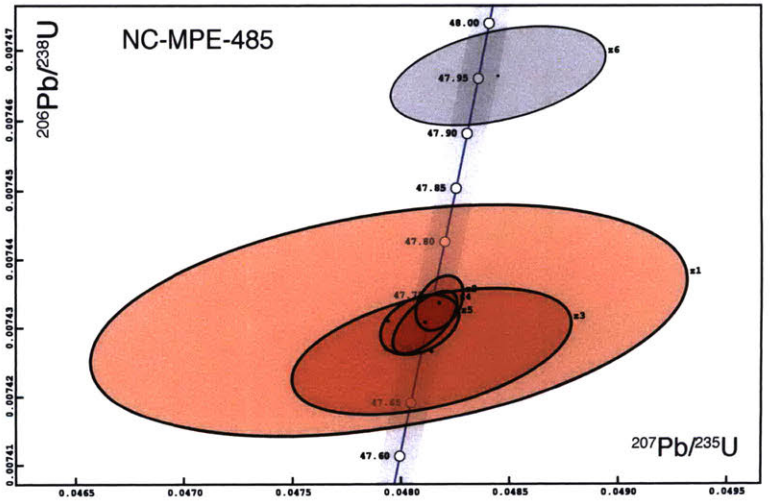
NC-MPE-485
$^{206}Pb/^{238}U$
$^{207}Pb/^{235}U$
48.00
47.95
47.90
47.85
47.80
47.60
0.00747
0.00746
0.00745
0.00744
0.00743
0.00742
0.00741
0.0465
0.0470
0.0475
0.0480
0.0485
0.0490
0.0495

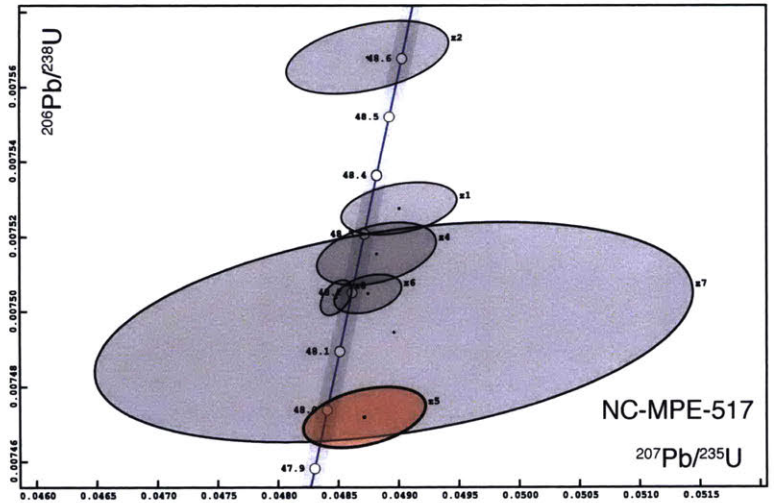
NC-MPE-517
$^{206}Pb/^{238}U$
$^{207}Pb/^{235}U$
48.6
48.5
48.4
48.1
47.9
0.00756
0.00754
0.00752
0.00750
0.00748
0.00746
0.0460
0.0465
0.0470
0.0475
0.0480
0.0485
0.0490
0.0495
0.0500
0.0505
0.0510
0.0515

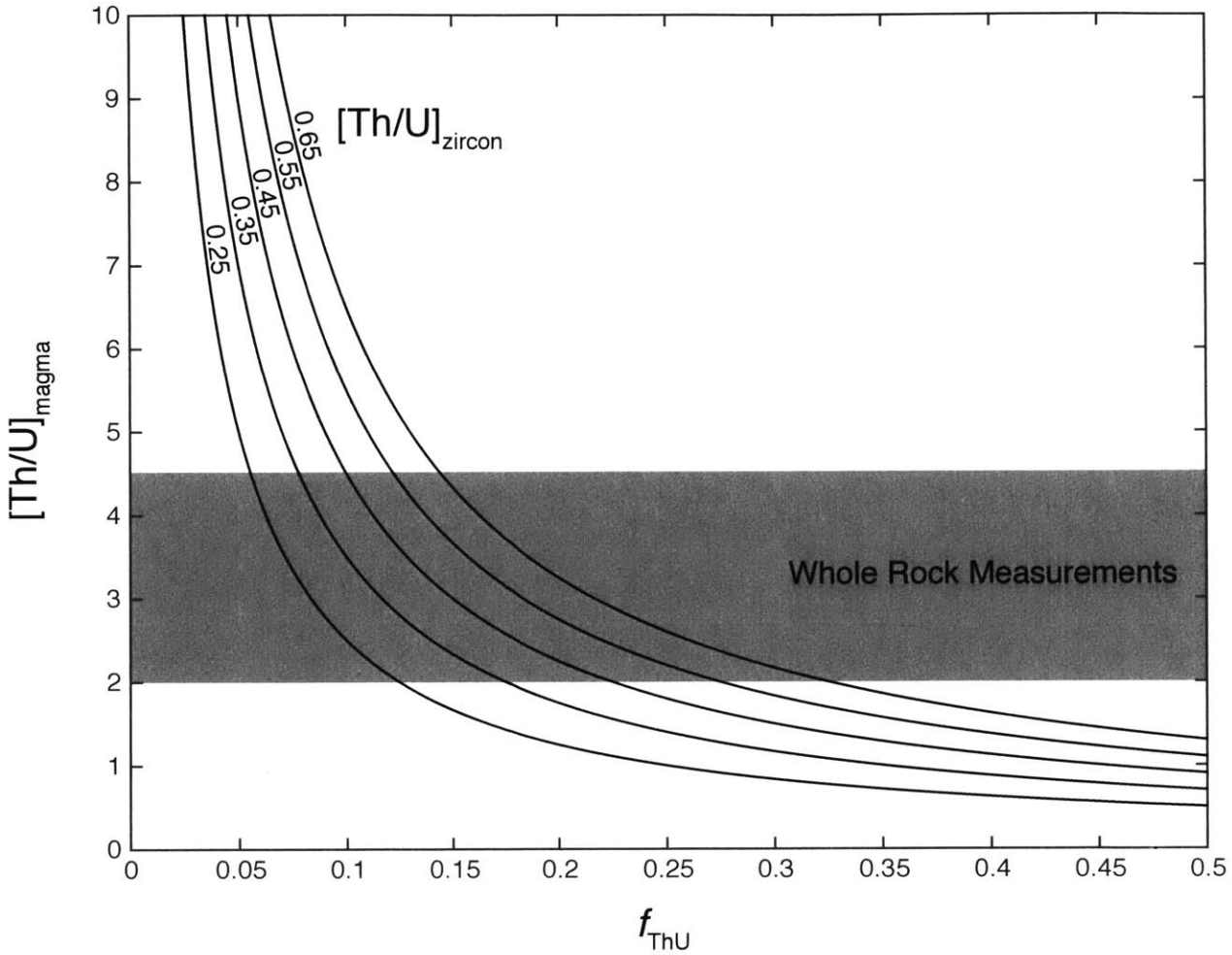

Figure A3: Plot showing the relationship between fThU and the calculated $[Th/U]_{melt}$ for different $[Th/U]_{zircon}$. The Stelten et al. (2015) value of f_{ThU}=0.138 reproduces the range of whole rock [Th/U] values seen in GHB rocks (Tepper, unpublished data) for the range of $[Th/U]_{zircon}$ seen in our analyses (Table A4).

Table 1: U-Pb Zircon Geochronology Results

Sample*	Weighted Mean $^{206}Pb/^{238}U$ Date (Ma) †,§
NC-MPE-438	48.468 ± 0.030/0.037/0.064 (n=5, MSWD=1.84)
NC-MPE-511	48.346 ± 0.015/0.026/0.058 (n=6, MSWD=0.69)
NC-MPE-093	48.281 ± 0.018/0.028/0.059 (n=6, MSWD=1.91)
NC-MPE-378A	48.223 ± 0.021/0.030/0.060 (n=5, MSWD=0.54)
NC-MPE-088	48.205 ± 0.020/0.030/0.060 (n=6, MSWD=0.42)
NC-MPE-583	48.185 ± 0.016/0.027/0.058 (n=6, MSWD=1.27)
NC-MPE-450	48.146 ± 0.018/0.028/0.059 (n=6, MSWD=1.08)
NC-MPE-523	48.144 ± 0.017/0.027/0.058 (n=6, MSWD=1.33)
NC-MPE-086	48.139 ± 0.014/0.025/0.057 (n=6, MSWD=1.44)
NC-MPE-510	48.129 ± 0.016/0.026/0.058 (n=6, MSWD=1.26)
NC-MPE-499	48.120 ± 0.017/0.027/0.058 (n=6, MSWD=0.50)
NC-MPE-200	48.045 ± 0.034/0.041/0.066 (n=5, MSWD=1.33)
NC-MPE-565A	47.799 ± 0.018/0.028/0.058 (n=5, MSWD=1.38)
NC-MPE-485	47.729 ± 0.015/0.026/0.057 (n=5, MSWD=0.64)
NC-MPE-517	< 47.988 ± 0.052/0.056/0.076 (n=1, Maximum Age)

*GPS locations are presented in Table DR4.

†Corrected for initial Th/U disequilibrium using $f_{Th/U}$=0.138 (Stelten et al., 2015)

§Uncertainties are reported in the format ±X/Y/Z where X is the analytical uncertainty, Y includes uncertainty in the EARTHTIME ^{205}Pb-^{235}U-^{238}U isotopic tracer (Condon et al., 2015, McLean et al., 2015), and Z includes uncertainty in the ^{238}U decay constant.

Table A1: Electron Microprobe Analysis of Hornblende

Sample Name	SiO_2	TiO_2	K_2O	MnO	Na_2O	Cr_2O_3	Al_2O_3	CaO	FeO_{tot}	MgO	Total*
NC-MPE-503 H1 Core	46.89	1.40	0.64	0.61	1.97	0.01	6.29	10.41	19.80	10.80	98.83
NC-MPE-503 H1 Rim	49.08	0.63	0.47	0.85	1.47	0.00	4.09	10.61	20.68	11.19	99.07
NC-MPE-503 H2 Core	45.75	1.68	0.68	0.52	2.09	0.00	6.85	10.63	21.43	9.26	98.89
NC-MPE-503 H2 Rim	48.68	0.75	0.56	0.83	1.43	0.00	4.75	10.88	20.30	10.59	98.78
NC-MPE-503 H3 Core	44.14	1.59	0.81	0.83	2.23	0.02	7.95	10.59	22.01	9.14	99.32
NC-MPE-503 H3 Rim	46.01	1.58	0.67	0.49	2.18	0.00	6.70	10.45	19.59	10.99	98.65
NC-MPE-503 H4 Core	45.87	1.78	0.67	0.58	2.05	0.00	6.76	10.56	20.74	10.17	99.18
NC-MPE-503 H4 Rim	47.68	0.90	0.63	0.86	1.71	0.00	5.08	10.76	20.75	10.59	98.96
NC-MPE-086 H1 Core	45.87	1.73	0.73	0.68	2.19	0.00	6.82	10.41	20.86	10.16	99.45
NC-MPE-086 H1 Rim	46.21	1.45	0.72	0.64	1.91	0.02	6.77	10.66	20.17	10.46	99.01
NC-MPE-086 H2 Core	47.32	1.10	0.66	0.80	1.86	0.00	5.56	10.62	20.60	10.74	99.26
NC-MPE-086 H2 Rim	46.16	1.35	0.76	0.77	1.88	0.03	6.58	10.59	20.98	9.76	98.86

* All analyses are reported in wt %.

Table A2: Electron Microprobe Analysis of Plagioclase

Sample	SiO_2	CaO	FeO	Na_2O	Al_2O_3	K_2O	Total
NC-MPE-503 P1 Core	65.91	2.29	0.06	10.50	21.41	0.34	100.52
NC-MPE-503 P1 Rim	67.89	0.59	0.19	11.72	19.85	0.09	100.33
NC-MPE-503 P2 Core	64.44	3.62	0.15	10.01	22.53	0.50	101.25
NC-MPE-503 P2 Rim	65.06	3.06	0.16	9.98	21.89	0.77	100.92
NC-MPE-503 P3 Core	64.19	3.96	0.18	9.32	22.63	0.49	100.77
NC-MPE-503 P3 Rim	66.68	1.76	0.12	10.49	20.89	0.53	100.47
NC-MPE-503 P4 Core	64.80	3.51	0.16	9.88	22.45	0.41	101.22
NC-MPE-503 P4 Rim	68.66	0.97	0.13	11.31	19.88	0.22	101.17
NC-MPE-086 P1 Core	65.72	2.57	0.11	9.98	21.53	0.88	100.79
NC-MPE-086 P1 Rim	66.46	2.06	0.26	10.40	20.89	0.63	100.70
NC-MPE-086 P2 Core	63.87	3.65	0.19	9.10	22.54	0.74	100.08
NC-MPE-086 P2 Rim	66.07	2.40	0.11	10.21	21.25	0.75	100.79

* All measurements are reported in wt %.

Table A3: Thermobarometry Results

Sample	Al-in-Hornblende Pressure* (GPa)	Plagioclase-Hornblende Temperature† (°C)
NC-MPE-503 H1-P1 Core	0.23	669.4
NC-MPE-503 H1-P1 Rim	0.05	613.5
NC-MPE-503 H2-P2 Core	0.27	686.3
NC-MPE-503 H2-P2 Rim	0.11	630.1
NC-MPE-503 H3-P3 Core	0.30	735.2
NC-MPE-503 H3-P3 Rim	0.26	677.8
NC-MPE-503 H4-P4 Core	0.25	691.6
NC-MPE-503 H4-P4 Rim	0.14	630.5
NC-MPE-086 H1-P1 Core	0.26	690.9
NC-MPE-086 H1-P1 Rim	0.26	676.9
NC-MPE-086 H1-P1 Core	0.17	672.1
NC-MPE-086 H1-P1 Rim	0.25	675.1

* All pressures were calculated using the calibration of Anderson and Smith (1995).
† Temperatures were calculated using Blundy and Holland (1990).

Table A4: CA-ID-TIMS U-Pb Zircon Geochronology Results

Frac.	Dates $^{206}Pb/^{238}U^{*}$	2σ abs.	$^{207}Pb/^{235}U^{\dagger}$	2σ abs.	$^{207}Pb/^{206}Pb^{\dagger}$	2σ abs.	% Disc.§	Corr. Coef.	Composition Th/U#	Pb_c (pg)**	Pb^{*}/Pb_c ††	Isotopic Ratios $^{206}Pb/^{204}Pb$§§	$^{208}Pb/^{206}Pb$##	$^{206}Pb/^{238}U^{*}$##	2σ %	$^{207}Pb/^{235}U$##	2σ %	$^{207}Pb/^{206}Pb^{*}$##	2σ %
NC-MPE-438 (48.50682 -120.66447***)																			
z1	48.467	0.063	48.55	0.42	56	21	14.09	0.275	0.25	0.62	25	1601	0.081	0.0075355	0.086	0.04898	0.88	0.04716	0.86
z2	48.567	0.087	48.96	0.85	72	41	32.64	0.362	0.29	1.98	12	743	0.094	0.007551	0.16	0.04940	1.8	0.04747	1.7
z3	48.472	0.071	48.39	0.62	48	30	-1.38	0.429	0.29	0.48	17	1101	0.092	0.0075361	0.12	0.04881	1.3	0.04699	1.3
z5	48.479	0.092	49.08	0.95	82	46	41.11	0.365	0.32	2.94	10	667	0.104	0.007537	0.18	0.04953	2.0	0.04768	1.9
z6	48.432	0.049	48.41	0.17	51.1	8.1	5.31	0.378	0.31	0.38	69	4374	0.098	0.0075298	0.066	0.04883	0.36	0.04706	0.34
NC-MPE-511 (48.50197 -120.62159***)																			
z1	48.362	0.033	48.403	0.072	55.1	2.9	12.32	0.625	0.45	0.37	189	11430	0.146	0.0075158	0.067	0.048824	0.15	0.047136	0.12
z3	48.347	0.046	48.57	0.44	64	22	25.11	0.319	0.42	5.20	22	1377	0.135	0.0075134	0.096	0.04900	0.94	0.04732	0.91
z4	48.325	0.033	48.39	0.13	56.1	5.8	13.98	0.456	0.37	0.51	97	5971	0.119	0.0075100	0.067	0.04881	0.27	0.04716	0.24
z5	48.328	0.058	48.35	0.10	54.2	3.9	10.97	0.625	0.40	0.46	193	11798	0.129	0.0075104	0.12	0.04877	0.21	0.047119	0.16
z6	48.357	0.032	48.44	0.13	57.3	6.1	15.73	0.533	0.42	0.41	91	5568	0.136	0.0075151	0.065	0.04886	0.28	0.04718	0.25
z7	48.345	0.034	48.266	0.096	49.0	4.1	1.52	0.570	0.42	0.55	142	8656	0.135	0.0075131	0.071	0.048683	0.20	0.047017	0.17
NC-MPE-093 (48.52964 -120.64862***)																			
z1	48.247	0.030	48.35	0.19	58.0	9.0	16.98	0.371	0.37	0.75	54	3377	0.118	0.0074978	0.063	0.04877	0.40	0.04719	0.38
z2	48.321	0.073	48.61	0.86	67	42	28.30	0.353	0.41	0.73	12	730	0.132	0.007509	0.15	0.04903	1.8	0.04738	1.8
z6	48.297	0.031	48.36	0.25	56	12	14.11	0.340	0.38	0.35	42	2620	0.123	0.0075056	0.064	0.04878	0.53	0.04716	0.51
z7	48.288	0.054	48.49	0.59	63	29	23.83	0.414	0.39	0.33	18	1099	0.125	0.0075042	0.11	0.04892	1.2	0.04730	1.2
z9	48.24	0.14	48.9	1.7	84	84	42.85	0.329	0.44	1.69	6	368	0.140	0.007496	0.29	0.0493	3.6	0.0477	3.6
z12	48.315	0.050	48.53	0.47	64	23	24.44	0.319	0.39	1.39	21	1300	0.125	0.0075084	0.10	0.04896	1.0	0.04731	0.97
NC-MPE-378A (48.57325 -120.84033***)																			
z16	48.235	0.062	48.54	0.70	68	34	29.43	0.350	0.38	1.17	14	881	0.123	0.0074960	0.13	0.04897	1.5	0.04740	1.4
z25	48.210	0.038	48.23	0.25	54	12	10.36	0.438	0.39	0.34	46	2830	0.125	0.0074920	0.079	0.04864	0.53	0.04711	0.49
z26	48.228	0.044	48.15	0.35	49	17	1.80	0.247	0.36	0.50	29	1831	0.115	0.0074948	0.091	0.04857	0.74	0.04702	0.72
z27	48.207	0.049	48.18	0.55	51	27	6.50	0.336	0.51	0.69	19	1132	0.162	0.0074915	0.10	0.04859	1.2	0.04707	1.1
z28	48.251	0.055	48.43	0.56	62	27	22.34	0.370	0.94	0.44	23	1241	0.300	0.0074984	0.11	0.04885	1.2	0.04727	1.1
z16	48.235	0.062	48.54	0.70	68	34	29.43	0.350	0.38	1.17	14	881	0.123	0.0074960	0.13	0.04897	1.5	0.04740	1.4
NC-MPE-088 (48.54091 -120.63500***)																			
z1	48.169	0.065	48.24	0.36	56	17	14.48	0.340	0.40	0.33	30	1840	0.127	0.007486	0.14	0.04865	0.76	0.04716	0.73
z2	48.199	0.042	48.71	0.43	79	21	38.79	0.400	0.38	0.36	24	1523	0.121	0.0074903	0.088	0.04914	0.90	0.04760	0.86
z3	48.205	0.035	48.29	0.30	57	14	15.51	0.393	0.38	0.36	36	2255	0.120	0.0074912	0.072	0.04870	0.63	0.04717	0.60
z4	48.224	0.046	48.50	0.45	67	22	28.12	0.297	0.37	0.23	25	1542	0.120	0.0074942	0.096	0.04893	0.95	0.04737	0.93
z5	48.207	0.053	48.42	0.58	63	28	24.11	0.387	0.37	0.30	18	1109	0.119	0.0074915	0.11	0.04884	1.2	0.04730	1.2
z6	48.223	0.099	48.4	1.3	61	65	21.36	0.289	0.37	0.44	8	496	0.119	0.007494	0.21	0.0488	2.8	0.0473	2.7
NC-MPE-583 (48.55848 -120.69115***)																			
z1	48.196	0.033	48.39	0.16	62.7	7.2	23.29	0.512	0.38	0.48	78	4818	0.123	0.0074898	0.068	0.04881	0.33	0.04729	0.30
z2	48.164	0.033	48.24	0.21	56	10	14.87	0.379	0.44	0.50	53	3223	0.141	0.0074848	0.067	0.04865	0.45	0.04716	0.43
z3	48.158	0.059	48.43	0.62	66	30	27.67	0.355	0.38	0.74	17	1051	0.121	0.0074838	0.12	0.04885	1.3	0.04736	1.3
z4	48.212	0.057	48.26	0.63	55	31	13.21	0.373	0.41	0.53	16	1005	0.131	0.0074923	0.12	0.04868	1.3	0.04714	1.3
z5	48.256	0.090	48.9	1.1	85	53	43.41	0.343	0.44	1.10	9	583	0.141	0.007499	0.19	0.0493	2.3	0.0477	2.2
z6	48.187	0.030	48.50	0.23	69	11	29.85	0.340	0.39	0.29	47	2931	0.123	0.0074883	0.061	0.04892	0.48	0.04740	0.46
NC-MPE-450 (48.65726 -120.81995***)																			
z4	48.194	0.074	48.63	0.77	75	37	35.55	0.390	0.37	0.41	14	857	0.118	0.007489	0.15	0.04905	1.6	0.04753	1.6
z5	48.105	0.092	47.8	1.1	36	54	-32.63	0.402	0.39	0.30	10	621	0.126	0.007476	0.19	0.0482	2.3	0.0468	2.2
z6	48.144	0.030	48.30	0.20	60.7	9.8	20.85	0.328	0.35	0.57	51	3195	0.111	0.0074817	0.061	0.04872	0.43	0.04725	0.41
z7	48.119	0.047	48.03	0.51	48	25	0.40	0.390	0.38	0.55	20	1248	0.122	0.0074778	0.098	0.04844	1.1	0.04700	1.1

z8	48.135	0.042	48.43	0.39	68	19	29.17	0.454	0.34	0.42	28	1746	0.108	0.0074803	0.088	0.04886	0.83	0.04739	0.79
z9	48.168	0.039	48.40	0.35	64	17	25.26	0.366	0.36	0.59	29	1806	0.114	0.0074855	0.080	0.04882	0.74	0.04732	0.71
NC-MPE-523 (48.54485 -120.68233***)																			
z2	48.132	0.036	47.99	0.27	46	13	-4.86	0.312	0.34	0.29	44	2724	0.110	0.0074798	0.074	0.04840	0.57	0.04695	0.55
z3	48.129	0.027	48.05	0.14	48.7	6.6	1.28	0.354	0.35	0.34	90	5588	0.113	0.0074794	0.055	0.04846	0.29	0.04701	0.27
z4	48.176	0.035	48.36	0.23	62	11	22.47	0.446	0.34	0.58	48	2981	0.108	0.0074867	0.072	0.04878	0.49	0.04727	0.46
z5	48.185	0.076	48.47	0.74	67	36	28.49	0.416	0.38	1.33	14	906	0.122	0.007488	0.16	0.04889	1.6	0.04738	1.5
z7	48.15	0.10	48.2	1.4	57	71	16.23	0.353	0.33	0.62	8	526	0.105	0.007482	0.21	0.0487	3.1	0.0472	3.0
z8	48.120	0.078	47.65	0.86	29	43	-66.98	0.423	0.39	0.92	13	799	0.124	0.007478	0.16	0.04805	1.8	0.04662	1.8
NC-MPE-086 (48.57338 -120.63071***)																			
z1	48.128	0.029	48.32	0.19	62.6	9.3	23.25	0.230	0.41	0.27	56	3459	0.131	0.0074792	0.059	0.04874	0.40	0.04729	0.39
z2	48.156	0.030	48.23	0.18	56.7	8.9	15.19	0.329	0.56	0.39	63	3706	0.180	0.0074835	0.062	0.04865	0.39	0.04717	0.37
z3	48.098	0.041	48.26	0.29	61	14	21.24	0.363	0.41	0.35	39	2419	0.132	0.0074744	0.085	0.04868	0.62	0.04725	0.60
z4	48.151	0.028	48.28	0.18	59.5	8.6	19.18	0.405	0.40	0.33	67	4091	0.127	0.0074828	0.057	0.04870	0.38	0.04722	0.36
z5	48.134	0.046	48.29	0.17	60.9	7.9	21.08	0.373	0.39	0.41	70	4277	0.126	0.0074801	0.096	0.04871	0.36	0.04725	0.33
z6	48.159	0.058	48.24	0.29	57	15	15.87	0.147	0.74	0.85	39	2197	0.236	0.0074841	0.12	0.04866	0.62	0.04718	0.62
NC-MPE-510 (48.62438 -120.76897***)																			
z1	48.130	0.032	48.15	0.24	54	12	10.77	0.435	0.39	0.34	49	3007	0.126	0.0074795	0.066	0.04856	0.51	0.04711	0.48
z2	48.126	0.045	47.92	0.41	42	20	-13.07	0.343	0.40	0.44	27	1691	0.128	0.0074788	0.094	0.04833	0.87	0.04689	0.84
z3	48.093	0.056	47.84	0.62	40	31	-21.08	0.361	0.33	0.49	16	1021	0.105	0.0074738	0.12	0.04824	1.3	0.04683	1.3
z4	48.152	0.029	48.12	0.21	51	10	6.04	0.273	0.39	0.48	49	3054	0.123	0.0074830	0.059	0.04853	0.44	0.04706	0.42
z5	48.155	0.076	48.58	0.92	74	45	35.42	0.327	0.35	2.63	10	663	0.112	0.007483	0.16	0.04901	1.9	0.04752	1.9
z6	48.109	0.032	48.29	0.26	62	12	22.73	0.404	0.40	0.56	43	2657	0.127	0.0074762	0.067	0.04871	0.54	0.04728	0.52
NC-MPE-499 (48.57868 -120.83591***)																			
z1	48.144	0.080	47.84	0.47	37	23	-28.15	0.310	0.36	0.76	31	1943	0.114	0.007482	0.17	0.04825	1.0	0.04679	0.96
z2	48.148	0.089	48.29	0.22	60	10	19.71	0.431	0.35	0.43	56	3476	0.111	0.007482	0.19	0.04870	0.47	0.04723	0.42
z3	48.119	0.030	48.20	0.19	56.9	9.2	15.64	0.404	0.33	0.51	56	3534	0.106	0.0074778	0.062	0.04862	0.41	0.04717	0.38
z4	48.101	0.033	48.16	0.18	55.5	8.6	13.53	0.349	0.36	0.45	60	3742	0.114	0.0074750	0.069	0.04857	0.38	0.04715	0.36
z5	48.132	0.036	48.19	0.33	56	16	14.17	0.345	0.36	0.44	35	2182	0.115	0.0074798	0.074	0.04861	0.70	0.04715	0.68
z6	48.124	0.045	48.27	0.28	60	14	20.52	0.295	0.39	0.87	38	2347	0.124	0.0074785	0.094	0.04869	0.59	0.04724	0.57
NC-MPE-200 (48.65371 -120.85905***)																			
z1	47.987	0.088	48.3	1.1	67	53	29.02	0.358	0.45	0.58	9	591	0.144	0.007457	0.18	0.0487	2.3	0.0474	2.2
z20	48.004	0.073	47.74	0.87	39	44	-21.89	0.343	0.53	1.14	12	712	0.169	0.007460	0.15	0.04814	1.9	0.04683	1.8
z25	48.080	0.073	48.30	0.87	64	43	25.04	0.342	0.48	1.28	12	716	0.153	0.007472	0.15	0.04872	1.8	0.04731	1.8
z32	48.078	0.059	47.92	0.49	45	24	-7.72	0.512	0.50	0.47	22	1335	0.161	0.0074715	0.12	0.04832	1.1	0.04693	0.99
z33	48.03	0.11	48.8	1.4	90	70	46.82	0.341	0.53	1.84	7	435	0.168	0.007464	0.24	0.0492	3.0	0.0478	2.9
NC-MPE-565A (48.63493 -120.84813***)																			
z1	47.808	0.029	47.83	0.21	53	10	10.57	0.336	0.44	0.31	59	3594	0.140	0.0074292	0.060	0.04823	0.44	0.04710	0.43
z2	47.792	0.046	47.87	0.32	56	16	15.19	0.375	0.54	0.70	34	2047	0.174	0.0074267	0.097	0.04827	0.69	0.04716	0.65
z3	47.732	0.073	47.82	0.43	57	21	16.38	0.375	0.41	0.80	25	1529	0.130	0.007417	0.15	0.04822	0.92	0.04717	0.88
z4	47.820	0.038	47.74	0.38	49	19	1.84	0.332	0.52	0.45	28	1649	0.167	0.0074311	0.080	0.04814	0.81	0.04701	0.79
z5	47.785	0.040	47.75	0.33	50	16	5.50	0.398	0.46	0.25	38	2284	0.146	0.0074255	0.083	0.04815	0.70	0.04705	0.67
NC-MPE-485 (48.66853 -120.90965***)																			
z1	47.73	0.11	47.5	1.3	43	67	-9.99	0.358	0.44	0.54	8	477	0.141	0.007416	0.23	0.0479	2.9	0.0469	2.8
z2	47.743	0.026	47.78	0.11	54.2	5.1	12.11	0.360	0.48	0.39	122	7312	0.155	0.0074191	0.053	0.04818	0.23	0.047119	0.21
z3	47.698	0.059	47.74	0.62	55	31	12.92	0.450	0.44	0.47	16	1000	0.141	0.0074120	0.12	0.04814	1.3	0.04713	1.3
z4	47.725	0.029	47.71	0.14	51.8	6.5	8.07	0.655	0.40	0.21	109	6721	0.127	0.0074162	0.061	0.04811	0.31	0.04707	0.27
z5	47.723	0.028	47.69	0.18	50.7	8.6	6.11	0.354	0.39	0.25	66	4096	0.124	0.0074159	0.058	0.04809	0.38	0.04705	0.36
z6	47.952	0.045	48.04	0.48	57	23	16.07	0.409	0.44	0.35	22	1361	0.140	0.0074517	0.094	0.04845	1.0	0.04718	0.98
NC-MPE-517 (48.63261 -120.80870***)																			

z1	48.344	0.044	48.58	0.46	65	23	25.56	0.340	0.39	1.03	21	1322	0.126	0.0075129	0.092	0.04901	0.98	0.04733	0.95
z2	48.603	0.062	48.33	0.65	39	32	-23.59	0.404	0.25	0.32	15	993	0.079	0.0075533	0.13	0.04874	1.4	0.04683	1.3
z4	48.266	0.054	48.40	0.48	60	23	19.05	0.384	0.44	0.40	24	1498	0.141	0.0075008	0.11	0.04882	1.0	0.04722	0.97
z5	47.988	0.052	48.30	0.49	68	24	30.00	0.380	0.79	0.66	25	1411	0.252	0.0074573	0.11	0.04872	1.0	0.04740	1.0
z6	48.198	0.033	48.33	0.27	59	13	19.04	0.360	0.42	0.47	39	2421	0.133	0.0074901	0.069	0.04875	0.57	0.04722	0.55
z7	48.13	0.19	48.5	2.4	73	120	34.31	0.364	0.93	0.69	5	274	0.297	0.007480	0.39	0.0490	5.1	0.0475	4.9
z8	48.192	0.030	48.07	0.13	46.8	5.9	-2.73	0.447	0.51	0.47	117	6941	0.164	0.0074891	0.062	0.04848	0.27	0.04697	0.24

* Corrected for initial Th/U disequilibrium using radiogenic ^{208}Pb and f_{ThU}=0.138 for granitoids (Stelten et al., 2015) or f_{ThU}=0.33 for the diorite (Rubatto and Hermann, 2007).

† Isotopic dates calculated using the decay constants λ238 = 1.55125E-10 and λ235 = 9.8485E-10 (Jaffey et al. 1971).

§ % discordance = 100 - (100 * ($^{206}Pb/^{238}U$ date) / ($^{207}Pb/^{206}Pb$ date))

Th contents calculated from radiogenic ^{208}Pb and the $^{207}Pb/^{206}Pb$ date of the sample, assuming concordance between U-Th and Pb systems.

** Total mass of common Pb.

†† Ratio of radiogenic Pb (including ^{208}Pb) to common Pb.

§§ Measured ratio corrected for fractionation and spike contribution only.

Measured ratios corrected for fractionation, tracer and blank.

*** All locations reported using WGS 84.

Table A5: Comparison of Different Th-correction Methods

Sample	Weighted Mean $^{206}Pb/^{238}U$ Date (Ma) Constant $f_{Th/U}$* Correction	Weighted Mean $^{206}Pb/^{238}U$ Date (Ma) Constant $[Th/U]_{Magma}$† Correction	Difference Between Methods (Ma)
NC-MPE-438	48.468 ± 0.030/0.037/0.064 (MSWD=1.84)	48.485 ± 0.022/0.031/0.060 (MSWD=2.87)	0.017
NC-MPE-511	48.346 ± 0.015/0.026/0.058 (MSWD=0.69)	48.345 ± 0.015/0.026/0.058 (MSWD=0.60)	0.001
NC-MPE-093	48.281 ± 0.018/0.028/0.059 (MSWD=1.91)	48.281 ± 0.018/0.028/0.059 (MSWD=1.88)	0.000
NC-MPE-378A	48.223 ± 0.021/0.030/0.060 (MSWD=0.54)	48.219 ± 0.021/0.030/0.060 (MSWD=0.34)	0.004
NC-MPE-088	48.205 ± 0.020/0.030/0.060 (MSWD=0.42)	48.205 ± 0.020/0.030/0.060 (MSWD=0.44)	0.000
NC-MPE-583	48.185 ± 0.016/0.027/0.058 (MSWD=1.27)	48.185 ± 0.016/0.027/0.058 (MSWD=1.29)	0.000
NC-MPE-450	48.146 ± 0.018/0.028/0.059 (MSWD=1.08)	48.147 ± 0.018/0.028/0.059 (MSWD=1.09)	0.001
NC-MPE-523	48.144 ± 0.017/0.027/0.058 (MSWD=1.33)	48.146 ± 0.017/0.027/0.058 (MSWD=1.35)	0.002
NC-MPE-086	48.139 ± 0.014/0.025/0.057 (MSWD=1.44)	48.136 ± 0.014/0.026/0.057 (MSWD=1.19)	0.003
NC-MPE-510	48.129 ± 0.016/0.026/0.058 (MSWD=1.26)	48.129 ± 0.016/0.026/0.058 (MSWD=1.24)	0.000
NC-MPE-499	48.120 ± 0.017/0.027/0.058 (MSWD=0.50)	48.121 ± 0.017/0.027/0.058 (MSWD=0.50)	0.001
NC-MPE-200	48.045 ± 0.034/0.041/0.066 (MSWD=1.33)	48.041 ± 0.034/0.041/0.066 (MSWD=1.32)	0.004
NC-MPE-565A	47.799 ± 0.018/0.028/0.058 (MSWD=1.38)	47.796 ± 0.018/0.028/0.058 (MSWD=1.30)	0.003
NC-MPE-485	47.729 ± 0.015/0.026/0.057 (MSWD=0.64)	47.727 ± 0.015/0.026/0.057 (MSWD=0.53)	0.002
NC-MPE-517	47.988 ± 0.052/0.056/0.076 (Max. Age)	47.972 ± 0.053/0.057/0.077 (Max. Age)	0.016

*$f_{Th/U}$=0.138 for granitoids (Stelten et al., 2015) or $f_{Th/U}$=0.33 for the diorite (Rubatto and Hermann, 2007).
†$[Th/U]_{Magma}$= 2.8 ± 1.0 (2σ) for all samples.

Table A6: Magma Emplacement Rates in Upper-crustal Granitoid Plutonic Complexes

Intrusive Complex	Intrusion Depth (km)	Area (km^2)	Vertical Relief (km)	Volume (km^3)	Oldest Date (Ma)*	Youngest Date (Ma)*	Emplacement Rate (km^3/yr) †	References
1) Lago della Vacca pluton	12	9.7	1.0	10	42.07 ± 0.04	41.76 ± 0.03	0.00003	John and Blundy (1993), Schoene et al. (2012)
2) Lamarck granodiorite	8-12	600	3.0	1800	94.26 ± 0.17	90.9 ± 0.2	0.00053	Davis et al. (2012)
3) Mt. Givens granodiorite	9	1500	3.0	4500	97.92 ± 0.06	90.87 ± 0.05	0.00133	McNulty et al. (2002), Frazer et al. (2014)
4) Mt. Princeton batholith	3	450	1.5	675	35.80 ± 0.09	35.37 ± 0.10	0.00153	Mills and Coleman (2013)
5) Mt. Stuart batholith (Old Domain)	6-12	194	2.5	485	95.88 ± 0.03	94.25 ± 0.14	0.00030	Matzel et al. (2006)
6) Mt. Stuart batholith (Young Domain)	6-12	208	2.5	520	90.92 ± 0.05	90.78 ± 0.08	0.00316	Matzel et al. (2006)
7) Muir intrusive suite	8-12	1700	3.0	5100	95.45 ± 0.32	83.5 ± 0.5§	0.00043	Davis et al. (2012)
8) Rio Honda pluton	< 5	90	1.2	108	22.98 ± 0.09	22.59 ± 0.06	0.00027	Tappa et al. (2011)
9) Torres del Paine complex	2-3	80	2.0	88	12.593 ± 0.009	12.431 ± 0.006	0.00054	Leuthold et al. (2012)
10) Tuolumne intrusive suite	3-9	1200	2.0	2400	94.4 ± 0.3	85.1 ± 0.9	0.00026	Coleman et al. (2004), Memeti et al. (2010)

* ID-TIMS $^{206}Pb/^{238}U$ zircon dates

† Emplacement rates were calculated using the mode of Monte Carlo simulations with 10^7 iterations

§ The uncertainty for this sample was not reported in Davis et al. (2011), we apply a conservative estimate of 0.5 Ma

Chapter 5

Timing the Rift-to-Drift Transition in the Newfoundland-Iberia Rift

Abstract

Broad areas of lithospheric mantle are exposed along ocean continent transition zones in rifts that extended slowly and are thought to be exhumed along large-scale detachment faults. However, the nature of the transition from asymmetric exhumation to symmetric spreading is controversial. We present new zircon U-Pb geochronology and Hf isotopic data from gabbros that intrude exhumed mantle at ODP sites 1070 and 1277 in the Newfoundland-Iberia rift. The sites are approximately conjugate to one another and within embryonic ocean crust, which is commonly considered to be emplaced during early symmetric spreading. Magnetic data suggests crustal accretion occurred at both sites during magnetic polarity chrons M3-M0 (126-121 Ma). However, our data indicates that asthenospheric melts were emplaced prior to or coeval with mantle exhumation at ~124 Ma at ODP site 1070 and ~115 Ma at ODP site 1277. We suggest that this asymmetry is the result of continued mantle exhumation along large-scale detachment faults until lithospheric breakup near the Aptian-Albian boundary. The breakup location is likely coincident with the large-amplitude magnetic J-anomaly, and our ~115 Ma date for magmatism above this anomaly provides the best available age constraint for this event.

Introduction

The end of continental rifting is marked by rupture of continental lithosphere and the formation of an oceanic spreading center. This process is geologically instantaneous in rifts that extend rapidly, and is manifested in the geologic record as thick sequences of basalt that mark an abrupt transition from continental to oceanic crust (e.g., Mutter et al., 1988). However, in rifts that extended slowly the ocean continent transition (OCT) includes broad areas of exhumed subcontinental lithospheric mantle with only minor syn-rift magmatic rocks (e.g., Whitmarsh et al., 2001). In these 'magma-poor' rifts mantle exhumation is thought to occur along lithospheric-scale detachment faults (e.g., Lemoine et al., 1987; Lavier and Manatschal, 2006; Manatschal and Müntener, 2009), but the nature of the change from asymmetric detachment faulting to

symmetric seafloor spreading remains debated between a gradual transition (e.g., Sibuet et al., 2007) and instantaneous lithospheric rupture (Bronner et al., 2011; Soares et al., 2012).

Newfoundland-Iberia Rift

Final rifting between Newfoundland and Iberia occurred from the latest Jurassic through early Cretaceous, when continental crust was hyper-extended and subcontinental lithospheric mantle was exhumed to the seafloor (e.g., Tucholke et al., 2007). Exhumed lithospheric mantle has been documented on both margins, and ocean drilling has revealed that the mantle rocks are capped by tectonic breccias that are thought to represent a system of westward-dipping, lithospheric-scale detachment faults (e.g., Péron-Pinvidic et al., 2009). A wider zone of exhumed mantle on the Iberian margin (Fig. 1B) and a westward younging trend of radiometric age constraints and the ages of the first sediments overlying exhumed mantle (Fig. 1B) are consistent with this interpretation. However, the timing and nature of the transition from broadly asymmetric exhumation to symmetric seafloor spreading is controversial.

The oceanward end of the OCT on both margins is defined by a series of weak magnetic anomalies that culminate with the large amplitude J-anomaly (Fig. 1B). Srivastava et al. (2000) and Sibuet et al. (2007) interpreted a spreading origin for these anomalies during magnetic polarity chrons M3-M0 (126-121 Ma: Malinverno et al., 2012), but the crust in this area is composed of serpentinized mantle (Shipboard Scientific Party, 1998; 2004). This observation led Jagoutz et al. (2007), Sibuet et al. (2007), Minshull et al. (2014), and others to speculate that this 'embryonic' ocean crust was emplaced symmetrically via processes similar to those seen at ultra-slow spreading ridges. Alternatively, Bronner et al. (2011) and Soares et al. (2012) have proposed that symmetric spreading did not begin until the Aptian-Albian boundary (~113 Ma), where an unconformity in proximal rift basins (Soares et al., 2012) and a major seismic reflector in the sedimentary record of the distal margin are interpreted to represent lithospheric breakup (Tucholke et al., 2007). Bronner et al. (2011) further suggested that the J-anomaly, and the surrounding weak magnetic anomalies, were generated by excess magmatism during ~113 Ma breakup and not by seafloor spreading.

The spatial and temporal record of magmatism within the embryonic oceanic crust has the potential to resolve discrepancies between these two hypotheses. Models that favor symmetric spreading during magnetic polarity chrons M3-M0 (126-121 Ma) predict a symmetric

history of magmatism within the embryonic oceanic crust during this time (e.g., Jagoutz et al., 2007), while models that propose that seafloor spreading did not start until the Aptian-Albian boundary predict that magmas would dominantly stall and crystallize in the footwall (Iberia) of the lithospheric-scale detachment fault(s), resulting in a spatial and temporal record of magmatism that is asymmetric (e.g., Lemoine et al., 1987). We assess these two models with new zircon U-Pb geochronology and Hf isotopic compositions from gabbros that intrude exhumed mantle at ODP sites 1277 and 1070, which are approximately conjugate to one another in the Newfoundland-Iberia rift (Fig. 1).

Embryonic Oceanic Crust

Embryonic ocean crust was sampled along two approximately conjugate transects through the Newfoundland-Iberia OCT. Both transects have been extensively studied geophysically and were drilled during ODP legs 149, 173, and 210 (Fig. A1). Locations where drilling penetrated exhumed mantle are shown in Fig. 1B and previous geo- and thermochronology from these cores is presented in Table A1. In both transects, the first crust with seismic properties similar to oceanic crust lies between inferred magnetic anomalies M1-M0 (Minshull et al., 2014), approximately coincident with the J-anomaly.

On the Iberian margin, drilling at ODP site 1070 penetrated exhumed mantle between inferred magnetic anomalies M3-M1 (Fig. 1B). Recovery includes a section of peridotite intruded by gabbroic dikes and veins, which is separated from late Aptian sedimentary rock by a tectonic breccia (Fig. A2: Shipboard Scientific Party, 1998). Magmatism at this site includes dikes and veins of gabbro that were emplaced prior to or coeval with mantle exhumation, because clasts of these rocks are included in the overlying tectonic breccia.

ODP site 1277 drilled within the J-anomaly on the Newfoundland margin, between inferred magnetic anomalies M1-M0 (Fig. 1B). Recovery includes a series of basalt flows separated from exhumed lithospheric mantle by a tectonic breccia (Fig. A2). The mantle at this site is subcontinental in origin and intruded by numerous gabbroic veins (Müntener and Manatschal, 2006), which were likely emplaced coeval with exhumation because they intruded mantle that was already serpentinized and clasts of the gabbroic rocks are found within the tectonic breccia (Shipboard Scientific Party, 2004).

Two magmatic lithologies attributed to distinct alkaline and MORB-like magmas are present at both ODP sites 1070 and 1277 (Müntener and Manatschal, 2006; Jagoutz et al., 2007). Previous geo- and thermochronology of these rocks suggested that the different magmas were emplaced during distinct events: MORB-like magmas during early symmetric spreading at a proto-ridge and off-axis alkaline magmatism during basin wide extensional events (Jagoutz et al., 2007). However, the dates used to make these interpretations had overlapping uncertainties at ODP site 1070 and included a poorly constrained $^{40}Ar/^{39}Ar$ biotite date at ODP site 1277.

U-Pb Zircon Geochronology and Hf Isotopic Analysis

Given the uncertainty in the timing of magmatic events within the embryonic ocean crust we dated seven gabbroic veins that intrude exhumed mantle and one gabbroic clast at ODP sites 1070 and 1277 using U-Pb zircon chemical abrasion-isotope dilution-thermal ionization mass spectrometry (CA-ID-TIMS) geochronology. Both alkaline and MORB-like lithologies were selected and the Hf isotopic composition of the dated zircons was analyzed to assess possible differences in mantle source between these two lithologies. A lithologic description for each sample can be found in Appendix B, the methods used for U-Pb analyses in Appendix C, and the methods used for Hf isotopic measurements in Appendix D. All U-Pb and Hf isotopic data is presented in Tables A2 and A3, and U-Pb data is shown as traditional concordia plots in Fig. A3. Our preferred crystallization date for each sample is presented in Table 1 and represents a weighted mean of Th-corrected $^{206}Pb/^{238}U$ dates. $\varepsilon Hf_{(t)}$ values are also presented in Table 1.

Dates from an alkaline gabbroic clast within the tectonic breccia (IB2) and a MORB-like gabbroic vein that intrudes peridotite (IB1) at ODP site 1070 are in good agreement with previous geochronology (Tables 1 & A1), and suggest that a single period of magmatism occurred ~124 Ma at this site. $\varepsilon Hf_{(t)}$ values for the two samples overlap within uncertainty (Table 1), indicating that both magmas were likely derived from the same mantle source. We consider them to have been derived from the asthenosphere, because they are within the variability of εHf values seen in MORB along this segment of the Mid-Atlantic ridge (Fig. 2).

At ODP site 1277 we dated two alkaline (NF2, NF13) and four MORB-like (NF3, NF8, NF15, NF19) gabbroic veins that intrude the exhumed mantle. Dates from all six samples range from 115.71 ± 0.65 to 114.741 ± 0.065 Ma (Table 1), suggesting that both magmas were emplaced during the same period of magmatism. Our dates for the alkaline veins disagree with

an earlier $^{40}Ar/^{39}Ar$ biotite date of 128 ± 3 Ma for a different alkaline vein at this site (Jagoutz et al., 2007), but we consider our dates to be more robust because the $^{40}Ar/^{39}Ar$ analysis did not produce an age plateau during step-heating and biotite is known to readily incorporate excess argon (e.g., Bachmann et al., 2010). Zircon from both lithologies give a narrow $\varepsilon Hf_{(t)}$ of 16.56 to 17.15 that is consistent with their derivation from the asthenospheric mantle (Fig. 2), and we interpret the different lithologies to reflect varying degrees of melting from this source. The overlying basalt flows have T- to N-MORB geochemistry (Robertson, 2007) and may be related to the same magmatic event.

Tectonic Implications

Magmatism and exhumation at ODP site 1070 is in good agreement with the proposed age of the magnetic anomaly that runs through the area, but at ODP site 1277 magmatism post-dates the inferred age of crustal accretion by ~8 Ma (Fig. 3). It is possible that this magmatism occurred long after initial exhumation since the veins intruded serpentinized mantle (Shipboard Scientific Party, 2004). However, we note that magmatic rocks are included as clasts in the overlying tectonic breccia and there is no reliable geo- or thermochronologic support for earlier magmatism and exhumation (Tables 1 and A1). Therefore, we consider it more likely that magmatism occurred coeval with exhumation at ~115 Ma, which is at odds with models of symmetric spreading during the young M-series magnetic anomalies (e.g., Sibuet et al., 2007). Instead, it is more consistent with a continuation of the westward younging trend of magmatism and exhumation seen on the Iberian margin (Fig. 3). Consequently, we propose that large-scale detachment faulting continued until lithospheric rupture occurred (Fig. 4). Based on unconformities in proximal basins and major seismic reflections in distal sedimentary sequences, Tucholke et al. (2007), Péron-Pinvidic et al. (2009), and Soares et al. (2012) proposed that lithospheric rupture occurred near the Aptian-Albian boundary (~113 Ma) and Bronner et al. (2011) suggested that the J-anomaly marks the region affected by excess magmatism during this breakup event. Because ODP site 1277 is within this anomaly (Figs. 1 and 3), the ~115 Ma magmatism at this location may mark the rift-to-drift transition in this area. However, we note that there is evidence that rupture was time-transgressive in the Newfoundland-Iberia rift and that the dates for this event may be older to the south and younger to the north (e.g., Bronner et al., 2011).

Magmatism at both ODP sites 1070 and 1277 occurred over brief (<1 Ma) intervals prior to or coeval with mantle exhumation. Based on this observation, we suggest that magmatism was focused near the point where mantle was exhumed to the seafloor along lithospheric-scale detachment faults (Fig. 4). Such focused magmatism likely served to weaken the footwall of the detachment system and may have ultimately controlled the location of lithospheric breakup. Calculating a pre-rupture extension rate is difficult without knowing the exact location of the first oceanic crust. However, by assuming that the first oceanic crust lies at the seaward limit of the J-Anomaly we calculate a maximum rate of ~8 mm/a (Fig. 3), which is much slower than the post-breakup full spreading rate of ~25 mm/a (Pittman and Talwani, 1972).

Conclusions

The magmatic record within embryonic oceanic crust in the Newfoundland-Iberia rift is inconsistent with symmetric spreading during the young M-series anomalies. Instead, it suggests that detachment faulting continued until final lithospheric rupture near the Aptian-Albian boundary. Magmatism appears to have been focused near the point of mantle exhumation on large-scale detachment faults, and may have played a key role in determining the location of breakup by weakening the overlying lithosphere. Breakup is likely marked by the magnetic J-Anomaly, and our ~115 Ma dates for gabbro emplaced within this anomaly at ODP site 1277 provide the best available date for this event.

Appendix A: Previous Geo- and Thermochronology

Figure A1 shows the location of all ODP drill sites that penetrated basement and/or magmatic rocks along the two studied transects. Previous geo- and thermochronology from these sites is presented in Table A1. On the Iberian margin, sites 901, 1065, and 1067 penetrated extended continental crust and site 1069 sampled an extensional allocthon of continental crust. Sites 900 and 1068 penetrated a tectonic breccia likely involved in exhumation of the lithospheric mantle and $^{40}Ar/^{39}Ar$ plagioclase dates (Feraud et al., 1996; Jagoutz et al., 2007) and a $^{40}Ar/^{39}Ar$ hornblende date (Jagoutz et al., 2007) from these sites suggest exhumation occurred between 140 and 133 Ma (Table 1). Further oceanward, sites 897 and 899 drilled exhumed mantle capped by tectonic breccias. Minor magmatic rocks were recovered from the overlying tectonic breccia at these sites (Shipboard Scientific Party, 1994), but no radiometric dates are

available. Nevertheless, the age of the first sediments overlying the mantle at ODP sites 897 and 899 is late Hauterivian to early Barremian, which provide a minimum age for mantle exhumation. The timing of magmatism and mantle exhumation at sites 1070 and 1277 is discussed within the text, and previous geo- and thermochronology results are presented in Table A1. Site 1276 did not reach basement, but sampled alkaline basalts of ~95-105 Ma in age (Hart and Blusztajn, 2004). These sills intrude late Aptian/early Albian sediments and likely represent off-axis magmatism that occurred after lithospheric breakup.

Appendix B: Sample Descriptions

IB1 (13R-4 36-42) was taken from a gabbroic vein that intrudes exhumed peridotite at ODP site 1070 (Fig. A2). The vein is almost completely altered to serpentine, talc, and chlorite with only minor relict ortho- and clinopyroxene and accessory zircon, apatite, and monazite. This mineralogy is similar to the E-MORB dike described by Beard et al. (2002). ***IB2 (8R-4 11-17)*** is from a gabbroic clast from the tectonic breccia that caps the basement at ODP site 1070 (Fig. A2). It is dominantly composed of coarse (several mm) grains of moderately to severely altered albite with minor amphibole and accessory zircon, and apatite. This sample is similar to the albitite clasts described by Beard et al. (2002), which Jagoutz et al. (2007) considered to represent alkaline magmas.

The exhumed peridotite at ODP site 1277 is intruded by numerous gabbroic veins (Fig. A2). These veins are largely altered to serpentine, talc, and chlorite. Nevertheless, Muntener and Manatschal (2006) and Jagoutz et al. (2007) described two vein lithologies based on relict igneous minerals. The first is defined by the assemblage plagioclase, clinopyroxene, orthopyroxene, ilmenite, and hornblende and was considered by Jagoutz et al. (2007) to be 'MORB-like'. ***NF3 (9R-5 26-33)***, ***NF8 (9R-7 45-50)***, ***NF15 (9R-2 11-17)***, and ***NF19 (9R-1 146-148)*** are all from highly altered (serpentine, talc, chlorite, calcite veins) gabbroic veins with all or part of this lithology. ***NF8 (9R-7 45-50)*** contains relict hornblende and accessory apatite and zircon and ***NF15 (9R-2 11-17)*** and ***NF19 (9R-1 146-148)*** contain relict hornblende with accessory zircon and ***NF3 (9R-5 26-33)*** contains highly altered pyroxenes with accessory zircon, apatite, and monazite. The second vein lithology identified by Muntener and Manatschal (2006) and Jagoutz et al. (2007) consists of phlogopite, albite, monazite, zircon, apatite, orthoamphibole, rutile, and ± xenotime and was considered 'alkaline' by Jagoutz et al. (2007).

NF2 (9R-5 50-56) and ***NF13 (9R-4 56-64)*** represent veins with this lithology and contain large relict grains of albite with accessory zircon and monazite ± xenotime. The location of each gabbroic vein is shown in Fig. A2.

Appendix C: U-Pb Zircon Geochronology Methods

Gabbroic veins within ODP cores 1070 and 1277 were crushed using a mortar and pestle and zircons were separated from this material using standard methods. U-Pb dates were produced using chemical abrasion- isotope dilution- thermal ionization mass spectrometry (CA-ID-TIMS) using methods slightly modified from Mattinson (2005) and outlined in Appendix A of Eddy et al. (2016). All of the isotopic measurements were made on the VG Sector 54 or Isotopx X62 thermal ionization mass spectrometers (TIMS) at the Massachusetts Institute of Technology and are presented in Table A2. Samples were spiked with the EARTHTIME ^{202}Pb-^{205}Pb-^{233}U-^{235}U isotopic tracer (Condon et al., 2015; McLean et al., 2015), which permits correction for both Pb and U fractionation using the tracer's known $^{202}Pb/^{205}Pb$ and $^{233}U/^{235}U$ ratios. We corrected for interferences under masses 202, 204, and 205 by measuring 201 and 203, assuming that they represent $^{202}BaPO_4$ and ^{203}Tl, and using natural isotopic abundances to correct for $^{202}BaPO_4$, $^{204}BaPO_4$, $^{205}BaPO_4$, and ^{205}Tl. We assume that zircon does not include any initial common Pb (Pb_c) during crystallization and that all measured ^{204}Pb is from laboratory contamination. We corrected for this contamination using the procedures outlined in McLean et al. (2011) and a laboratory Pb_c isotopic composition of $^{206}Pb/^{204}Pb = 18.145833 \pm 0.475155$ (1σ abs.), $^{207}Pb/^{204}Pb = 15.303903 \pm 0.295535$ (1σ abs.), and $^{208}Pb/^{204}Pb = 37.107788 \pm 0.875051$ (1σ abs.), calculated from 149 procedural blanks measured in the MIT isotope geochemistry lab between 2009 and 2015. The mass of Pb_c measured in our analyses is comparable to those seen in total procedural blanks and supports the assumption that zircon does not include Pb_c during crystallization. Initial secular disequilibrium in the ^{238}U-^{206}Pb decay system occurs due to exclusion of Th during zircon crystallization (Scharer, 1984). We corrected for this disequilibrium using the calculated $[Th/U]_{zircon}$ and a $[Th/U]_{magma} = 3.2$ based on the average MORB composition presented by Gale et al. (2013) and an arbitrary uncertainty of ± 1 (2σ). Data reduction was done with the U-Pb_Redux software package (Bowring et al., 2011) and used the decay constants for ^{235}U and ^{238}U presented in Jaffey et al. (1971). All isotopic ratios are presented in Table A2 and shown as concordia plots in Fig. A2.

All dates in Table 1 represent weighted means of Th-corrected $^{206}Pb/^{238}U$ dates. We used the mean square of weighted deviates (MSWD) to assess whether the spread in dates from individual zircons represented real age dispersion (MSWD >> 1) or could be attributed to analytical uncertainty. Only NF2 contained a zircon that was demonstrably older than the main population. This zircon (z6) is discordant (Fig. A3) and may contain an inherited core. The presence of a xenocrystic core in this sample would provide further evidence for the exhumed mantle at ODP site 1277 to be lithospheric in origin (e.g., Muntener and Manatschal, 2006). However, in order to preserve as much material for U-Pb analysis as possible, the zircons used in this study were not imaged and we cannot conclusively say whether or not this grain contained a core.

Appendix D: Hf Isotopic Measurements

Trace element aliquots were collected from all dated zircons using the methods of Schoene et al. (2010). These aliquots were dried down to chloride salts, converted to 200 µl of 1 M HCl- 0.1M HF and split into two new aliquots: 30 µl for trace element analysis and 170 µl for Hf isotopic measurement. Hf was purified from the 170 µl aliquot using AG50W-X8 cation resin following methods slightly modified from Goodge and Vervoort (2006) to minimize isobaric interferences to ^{176}Hf caused by ^{176}Lu and ^{176}Yb. Our elution scheme is very similar to that presented in Goodge and Vervoort (2006) and uses micro-columns holding ca. 100 µl of un-used, pre-cleaned, and equilibrated AG50W-X8 resin. After column chemistry, approximately 450 µl of 1 M HCl- 0.1M HF were added to the purified Hf cut in order to bring the volume of each aliquot up to ~1.2 ml, and the Hf isotopic composition of the purified solutions was measured on a Nu Plasma II-ES multi collector-inductively coupled plasma-mass spectrometer (MC-ICP-MS) at the MIT Department of Earth, Atmospheric, and Planetary Sciences. All Hf isotopic data is presented in Table A3. Repeat runs of JMC-475 standard solution at 25 ppb concentration were measured in order to monitor instrument stability, determine the reproducibility of the measured ratios, and adjust the obtained values for instrumental bias. Two or three measurements of JMC-475 were conducted every 8 or 10 unknowns during our analytical sessions, and unknowns were corrected using a standard-sample bracketing approach. External reproducibility for any given set of unknowns was estimated as the 2 SD of the bracketing standards used for correction, and was propagated in quadrature to the internal

uncertainties (i.e., based on counting statistics) in order to assign a total uncertainty to each unknown; using this approach, the determined 2 SD external reproducibility of the measured $^{176}Hf/^{177}Hf$ from JMC-475 solutions varied for each set of unknowns from ± 0.000007 (± 0.25 εHf) and ± 0.000011 (± 0.39 εHf). Overall, 89 measurements of JMC-475 from three separate analytical sessions resulted in a $^{176}Hf/^{177}Hf$= 0.282160 ± 0.000009 (± 0.32 εHf), which agrees with the value of 0.282161 ± 0.000014 reported by Vervoort and Blichert-Toft (1999), and provides a reasonable measure of our reproducibility. Because this is the first contribution presenting Hf isotopic results from the MIT-IG laboratory, repeat runs of established zircon reference materials were also conducted in order to asses the accuracy of our results. Measurements conducted on dissolved single-crystals of FC1, 91500 and R33 gave $^{176}Hf/^{177}Hf$=0.282179 ± 0.000012 (2 SD), $^{176}Hf/^{177}Hf$= 0.282305 ± 0.000006 (2 SD) and $^{176}Hf/^{177}Hf$=0.282751 ± 0.000005 (2 SD), respectively (Table A3). These results are in good agreement with the their respective reference values (i.e., 0.282183 ± 0.000012 for FC1, Fisher et al., 2014; 0.282308 ± 0.000006 for 91500, Blichert-Toft, 2008; 0.282764 ± 0.000014 for R33, Fisher et al., 2014). Epsilon Hf (εHf) values were calculated for each zircon using the values for the chondritic uniform reservoir (CHUR) presented in Bouvier et al. (2008). The 30 µl trace element aliquots were brought up in 1.0 ml of 3 % HNO_3 – 0.2 % HF solution, previously spiked with 2 ppb In. Trace element concentrations were measured by solution aspiration on an Agilent 7900 quadrapole-ICP-MS in the Center for Environmental Health Sciences at MIT, using a standardization scheme similar to that of Schoene et al. (2010). Calibration solutions were prepared gravimetrically from elemental standards to approximate the proportions expected in natural zircons, and mixed using the same In-spiked 3 % HNO_3 – 0.2 % HF solution used for our sample zircon aliquots as described above. The measured $^{176}Lu/^{177}Hf$ ratio for each crystal, calculated using the elemental Lu/Hf concentrations determined by quadrapole-ICP-MS and the natural Lu isotopic composition of Vervoort et al. (2004), was used to re-calculate the initial εHf ($\varepsilon Hf_{(t)}$) for each zircon at the crystallization age for each sample (Tables A3 and A4).

To assess the significance of the spread in $\varepsilon Hf_{(t)}$ observed between the different samples, we constructed a curve for the Hf isotopic evolution of depleted Atlantic mantle (DAM) for the studied area. We compiled $^{176}Hf/^{177}Hf$ measurements for modern MORB collected between the Azores and the Charlie-Gibbs Fracture zone (Table A4) and calculated a mean and 2σ variability (0.28327 ± 0.00013), which we assume to approximate the $^{176}Hf/^{177}Hf$ of the depleted mantle in

this area. We projected the evolution of this reservoir back through time using a $^{176}Lu/^{177}Hf$=0.03898 calculated from the Bouvier et al. (2008) $^{176}Lu/^{177}Hf$ value for CHUR and the fractionation factor of f=0.16 from Vervoort and Blichert-Toft (1999) and the resulting εHf_{DAM} curve is shown in Fig. 2. This figure includes previously published εHf_i for gabbros that intrude exhumed mantle on the Iberia margin (Scharer et al., 2000) recalculated using the values for CHUR presented in Bouvier et al. (2008) and an average $^{176}Lu/^{177}Hf$=0.0016 for zircon (Faure and Mensing, 2005). All of the $\varepsilon Hf_{(t)}$ values for magmas intruding exhumed mantle within the Newfoundland-Iberia rift are consistent with derivation from the depleted mantle in this area (Fig. 2).

REFERENCES

Agranier, A., Blichert-Toft, J., Graham, D., Debaille, V., Schiano, P., and Albarede, F., 2005, The spectra of isotopic heterogeneities along the mid-Atlantic ridge: Earth and Planetary Science Letters, v. 238, p. 96-109, doi: 10.1016/j.epsl.2005.07.011.

Andres, M., Blichert-Toft, J., and Schilling, J.G., 2004, Nature of the depleted upper mantle beneath the Atlantic: evidence from Hf isotopes in normal mid-ocean ridge basalts from 79°N to 55°S: Earth and Planetary Science Letters, v. 225, p. 89-103, doi: 10.1016/j.epsl.2004.05.041.

Bachmann, O., Schoene, B., Schnyder, C., and Spikings, R., 2010, The $^{40}Ar/^{39}Ar$ and U/Pb dating of young rhyolites in the Kos-Nisyros volcanic complex, eastern Aegean arc, Greece: Age discordance due to excess ^{40}Ar in biotite: Geochemistry, Geophysics, Geosystems, v. 11, Q0AA08, doi: 10.1029/2010GC003073.

Beard, J.S., Fullager, P.D., and Sinha, A.K., 2002, Gabbroic pegmatite intrusions, Iberia Abyssal Plain, ODP leg 173, site 1070: magmatism during a transition from non-volcanic rifting to seafloor spreading: Journal of Petrology, v. 43, p. 885-905, doi: 10.1093/petrology/43.5.885.

Blichert-Toft, J., Agranier, A., Andres, M., Kingsley, R., Schilling, J.G., and Albarede, F., 2005, Geochemical segmentation of the Mid-Atlantic Ridge north of Iceland and ridge-hot spot interaction in the North Atlantic: Geochemistry, Geophysics, Geosystems, v. 6, Q01E19, doi: 10.1029/2004GC000788.

Bouvier, A., Vervoort, J.D., and Patchett, P.J., 2008, The Lu-Hf and Sm-Nd isotopic composition of CHUR: constraints from unequilibrated chondrites and implications for the bulk composition of terrestrial planets: Earth and Planetary Science Letters, v. 273, p. 48-57, doi: 10.1016/j.epsl.2008.06.010.

Bowring, J.F., McLean, N.M., and Bowring, S.A., 2011, Engineering cyber infrastructure for U-Pb geochronology: Tripoli and U-Pb_Redux: Geochemistry, Geophysics, and Geosystems, v. 12, doi: 10.1029/2010GC003479.

Bronner, A., Sauter, D., Manatschal, G., Péron-Pinvidic, G., and Munschy, M., 2011, Magmatic breakup as an explanation for magnetic anomalies at magma-poor rifted margins: Nature Geoscience, v. 4, p. 549-553, doi: 10.1038/ngeo1201.

Condon, D.J., Schoene, B., McLean, N.M., Bowring, S.A., and Parrish, R.R., 2015, Metrology and traceability of U-Pb isotopic dilution geochronology (EARTHTIME tracer calibration part I): Geochimica et Cosmochimica, v. 164, p 464-480, doi: 10.1016/j.gca.2015.05.026.

Eddy, M.P., Bowring, S.A., Umhoefer, P.J., Miller, R.B., McLean, N.M., and Donaghy, E.E., 2016, High resolution temporal and stratigraphic record of Siletzia's accretion and triple junction migration from nonmarine sedimentary basins in central and western Washington: Geological Society of America Bulletin, doi: 10.1130/B31335.1.

Faure, G., and Mensing, T.M., 2005, Isotopes: Principles and Applications: Hoboken, NJ, John Wiley and Sons, 897 p.

Feraud, G., Beslier, M.O., and Cornen, G., 1996, 40Ar/39Ar dating of gabbros from the ocean/continent transition of the western Iberian margin: preliminary results, in, Whitmarsh, R.B., Sawyer, D.S., Klaus, A., and Masson, D.G., eds., Proceedings of the Ocean Drilling Program, Scientific Results, v. 149, p. 489-495, doi: 10.2973/odp.proc.sr.149.224.1996.

Fisher, C. M., Vervoort, J. D., and DuFrane, S. A., 2014, Accurate Hf isotope determinations of complex zircons using the "laser ablation split stream" method: Geochemistry Geophysics Geosystems, v. 15, p. 121–139, doi: 10.1002/2013GC004962.

Gale, A., Dalton, C.A., Langmuir, C.H., Su, Y. and Schilling, J.G., 2013, The mean composition of ocean ridge basalts: Geochemistry, Geophysics, Geosystems, v. 14, p. 489-518, doi: 10.1029/2012GC004334.

Gardien, V., and Paquette, J.L., 2004, Ion microprobe and ID-TIMS U-Pb dating on zircon grains from Leg 173 amphibolites: evidence for Permian magmatism on the west Iberian margin: Terra Nova, v. 16, p. 226-231, doi: 10.1111/j.1365-3121.2004.00554.x.

Goodge, J.W., and Vervoort, J.D., 2006, Origin of Mesoproterozoic A-type granites in Laurentia: Hf isotope evidence: Earth and Planetary Science Letters, v. 243, p. 711-731, doi: 10.1016/j.epsl.2006.01.040.

Hart, S.R., and Blusztajn, 2006, Age and geochemistry of the mafic sills, ODP site 1276, Newfoundland margin: Chemical Geology, v. 235, p. 222-237, doi: 10.1016/j.chemgeo.2006.07.001.

Jaffey, A.H., Flynn, K.F., Glendenin, L.E., Bentley, W.C., and Essling, A.M., 1971, Precision measurement of half-lives and specific activities of 235U and 38U: Physical Review C, v. 4, p. 1889-1906, doi: 10.1103/PhysRevC.4.1889.

Jagoutz, O., Müntener, O., Manatschal, G., Rubatto, D., Péron-Pinvidic, G., Turrin, B.D., and Villa, I.M., 2007, The rift-to-drift transition in the North Atlantic: A stuttering start of the MORB machine?: Geology, v. 35, p. 1087-1090, doi: 10.1130/G23613A.1.

Kelley, K.A., Kingsley, R., and Schilling, J.G., 2013, Composition of plume-influenced mid-ocean ridge lavas and glasses from the Mid-Atlantic Ridge, East Pacific Rise, Galapagos Spreading Center, and Gulf of Aden: Geochemistry, Geophysics, Geosystems, v. 14, p. 223-242, doi: 10.1029/2012GC004415.

Lemoine, M., Tricart, P., and Boillot, G., 1987, Ultramafic and gabbroic ocean floor of the Ligurian Tethys (Alps, Corsica, Apennines): in search of a genetic model: Geology, v. 15, p. 622-625, doi: 10.1130/0091-7613(1987)15<622:UAGOFO>2.0.CO;2.

Lavier, L.L., and Manatschal, G., 2006, A mechanism to thin the continental lithosphere at magma-poor margins: Nature, v. 440, p. 324-328, doi: 10.1038/nature04608.

Malinverno, A., Hildebrandt, J., Tominaga, M., and Channell, J.E.T., 2012, M-sequence geomagnetic polarity time scale (MHTC12) that steadies global spreading rates and incorporates astrochronology constraints: Journal of Geophysical Research, v. 117, B06104, doi: 10.1029/2012JB009260, 2012.

Manatschal, G., Froitzheim, N., Rubenach, M., and Turrin, B.D., 2001, The role of detachment faulting in the formation of an ocean-continent transition : insights from the Iberia

Abyssal Plain: Geological Society Special Publications, v. 187, p. 405-428, doi: 10.1144/GSL.SP.2001.187.01.20.

Manatschal, G., and Müntener, O., 2009, A type sequence across an ancient magma-poor ocean-continent transition: the example of the western Alpine Tethys ophiolites: Tectonophysics, v. 473, p. 4-19, doi: 10.1016/j.tecto.2008.07.021.

Mattinson, J.M., 2005, Zircon U-Pb chemical abrasion ("CA-TIMS") method: Combined annealing and multi-step partial dissolution analysis for improved precision and accuracy of zircon ages: Chemical Geology, v. 220, p. 47-66, doi: 10.1016/j.chemgeo.2005.03.011.

McLean, N.M., Bowring, J.F., and Bowring, S.A., 2011, An algorithm for U-Pb isotope dilution data reduction and uncertainty propagation: Geochemistry, Geophysics, Geosystems, v. 12, Q0AA19, doi: 10.1029/2010GC003478.

McLean, N.M., Condon, D.J., Condon, B., and Bowring, S.A., 2015, Evaluating uncertainties in the calibration of isotopic reference materials and multi-element isotopic tracers (EARTHTIME tracer calibration II): Geochimica et Cosmochimica, v. 164, p. 481-501, doi: 10.1016/j.gca.2015.02.040.

Minshull, T.A., Dean, S.M., and Whitmarsh, R.B., 2014, The peridotite ridge province in the southern Iberia Abyssal Plain: seismic constraints revisited: Journal of Geophysical Research: Solid Earth, v. 119, p. 1580-1598, doi:10.1002/2014JB011011.

Müntener, O., and Manatschal, G., 2006, High degrees of melt extraction recorded by spinel harzburgite of the Newfoundland margin: the role of inheritance and consequences for the evolution of the southern North Atlantic: Earth and Planetary Science Letters, v. 252, p. 437-452, doi: 10.1016/j.epsl.2006.10.009.

Mutter, J.C., Buck, W.R., and Zehnder, C.M., 1988, Convective partial melting I: a model for the formation of thick basaltic sequences during the initiation of spreading: Journal of Geophysical Research, v. 93, p. 1031-1048, doi: 10.1029/JB093iB02p01031.

Péron-Pinvidic, G., and Manatschal, G., 2009, The final rifting evolution at deep magma-poor passive margins from Iberia-Newfoundland: a new point of view: International Journal of Earth Science, v. 98, p. 1581-1597, doi: 10.1007/s00531-008-0337-9.

Pitman III, W.C., and Talwani, M., 1972, Sea-floor spreading in the North Atlantic: Geological Society of America Bulletin, v. 83, p. 619-646, doi: 10.1130/0016-7606(1972)83[619:SSITNA]2.0.CO;2.

Robertson, A.H.F., 2007, Evidence of continental breakup from the Newfoundland rifted margin (Ocean Drilling Program leg 210): lower Cretaceous seafloor formed by exhumation of subcontinental mantle lithosphere and the transition to seafloor spreading, *in*, Tucholke, B.E., Sibuet, J.C., and Klaus, A., eds., Proceedings of the Ocean Drilling Program, Scientific Results, v. 2010, p. 1-69, doi: 10.2973/odp.proc.sr.210.104.2007.

Scharer, U., Girardeau, J., Cornen, G., and Boillot, G., 2000, 138-121 Ma asthenospheric magmatism prior to continental break-up in the North Atlantic and geodynamic implications: Earth and Planetary Science Letters, v. 181, p. 555-572, doi: 10.1016/S0012-821X(00)00220-X.

Scharer, U., 1984, The effect of initial ^{230}Th disequilibrium on young U-Pb ages: the Makalu case, Himalaya: Earth and Planetary Science Letters, v. 67, p. 191-204, doi: 10.1016/0012-821X(84)90114-6.

Schoene, B., Latkoczy, C., Schaltegger, U., and Gunther, D., 2010, A new method integrating high-precision U-Pb geochronology with zircon trace element analysis (U-Pb TIMS-TEA): Geochimica et Cosmochimica Acta, v. 74, p. 7144-7159, doi: 10.1016/j.gca.2010.09.016.

Sibuet, J.C., Srivastava, S., and Manatschal, G., 2007, Exhumed mantle-forming transitional crust in the Newfoundland-Iberia rift and associated magnetic anomalies: Journal of Geophysical Research, v. 112, B06105, doi:10.1029/2005JB003856.

Shipboard Scientific Party, 1994, Site 897, *in* Sawyer, D.S., Whitmarsh, R.B., Klaus, A., et al. (eds.): Proceedings of the Ocean Drilling Program, Initial Reports, v. 149, p. 41-113, doi: 10.2973/odp.proc.ir.149.104.1994.

Shipboard Scientific Party, 1994, Site 899, *in* Sawyer, D.S., Whitmarsh, R.B., Klaus, A., et al. (eds.): Proceedings of the Ocean Drilling Program, Initial Reports, v. 149, p. 147-209, doi: 10.2973/odp.proc.ir.149.106.1994.

Shipboard Scientific Party, 1998, Site 1070, *in* Whitmarsh, R.B., Beslier, M.O., Wallace, P.J., et al. (eds.): Proceedings of the Ocean Drilling Program, Initial Reports, v. 173, p. 265-294, doi: 10.2973/odp.proc.ir.173.108.1998.

Shipboard Scientific Party, 2004, Site 1277, *in* Tucholke, B.E., Sibuet, J.-C., Klaus, A., et al., (eds.): Proceedings of the Ocean Drilling Program, Initial Reports, v. 210, p. 1–39, doi: 10.2973/odp.proc.ir.210.104.2004.

Soares, D.M., Alves, T.M., and Terrinha, P., 2012, The breakup sequence and associated lithospheric breakup surface: their significance in the context of rifted continental margins (West Iberia and Newfoundland margins, North Atlantic): Earth and Planetary Science Letters, v. 355-356, p. 311-326, doi: 10.1016/j.epsl.2012.08.036.

Soderlund, U., Patchett, P.J., Vervoort, J.D., and Isachsen, C.E., 2004, The 176Lu decay constant determined by Lu-Hf and U-Pb isotope systematics of Precambrian mafic intrusions: Earth and Planetary Science Letters, v. 219, p. 311-324, doi: 10.1016/S0012-821X(04)00012-3.

Srivastava, S.P., Sibuet, J.C., Cande, S., Roest, W.R., and Reid, I.D., 2000, Magnetic evidence for slow seafloor spreading during the formation of the Newfoundland and Iberian margins: Earth and Planetary Science Letters, v. 182, p. 61-76, doi: 10.1016/S0012-821X(00)00231-4.

Tucholke, B.E., Sawyer, D.S., and Sibuet, J.C., 2007, Breakup of the Newfoundland-Iberia rift, Geological Society of London Special Publcations, v. 282, p. 9-46, doi: 10.1144/SP282.2.

Van Avendonk, H.J.A., Holbrook, W.S., Nunes, G.T., Shillington, D.J., Tucholke, B.E., Louden, K.E., Larsen, H.C., and Hopper, J.R., 2006, Seismic velocity structure of the rifted margin of the eastern Grand Banks of Newfoundland, Canada: Journal of Geophysical Research, v. 111, B11404, doi: 10.1029/2005JB004156.

Vervoort, J.D., and Blichert-Toft, J., 1999, Evolution of the depleted mantle: Hf isotope evidence from juvenile rocks through time: Geochimica et Cosmochimica Acta, v. 63, p. 533-556, doi: 10.1016/S0016-7037(98)00274-9.

Vervoort, J.D., Patchett, P.J., Soderlund, U., and Baker, M., 2004, Isotopic composition of Yb and the determination of Lu concentratiosn and Lu/Hf ratios by isotope dilution using MC-ICPMs: Geochemistry, Geophysics, Geosystems, v. 5, Q11002, doi: 10.1029/2004GC000721.

Whitmarsh, R.B., Manatschal, G., and Minshull, T.A., 2001, Evolution of magma-poor continental margins from rifting to seafloor spreading: Nature, v. 413, p. 150-154, doi: 10.1038/35093085.

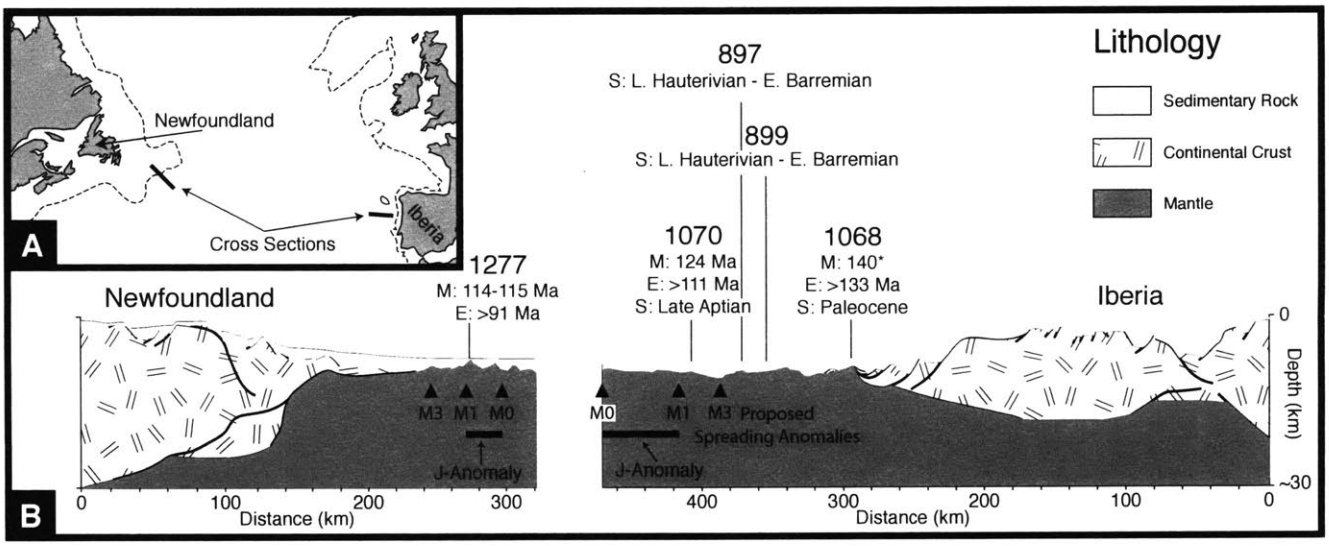

re 1: **(A)** Map of the north Atlantic showing the two studied transects. **(B)** Crustal sections modified from Péron-Pinvidic
). The transect along the Newfoundland margin is interpreted from the SCREECH 2 seismic refraction line (Van Avendon
) and the transect from the Iberian margin is a composite section interpreted from the IAM9, LG12, ISE1, and ISE17 lines
ion of ODP sites that sampled exhumed mantle are shown, as well as the location of magnetic anomalies. The ages of mag
exhumation (E), and the first sediments (S) overlying exhumed mantle are shown and represent U-Pb zircon dates or $^{40}Ar/$
ibole dates (M), the oldest $^{40}Ar/^{39}Ar$ plagioclase date at each site (E), and biostratigraphic ages (S) (Table A1). *It is uncle
ner the $^{40}Ar/^{39}Ar$ amphibole date at site 1068 represents magma emplacement or cooling of pre-rift gabbro during exhumat

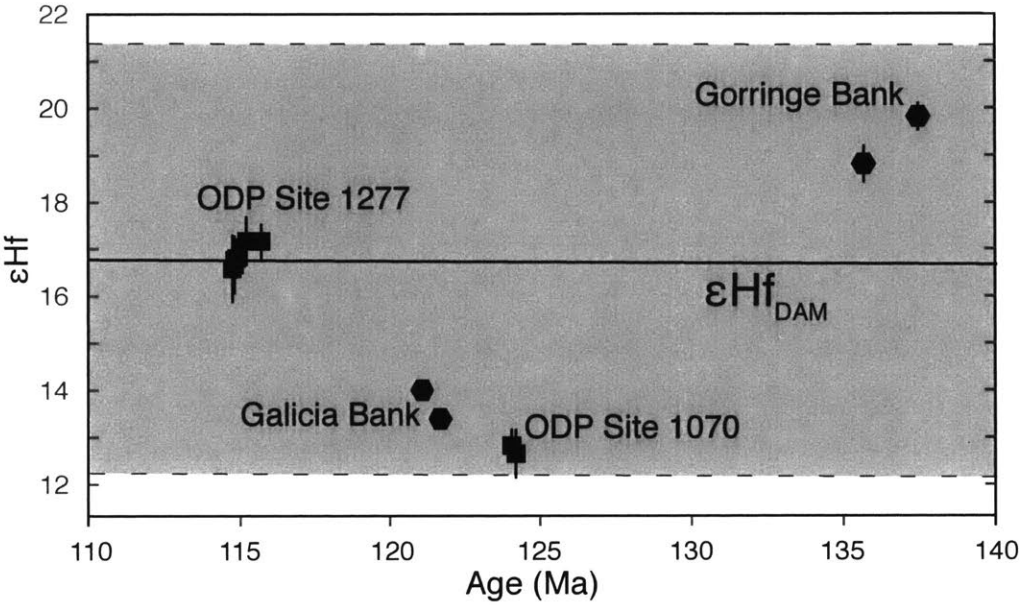

Figure 2: $\varepsilon Hf_{(t)}$ data for gabbros that intrude the Iberian-Newfoundland conjugate margins including samples reported in Scharer et al. (2000) from the Galicia Margin and Gorringe Bank, which are north and south of the Iberian transect, respectively. All $\varepsilon Hf_{(t)}$ data was calculated using the values for the chondritic uniform reservoir (CHUR) presented in Bouvier et al. (2008). The heavy black line labeled εHf_{DAM} and surrounding shaded region represents the εHf of depleted mantle under this part of the north Atlantic and its 2σ variability (see Appendix D for further explanation).

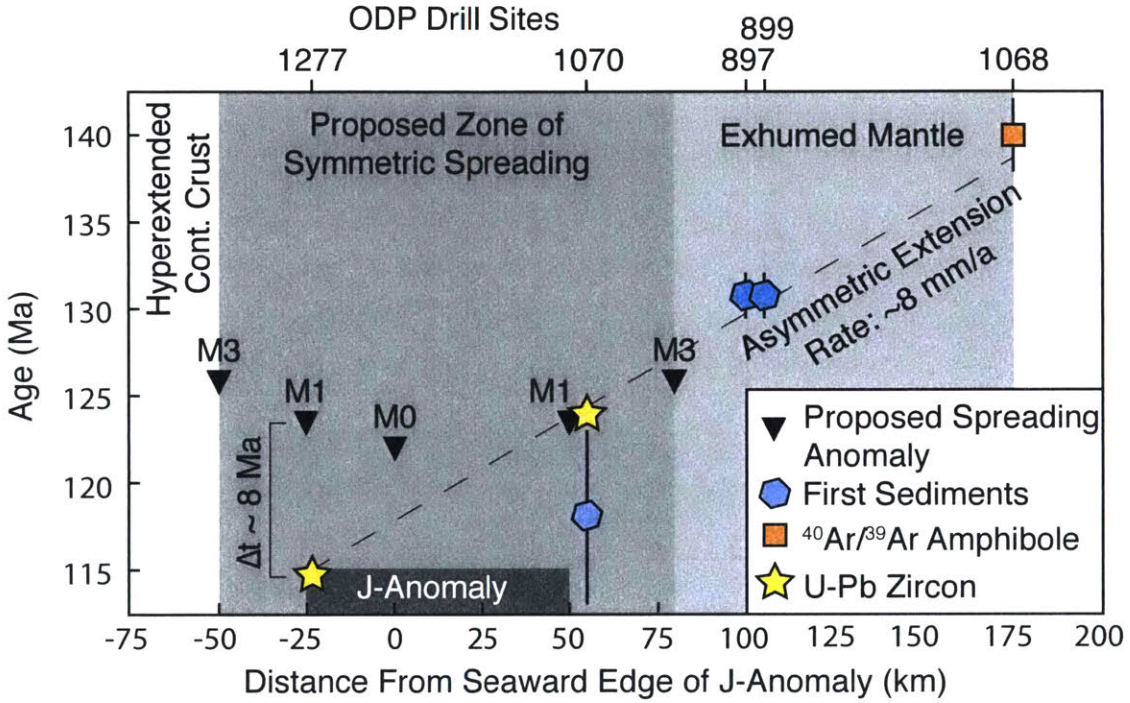

Figure 3: U-Pb geochronology, $^{40}Ar/^{39}Ar$ amphibole dates, and the biostratigraphic age of the first sediments overlying exhumed mantle relative to the seaward limit of the J-anomaly, which Srivastava et al. (2000) identified as anomaly M0. For ODP sites 1277 and 1070, we only show the U-Pb data presented in this paper as it more precise than the previous data from these sites (Table A1). The expected age of each site according to interpretations of magnetic data is also shown.

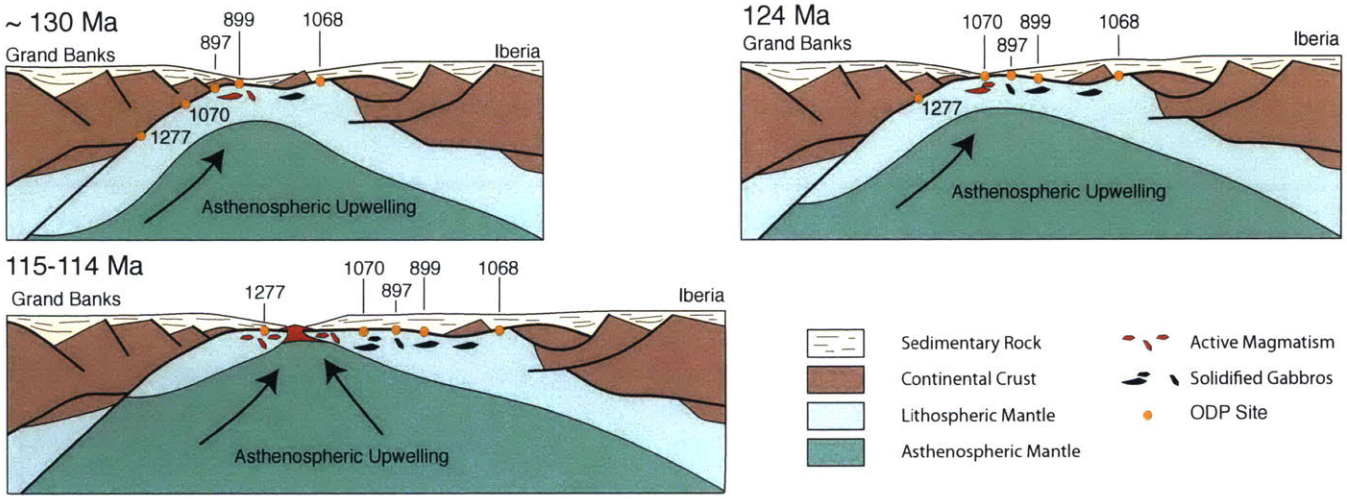

Figure 4: Cartoon of proposed tectonic evolution modified from Péron-Pinvidic et al. (2009). **(A)** Following separation of continental crust, lithospheric mantle is exhumed along a westward dipping detachment system and is accompanied by decompression melting of the asthenospheric mantle. **(B)** Extension along the lithospheric-scale detachment system results in continued mantle exhumation and a record of mantle exhumation and magmatism that is time-transgressive from east to west. **(C)** Final separation of lithospheric mantle occurs ~115 Ma near the point where lithospheric mantle is exhumed to the seafloor and leads to the formation of an oceanic spreading center. The exhumed lithospheric mantle at ODP site 1277 is stranded on the Newfoundland margin during this process.

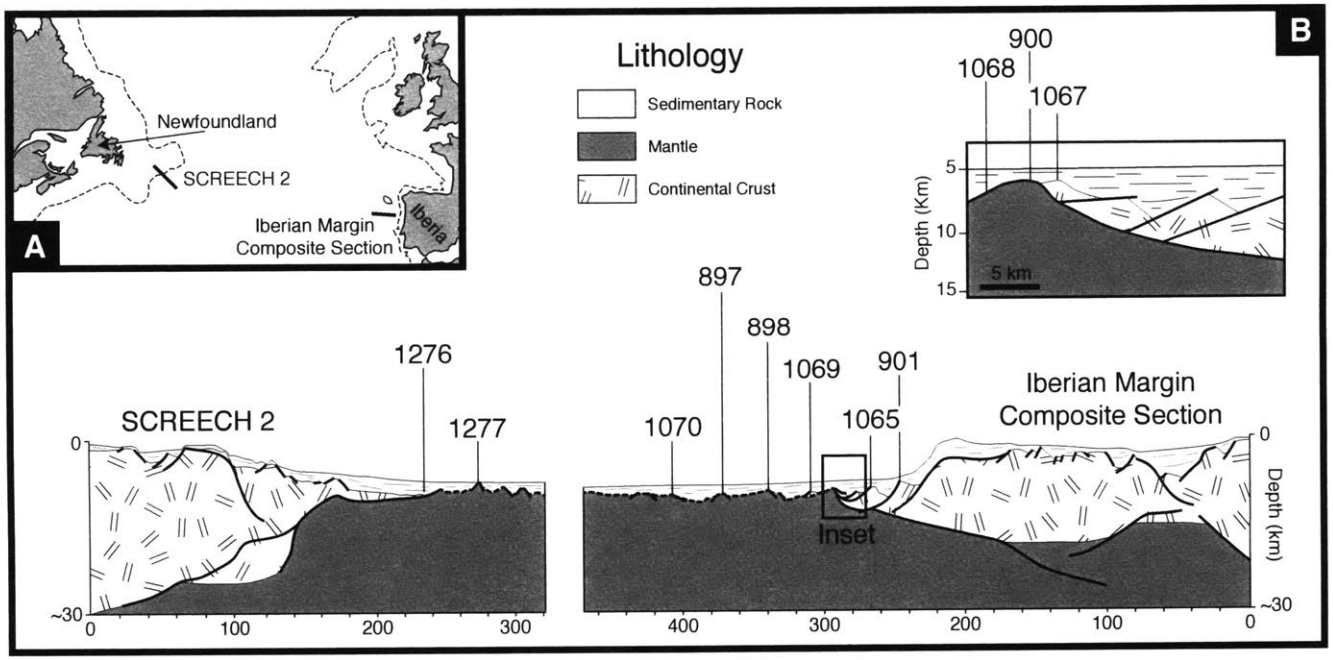

Figure A1: (A) Location of studied transects. **(B)** Cross-sections of the two transects modified from Peron-Pinvidic et al. (2009) and Manatschal et al. (2001). The locations of all ODP drill sites that penetrated basement are shown. ODP site 1276 did not reach basement, but is also shown because it penetrated Cretaceous basaltic sills.

ODP Leg 210 Site 1277

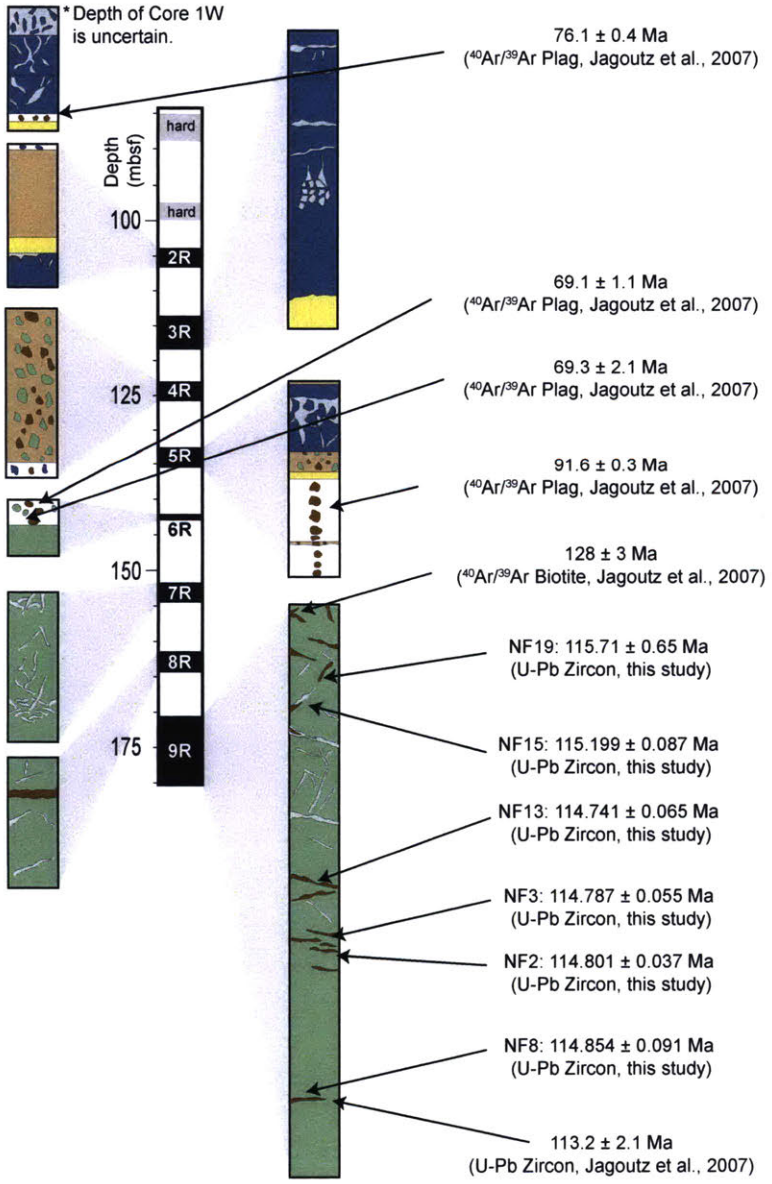

ODP Leg 173 Site 1070

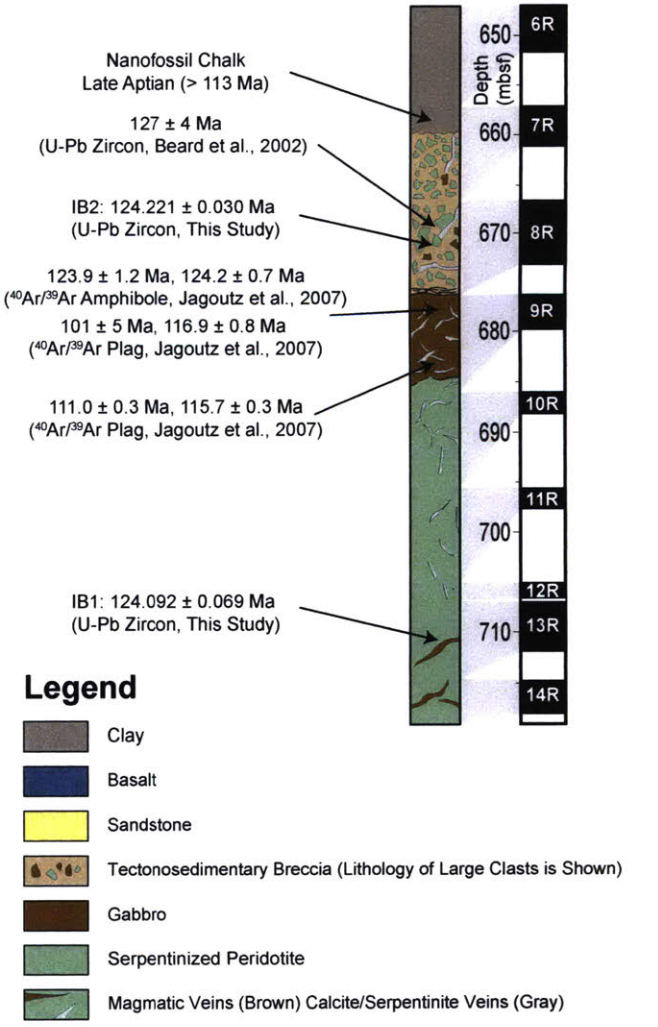

Figure A2 (*on previous page*)**:** Core recovery and lithology from ODP sites 1070 and 1277 modified from Shipboard Scientific Party (2004) and Jagoutz et al. (2007). The locations of $^{40}Ar/^{39}Ar$ and U-Pb dates (Tables 1 and A1) from these two cores are also shown. Only analytical uncertainties are reported for samples dated as part of this study.

Figure A3: Traditional concordia plots for each dates sample.

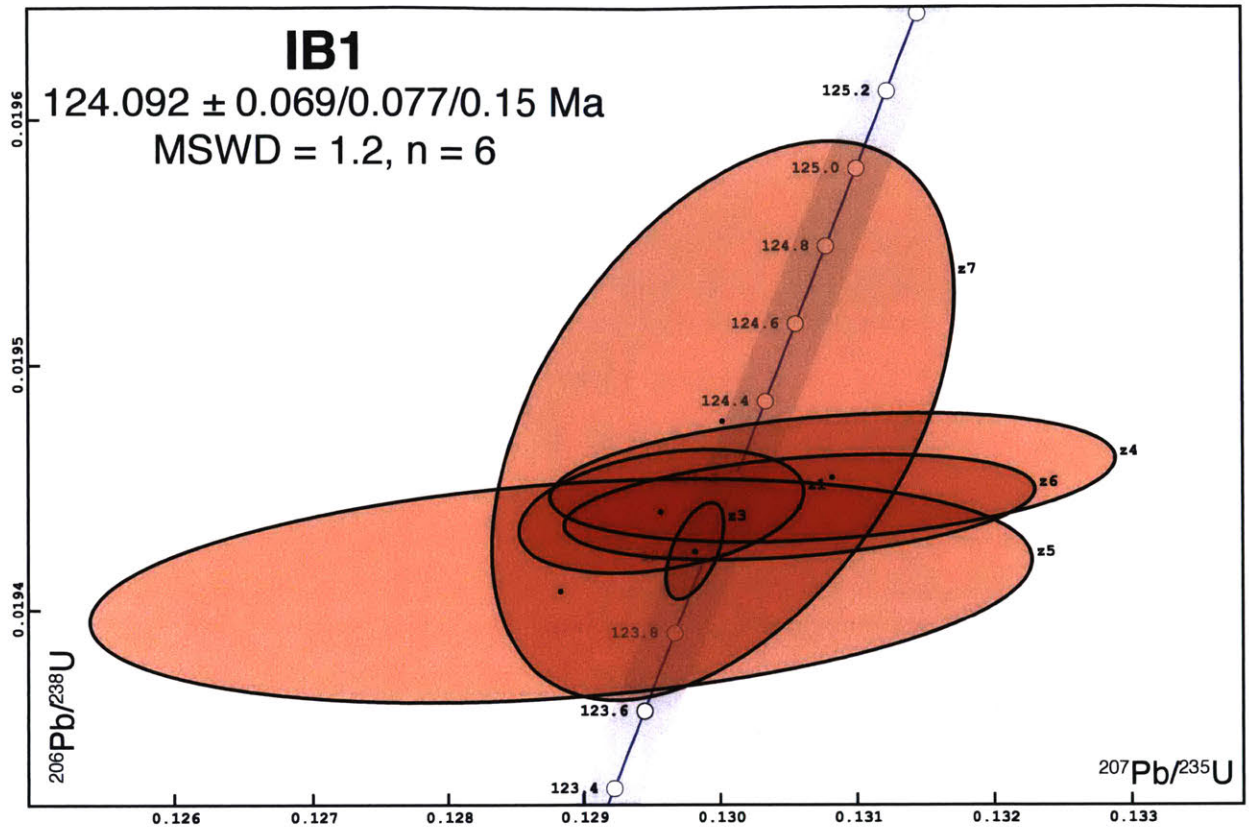

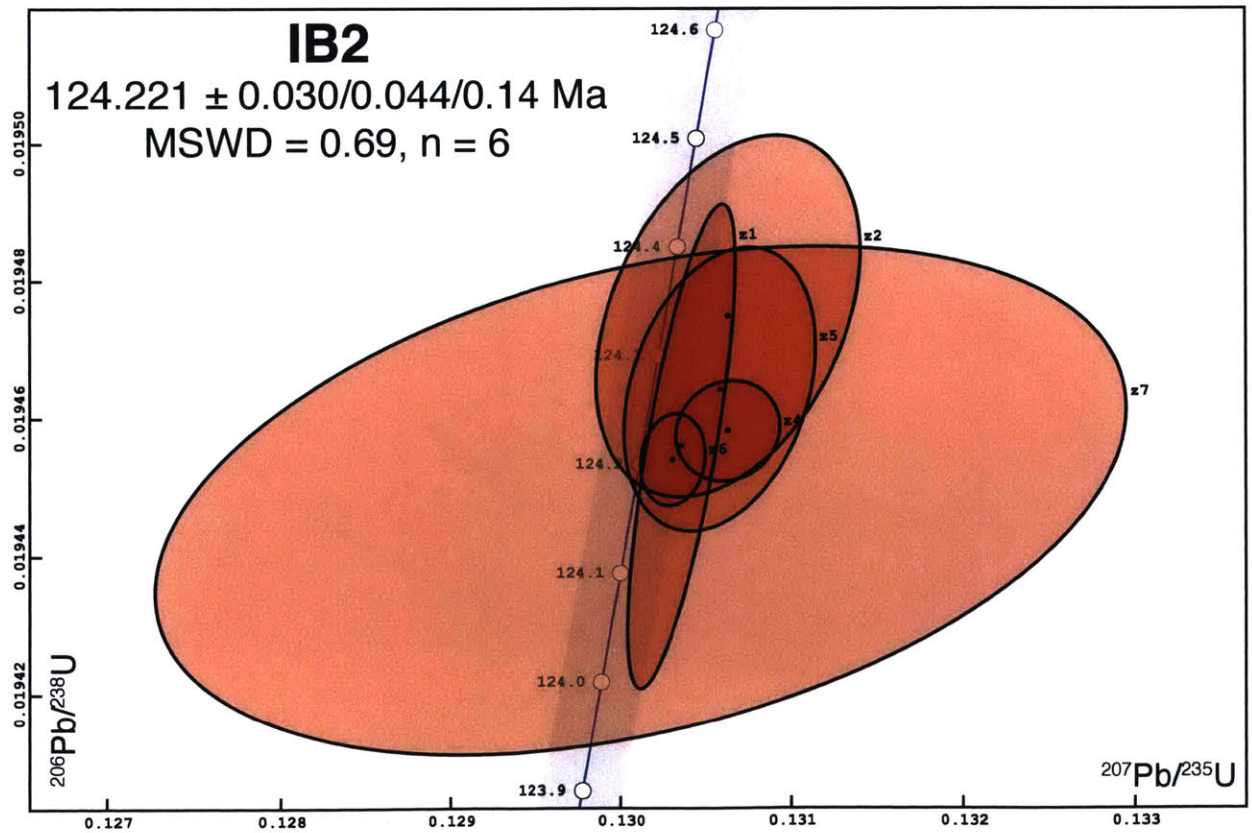

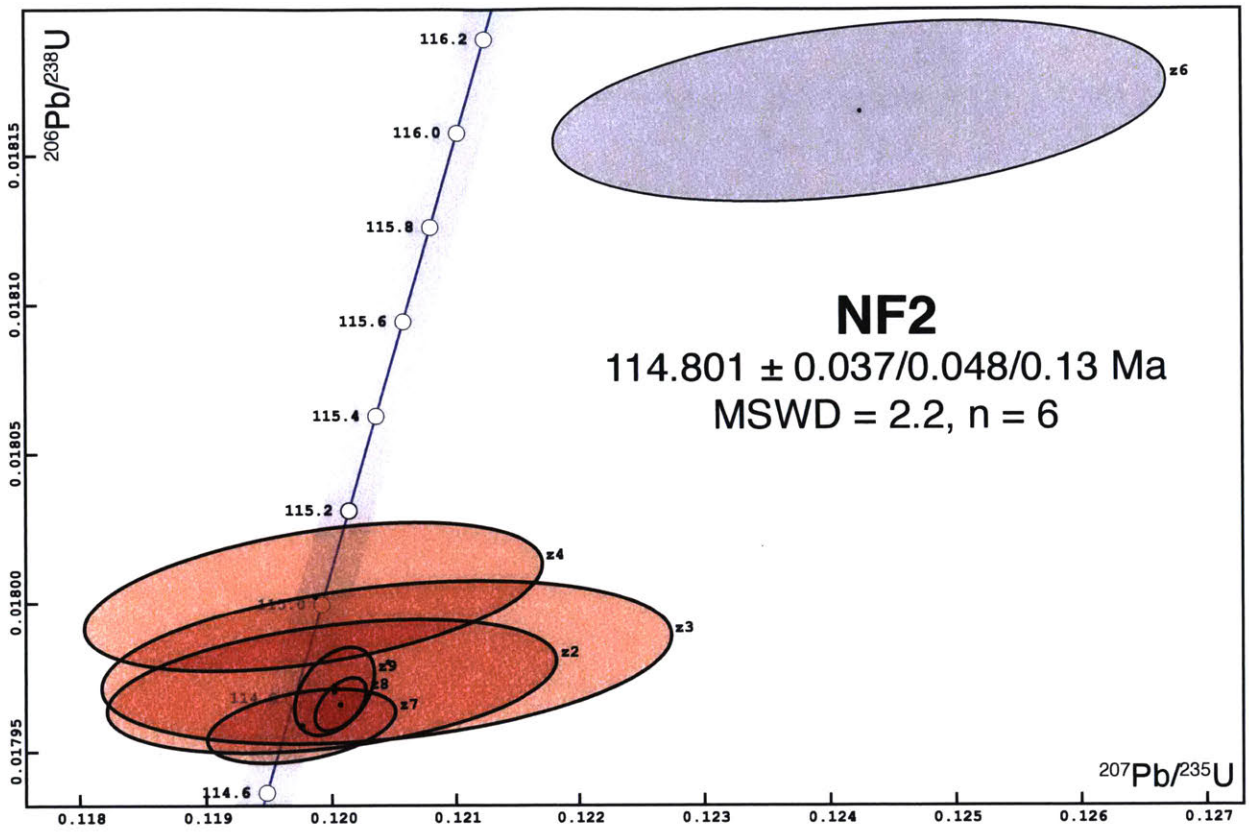
NF2
114.801 ± 0.037/0.048/0.13 Ma
MSWD = 2.2, n = 6
$^{206}Pb/^{238}U$
$^{207}Pb/^{235}U$
116.2
116.0
115.8
115.6
115.4
115.2
114.6
z6
z4
z3
z2
z9
z8
z7
0.01815
0.01810
0.01805
0.01800
0.01795
0.118
0.119
0.120
0.121
0.122
0.123
0.124
0.125
0.126
0.127

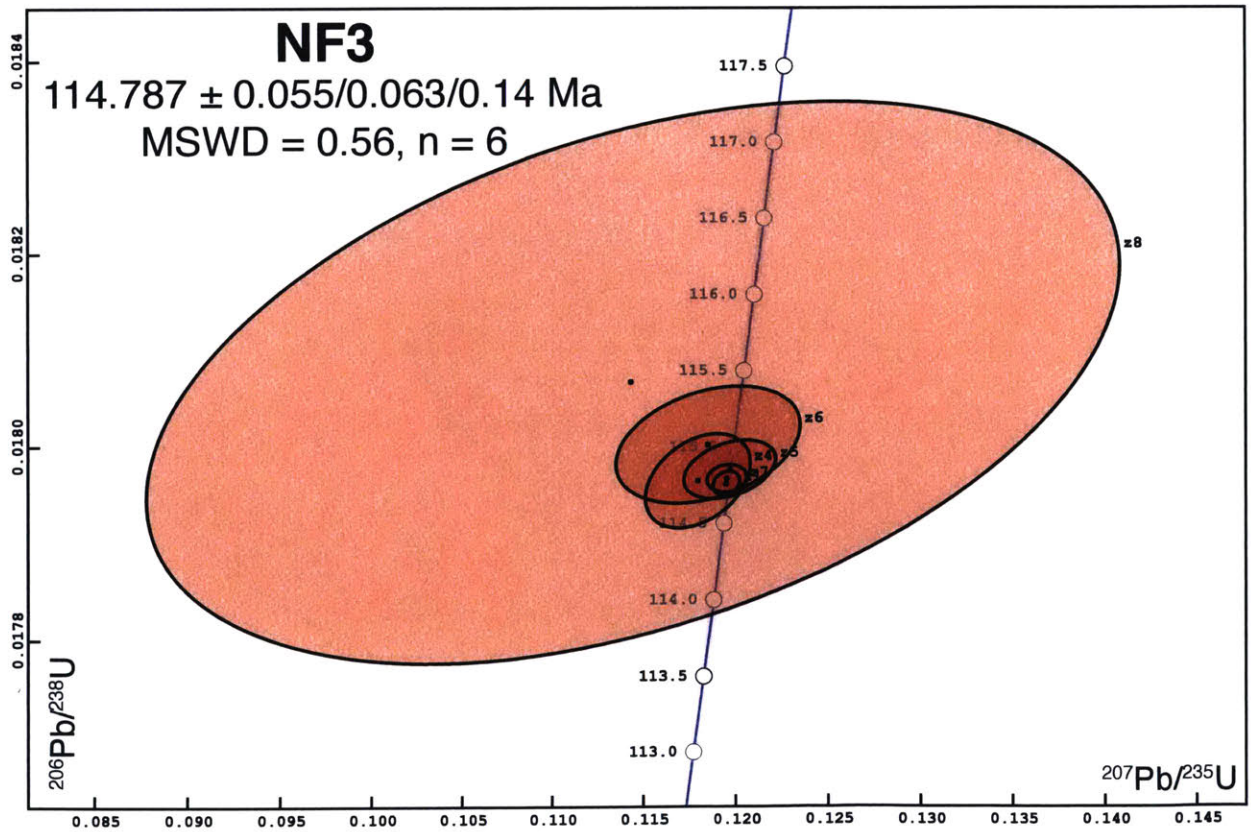
NF3
114.787 ± 0.055/0.063/0.14 Ma
MSWD = 0.56, n = 6
$^{206}Pb/^{238}U$
$^{207}Pb/^{235}U$
117.5
117.0
116.5
116.0
115.5
114.0
113.5
113.0
z8
z6
0.0184
0.0182
0.0180
0.0178
0.085
0.090
0.095
0.100
0.105
0.110
0.115
0.120
0.125
0.130
0.135
0.140
0.145

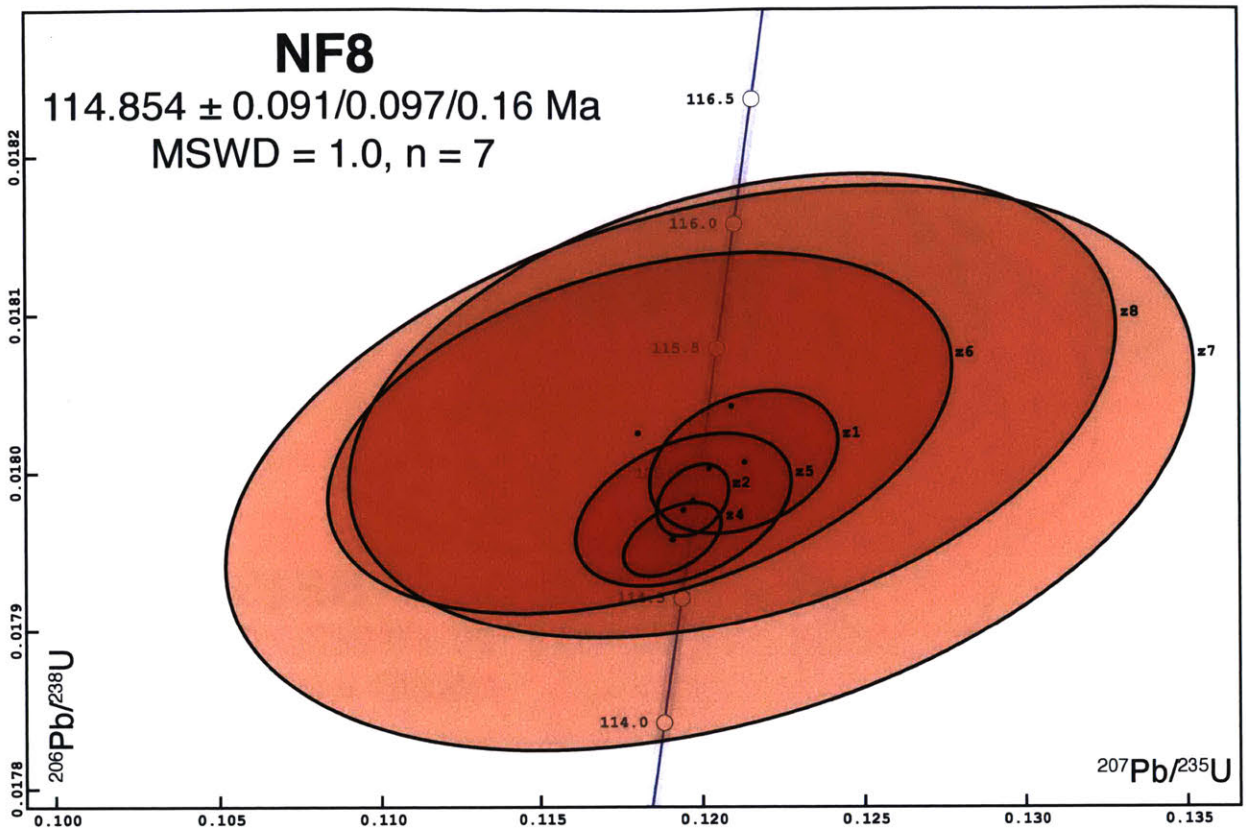
NF8
114.854 ± 0.091/0.097/0.16 Ma
MSWD = 1.0, n = 7
116.5
116.0
115.5
114.0
z8
z7
z6
z1
z5
z2
z4
0.0182
0.0181
0.0180
0.0179
0.0178
206Pb/238U
0.100
0.105
0.110
0.115
0.120
0.125
0.130
0.135
207Pb/235U

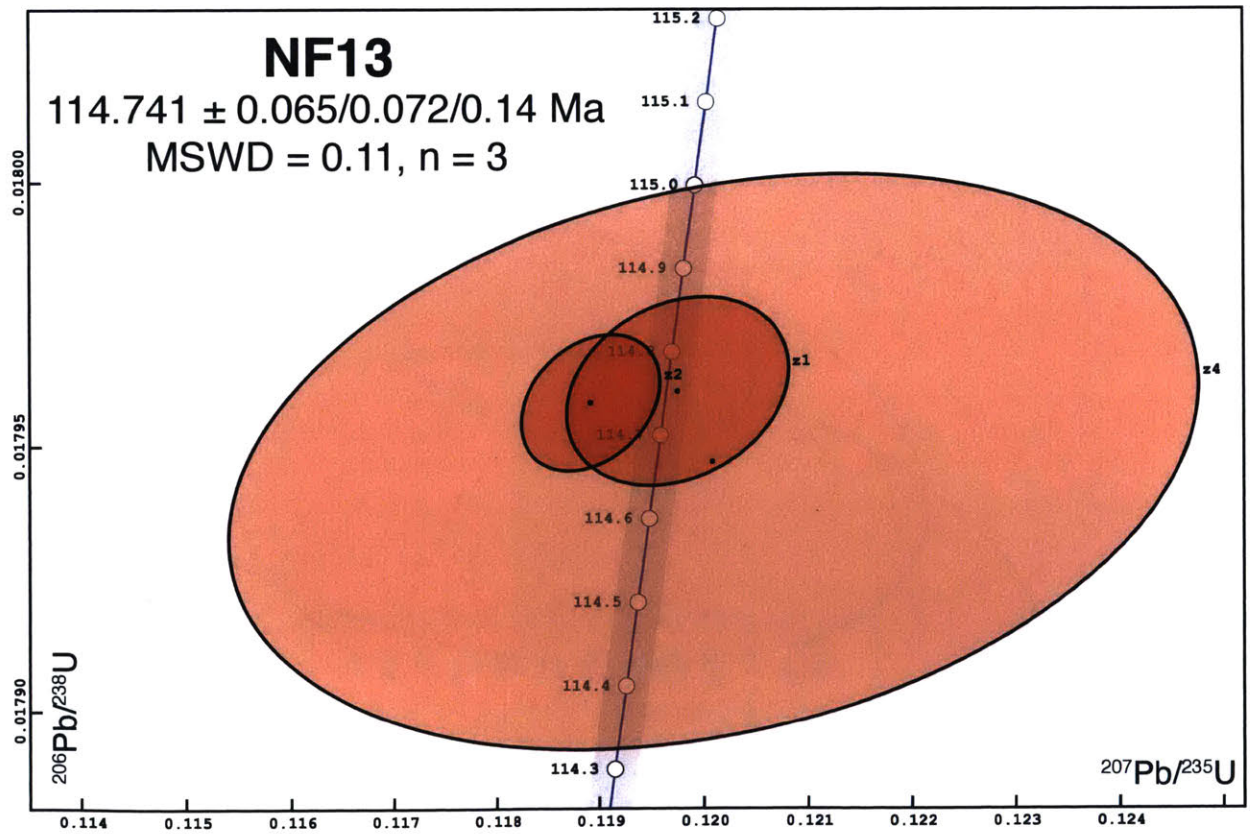
NF13
114.741 ± 0.065/0.072/0.14 Ma
MSWD = 0.11, n = 3
115.2
115.1
115.0
114.9
114.6
114.5
114.4
114.3
z1
z2
z4
0.01800
0.01795
0.01790
206Pb/238U
0.114
0.115
0.116
0.117
0.118
0.119
0.120
0.121
0.122
0.123
0.124
207Pb/235U

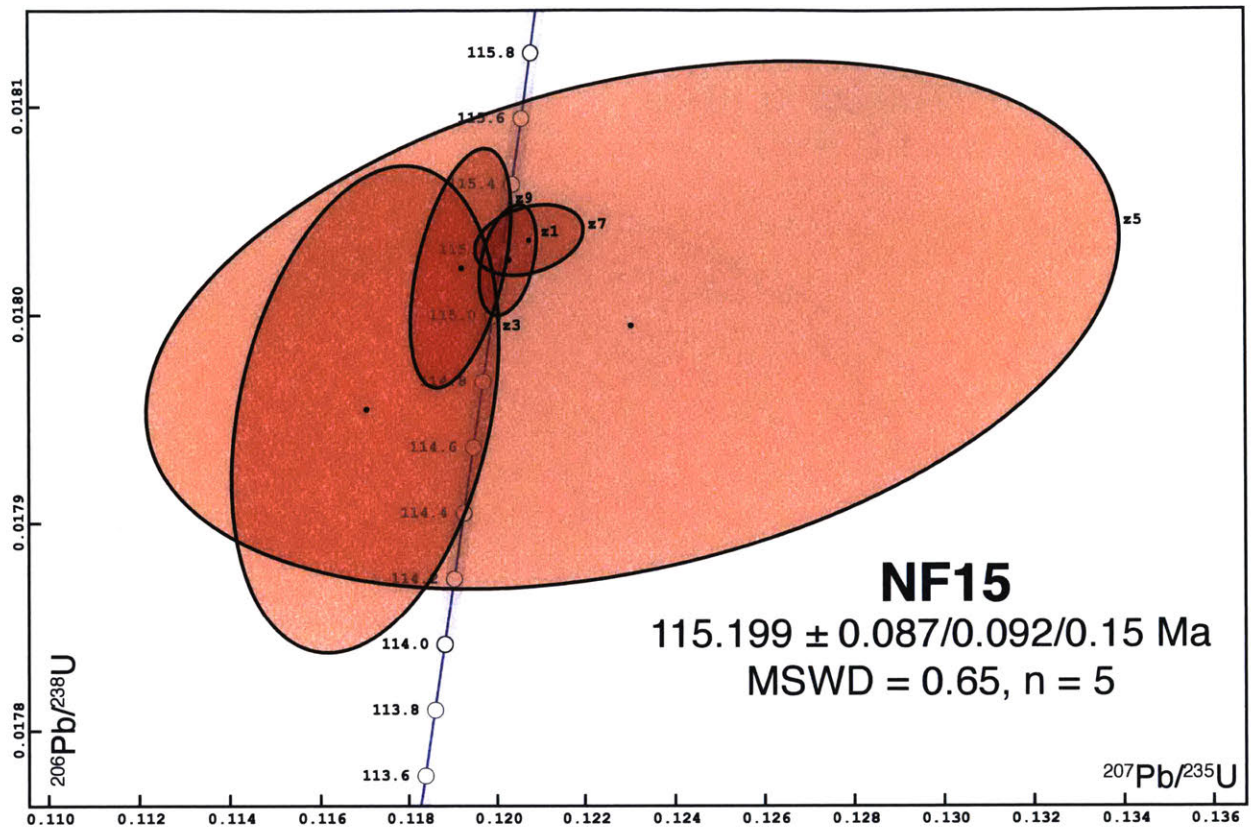
NF15
115.199 ± 0.087/0.092/0.15 Ma
MSWD = 0.65, n = 5
z1
z3
z5
z7
z9
115.8
115.6
115.4
115.0
114.6
114.4
114.2
114.0
113.8
113.6
0.0181
0.0180
0.0179
0.0178
0.110
0.112
0.114
0.116
0.118
0.120
0.122
0.124
0.126
0.128
0.130
0.132
0.134
0.136
206Pb/238U
207Pb/235U

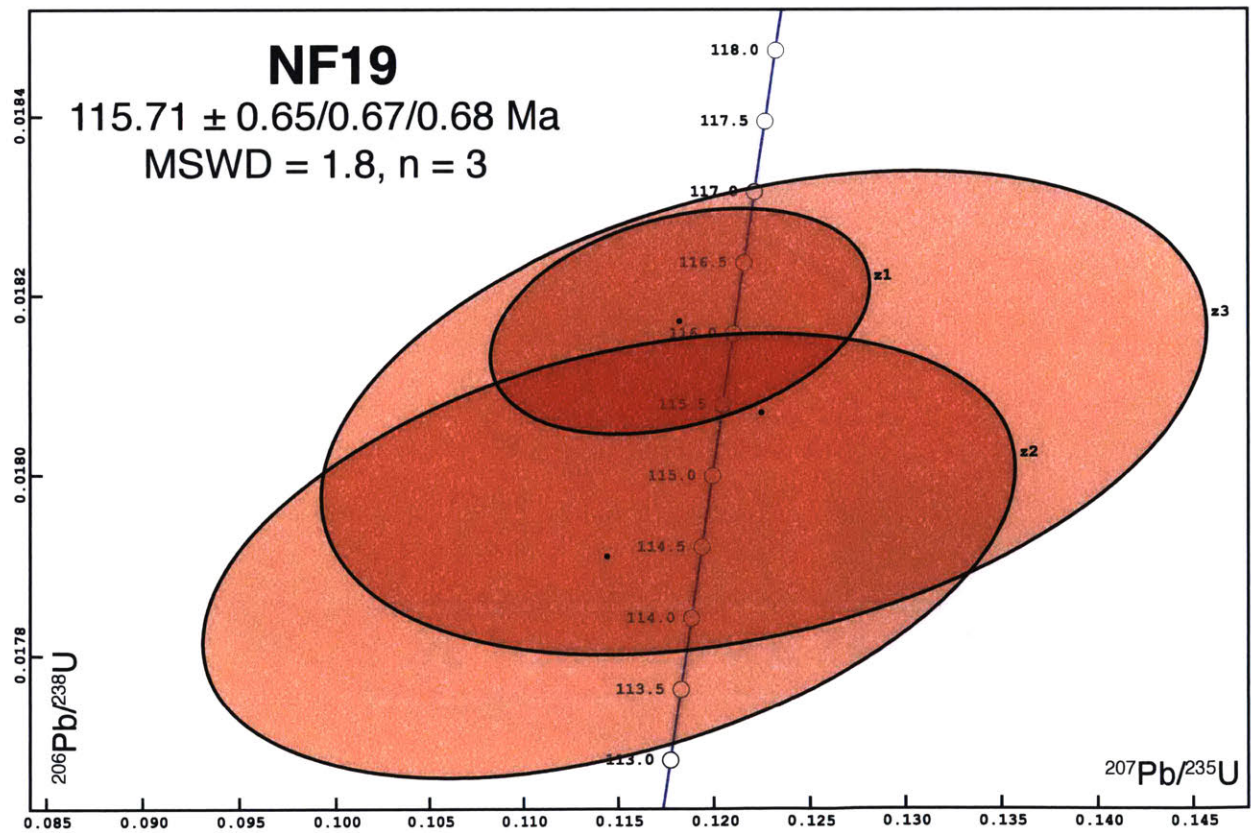
NF19
115.71 ± 0.65/0.67/0.68 Ma
MSWD = 1.8, n = 3
z1
z2
z3
118.0
117.5
117.0
116.5
116.0
115.5
115.0
114.5
114.0
113.5
113.0
0.0184
0.0182
0.0180
0.0178
0.085
0.090
0.095
0.100
0.105
0.110
0.115
0.120
0.125
0.130
0.135
0.140
0.145
206Pb/238U
207Pb/235U

Table 1: U-Pb Zircon Geochronology and Hf Results

Sample*		$^{206}Pb/^{238}U$ Date (Ma)†, §	$\varepsilon Hf_{(t)}$ #
IB1	M	124.092 ± 0.069/0.077/0.15 (MSWD=1.2, n=6)	12.80 ± 0.28
IB2	A	124.221 ± 0.030/0.044/0.14 (MSWD=0.7, n=6)	12.63 ± 0.49
NF2	A	114.801 ± 0.037/0.048/0.13 (MSWD=2.2, n=6)	16.74 ± 0.42
NF3	M	114.787 ± 0.055/0.063/0.14 (MSWD=0.6, n=6)	16.65 ± 0.60
NF8	M	114.854 ± 0.091/0.097/0.16 (MSWD=1.0, n=7)	16.81 ± 0.43
NF13	A	114.741 ± 0.065/0.072/0.14 (MSWD=0.1, n=3)	16.56 ± 0.70
NF15	M	115.199 ± 0.087/0.092/0.15 (MSWD=0.7, n=5)	17.12 ± 0.52
NF19	M	115.710 ± 0.650/0.670/0.68 (MSWD=1.8, n=3)	17.15 ± 0.35

* Sample locations within each core are provided in the Data Repository. Sample prefix IB represents samples from ODP site 1070 on the Iberian margin and NF represents samples from ODP site 1277 off of Newfoundland. M indicates MORB-like lithologies and A indicates alkaline lithologies.

† Corrected for initial secular disequilibrium using $[Th/U]_{Magma} = 3.2 \pm 1$.

§ Uncertainties are reported in the format ±X/Y/Z where X is the analytical uncertainty, Y includes uncertainty in the EARTHTIME ^{205}Pb-^{235}U-^{238}U isotopic tracer, and Z includes uncertainty in the ^{238}U decay constant.

Reported uncertainty is 2σ.

Table A1: Previous Geo- and Thermochronology

ODP Site	Lithology	Mineral	$^{40}Ar/^{39}Ar$ Date (Ma)	2σ (Ma)	U-Pb Date (Ma)	2σ (Ma)	Reference
1067	Amphibolite	Amphibole	160.5	0.8	-	-	Jagoutz et al. (2007)
1067	Amphibolite	Amphibole	152.6	0.9	-	-	Jagoutz et al. (2007)
1067	Amphibolite	Plagioclase	141.8	0.4	-	-	Jagoutz et al. (2007)
1067	Amphibolite	Amphibole	164.6	0.5	-	-	Jagoutz et al. (2007)
1067	Amphibolite	Amphibole	167.3	0.9	-	-	Jagoutz et al. (2007)
1067	Amphibolite	Zircon	-	-	246.0	5.0	Gardien and Paquette (2004)
900	Gabbro	Plagioclase	136.4	0.6	-	-	Feraud et al. (1996)
1068	Gabbro	Plagioclase	133.1	0.3	-	-	Jagoutz et al. (2007)
1068	Gabbro	Amphibole	131.7	1.1	-	-	Jagoutz et al. (2007)
1068	Gabbro	Amphibole	140.0	2.0	-	-	Jagoutz et al. (2007)
1069	Schist	Muscovite	361.5	0.5	-	-	Jagoutz et al. (2007)
1070	Gabbro	Plagioclase	115.7	0.3	-	-	Jagoutz et al. (2007)
1070	Gabbro	Plagioclase	111.0	0.3	-	-	Jagoutz et al. (2007)
1070	Gabbro	Plagioclase	116.9	0.8	-	-	Jagoutz et al. (2007)
1070	Gabbro	Amphibole	123.9	1.2	-	-	Jagoutz et al. (2007)
1070	Gabbroic Clast	Zircon	-	-	127.0	4.0	Beard et al. (2002)
1277	Gabbro	Zircon	-	-	113.2	2.1	Jagoutz et al. (2007)
1277	Gabbro	Biotite	128.0	3.0	-	-	Jagoutz et al. (2007)
1277	Gabbroic Clast	Plagioclase	69.3	2.1	-	-	Jagoutz et al. (2007)
1277	Gabbroic Clast	Plagioclase	69.1	1.1	-	-	Jagoutz et al. (2007)
1277	Gabbroic Clast	Plagioclase	91.6	0.3	-	-	Jagoutz et al. (2007)
1277	Gabbroic Clast	Plagioclase	76.1	0.4	-	-	Jagoutz et al. (2007)
1276	Basaltic Sill	Whole Rock	104.7	1.7	-	-	Hart and Blujstein (2006)
1276	Basaltic Sill	Whole Rock	105.9	1.8	-	-	Hart and Blujstein (2006)
1276	Basaltic Sill	Whole Rock	99.7	1.8	-	-	Hart and Blujstein (2006)
1276	Basaltic Sill	Whole Rock	95.9	2.0	-	-	Hart and Blujstein (2006)

Table A2: CA-ID-TIMS U-Pb Zircon Geochronology Results

Frac.	Dates $^{206}Pb/^{238}U^{*}$	2σ abs.	$^{207}Pb/^{235}U^{\dagger}$	2σ abs.	$^{207}Pb/^{206}Pb^{*,\dagger}$	2σ abs.	% Disc.[§]	Corr. Coef.	Composition Th/U[#]	Pb_c (pg)[**]	Pb^{*}/Pb_c[††]	Isotopic Ratios $^{206}Pb/^{204}Pb$[§§]	$^{208}Pb/^{206}Pb$[##]	$^{206}Pb/^{238}U^{*,\#\#}$	2σ %	$^{207}Pb/^{235}U^{\#\#}$	2σ %	$^{207}Pb/^{206}Pb^{*,\#\#}$	2σ %
IB1 (13R-4 36-42)																			
z1	124.12	0.16	123.71	0.94	116	18	-5.55	0.320	0.79	0.31	31	1734	0.252	0.019440	0.13	0.1296	0.81	0.048362	0.77
z3	124.01	0.12	123.93	0.19	122.4	3.2	0.03	0.564	0.76	0.36	184	10273	0.243	0.019424	0.10	0.12982	0.16	0.048494	0.13
z4	124.20	0.17	124.8	1.9	137	36	10.40	0.302	0.67	1.48	14	793	0.214	0.019454	0.14	0.1308	1.6	0.048795	1.5
z5	123.91	0.29	123.0	3.1	106	62	-14.75	0.279	0.96	0.45	10	530	0.306	0.019407	0.24	0.1288	2.7	0.048168	2.6
z6	124.13	0.14	124.6	1.5	134	30	8.48	0.344	0.86	0.59	18	973	0.274	0.019442	0.11	0.1306	1.3	0.048735	1.3
z7	124.35	0.72	124.1	1.5	120	27	-2.57	0.462	0.88	0.42	24	1298	0.281	0.019477	0.59	0.1300	1.3	0.048438	1.2
IB2 (8R-4 11-17)																			
z1	124.22	0.22	124.42	0.28	128.3	3.7	4.43	0.761	0.79	0.45	175	9662	0.252	0.019456	0.18	0.13036	0.24	0.048617	0.15
z2	124.33	0.17	124.67	0.69	131	13	6.23	0.366	0.79	0.38	47	2607	0.252	0.019475	0.14	0.13063	0.59	0.048671	0.56
z4	124.230	0.046	124.66	0.27	133.0	5.4	7.77	0.101	0.62	0.36	115	6633	0.198	0.019458	0.038	0.13063	0.23	0.048713	0.23
z5	124.27	0.13	124.62	0.50	131.4	9.7	6.58	0.305	0.78	0.30	58	3209	0.249	0.019464	0.11	0.13058	0.43	0.048680	0.41
z6	124.203	0.043	124.37	0.17	127.7	3.4	3.99	0.120	0.69	0.40	176	10006	0.218	0.019454	0.035	0.13031	0.15	0.048603	0.14
z7	124.17	0.23	124.2	2.5	125	50	1.90	0.364	0.68	0.58	10	614	0.216	0.019448	0.19	0.1301	2.2	0.048545	2.1
NF2 (9R-5 50-56)																			
z2	114.83	0.14	115.1	1.6	120	34	6.20	0.382	0.58	0.43	15	905	0.186	0.017972	0.12	0.1200	1.5	0.048455	1.5
z3	114.88	0.17	115.5	2.1	128	44	11.73	0.323	0.33	0.55	11	712	0.105	0.017980	0.15	0.1205	1.9	0.048611	1.9
z4	115.02	0.16	115.0	1.7	114	35	0.62	0.438	0.42	0.29	14	895	0.132	0.018002	0.14	0.1199	1.5	0.048316	1.5
z6	116.05	0.19	118.9	2.2	177	45	35.09	0.340	0.37	0.44	10	650	0.118	0.018165	0.17	0.1242	2.0	0.049631	1.9
z7	114.741	0.079	114.85	0.68	117	14	3.75	0.387	0.42	0.59	36	2189	0.132	0.017959	0.069	0.11976	0.63	0.048387	0.60
z8	114.788	0.056	115.13	0.19	122.3	3.6	7.82	0.507	0.15	0.29	149	9813	0.046	0.017966	0.049	0.12007	0.17	0.048492	0.15
z9	114.815	0.093	115.09	0.29	120.8	5.8	6.59	0.406	0.31	1.01	80	5064	0.098	0.017970	0.082	0.12002	0.27	0.048462	0.24
NF3 (9R-5 26-33)																			
z1	114.761	0.079	114.62	0.67	112	14	-0.89	0.232	0.43	0.37	35	2152	0.136	0.017962	0.069	0.11950	0.62	0.048275	0.60
z4	114.78	0.31	113.2	2.6	81	55	-39.11	0.372	0.63	0.46	10	595	0.200	0.017964	0.27	0.1180	2.4	0.047646	2.3
z5	114.85	0.19	114.8	2.3	113	48	0.46	0.365	0.57	0.51	11	652	0.182	0.017976	0.17	0.1197	2.1	0.048311	2.0
z6	115.01	0.38	113.7	4.5	87	98	-29.61	0.339	0.52	0.32	5	320	0.167	0.018002	0.34	0.1185	4.2	0.047770	4.1
z7	114.793	0.090	114.65	0.98	112	21	-1.01	0.128	0.58	0.35	25	1489	0.184	0.017967	0.079	0.1195	0.90	0.048276	0.89
z8	115.4	1.8	110	24	-8	540	2078.78	0.418	0.40	0.28	1	81	0.127	0.018067	1.6	0.114	23	0.045917	23
NF8 (9R-7 45-50)																			
z1	115.05	0.29	116.2	2.6	141	55	19.43	0.309	0.52	0.32	9	565	0.166	0.018007	0.25	0.1213	2.4	0.048876	2.3
z2	114.89	0.14	114.8	1.0	113	21	0.26	0.323	0.47	0.30	24	1476	0.150	0.017983	0.13	0.1197	0.93	0.048306	0.90
z4	114.74	0.15	114.2	1.4	104	29	-8.42	0.472	0.48	0.36	19	1144	0.153	0.017958	0.13	0.1191	1.3	0.048115	1.2
z5	114.86	0.31	114.6	3.0	108	64	-4.21	0.387	0.49	0.42	8	489	0.157	0.017977	0.27	0.1194	2.8	0.048204	2.7
z6	115.16	0.72	113.3	8.8	74	190	-51.26	0.371	0.48	0.35	3	180	0.153	0.018025	0.63	0.1180	8.2	0.047516	8.0
z7	115.0	1.1	115	14	120	290	5.96	0.347	0.46	1.49	2	119	0.147	0.018003	0.99	0.120	12	0.048452	12
z8	115.27	0.93	116	11	129	230	11.83	0.339	0.48	0.98	2	148	0.153	0.018042	0.81	0.121	9.9	0.048626	9.6
NF13 (9R-4 56-64)																			
z1	114.75	0.11	114.85	0.96	117	20	3.56	0.246	0.24	0.36	23	1500	0.076	0.017960	0.099	0.1198	0.89	0.048380	0.87
z2	114.739	0.082	114.09	0.61	101	13	-11.78	0.305	0.31	0.59	38	2424	0.099	0.017958	0.072	0.11892	0.56	0.048047	0.54
z4	114.67	0.34	115.1	4.2	125	90	9.83	0.271	0.38	0.58	6	389	0.122	0.017947	0.30	0.1201	3.9	0.048550	3.8
NF15 (9R-2 11-17)																			
z1	115.17	0.17	115.32	0.60	118	12	4.38	0.380	0.51	0.38	69	4136	0.163	0.018026	0.15	0.12028	0.55	0.048414	0.51
z3	114.71	0.74	112.4	2.7	63	59	-75.60	0.294	0.64	1.07	10	571	0.205	0.017954	0.65	0.1170	2.6	0.047303	2.5
z5	114.97	0.80	117.8	9.8	176	200	35.32	0.335	0.46	1.14	2	156	0.147	0.017995	0.70	0.123	8.8	0.049611	8.6
z7	115.23	0.11	115.8	1.1	127	23	10.30	0.297	0.59	0.82	21	1238	0.188	0.018036	0.094	0.1208	1.0	0.048580	1.0

z9	115.14	0.36	114.3	1.0	98	20	-15.83	0.481	0.88	0.69	43	2354	0.280	0.018022	0.32	0.1192	0.96	0.047990	0.85
NF19 (9R-1 146-148)																			
z1	116.09	0.79	113.4	9.0	58	200	-94.21	0.323	0.57	0.33	3	172	0.180	0.018171	0.69	0.118	8.4	0.047192	8.2
z2	114.4	1.6	110	19	15	440	-588.85	0.392	0.51	0.35	1	96	0.164	0.017911	1.4	0.114	19	0.046348	18
z3	115.4	1.7	117	21	155	430	26.72	0.351	0.32	0.37	1	84	0.101	0.018070	1.5	0.122	19	0.049182	19

* Corrected for initial Th/U disequilibrium using radiogenic ^{208}Pb and $Th/U_{[Magma]} = 3.2 \pm 1$ (2σ) from the Gale et al. (2013) average MORB composition.
† Isotopic dates calculated using the decay constants λ238 = 1.55125E-10 and λ235 = 9.8485E-10 (Jaffey et al. 1971).
§ % discordance = 100 - (100 * ($^{206}Pb/^{238}U$ date) / ($^{207}Pb/^{206}Pb$ date))
# Th contents calculated from radiogenic ^{208}Pb and the $^{207}Pb/^{206}Pb$ date of the sample, assuming concordance between U-Th and Pb systems.
¨ Total mass of common Pb.
†† Ratio of radiogenic Pb (including ^{208}Pb) to common Pb.
§§ Measured ratio corrected for fractionation and spike contribution only.
Measured ratios corrected for fractionation, tracer and blank.

Table A3: Hf Isotopic Results

Frac.	$^{176}Hf/^{177}Hf$*	$\pm 2\sigma_{int}$†	$\pm 2\sigma_{tot}$§	$^{176}Lu/^{177}Hf$#	Age (Ma)	$^{176}Hf/^{177}Hf_{(i)}$**	$\pm 2\sigma$††	$\varepsilon Hf_{(i)}$	$\pm 2\sigma$	Total Hf (V)
IB1 (13R-4 36-42)										
z1	0.283078	0.000002	0.000008	0.0008	124.092	0.283076	0.000008	13.04	0.27	75.8
z3	0.283066	0.000002	0.000010	0.0005	124.092	0.283064	0.000010	12.64	0.35	76.3
z4	0.283068	0.000002	0.000010	0.0005	124.092	0.283066	0.000010	12.71	0.35	96.6
z5	0.283070	0.000006	0.000009	0.0008	124.092	0.283069	0.000009	12.79	0.33	10.7
z6	0.283070	0.000002	0.000010	0.0008	124.092	0.283068	0.000010	12.76	0.35	56.1
z7	0.283073	0.000002	0.000008	0.0009	124.092	0.283071	0.000008	12.88	0.28	62.7
IB2 (8R-4 11-17)										
z1	0.283074	0.000002	0.000010	0.0024	124.221	0.283068	0.000010	12.78	0.34	167.4
z2	0.283071	0.000002	0.000010	0.0021	124.221	0.283066	0.000010	12.70	0.35	78.0
z4	0.283077	0.000002	0.000009	0.0019	124.221	0.283072	0.000009	12.92	0.31	190.1
z5	0.283061	0.000002	0.000010	0.0012	124.221	0.283058	0.000010	12.43	0.34	132.1
z6	0.283060	0.000002	0.000010	0.0020	124.221	0.283055	0.000010	12.33	0.35	125.3
z7	0.283079	0.000007	0.000010	0.0014	124.221	0.283075	0.000010	13.03	0.36	8.3
NF2 (9R-5 50-56)										
z1	0.283206	0.000011	0.000014	0.0035	114.801	0.283199	0.000014	17.18	0.51	4.7
z2	0.283194	0.000006	0.000011	0.0041	114.801	0.283185	0.000011	16.70	0.39	11.4
z3	0.283190	0.000007	0.000012	0.0039	114.801	0.283182	0.000012	16.59	0.41	11.7
z4	0.283197	0.000007	0.000010	0.0042	114.801	0.283188	0.000010	16.82	0.36	7.5
z5	0.283198	0.000006	0.000010	0.0047	114.801	0.283188	0.000010	16.82	0.34	12.1
z6	0.283185	0.000005	0.000011	0.0029	114.801	0.283179	0.000011	16.49	0.38	12.7
z7	0.283199	0.000005	0.000010	0.0044	114.801	0.283189	0.000010	16.85	0.37	16.5
z8	0.283197	0.000003	0.000010	0.0056	114.801	0.283185	0.000010	16.69	0.36	29.7
z9	0.283189	0.000003	0.000012	0.0039	114.801	0.283181	0.000012	16.55	0.45	84.1
NF3 (9R-5 26-33)										
z1	0.283194	0.000005	0.000011	0.0030	114.787	0.283187	0.000011	16.78	0.38	12.7
z4	0.283191	0.000007	0.000012	0.0025	114.787	0.283185	0.000012	16.71	0.42	8.0
z5	0.283177	0.000008	0.000012	0.0034	114.787	0.283169	0.000012	16.14	0.44	7.4
z6	0.283199	0.000008	0.000011	0.0030	114.787	0.283192	0.000011	16.95	0.38	6.1
z7	0.283197	0.000004	0.000008	0.0037	114.787	0.283189	0.000008	16.84	0.30	20.9
z8	0.283180	0.000011	0.000016	0.0006	114.787	0.283178	0.000016	16.46	0.58	4.1
NF8 (9R-7 45-50)										
z1	0.283185	0.000004	0.000010	0.0013	114.854	0.283182	0.000010	16.59	0.36	34.3
z2	0.283196	0.000004	0.000010	0.0010	114.854	0.283193	0.000010	16.99	0.37	16.2
z3	0.283191	0.000007	0.000010	0.0012	114.854	0.283188	0.000010	16.81	0.36	10.3
z4	0.283188	0.000003	0.000010	0.0014	114.854	0.283185	0.000010	16.70	0.35	41.1
z5	0.283190	0.000002	0.000010	0.0011	114.854	0.283188	0.000010	16.80	0.35	63.5
z6	0.283201	0.000004	0.000010	0.0008	114.854	0.283199	0.000010	17.21	0.37	22.9
z7	0.283192	0.000003	0.000010	0.0011	114.854	0.283190	0.000010	16.87	0.35	31.3
z8	0.283183	0.000005	0.000011	0.0013	114.854	0.283181	0.000011	16.54	0.38	14.6
NF13 (9R-4 56-64)										
z1	0.283195	0.000003	0.000010	0.0033	114.741	0.283188	0.000010	16.81	0.36	23.5
z2	0.283184	0.000003	0.000010	0.0044	114.741	0.283174	0.000010	16.32	0.35	61.6
NF15 (9R-2 11-17)										
z1	0.283198	0.000002	0.000008	0.0013	115.199	0.283196	0.000008	17.08	0.27	141.6
z3	0.283195	0.000002	0.000010	0.0012	115.199	0.283192	0.000010	16.97	0.35	78.7
z5	0.283206	0.000003	0.000010	0.0010	115.199	0.283203	0.000010	17.36	0.36	46.7
z6dil	0.283192	0.000002	0.000010	0.0013	115.199	0.283189	0.000010	16.86	0.35	99.0
z7	0.283193	0.000002	0.000010	0.0010	115.199	0.283191	0.000010	16.92	0.34	122.0
z9	0.283211	0.000001	0.000007	0.0018	115.199	0.283207	0.000007	17.50	0.27	204.8
NF19 (9R-1 146-148)										
z1	0.283203	0.000016	0.000019	0.0011	115.71	0.283201	0.000019	17.28	0.66	2.3
z2	0.283196	0.000010	0.000014	0.0012	115.71	0.283194	0.000014	17.03	0.50	3.8
FC1										
za	0.282184	0.000005	0.000010	0.0011	1099	0.282162	0.000010	2.60	0.34	11.6
zb	0.282171	0.000003	0.000008	0.0008	1099	0.282156	0.000008	2.38	0.30	52.2
zc	0.282173	0.000003	0.000008	0.0009	1099	0.282154	0.000008	2.32	0.30	75.0
zd	0.282187	0.000003	0.000009	0.0014	1099	0.282157	0.000009	2.44	0.31	51.5
ze	0.282179	0.000003	0.000008	0.0010	1099	0.282158	0.000008	2.46	0.30	48.0
zf	0.282179	0.000003	0.000008	0.0010	1099	0.282158	0.000008	2.46	0.30	53.0
R33 (University of Arizona)										
za	0.282751	0.000003	0.000008	0.0017	419	0.282737	0.000008	7.66	0.30	58.2
zb	0.282753	0.000003	0.000008	0.0015	419	0.282741	0.000008	7.79	0.30	52.3
zc	0.282751	0.000002	0.000008	0.0016	419	0.282738	0.000008	7.66	0.30	115.5
zd	0.282752	0.000003	0.000008	0.0018	419	0.282738	0.000008	7.67	0.30	49.8
ze	0.282746	0.000002	0.000008	0.0011	419	0.282738	0.000008	7.66	0.29	99.6
zf	0.282753	0.000002	0.000008	0.0013	419	0.282743	0.000008	7.85	0.30	64.9

91500										
zb	0.282308	0.000003	0.000008	0.0003	1063.6	0.282301	0.000008	6.74	0.28	34.3
zc	0.282301	0.000005	0.000009	0.0003	1063.6	0.282295	0.000009	6.53	0.31	16.2
zd	0.282304	0.000003	0.000008	0.0003	1063.6	0.282297	0.000008	6.60	0.28	41.9
ze	0.282306	0.000004	0.000008	0.0003	1063.6	0.282300	0.000008	6.69	0.29	28.5

* Modern $^{176}Hf/^{177}Hf$ ratios measured by MC-ICP-MS on purified Hf aliquots. See supplementary file with analytical methods for details

† Internal uncertainties (2 SE) estimated for each individual run based on counting statistics

§ Total analysis uncertainty (2 SE) estimated from the propagation of individual internal uncertainties and 2 SD reproducibility of bracketing 25 ppb JMC-475 Hf standards used for correction. See supplementary file with analytical methods for details

$^{176}Lu/^{177}Hf$ compositions estimated from elemental Lu/Hf ratios measured on our 'trace element' aliquots and using a 'natural' $^{175}Lu/^{176}Lu$ = 0.02655 from Vervoort et al. (2004). See supplementary file with analytical methods for details

** Initial $^{176}Hf/^{177}Hf$ ratios corrected for radiogenic ingrowth using the calculated $^{176}Lu/^{177}Hf$ composition of each zircon and the decay constant of Söderlund et al. (2004); 1.867×10^{-11} y^{-1}

†† Uncertainty on the initial $^{176}Hf/^{177}Hf$ ratio assumed as the total uncertainty of the $^{176}Hf/^{177}Hf_{(0)}$ ratio. No uncertainties on the estimated $^{176}Lu/^{177}Hf$ or $\lambda^{176}Lu$ were propagated

Table A4: $^{176}Hf/^{177}Hf$ Isotopic Composition of MORB between the Azores and the Charlie Gibbs Fracture Zone

Sample Name	Reference	Latitude	Longitude	$^{176}Hf/^{177}Hf^{*}$
TRI0154-019-003	Agranier et al. (2005)	40.74	-29.25	0.283359
TRI0154-018-002	Agranier et al. (2005)	41.18	-29.31	0.283269
TRI0154-017-002	Agranier et al. (2005)	41.67	-29.26	0.283252
TRI0154-016-003	Agranier et al. (2005)	42.39	-29.4	0.283233
TRI0154-015-002	Agranier et al. (2005)	42.79	-29.36	0.283173
AII0032-3-012-008	Agranier et al. (2005)	42.96	-29.18	0.283142
TRI0154-012-001	Agranier et al. (2005)	43.37	-28.98	0.283233
TRI0154-012-002	Agranier et al. (2005)	43.37	-28.98	0.28325
TRI0154-013-001	Agranier et al. (2005)	44.00	-28.39	0.283247
TRI0154-014-005	Agranier et al. (2005)	44.82	-28.04	0.283238
TRI0154-014-001	Kelley et al. (2013)	44.82	-28.04	0.283256
CHR0043-104-016	Agranier et al. (2005)	45.18	-27.9	0.283351
HUD1966-047-B1	Agranier et al. (2005)	45.37	-28.22	0.283229
TRI0138-001-002	Agranier et al. (2005)	46.23	-27.39	0.283254
TRI0138-002-003	Agranier et al. (2005)	47.05	-27.35	0.283273
TRI0138-003-001	Agranier et al. (2005)	47.78	-27.64	0.283248
TRI0138-005-001	Agranier et al. (2005)	49.52	-28.54	0.283246
TRI0138-006-001B	Andres et al. (2004)	50.043	-28.933	0.283429
TRI0138-007-001A	Blichert-Toft et al. (2005)	50.46	-29.42	0.283346
TRI0138-008-001	Blichert-Toft et al. (2005)	51.28	-30.02	0.283301
TRI0138-009-002	Blichert-Toft et al. (2005)	51.56	-29.92	0.283324
TRI0138-011-001	Blichert-Toft et al. (2005)	52.01	-29.95	0.283292

*Mean is 0.28327 ± 0.00013 (2σ).